



HAL
open science

Synthesis and Shaping of Functionalized Microporous Materials for the Catalytic Transformation of Monosaccharides

Bakytzhan Yeskendir

► **To cite this version:**

Bakytzhan Yeskendir. Synthesis and Shaping of Functionalized Microporous Materials for the Catalytic Transformation of Monosaccharides. Material chemistry. Université Polytechnique Hauts-de-France, 2022. English. NNT : 2022UPHF0023 . tel-04144002

HAL Id: tel-04144002

<https://theses.hal.science/tel-04144002>

Submitted on 28 Jun 2023

HAL is a multi-disciplinary open access archive for the deposit and dissemination of scientific research documents, whether they are published or not. The documents may come from teaching and research institutions in France or abroad, or from public or private research centers.

L'archive ouverte pluridisciplinaire **HAL**, est destinée au dépôt et à la diffusion de documents scientifiques de niveau recherche, publiés ou non, émanant des établissements d'enseignement et de recherche français ou étrangers, des laboratoires publics ou privés.

Thèse de doctorat

Pour obtenir le grade de Docteur de l'UNIVERSITÉ POLYTECHNIQUE HAUTS-DE-FRANCE et de l'INSA HAUTS-DE-FRANCE et de l'UNIVERSITÉ DE LILLE

Discipline, spécialité selon la liste des spécialités pour lesquelles l'École Doctorale est accréditée :
Chimie, Spécialité Chimie des Matériaux

Présentée et soutenue par **Bakytzhan YESKENDIR**

Le **29/06/2022**, à Villeneuve d'Ascq

École doctorale :

École Doctorale Polytechnique Hauts-de-France (ED PHF n°635)

Unités de recherche :

Laboratoire de Matériaux Céramiques et de Mathématiques (CERAMATHS)
Unité de Catalyse et Chimie du Solide (UCCS)

Synthèse et mise en forme de matériaux microporeux fonctionnalisés pour la transformation catalytique des monosaccharides

JURY

President du jury

-De Oliveira Vigier Karine. Professeur des Universités. Université de Poitiers.

Rapporteurs

-Essayem Nadine. Directeur de Recherche CNRS. Université Claude Bernard Lyon 1.
-Paillaud Jean-Louis. Directeur de Recherche CNRS. Université de Haute-Alsace.

Examineurs

-De Weireld Guy. Professeur des Universités. Université de Mons.

Co-directeur de thèse : Courtois Christian. Professeur des Universités. Université Polytechnique Hauts-de-France.

Co-directeur de thèse : Dacquain Jean-Philippe. Maître de Conférences. Université de Lille.

Co-encadrant : Lorgouilloux Yannick. Maître de Conférences. Université Polytechnique Hauts-de-France.

Co-encadrant : Dhainaut Jérémy. Chargé de Recherche CNRS. Université de Lille.

Membres invités

-Royer Sébastien. Professeur des Universités. Université de Lille.

**Submitted for the degree of Doctor of Philosophy from
UNIVERSITÉ POLYTECHNIQUE HAUTS-DE-FRANCE
and INSA HAUTS-DE-FRANCE
and UNIVERSITY OF LILLE**

Specialty:
Chemistry of Materials

Presented and defended by Bakytzhan YESKENDIR

On 29/06/2022, Villeneuve d'Ascq

Doctoral school:

Doctoral School Polytechnique Hauts-de-France (ED PHF n°635)

Research units:

Laboratory of Ceramic Materials and Mathematics (CERAMATHS)
Unit of Catalysis and Chemistry of Solids (UCCS)

**Synthesis and Shaping of Functionalized Microporous Materials for the Catalytic
Transformation of Monosaccharides**

JURY

Jury president:

-De Oliveira Vigier Karine. Professor. University of Poitiers.

Reviewers

-Essayem Nadine. CNRS Research Director. University Claude Bernard Lyon 1.
-Paillaud Jean-Louis. CNRS Research Director. University of Haute-Alsace.

Examiners

-De Weireld Guy. Professor. University of Mons.

Thesis co-director: Courtois Christian. Professor. Université Polytechnique Hauts-de-France.

Thesis co-director: Dacquain Jean-Philippe. Associated Professor. University of Lille.

Co-supervisor: Lorgouilloux Yannick. Associated Professor. Université Polytechnique Hauts-de-France.

Co-supervisor: Dhainaut Jérémy. CNRS Researcher. University of Lille.

Invited members: Royer Sébastien. Professor. University of Lille.

Acknowledgments

Firstly, I would like to thank my supervisors for giving me this opportunity to work on such an interesting and diverse topic. I thank Sébastien ROYER who first accepted me for a short internship back in 2017 when the world was a lot more joyful than now. Since that time, I have known you as a true leader: professional and supportive in any situation. I appreciate every day I have worked in your team. Jérémy DHAINAUT, I thank you for all the help and assistance you provided me with during this time. There are many directions to lead this work and I am sure with your determined mind and enthusiasm it will have a great continuation. I wish you good luck. Jean-Philippe DACQUIN, I am not quite sure that words can express how lucky I was to have you as a supervisor. You are a great teacher and a wonderful person. Your outstanding professional and personal qualities is a gem for the scientific community. I have learnt a lot from you and I am endlessly grateful to you for that.

I would like to thank l'Université Polytechnique Hauts-de-France for financing this project. Also, I thank Christian COURTOIS and Yannick LORGOUILLOUX for directing it and helping when it was needed.

I sincerely thank all the staff of Université de Lille and especially of Unité de Catalyse et Chimie du Solide (UCCS) for their professional assistance and the friendly environment they create at work. Each of them has greatly contributed to this work and for this I say merci beaucoup: Olivier GARDOLL for the TGA, TPD and many more, especially for the pleasant every day small talks. Pardis SIMON for the XPS and see below; Jean-Charles MORIN and Mélanie DUBOIS for IR measurements followed by nice discussions; Martine TRENTESAUX for the RAMAN studies accompanied by a very productive training; Mickaël CAPRON for the batch reactor and the full access to HPLC (in fact you saved this work). Laurence BURYLO for the PXRD and quick results; Natacha HENRY for the XRD training and structural simulations. Nicolas NUNS for the ToF-SIMS analyses and good results; Joëlle THURIOT for the elemental analyses and rapidity; Robert WOJCIESZAK for the carousel reactors and especially Priscilla MAGALHAES de SOUZA for catalytic tests and overall support.

Many people outside the UCCS lab have also greatly contributed to this work and I thank them truly: Alexandre FADEL (SEM and see below), Ahmed ADDAD (TEM) and Maya MARINOVA (HRTEM), Hervé VEZIN (EPR), Alain MOISETTE (IR and Raman).

This wonderful PhD journey has given me a lot of friends who have become close to my heart and with whom I share the most remarkable and joyful moments within the past few years. Carmen CIOTONEA, superwoman, the first person who I made friends with back in 2017. Your talent goes beyond the lab doors and strikes every aspect of this life. Thank you for the endless support, true friendship and of course delicious food (hello to Vlad and ZuZu). Pardis SIMON, I admire the way you are: highly professional at work and yet humble and adorable in everyday life. I thank you for the moments of joy that we have shared that will always warm my heart and who knows maybe one day they will melt that snowball. Alexandre FADEL with whom I share common views on life and from whom I have learnt a lot including the electron-matter interaction. Follow your dream, I wish you good luck wherever you go and whatever you do. I also thank my friends who

have already finished their work and who are now somewhere around the globe: Guillaume POMALAZA, I admire your mindset and sense of humor; Guillaume ROCHARD, what happens in Dunkerque stays in Dunkerque...

I would like to acknowledge Pacôme CHAPEL, who did his M2 internship with me. I hope it was of good use and that you have gained knowledge. I used to call you "monsieur le stagiaire" for fun but I see your passion for science. So, keep it up and stay motivated. I wish you the best of luck for your future et surtout sois heureux.

I would also like to acknowledge my colleagues from MATCAT team: Amanda SFEIR (a.k.a. Swagelok), Joseph BOULOS (oven-holder), Rénald BEZY (a.k.a. professeur Rénald) and Roger DEPLAZES (our newcomer) and wish them a great debut/continuation of the adventure that is PhD. I would also like to thank my friends with whom I worked for a little while and with whom I shared some truly wonderful time: Camila ABREU TELES (viens là) and Andrea OSTI (an Italian man in Lille).

I would also like to thank my next-door colleagues from the LASIRE group Hania AHOUARI and Giuseppe SICOLI with whom I had the everyday pleasure to share some great moments. Thank you for your care, Hania and for your great sense of humor, Giuseppe. Also, to my colleague, Mahdi KHALIL, who joined our office a short time ago and quickly became a friend of mine: good luck to you and do what Giuseppe tells you to do.

Last but not least, with all my heart I thank my family: my mom, my brother and my sisters for simply being the best family I could ever wish for. It is amazing how love and support can cross distances. Love you! Also, I thank my friends in my home country who, for some unknown reason, still have my number and call me occasionally to get on my nerves. Friendship lasts a lifetime!

Abstract

Biomass valorization is a process of converting different types of plants and residual wastes into high-value chemicals and energies carriers. Zeolites and Metal-Organic Frameworks (MOFs) have attracted a great deal of interest as solid catalysts owing to their developed chemical properties as well as large available surface areas. A further functionalization can tune their intrinsic acid-base properties to boost their catalytic performance in a given reaction. Such tailoring mostly implies framework functionalization in MOFs and isomorphous substitution in zeolites. However, both processes are accompanied with several challenges associated with the realization and characterization of such-modified solids.

In this regard, a series of framework functionalization was performed on UiO-66 to produce UiO-66-SO₃H, UiO-66-COOH, UiO-66-NH₂ and UiO-66-OH MOFs. On the other hand, isomorphous substitution in a [Si,Al]-MFI type zeolite was conducted in order to replace Al by Zr atoms to make [Si,Zr]-MFI zeolitic solids. Thus-formed solids were exposed to a detailed characterization on structural, textural and chemical properties and eventually applied as solid catalysts. Thus, UiO-66-SO₃H demonstrated superior performance in fructose dehydration to 5-hydroxymethylfurfural due to its pronounced Brønsted acid properties making it the best catalyst with respect to other tested solids. Subsequently, this was followed by upscaling of its small-scale synthesis and shaping by extrusion. At the same time, [Si,Zr]-MFI showed the highest activity in glucose isomerization to fructose as compared to other solids owing to its basic features.

KEYWORDS: MOFs, Zeolites, Biomass Valorization, Shaping, Dehydration, Isomerization

Résumé

La valorisation de la biomasse inclut les processus de conversion de différents types de plantes et de déchets végétaux en produits chimiques et biocarburants à haute valeur ajoutée. Les zéolithes et une classe récente de matériaux appelés Metal-Organic Frameworks (MOFs) ont suscité un grand intérêt en tant que catalyseurs solides en raison de leurs propriétés chimiques développées ainsi que de leurs grandes surfaces spécifiques. Une modification spécifique peut moduler leurs propriétés acido-basiques afin d'améliorer leurs performances catalytiques dans une réaction donnée. De telles modifications impliquent notamment une fonctionnalisation du réseau des MOFs, ou une substitution isomorphe dans la charpente de la zéolithe. Cependant, les deux procédés sont accompagnés de plusieurs difficultés associées à la réalisation et à la caractérisation des solides ainsi modifiés.

À cet égard, différentes fonctionnalisations chimiques ont été réalisées sur la phase UiO-66 pour produire des matériaux UiO-66-SO₃H, UiO-66-COOH, UiO-66-NH₂ et UiO-66-OH. D'autre part, une substitution isomorphe dans une zéolithe de type [Si,Al]-MFI a été réalisée afin de remplacer les atomes Al par des atomes Zr pour fabriquer des solides zéolithiques de type [Si,Zr]-MFI. Les solides ainsi formés ont été caractérisés pour obtenir une description détaillée des propriétés structurales, texturales et chimiques, et finalement ont été appliqués en tant que catalyseurs. Parmi les solides testés, l'UiO-66-SO₃H a démontré des performances supérieures pour la déshydratation du fructose en 5-hydroxyméthylfurfural, en raison de ses propriétés acides Brønsted prononcées. À cet égard, une synthèse à grande échelle de l'UiO-66-SO₃H a été réalisée suivi de sa mise en forme par le procédé d'extrusion. D'autre part, [Si,Zr]-MFI a montré l'activité la plus élevée pour

l'isomérisation du glucose en fructose par rapport aux autres solides testés en raison de ses propriétés basiques.

MOTS-CLÉS : MOFs, Zéolithes, Biomasse, Mise en forme, Déshydratation, Isomérisation

Table of Contents

General introduction.....	1
Chapter I - Literature Overview.....	8
1. Biomass Valorization	9
1.1. General Concepts	9
1.2. Lignocellulosic Biomass	10
1.3. Valorization of Glucose	12
1.4. Valorization of Fructose	14
2. Solid Acids as Catalysts	16
2.1. Zeolites.....	17
2.2. Metal-Organic Frameworks (MOFs)	19
2.3. Tuning of Acidic Properties in Zeolites and MOFs	23
2.4. MOFs vs Zeolites – Chemical and Structural Comparison.....	26
3. Fructose Dehydration on Solid Catalysts	29
3.1. Zeolites.....	29
3.2. MOFs.....	33
4. Glucose Isomerization on Solid Catalysts	37
4.1. Basic Zeolites	37
4.2. Lewis Acid Zeolites	41
4.3. MOFs.....	44
5. Upscaling and Limitations	50
5.1. Large Scale Synthesis.....	50
5.2 Shaping.....	51
References:.....	55
Chapter II - Experimental Part	67
1. Materials and Synthesis	68
1.1. Synthesis of UiO-66-based MOFs	68
1.1.1. UiO-66	68
1.1.2. UiO-66-SO ₃ H Traditional Approach	69
1.1.3. UiO-66-SO ₃ H Green Approach	69

1.1.4. UiO-66-OH.....	70
1.1.5. UiO-66-COOH.....	70
1.1.6. UiO-66-NH ₂	70
1.2. MFI Zeolitic Materials	72
1.2.1. [Si]-MFI	72
1.2.2. [Si,Al]-MFI	72
1.2.3. [Si,Zr]-MFI-in.....	73
1.2.4. [Si,Zr]-MFI-ex	73
1.3. Upscaling.....	74
1.4. Shaping.....	75
1.4.1. Extrusion	75
1.4.2. Pelletization.....	76
2. Characterization	76
2.1. Structural Properties	76
2.1.1. Powder X-Ray Diffraction (PXRD).....	76
2.1.2. ATR-IR (Attenuated Total Reflectance-Infrared Spectroscopy)	78
2.1.3. Raman Spectroscopy.....	79
2.2. Textural Properties	80
2.2.1. N ₂ Physisorption	80
2.3. Morphological Properties	82
2.3.1. Scanning Electron Microscopy (SEM)	84
2.3.2. High Resolution Transmission Electron Microscopy (HRTEM)	84
2.4. Surface Properties	84
2.4.1. X-Ray Photoelectron Spectroscopy (XPS)	84
2.4.2. ToF-SIMS (Time-of-Flight – Secondary Ion Mass Spectrometry)	85
2.5. Elemental Analysis.....	86
2.5.1. Inductively Coupled Plasma – Optical Emission Spectroscopy (ICP-OES)	86
2.5.2. Carbon, Hydrogen, Nitrogen and Sulfur (CHNS) Analysis	86
2.6. Chemical Properties	87
2.6.1. Temperature-Programmed Desorption (TPD)	87
2.6.2. Pyridine Adsorbed Infrared Spectroscopy (Py-FTIR)	88
2.7. Thermal Stability Properties.....	88

2.7.1. Thermogravimetric Analysis with Differential Scanning Calorimetry (TGA-DSC) .	88
3. Catalytic Tests	89
3.1. Fructose Dehydration	89
3.2. Fructose Dehydration on Shaped MOFs	90
3.3. Glucose Isomerization.....	90
4. References:.....	92
Chapter III - Properties and Catalytic Performance of Zeolites.....	93
1. Characterization of Zeolitic Materials	94
1.1. Structural Properties	94
1.1.2. XRD	94
1.1.3. ATR-FTIR and Raman Spectroscopy.....	96
1.2. Textural Properties	98
1.2.1. N ₂ Physisorption	98
1.3. Elemental Analysis.....	99
1.3.1. ICP-OES	99
1.4. Chemical Properties	100
1.4.1. TPD and Py-FTIR.....	100
1.5. Morphological Properties	102
1.5.1. SEM	102
1.5.2. HRTEM.....	103
1.6. Surface Properties	106
1.6.1. ToF-SIMS	106
1.6.2. XPS	107
2. Catalytic Tests	109
2.1. Fructose Dehydration to HMF	109
2.2. Glucose Isomerization to Fructose	112
3. Conclusion.....	117
4. References:.....	119
Chapter IV- Properties and Catalytic Performance of MOFs.....	122
1. Characterization of the Synthesized MOFs	124
1.1. UiO-66 and UiO-66-SO ₃ H by Traditional Way.....	124

1.1.1. Structural Properties (XRD)	124
1.1.2. Structural Properties (ATR-IR).....	124
1.1.3. Textural Properties (N ₂ physisorption)	126
1.1.4. Morphological Properties (SEM).....	127
1.2. UiO-66-SO ₃ H, UiO-66-COOH, UiO-66-OH and UiO-66-NH ₂ Green Way	128
1.2.1. Structural Properties (XRD)	129
1.2.2. Structural Properties (ATR-IR Spectroscopy)	131
1.2.3. Textural Properties (N ₂ physisorption)	132
1.2.4. Thermal Stability (TGA).....	133
1.2.5. Elemental Analysis (CHNS).....	135
1.2.6. Surface Properties and Elemental Composition (XPS)	136
2. Catalytic Tests	138
2.1. Fructose Dehydration on MOFs	138
2.1.1. Kinetic Profiles	141
2.1.2. Temperature Effect	144
2.1.3. Catalyst Reusability	145
2.1.4. Comparison with a Commercial Solid Acid Catalyst	149
2.2. Glucose Isomerization.....	150
3. Conclusion.....	152
4. References:.....	154
Chapter V - Upscaling and Shaping of UiO-66-SO₃H MOF	158
1. Upscaling and Shaping	160
1.1. Powder vs Shaped Object: Characterization	160
1.2. Powder vs Shaped Object: Catalytic Performance	166
2. Conclusion.....	169
3. References:.....	170
6. General Conclusion and Perspectives	172
ANNEX	178

General introduction

For decades, the worldwide production of energy and energy carriers has been based on traditional fossil fuels derived from natural sources of hydrocarbons such as coal, petroleum and natural gas. They enable heat and electricity generation used in everyday household as well as manufacture of transportation fuels such as gasoline and diesel. Technological breakthroughs and rapid progress of humankind economic development within the past decades lead to a growing demand of energy thus provoking further increase of its production and consumption. This unavoidably leads to a higher release of exhaust gases mainly carbon dioxide into the surrounding environment. As a consequence, concentration of CO₂ and other greenhouse gases in the atmosphere increases surpassing the cycling capacity of biogeochemical processes occurring in nature. Indeed, within the past 15-20 years the scientific community has alerted the world to the irreversible climate change caused by the elevated emission of greenhouse gases, notably CO₂. As a response to this call, the world's developed countries have launched numerous common policies to reduce these emissions and reach carbon neutrality by establishing low-carbon economies. This is one of the central points of the famous Paris Agreement adopted at the United Nations Climate Change Conference in 2015.

General strategy towards the carbon neutrality is based on a gradual reduction of carbon emissions while moving progressively towards renewable energy such as solar, wind or hydro as well as towards cleaner energy derived from nuclear power. The latter is of particular importance in France which is one of the world's three biggest nuclear power generating countries alongside the USA and China. According to Eurostat, total energy produced in the European Union in 2018 originated from fossil (35 %) and renewable sources (34 %) as well as nuclear power (31 %). Of note, France

General Introduction

and Belgium are the biggest nuclear energy producers with 78 % and 65 % of their total national energy productions, respectively.

At the same time, renewable energy is more diverse and mainly includes biomass burning for generation of heat and electricity as well as the electricity produced from wind, hydro and solar power plants. According to the ministry of ecological transition of France, biomass burning represented 41 % of the total renewable energy produced in the country in 2018. Whereas, hydro, wind and solar energy accounted for 20 %, 7 % and 3 %, respectively. Therefore, biomass is characterized as the main source of renewable source covering around the half of the producible energy. In addition to that, it is the only carbon-based renewable source which enables manufacturing liquid hydrocarbon alternatives to the traditional fossil fuels *i.e.* biofuels. Over the past 30 years, sustainable production of bioethanol and biodiesel has been successfully developed and industrially implemented by many countries in the world.

The potential of biomass can also cover the needs of chemical industry by providing renewable feedstocks in numerous productions. This is especially true in the case of the plastic industry which has become a central point of the environmental pollution. In this regard, using biomass as feedstock allows for biodegradable polymers as promising alternatives to the traditionally used petroleum-derived polymers and therefore contributing to a cleaner and safer environment.

Special attention has been drawn in recent years to production of renewable alternatives to the conventional solvents used in chemical industry. Primarily, this implies the replacement of the petroleum-based feedstock by biomass for production of alcohols, diols, esters and so on. However, it is also relevant to use biomass for production of entirely new green organic solvents such as, for instance, cyrene which has become a hot topic recently.

General Introduction

Another interesting aspect is that biomass enables production of biomolecules such as, for instance, sorbitol which are either impossible or highly challenging to produce from petroleum-based feedstock. Thus, more and more newly-derived compounds have found application in such fields as medicine, pharmacy and food industry further expanding the relevance of biomass.

Among different existing types of biomass, the so-called lignocellulose is of particular interest as it is the most abundant biomass and not used in food production. Its complex molecular and structural composition requires a certain pre-treatment prior to its conversion into useful chemicals. The latter depends on the targeted compound and in some cases might proceed through a chain of complex transformations. The majority of them are conditioned by the presence of a catalyst and therefore falls into the domain of enzymatic, homogeneous or heterogeneous catalysis. It is well known that the latter is characterized by the reaction mixture (typically liquid or gas) and the catalyst (typically solid) being in different phases. This allows for an easier separation of the catalyst from the reaction mixture as compared to homogeneous catalysis. Additionally, enzymes are generally highly sensitive to reaction conditions *i.e.* temperature and pH thus further highlighting the advantages of heterogeneous catalysis. Therefore, the latter is beneficial and stimulates the development of solid catalysts for various transformations within the field of biomass conversion.

In 2019, in MATCAT team (MATériaux pour la CATalyse) at UCCS (Unité de Catalyse et de Chimie du Solide) at Université de Lille, a study on application of microporous solids in biomass valorization was launched. It has resulted in a 3-year PhD project in collaboration with UPHF (Université Polytechnique Hauts-de-France) for which I was recruited. Essentially, the Matériaux Céramiques et de Mathématiques (CERAMATHS) team at UPHF has a great competence in upscaling and characterization of shaped objects based on ceramics. Whereas, MATCAT team has

General Introduction

a great expertise in synthesis and application of bulk (perovskites, mixed oxides) and supported mesoporous (SBA-15) materials in biomass conversion with several scientific contributions to this topic. Therefore, this new project has been initiated with the attempt to respond to the dynamics with which microporous solids are designed and successfully applied in biomass conversion with a certain effort made on their upscaling and shaping.

With this being said, the primary attention was given to zeolites which are among the most recognized and widely used microporous solids. Their unique structure composed of mixed SiO_2 - Al_2O_3 grants them crucial physico-chemical properties which make them excellent catalysts in numerous applications even without further deposition of active sites. This is because zeolites exhibit intrinsic acidic properties making them important solid acids. One of the appealing and yet challenging subjects in zeolite synthesis is the possibility to replace Al atoms by another element which unavoidably leads to alteration of their acid properties. Such replacement is known in the literature as isomorphous substitution and many elements have been successfully incorporated and some of them are poorly described in the literature.

Metal-Organic Frameworks (MOFs) are another type of microporous solids which were first discovered in the end of the 1990s. As compared to zeolites, they are considered new and have already attracted a great deal of both academic and industrial interest. The period from the late 1990s to the 2010s was the time of intense discovery of new MOFs leading to the outstanding 90 000 structures known so far. The application-targeted studies on MOFs vastly increased from the 2010s onwards. Essentially, MOFs are constituted from a metal node (ions or clusters) coordinated by organic linkers (acids or heterocyclic compounds) resulting in a crystalline, highly porous framework. Similar to zeolites, MOFs can be considered solid acids with their acid properties possible to modify *via* framework functionalization.

General Introduction

Therefore, this project aims at designing zeolites and MOFs with varied functionalities for further application as solid catalysts in the catalytic transformation of monosaccharides. It was decided to pick two representative reactions namely fructose dehydration to 5-hydroxymethylfurfural (HMF) and glucose isomerization to fructose. The idea behind this choice was dictated by the simplicity of both reactions as well as the different nature of active sites they require. Therefore, MOFs and zeolites produced in this work were subjected to modification of their acid-base properties in order to make them active in the Brønsted acid catalyzed fructose dehydration as well as in the Lewis acid (or base) catalyzed glucose isomerization.

The work has been done in the period from March 2019 to June 2022 and this manuscript is written in five chapters:

- Chapter I introduces general concepts of the work including biomass conversion, fructose dehydration and glucose isomerization with a short review of the active sites needed for each of the two reactions. It covers also the bibliographic research on the typical solid catalysts used for this purpose. A certain attention was given to the classical zeolites and MOFs and their comparison when applied in fructose dehydration and glucose isomerization. Chapter I also reviews the existing literature on upscaling and shaping of MOFs as it has recently become a central research interest in order to facilitate their industrial implementation.

- Chapter II summarizes the materials and methods used to accomplish the experimental part of this thesis. This includes the synthesis of a classical zeolite as well as isomorphous substitution performed to replace Al by Zr. As for MOFs, chapter II also describes the synthesis of the classical UiO-66 as well as its functional analogues *via* insertion of different groups into its framework: -SO₃H, -COOH, -OH and -NH₂. Besides, a detailed information on characterization methods applied on both zeolites and MOFs was provided. A special care was given to establish a green,

General Introduction

scalable synthesis of the functionalized MOFs in order to facilitate their upscaling and further shaping.

- Chapter III contains insights into the synthesized zeolites and includes detailed discussion of their characterization. It includes the classical MFI-type zeolite composed of $\text{SiO}_2\text{-Al}_2\text{O}_3$ and its isomorphously substituted analogues *i.e.* MFI-type metallosilicate composed of $\text{SiO}_2\text{-ZrO}_2$. The role of Zr and especially its location (either inside or outside the framework) will be discussed in detail. Therefore, a special attention was drawn to the evolution of their acid-base properties caused by the presence of Zr and its impact on the catalytic performance in fructose dehydration and glucose isomerization.

- Chapter IV comprises discussions on the synthesized MOFs and firstly includes the results of their functionalization *i.e.* characterization of the classical UiO-66 and its functionalized counterparts, UiO-66-SO₃H. Secondly, a certain effort was made to replace a hazardous and toxic solvent used for the synthesis of UiO-66-SO₃H by water thus providing green synthesis conditions. The solvent replacement led to some irreversible structural changes which were discussed in detail. This strategy was further successfully applied to a series of MOFs such as UiO-66-COOH, UiO-66-OH and UiO-66-NH₂. Chapter IV also provides insights into catalytic performance in fructose dehydration and glucose isomerization of thus-synthesized MOFs. This is followed by correlating the results with the acid-base properties induced by the functional groups.

- Chapter V represents a small contribution into the growing need for MOFs commercialization. It includes the outcome of the UiO-66-SO₃H synthesis upscaling after the optimization of its small-scale synthesis in green conditions. This was made in order to ensure the large amount of powdery UiO-66-SO₃H needed for its further shaping. For the latter, pelletization and extrusion were chosen as preliminary techniques to probe applicability of shaping on UiO-66-SO₃H. Therefore, chapter V

General Introduction

includes discussions on the effect of shaping on structural and textural properties of the MOF. This was followed by a quick evaluation of usability of thus-shaped UiO-66-SO₃H in fructose dehydration and their overall catalytic performance.

At the end, this manuscript contains the general conclusion of the performed work by outlining the critical and relevant points. Some future perspectives on the possible continuation of this project were also given.

Chapter I

Literature Overview

1. Biomass Valorization

1.1. General Concepts

Over the past few decades, the world has faced several global problems. One of them is climate change, which would inevitably occur due to uncontrollable emissions of greenhouse gases into the atmosphere. Nowadays it is becoming a central topic of debates as its first effects (higher temperatures, wildfires more frequent, storms more severe) became significant. Also, others, even more dramatic effects, are expected (sea level rise, more health risks, less food, loss of biodiversity). On the other hand, there is a full awareness that social and economic growth especially in developing countries will necessarily require a larger amount of energy. The latter, in turn, will unavoidably trigger even more emissions of greenhouse gases, especially carbon dioxide. Therefore, there is a strong need for developing sustainable fuels, power, heat and biomaterials to gradually substitute traditional fossil feedstocks. Due to the finite nature of the latter, a great deal of attention was drawn towards biofuels and biopower derived from renewable sources [1]. Among different types of renewable sources such as hydropower, wind power, solar power, geothermal energy and others, biomass is considered the only carbon-based energy source and therefore can potentially yield liquid hydrocarbon energy carriers. Generally speaking, biomass is any organic matter which can be used as energy source. This includes herbaceous biomass such as agricultural crops, woody biomass, marine algae or even animal organic matter [2]. Over the past decades, a great deal of attention has been drawn into biomass-derived biofuels for needs of transportation. Thus, one of the first biofuels of this kind is the famous bioethanol which has been used as a blend with gasoline for more than 40 years now. Besides, biodiesel or the so-called FAME (fatty acids methyl esters) can be added to this list of commercially available biofuels so far [3]. However, the major concern about the use of such

biofuels lies in the way they are produced. More precisely, they are both made of the crops traditionally used for food and animal feed. Thus, bioethanol production relies on corn or sugar cane while biodiesel requires vegetable oils and soybeans as raw materials. Therefore, there is a need nowadays for production of biofuels and biomass-derived fine chemicals from “non-food” *i.e.* inedible biomass mostly originated from residues of different nature: agriculture, food or wood production.

1.2. Lignocellulosic Biomass

Among different sources of biomass, lignocellulosic biomass is without a doubt the most attractive simply because it is the most abundant. The term “lignocellulosic” implies biomass mainly derived from agricultural wastes, hard or soft wood and grasses. It consists of three major components: cellulose, hemicellulose and lignin (figure I-1) and the ratio between each component varies depending on the plant it was issued from [3–5].

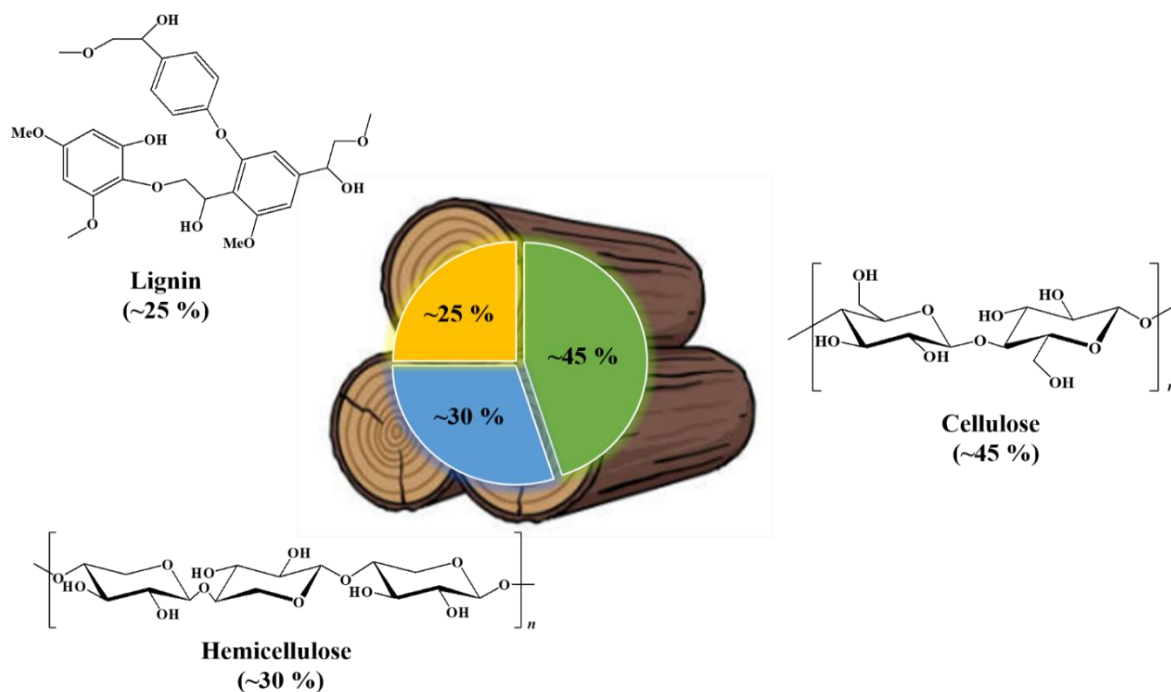


Figure I-1. Schematic representation of a typical chemical composition of lignocellulosic biomass derived from a wood-based biomass. Lignin’s composition is simplified due to its complex structure. Adapted from [4,5].

Typical valorization of lignocellulosic biomass upon harvesting includes drying and thermal processing *via* combustion, pyrolysis, gasification, liquefaction or fermentation to produce biofuels (gas, liquid, bioethanol) and bioenergy (heat, electricity) [2,5]. In addition, lignocellulosic biomass has a great potential towards production of a wide variety of high-value chemicals. For this, a certain pretreatment is needed. This step is crucial as it allows to convert carbohydrate polymers into sugar monomers in a cost-effective way, however technologically challenging at large scale due to separation issues. Nevertheless, general pretreatment technologies include physical (ultrasonic, irradiation), chemical (acid, alkali), and biological (microbes/enzymes) methods [5]. Upon typical acidic or enzymatic pretreatment used oftentimes, cellulose and hemicellulose are depolymerized into hexoses and pentoses, respectively, whereas the lignin component breaks down into phenolic compounds [6,7]. Thereafter, many reactions may be performed to convert the sugar monomers and the phenolic compounds derived hereafter into more valuable products, such as hydrogenation, isomerization, and deoxygenation (figure I-2).

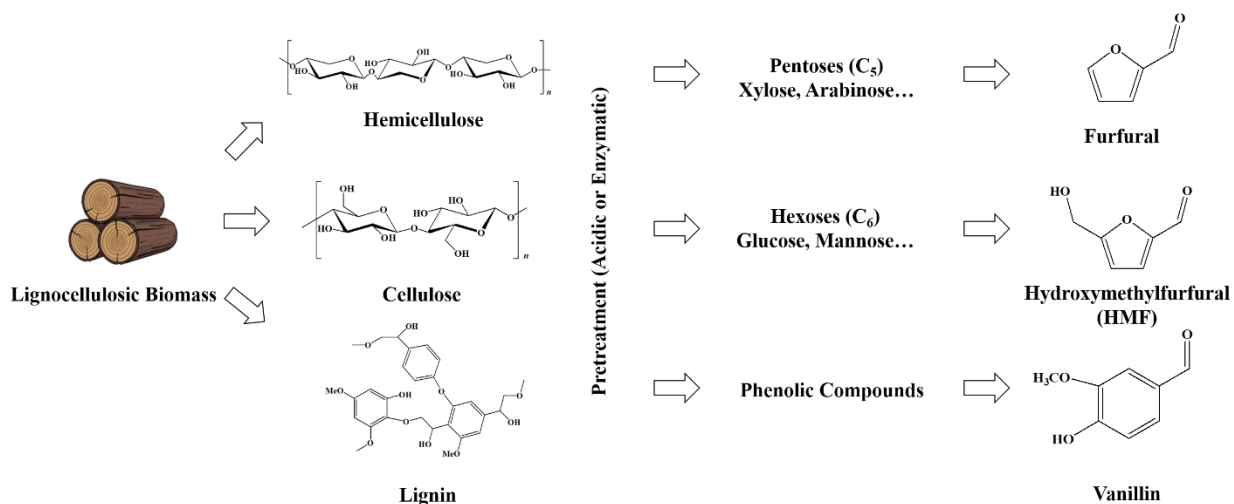


Figure I-2. Schematic representation of examples of valuable chemicals derived from lignocellulosic biomass upon its pretreatment step. Adapted from [8,9].

Some of them, such as furfural, can only be produced from lignocellulosic biomass, while for others, such as lactic acid, the traditional petroleum-derived production is progressively replaced by a sustainable route *via* fermentation of lignocellulosic biomass [10]. Interestingly, vanillin, which is widely-used in food industry and traditionally made from the petroleum-derived guaiacol, was shown to be sustainably produced from lignin with the remarkable 15 % of the total annual vanillin production [11,12].

1.3. Valorization of Glucose

One of the critically important biosourced molecules is glucose, a six-membered monosaccharide. Glucose is naturally found in plants, mostly in fruits and berries, and is primarily used in the food industry as a sweetener. In chemical industry, glucose is a well-known starting material for the synthesis of high-value platform chemicals [13]. Industrial production of glucose consists of acid or enzyme catalyzed hydrolysis of polysaccharides, notably starch derived from corn or wheat [14]. At the same time, glucose can be produced from lignocellulosic biomass as well *via* acid or enzyme catalyzed process [15]. However, it is more challenging due to the composition of lignocellulosic biomass from which only the cellulose fraction can break into glucose monomers. This requires additional separation and purification steps. Moreover, cellulose is generally less soluble in water than starch which further complicates the treatment.

Nevertheless, glucose has a high potential for further chemical transformations. Thus, upon hydrogenation, it is converted into sorbitol, an important sugar alcohol with numerous applications especially as a precursor for the synthesis of vitamin C [16]. Upon further dehydration, sorbitol yields isosorbide, another important biosourced molecule with a high potential as a renewable and biodegradable monomer for the production of biopolymers such as polyesters and polycarbonates (figure I-3) [17].

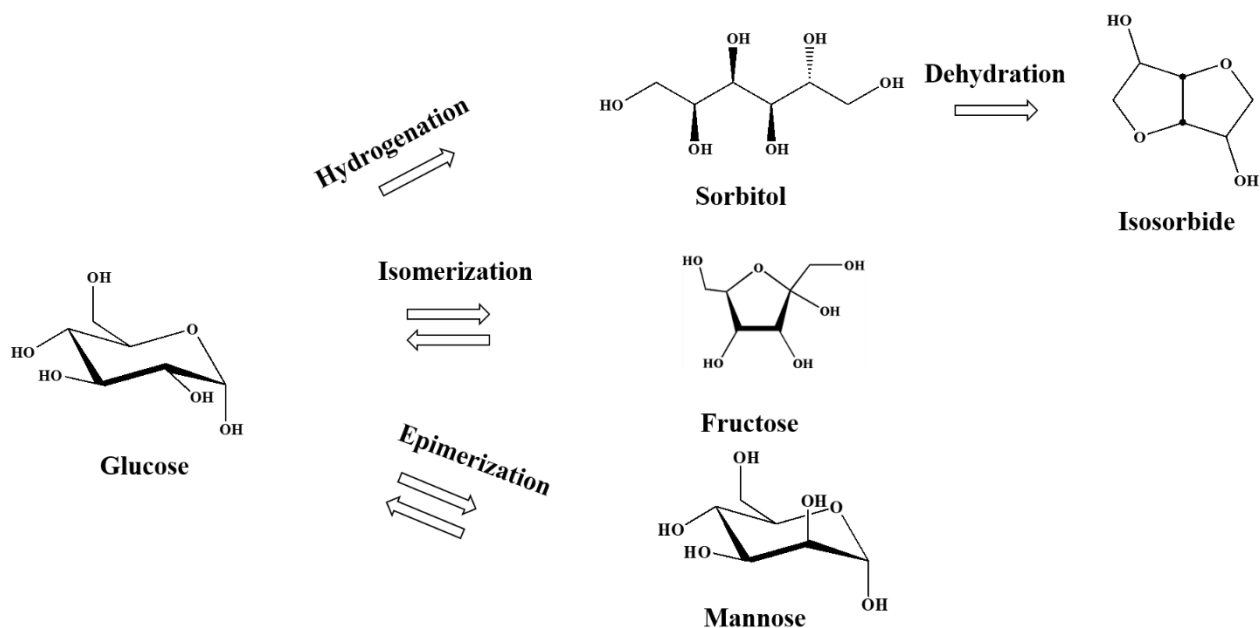


Figure I-3. Schematic representation of the routes towards glucose-derived biomolecules [13].

Glucose isomerization into fructose is a critical process as the latter opens up the doors towards a large variety of bio-derived platform chemicals. Glucose isomerization is a reaction typically catalyzed by Lewis acids therefore a plethora of classical Lewis acids have been applied for this purpose [18–20]. Generally, glucose isomerization over Lewis acids proceeds *via* the so-called “intramolecular hydride shift” multi-step mechanism (figure I-4). The latter includes glucose ring-opening to the acyclic form once adsorbed on a catalyst. This is followed by glucose-to-fructose isomerization at C₁ to C₂ positions (at this stage hydride shift occurs on a Lewis acid site). Finally, ring-closure proceeds in order to release the formed fructose. On the other hand, bases can also catalyze the glucose-to-fructose isomerization and many bases have also been examined in both heterogeneous [21–25] and homogeneous [26–28] catalysis domains. Of note, over a solid base catalyst, the reaction proceeds in a different fashion, *via* the so-called “proton transfer” mechanism which implies deprotonation of glucose by a base catalyst. Upon isomerization at C₁ to C₂ positions the proton is moved back from the catalyst to release fructose (figure I-4).

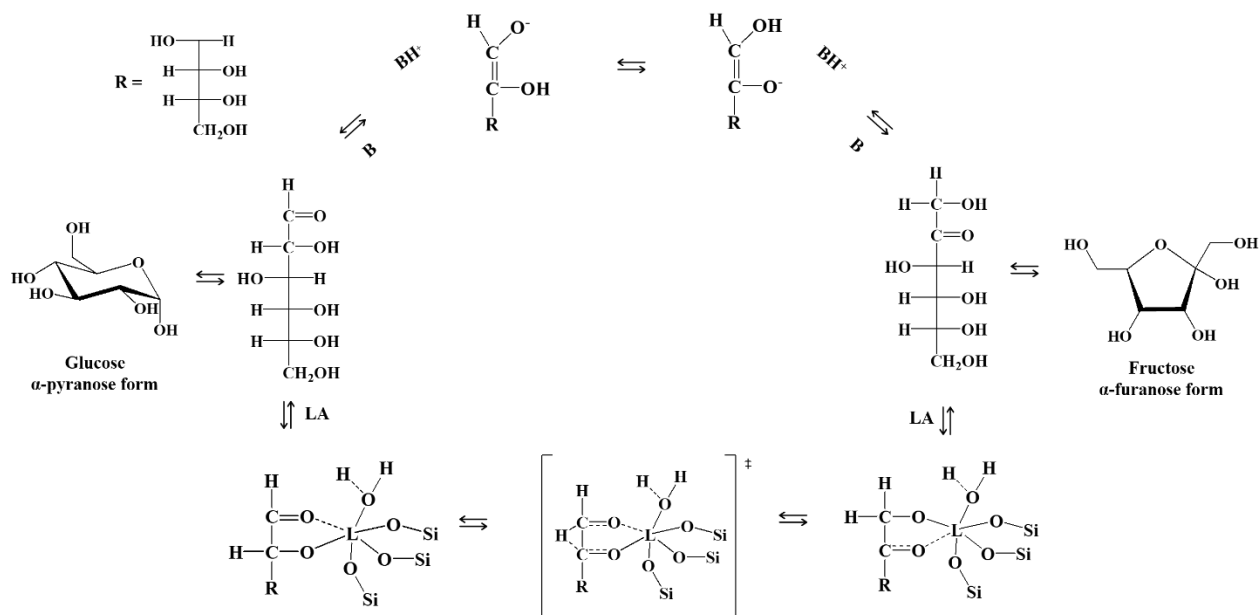


Figure I-4. Schematic representation of the mechanisms of glucose isomerization into fructose catalyzed by bases (B, top: “proton transfer”) and Lewis acids (LA, bottom: “intramolecular hydride shift”). The Lewis acid site (L) is represented here as a metal site on a typical zeolitic material. Adapted from [29].

1.4. Valorization of Fructose

Fructose is another important biomass derived molecule, a simple six-membered monosaccharide. As a glucose isomer, fructose has the same natural occurrence as glucose and is used as well mainly in the food industry, more precisely for the production of beverages. It is an important starting material in chemical industry which enables high-value chemicals and is produced from glucose *via* isomerization as discussed above. Also, the industrial production of fructose mainly implies isomerization of glucose obtained from hydrolysis of corn or wheat starch. This process is catalyzed by enzymes and is considered one of the first examples of industrial implementation of enzymatic catalysis [30].

Fructose dehydration into 5-hydroxymethylfurfural (5-HMF or HMF) (figure I-5) is of particular interest as it is considered as a key renewable platform chemical for the production of additives

for conventional hydrocarbon fuels as well as a substitute for the preparation of building blocks in polymers production. Industrial production of HMF was only implemented a few years ago, in 2014, by a Swiss company “AVA Biochem” with the annual capacity of 20 tons. HMF formation *via* fructose dehydration is typically catalyzed by Brønsted acids, however, direct formation from glucose is also possible through the initial isomerization step catalyzed by Lewis acids or bases as shown above. The latter is more desirable as glucose is more abundant and cheaper than fructose, however, the yields are much lower due to the additional isomerization step which limits the overall reaction rate. Typically, the direct fructose-to-HMF dehydration is a one step process which, due to the simplicity, has been extensively studied for many years, therefore constantly enriching the existing literature on this subject. Accordingly, it includes studies on fructose dehydration in many different solvents (organics, water, binary systems) as well as ionic liquids [31–36]. Besides, there is a wide variety of applied catalysts such as mineral/organic acids [37–41] and solid acids [42–47] bringing this reaction in both homogeneous and heterogeneous catalysis domains, respectively.

Of note, it is clear that the choice on heterogeneous catalysis profits the product-catalyst separation and therefore is more beneficial over homogeneous catalysis. At the same time, water as the solvent is a poor choice as it does not favor dehydration and shifts the chemical equilibrium towards the reactant. Ionic liquids, on the other hand, despite their activity are expensive as compared to the conventional solvents. Therefore, a reasonable fructose dehydration process would be performed over a solid catalyst in an organic solvent. The choice of the latter is limited due to the poor solubility of fructose, and sugars in general, in organic solvents.

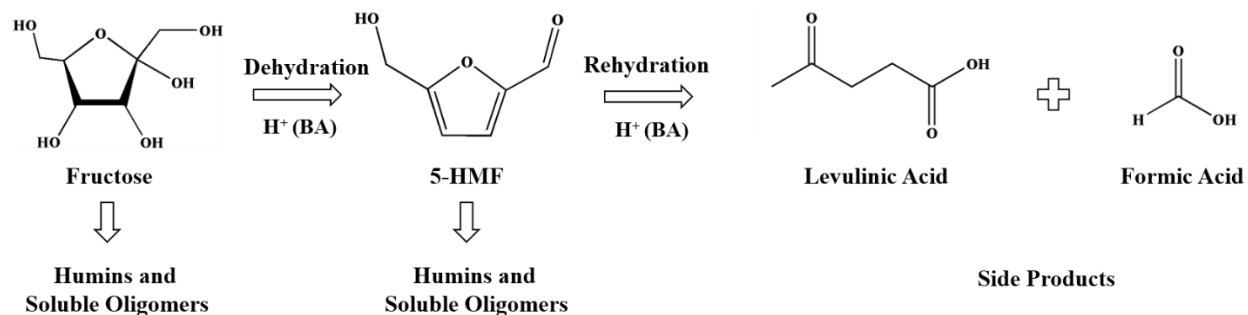


Figure I-5. Schematic representation of fructose dehydration over Brønsted acids and potential side reactions. Adapted from [48].

Nevertheless, upon further dehydration HMF can undergo ring-opening due to rehydration leading to levulinic acid, another important platform chemical formed equimolarly together with formic acid [49,50] (figure I-5). The former is a precursor to ethyl-levulinate and gamma-valerolactone (GVL), two potential biofuels which can be also used as green solvents [51,52]. Lastly, despite challenges a cascade reaction starting from glucose to form HMF is possible using conventional solid acids with pronounced acidic properties (dual Brønsted-Lewis) [53,54].

2. Solid Acids as Catalysts

Typical solid acids classically include oxides such as Al₂O₃; mixed oxides: amorphous or crystalline SiO₂-Al₂O₃; mixed metal oxides: Nb₂O₃-WO₃; resins: Amberlyst or Nafion; or promoted oxides: SiO₂-SO₃H, ZrO₂-SO₃H. Traditionally, acidic properties of solid acids are described by the following features:

- 1) nature of acid sites: Lewis and/or Brønsted;
- 2) number of acid sites which is analogous to concentration of liquid acids;
- 3) acid site strength which is analogous to pK_a values of liquid acids.

2.1. Zeolites

Zeolites are crystalline microporous aluminosilicates. As the name suggests they are composed of silicalite (SiO_4) and aluminate (AlO_4^-) tetrahedral units (or Primary Building Units, PBUs) with an approximate molecular formula $\text{M}_{x/n}(\text{AlO}_2)_x(\text{SiO}_2)_y \cdot z\text{H}_2\text{O}$, where M is the cation of valence n ($n = 1$ or 2) compensating the negatively charged framework originated from the tetrahedrally coordinated Al atom. Interconnection of the PBUs *via* bridging oxygen atoms enables formation of the so-called Secondary Building Units (SBUs) which upon further interconnection define the final zeolite framework. Nowadays, there are around 255 unique structures approved by IZA (International Zeolite Association) and the number continues to grow [55]. The frameworks are usually named after the scientists or companies who first discovered them. For example, the famous FAU zeolite is named after the French geologist Barthélemy Faujas de Saint-Fond. Additionally, zeolites are oftentimes described by the number of framework atoms constituting the “rings” *i.e.* the associated pores. “Members” in a zeolite ring are represented by Si and Al atoms (or more generally T-atoms) and serve as an additional way to distinguish zeolites frameworks. For instance, there are frameworks with 8-membered rings (MR) having 8 Si or Al atoms forming pores with a size of <0.45 nm, 10-membered rings with <0.6 nm, 12-membered rings with <0.8 nm and even 14-membered rings with >0.8 nm pore size [55,56].

Thanks to their excellent textural and physico-chemical properties as well as their high thermal stability, zeolites have been used in numerous applications including ion-exchange, adsorption, heterogeneous catalysis and many more [57–60]. Among these 255 zeolite structures, only a few retained most of academic and industrial interest making up the “Top-5” zeolites: Mordenite which belongs to MOR framework type according to IZA, Ferrierite (FER), beta (*BEA), Y (FAU) and ZSM-5 (MFI) (figure I-6). Notably, the ZSM-5 zeolite is composed of SBUs of “pentasil” type,

forming a continuous 3-dimensional organization. Its framework consists of intersecting straight and sinusoidal pores of around 0.55 nm originated from the interconnection of the pentasil SBUs and thus resulting in 10-membered rings. Specifically, the ZSM-5 has been used as an industrial catalyst for cracking, isomerization and alkylation processes over decades and continues to be the benchmark catalyst in petrochemical industry [61].

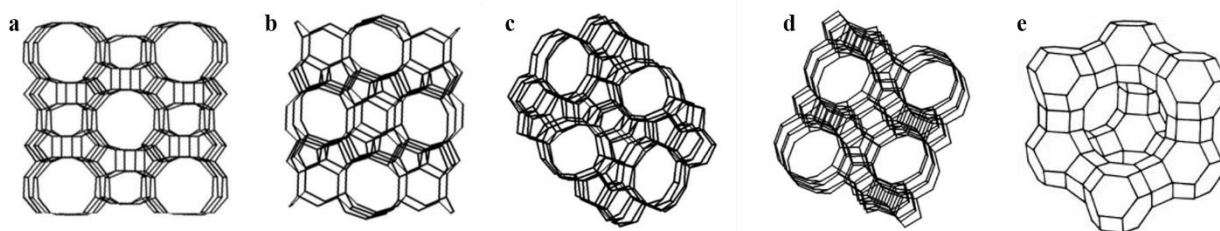


Figure I-6. The “Top-5” zeolite frameworks: MOR (12 MR, a) with pore size of 0.65 nm x 0.70 nm; FER (10 MR, b) with pore size of 0.48 nm x 0.55 nm; MFI (10 MR, c) with pore size of 0.51 nm x 0.55 nm; *BEA (12 MR, d) with pore size of 0.67 nm x 0.66 nm and FAU (12 MR, e) with pore size of 0.74 nm x 0.74 nm [56]. Adapted from [62].

Traditionally, zeolites are produced *via* hydrothermal method *i.e.* under elevated pressure and temperature using a Si-source (colloidal SiO₂ or tetraethyl orthosilicate, TEOS) and an Al-source (Al-salts). Besides, their synthesis relies on the use of organic structure-directing agents (OSDAs) to form the desired types of pores and channels. These represent a large class of compounds and include tetrapropylammonium hydroxide (TPAOH), ethylenediamine (EDA), diethanolamine (DEA) and many others. Last but not least, crystallization of zeolites during hydrothermal treatment is ensured by the alkalinity of the synthesis solution, therefore implying the use of classical alkali hydroxides such as NaOH [63,64]. The latter results in Na⁺ acting as cations compensating the negatively charged zeolite framework once the synthesis is accomplished.

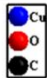
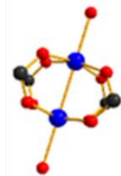
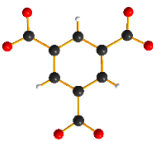
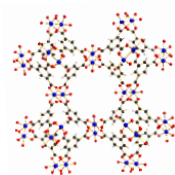
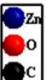
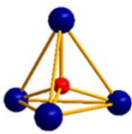
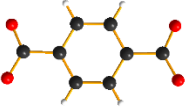
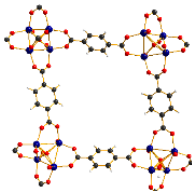
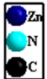
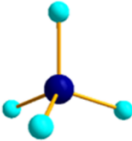

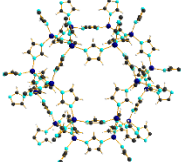
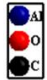

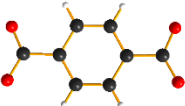
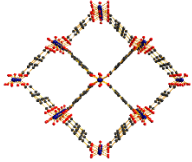
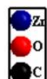
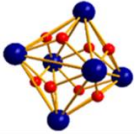
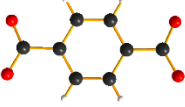
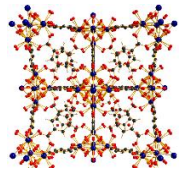
As for acidic properties, when the charge is compensated by a proton (H⁺), thus-formed bridging hydroxyl groups Si-(OH)-Al serve as Brønsted acid sites; while their Lewis counterparts are

generally associated with the so-called extra-framework Al atoms or framework defects on the surface (figure I-7). At the same time, acid site density is directly linked to the number of Al atoms and therefore associated with the Si/Al ratio; whereas acid strength is dictated by the position of Al atoms with respect to the next nearest neighbors (NNN). Thus, the more Al-atoms occupy these NNN positions the lower the resulting acid strength will be [65]. With this being said, one of the possibilities to vary the acidic properties of zeolite implies changing the number of Al atoms in their framework.

2.2. Metal-Organic Frameworks (MOFs)

Over the past ten years, MOFs have been extensively investigated until becoming a major material for studies on adsorption and catalysis. Their structure is comprised of a metal node (ion or cluster) and an organic linker (for example, organic acids). Together they form highly crystalline 1-, 2- or 3-dimensional microporous solids. Due to their large surface area and tunable physicochemical properties, they have been used in different applications such as heterogeneous catalysis, wastewater purification with a special interest in toxic gas removal and gas storage [76–80]. During the past years, new MOFs have appeared to achieve the outstanding 90 000 structures known so far and the number continues to grow [81]. A selection of 5 most studied MOFs as in the case of the “TOP-5” zeolites is depicted in Table I.1.

Table I.1 – “TOP 5” selected MOFs among the most studied structures as for now.

MOF	Space group	Metal Cluster	Organic linker	Framework
HKUST-1	<i>Fm-3m</i>	  Cu ²⁺	 Benzene-1,3,5-tricarboxylate	
MOF-5	<i>Fm-3m</i>	  Zn ²⁺	 Benzene-1,4-dicarboxylate	
ZIF-8	<i>I-43m</i>	  Zn ²⁺	 2-Methylimidazole	
MIL-53	<i>Imma</i>	  Al ³⁺	 Benzene-1,4-dicarboxylate	
UiO-66	<i>Fm-3m</i>	  Zr ⁴⁺	 Benzene-1,4-dicarboxylate	

Once it was first described in 1999 by Chiu *et al.* [82], HKUST-1 (Hong Kong University of Science and Technology) also named MOF-199, raised a great deal of academic interest in MOFs. Its well-defined 3-dimensional structure composed of the so-called “paddlewheel” building units based on Cu^{2+} clusters and benzene-1,3,5-tricarboxylate linkers give rise to a highly crystalline microporous framework (Table I.1). Its textural features are governed by a high surface area $\sim 1500 \text{ m}^2 \cdot \text{g}^{-1}$ and pore size originated from 3 different cavities within its framework: 0.5 nm, 1.1 nm and 1.4 nm. At the same time, HKUST-1 was shown to be easily scalable with high space-time yields in industrially relevant and “green” conditions [83]. Nevertheless, HKUST-1 exhibits low hydrostability *i.e.* it is highly sensitive to moisture even after short exposure to ambient conditions [84]. It leads to continuous coordination of water molecules on Cu centers over time leading to their complete hydration and subsequently structural collapse due to formation of copper hydroxide. Consequently, it requires special storage conditions which seriously limit its industrial application.

Around the same time as HKUST-1, IRMOF-1 also called MOF-5 in reminiscence of the famous ZSM-5 zeolite was first described by Yaghi *et al.* [85]. It is built from Zn_4O^{6-} clusters interconnected by benzene-1,4-dicarboxylate linkers. This MOF has a high thermal stability exceeding $300 \text{ }^\circ\text{C}$ and exceptional textural properties with a surface area of around $3000 \text{ m}^2 \cdot \text{g}^{-1}$ and pore size of around 1.85 nm. As a consequence, MOF-5 became a promising candidate for gas storage application [86]. Nevertheless, the chemical stability of MOF-5 is considered moderate as it is prone to structural degradation in the presence of moisture, similar to HKUST-1 [87,88].

In 2006, Yaghi *et al.* [89] reported on the large family of ZIFs, zeolitic imidazolate frameworks, consisting of Zn^{2+} (or Co^{2+}) bound together by 2-methylimidazole linkers in the same manner as Si and Al are bound *via* bridging oxygen atoms in conventional zeolites. Among the reported

MOFs, ZIF-8 gained the most attention due to its exceptional thermal stability up to 500 °C which is one of the highest reported for MOFs in general [90]. This is due to the strong bonding between Zn and nitrogen atoms of 2-methylimidazole which also provides high chemical stability [89]. In addition, ZIF-8 is highly porous with a typical surface area around 2000 m²·g⁻¹ and pore size around 1.2 nm.

In 2002, the group of Férey [91] reported the family of MIL (Matériaux de l'Institut Lavoisier) MOFs. Typically, they consist of a M(III): Al, Fe or Cr octahedra interconnected *via* benzene-1,4-dicarboxylate linkers leading to three-dimensional porous structures with surface areas above 1000 m²·g⁻¹. Interestingly, some MOFs issued from this family exhibit a unique pore breathing feature which implies a change of its intrinsic pore dimensions. Indeed, it was shown that Al-based MIL-53 underwent pore expansion from an average size of 0.77 nm x 0.73 nm to 0.85 nm x 0.85 nm upon removal of guest molecules by thermal treatment. This was followed by the reversible pore contraction down to 0.26 nm x 1.36 nm upon re-adsorption of water molecules which apparently bind Al clusters *via* H-bonding and therefore decreases the pore size [92].

Lastly, among the most famous and well-studied MOFs there is the so-called UiO-66 (Universitetet i Oslo) first described in 2008 by Lillerud and co-workers [93]. This MOF is composed of Zr₆O₄(OH)₄¹²⁺ clusters connected by terephthalate linkers to form a continuous 3D structure with a cubic orientation of the unit cell (*Fm-3m* space group). Its approximate surface area accounts for 1000-1200 m²·g⁻¹ with pore sizes below 2 nm derived from the tetrahedral and octahedral cages of 0.8 nm and 1.2 nm, respectively. Importantly, UiO-66 is considered as one of the most stable MOFs both thermally (with decomposition temperature above 300 °C) and chemically [94,95]. Due to the phenomenon known as “missing linkers”, the classical UiO-66 exhibits Coordinatively Unsaturated Sites (CUS) on Zr-clusters which serve as a source of Lewis

acidity. Besides, -OH groups on the clusters give rise to Brønsted acidity making them typical solid acids (figure I-7).

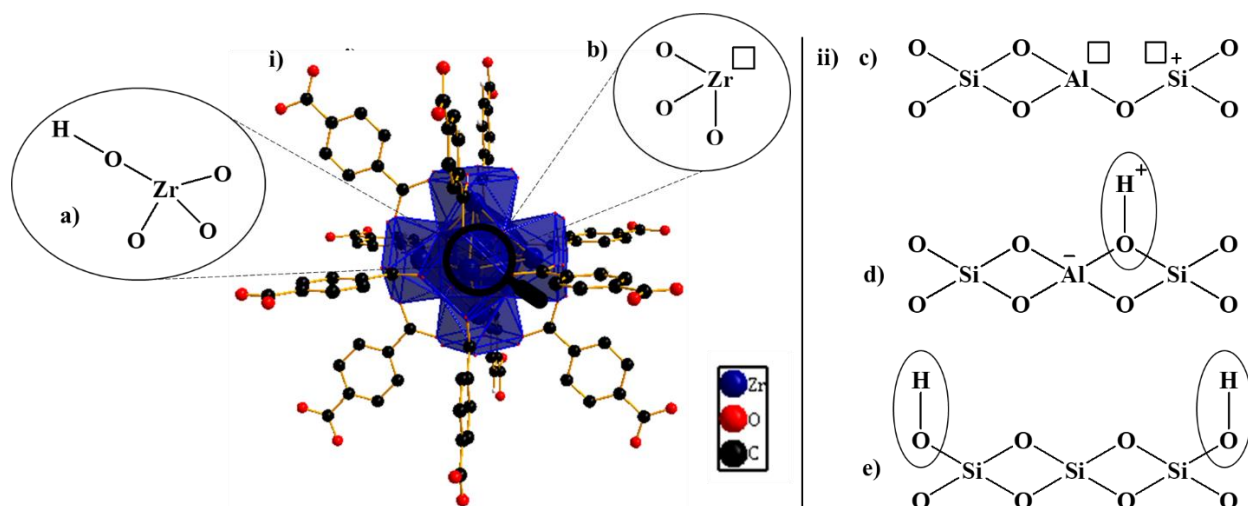


Figure I-7. Schematic representation of acid sites in UiO-66 (i): hydroxyl groups acting as Brønsted sites (a) and open sites on Zr atoms acting as Lewis sites (b) due to a missing linker on the cluster represented as a blue polyhedron; as well as in a zeolite (ii): Lewis sites due to the defects on Si and Al atoms (c) and Brønsted sites as bridging hydroxyl groups (d) and terminal silanol groups (e). Hydrogen atoms in the MOF's structure are omitted for simplicity.

2.3. Tuning of Acidic Properties in Zeolites and MOFs

Varying the Si/Al ratio in zeolite compositions is one of the well-known and straightforward strategies to modify the number of acid sites and the strength of a single site. It has been successfully employed for different zeolite structures [66–68] for various applications. Importantly, it was experimentally proven that zeolites with a high Al content exhibited a higher fraction of weak acid sites. Thus, H-MOR zeolite with Si/Al = 6 displayed 75 % of weak acid sites as compared to 68 % of the H-MOR with Si/Al = 16 [69]. This further supports the hypothesis on Al atoms occupying the NNN positions discussed above.

Another widely-used and yet challenging methods to vary acidic properties of zeolite is the so-called isomorphous substitution of Al by a heteroatom [70]. The term “isomorphous” implies the

tetrahedral coordination of the newly-inserted heteroatom into the framework. The latter includes main group metals (Ga, Ge, Sn), non-metals (B) and transition metals (Ti, Fe). Thus-formed solids can no longer be called “zeolites” as they contain no Al but rather “zeotypes” or simply “element-silicates”, for example “Ti-silicates”. It is important to understand that quadrivalent elements such as Ti or Sn cause no negative framework charge when in tetrahedral coordination. Thus, when replacing Al, they are believed to decrease the number of Brønsted sites to a great extent and mainly generate Lewis acid sites which was confirmed by several authors [71,72]. On the other hand, isomorphous substitution of Al by another trivalent element retains the intrinsic acidic properties of classical zeolites, however considerably modifying them. Thus, the milestone study conducted on several zeotypes with B, Fe and Ga as heteroatoms in the MFI framework experimentally revealed the decrease in strength of Brønsted acid sites in the following order: [B]-MFI < [Fe]-MFI ~ [Ga]-MFI < [Al]-MFI [73]. These observations were later confirmed by several authors [74,75]. Thus, such tunability of acidic properties *via* variation of the Si/Al ratio or isomorphous substitution in zeolites allows modification of their chemical properties and hence their application.

Lastly, although zeolites are predominantly known as solid acids they also exhibit intrinsic basic properties. They are less pronounced and only ascribed to the presence of alkali (Li, Na, K or Cs) and alkali-earth metals (Ca, Mg) as the charge compensating cations. Therefore, their number also primarily depends on the number of Al atoms as the source of the negative charge and tuned accordingly *via* the Si/Al ratio. Whereas the strength of basic sites in zeolites are considered to increase in the following order: Li < Na < K < Cs and Mg < Ca and simply modified by performing ion-exchange to replace one by another.

Like zeolites, MOFs are capable of tuning the acidic properties in order to modify their performance in the targeted application. Nevertheless, owing to their relative novelty as compared to zeolites, the research in this field is still gaining momentum. Accordingly, there are several ways towards alteration of their acidic properties. Firstly, the metallic center in isostructural MOFs can be replaced by another metal. Thus, when Cr was replaced by Fe in MIL-100, the strength of Lewis acid sites was considered to increase as confirmed by higher activity of MIL-100(Cr) in isomerization of dicyclopentadiene as compared to MIL-100(Fe). Same conclusion was made on MIL-101(Cr) and MIL-101(Fe) [96]. Similar study was conducted on a series of isostructural UiO-66 composed of Zr, Ce and Hf. Specifically, strength of the Brønsted acid sites (-OH) on the metal cluster were shown to increase in the following order: UiO-66(Zr) < UiO-66(Ce) < UiO-66(Hf) supported by the highest activity of the latter in glycerol acetalization [97].

Besides, MOFs are known for their excellent capacity towards framework functionalization. For instance, acidic groups (-COOH or -SO₃H) can be inserted on their frameworks in order to generate Brønsted acid sites. This can be done by grafting a functional group on the linker *via* post-synthetic modification [98]. Such method requires the use of aggressive oxidizing agents and therefore cannot be employed for many MOFs due to their limited chemical stabilities. Contrary, direct framework functionalization allows to avoid this problem and consists of using linkers functionalized before the actual MOF synthesis. For instance, employing benzene-1,2,4-dicarboxylate linker with one additional carboxylic group instead of the original benzene-1,4-dicarboxylate linker for the synthesis of UiO-66(Zr) allows to make UiO-66(Zr)-COOH. This method is therefore considered more pertinent and is applied for variety of MOFs. Thus, generation of Brønsted acid sites was successfully performed on UiO-66(Zr), MIL-101(Cr), MIL-53(Al) and others [99–101].

Importantly, basic functional groups such as -NH_2 can also be easily inserted to generate basic sites and therefore expand their intrinsic applications. The list of such basic MOFs continuously increases and includes UiO-66(Zr)- NH_2 , MIL-101(Cr)- NH_2 , MIL-53(Al)- NH_2 and many others [102,103].

2.4. MOFs vs Zeolites – Chemical and Structural Comparison

Both classes of solids exhibit intrinsic acid properties which are originated from their unique chemical compositions as discussed above. Table I.2 summarizes corresponding features of each class depending on the nature, number and strength of acid sites as well as the ways to modify them.

Table I.2 – Comparison of acid properties of MOFs and zeolites and the ways to their tunability.

MOFs		Zeolites
<i>Lewis:</i>		<i>Lewis:</i>
1) Structural defects <i>i.e.</i> missing linkers.		1) Extra-framework Al species; 2) Defects on Si or Al atoms.
<i>Brønsted:</i>	Nature of Acid Sites	<i>Brønsted:</i>
-OH groups on metal clusters. Usually weak.		1) -OH groups in Si-(OH)-Al. 2) Si-OH silanol groups. Usually weak.
Depends on the nature of the metal constituting the MOF and of the linker.	Number of Acid Sites	Depends on the number of Al atoms <i>i.e.</i> Si/Al ratio.
Depends on the metal and linker constituting the MOF.	Strength of Acid Sites	Depends on the number of Al atoms and their position (NNN).
1) Replacement of the metal; 2) Defects control; 3) Framework functionalization.	Modification Strategy	1) Variation of the Si/Al ratio; 2) Replacement of Al by another element <i>i.e.</i> isomorphous substitution.

As seen from Table I.2, both MOFs and zeolites share common features. Nevertheless, despite the similarities in chemical properties, MOFs and zeolites are much different in terms of structural properties. Indeed, built completely from inorganic SiO₂ and Al₂O₃ units, zeolites are usually more chemically and thermally stable than MOFs which exhibit rather a hybrid (inorganic + organic) composition (Table I.3).

Table I.3 – Comparison of general features of MOFs and zeolites.

MOFs		Zeolites
less	Synthesis Difficulty	higher
higher	Surface Area and Pore Volume	lower
less	Thermal Stability	higher
less	Chemical Stability	higher
higher	Properties Tunability	lower
higher	Cost	lower
lower	Regeneration	higher

To sum up, each of the materials have their “pros and cons” and the final choice depends on the targeted application. However, due to their superior surface area and pore volume and therefore higher hosting capacities, MOFs are slowly but surely replacing zeolites in gas adsorption applications (storage, separation, purification). This applies especially to inert gases (H₂, N₂, He) or gases having low reactivity (CH₄, CO₂, CO). Otherwise, in the case of reactive gases, for example, in NH₃ or HCOH removal, regeneration might be challenging due to possible strong interactions with MOF surfaces as the latter is intolerant to high temperatures or washing media. On the other hand, due to their superior thermal stability, zeolites remain indispensable for processes operating at high temperatures (>300 °C).

3. Fructose Dehydration on Solid Catalysts

3.1. Zeolites

Zeolites have been used in biomass conversion for decades now. Particularly, the first work on direct fructose dehydration over zeolites was published in 1994 by Moreau *et al.* [104]. The authors consistently studied different zeolites in their acidic form: H-beta, H-ZSM-5, H-faujasite and H-mordenite in H₂O/MIBK (methyl isobutyl ketone) biphasic system with the latter acting as a simultaneous extraction solvent (Table I.4).

Table I.4 – List of zeolites applied in fructose dehydration under different conditions.

Catalyst [▲]	$m_{\text{fruc}}/m_{\text{cat}}$, mg/mg	Solvent	T, °C	t, h	Fructose conv., %	HMF yield (selec.), %	Ref
Blank	-	H ₂ O/MIBK	160	1	32	12 (38)	[104]
H-beta (15)*	35/10	H ₂ O/MIBK	160	1	85	34 (40)	[104]
H-ZSM-5 (25)	35/10	H ₂ O/MIBK	160	1	90	53 (59)	[104]
H-faujasite (15)	35/10	H ₂ O/MIBK	160	1	76	40 (53)	[104]
H-mordenite (11)	35/10	H ₂ O/MIBK	160	1	76	69 (91)	[104]
H-beta (16)	20/4	H ₂ O	165	-	~80	20 (25)	[105]
H-ZSM-5 (13)	20/4	H ₂ O	165	-	~80	20 (25)	[105]
H-mordenite (12)	20/4	H ₂ O	165	-	~80	32 (40)	[105]
H-beta (16)	20/4	H ₂ O/MIBK	165	-	~80	32 (40)	[105]
H-ZSM-5 (13)	20/4	H ₂ O/MIBK	165	-	~80	50 (62)	[105]
H-mordenite (12)	20/4	H ₂ O/MIBK	165	-	~80	56 (70)	[105]
H-ZSM-5 (25), micro	60/8	H ₂ O	130	10	63	3 (5)	[106]

Table I.4 continued

H-ZSM-5 (25), hierar	60/8	H ₂ O	130	10	73	15 (21)	[106]
H-beta (12), micro	60/8	H ₂ O	130	10	75	5 (7)	[106]
H-beta (10), hierar	60/8	H ₂ O	130	10	77	10 (13)	[106]
H-USY (30), micro	60/8	H ₂ O	130	10	59	4 (7)	[106]
H-USY (26), hierar	60/8	H ₂ O	130	10	65	6 (9)	[106]
H-beta (19)	625/62	H ₂ O	150	4	76	13 (17)	[107]
H-beta (19) + BP2000	625/62	H ₂ O	150	4	82	28 (34)	[107]
H-beta (22), nano	218/18	DMSO	120	5	73	52 (71)	[108]
H-beta (22), microsph.	218/18	DMSO	120	5	78	68 (87)	[108]

▲ Powder catalyst dispersed in a batch reactor;

* Numbers in brackets correspond to the Si/Al ratios;

BP2000 – carbon black.

They found that the presence of acidic zeolites largely increases fructose conversion and HMF yield as compared to the “no catalyst” runs. Thus, after 1 h of reaction at 160 °C, fructose conversion increased from 32 % (blank test) up to 85 % over H-beta, 90 % over H-ZSM-5, 76 % over H-faujasite and 76 % over H-mordenite. The corresponding selectivities towards HMF accounted for 38 %, 40 %, 59 %, 53 % and 91 %, respectively. The higher selectivity over H-mordenite was attributed to the structural features of the zeolite *i.e.* to its two-dimensional pore organization which limits HMF rehydration into side products or its oligomerization. Whereas the lower HMF selectivity over H-faujasite and H-beta probably originates from the three-dimensional pore organization with larger apertures. Thus, H-mordenite can be considered as the catalyst with the highest shape selectivity towards HMF among the studied zeolites. Their further work [109] addressed the diffusion of fructose and HMF in H-mordenite as-such or after dealumination which led to the formation of mesopores. Thus, they found that the selectivity towards HMF decreased

from 91 % to ~61 % over H-mordenite with an increase in mesopore volume from $0.056 \text{ cm}^3 \cdot \text{g}^{-1}$ to $0.163 \text{ cm}^3 \cdot \text{g}^{-1}$, respectively.

Similarly, Ordonsky *et al.* [105] examined H-ZSM-5, H-beta and H-mordenite zeolites in fructose dehydration both in H_2O and $\text{H}_2\text{O}/\text{MIBK}$ biphasic system. They found that H-ZSM-5 was the most active in fructose dehydration reaching the complete conversion after ~4 h of reaction at $165 \text{ }^\circ\text{C}$ in H_2O as solvent whereas H-mordenite and H-beta reached their maximum conversion with ~85 % and ~70 % after ~5 h, respectively. At the same time, at 80 % fructose conversion HMF selectivity accounted for ~40 % for H-mordenite and ~25 % both for H-ZSM-5 and H-beta. The higher selectivity over the former agrees well with the results reported by Moreau [104]. Besides, the authors confirmed an increased selectivity towards HMF when using the biphasic $\text{H}_2\text{O}/\text{MIBK}$ solvent system as compared to monophasic aqueous system over all of the studied solids. At ~80 % fructose conversion, HMF selectivity raised to nearly 70 %, 62 % and 40 % respectively over H-mordenite, H-ZSM-5 and H-beta. These results, therefore, also proved the positive effect of using MIBK as the HMF extracting solvent in $\text{H}_2\text{O}/\text{MIBK}$ biphasic system and thus its protection from further rehydration into side products.

Importantly, contrary to the work of Moreau [104] the authors attributed the higher HMF selectivity over H-mordenite to its higher acid site strength rather than to shape selectivity features *i.e.* two-dimensional pore organization. Indeed, the latter exhibited stronger acid sites examined by NH_3 -TPD measurements as compared to H-ZSM-5 and H-beta.

Rac *et al.* [106] studied the effect of mesopores insertion into a series of zeolites and its impact on HMF selectivity. The results suggested higher fructose conversion at $130 \text{ }^\circ\text{C}$ in H_2O over hierarchical micro/mesoporous H-ZSM-5, H-beta and H-USY as compared to their microporous counterparts with nearly 10 %, 3 % and 7 % increase, respectively. This is also true when

considering HMF selectivity. Moreover, mesopores avoid deactivation and therefore maintain selectivity at a nearly fixed value for up to 10 h of reaction time: ~22 %, 15 % and 12 % respectively over H-ZSM-5, H-beta and H-USY. At the same time, their microporous analogues exhibited a progressive decline in selectivity after 6 h. Overall, considering the works by Ordonsky *et al.* [105] and Rac *et al.* [106] it is possible to conclude that selectivity towards HMF upon fructose dehydration in various solvents systems depends mostly on the acid site strength of the microporous zeolites used as catalysts instead of their structural properties.

Interestingly, Dornath *et al.* [107] applied a different strategy in order to increase HMF selectivity. Namely, they used carbon black in addition to the catalyst, H-beta, in order to adsorb the HMF formed during fructose dehydration. This imitates the effect of MIBK which serves as HMF extracting solvent except that carbon black is a solid which adsorbs and therefore protects the newly formed HMF from further rehydration into levulinic or formic acids. Indeed, the porous and hydrophobic nature of BP2000 carbon black favors adsorption of HMF in its pores. Thus, addition of 4 wt.% carbon black for fructose dehydration over H-beta at 150 °C in H₂O doubled HMF selectivity from ~17 % to ~34 % while decreasing the combined levulinic and formic acid selectivity from ~17 % to ~4 %.

Shi *et al.* [108] studied the assembly of H-beta nanocrystals into microspheres in order to generate hierarchical micro/meso-porosity. This was done by the so-called polymer-induced colloidal aggregation method (PICA) using a urea-formaldehyde resin as the template for aggregation of the zeolite crystals. This procedure yielded H-beta microspheres with large pores of around 50 nm between zeolite nanocrystals, which were subsequently applied in fructose dehydration. The results suggested an increase in fructose conversion over the hierarchical H-beta microspheres up to ~78 % as compared to 73 % over the conventional microporous H-beta with HMF yields of

~68 % and ~52 %, respectively. This suggests that insertion of larger voids between individual zeolite crystals increases its external surface and therefore positively affects fructose dehydration by providing more accessible acid sites.

Lastly, Kruger *et al.* [110] highlighted several critical points to consider during fructose dehydration over zeolites. As an example, they performed catalytic tests over H-beta zeolite in H₂O as the solvent. They noticed that extra-framework Al species serving as Lewis acid sites could catalyze fructose-to-glucose isomerization. As for fructose dehydration, they concluded that the use of H-beta increased the overall conversion and HMF yield. Interestingly, they stated that the zeolite exhibited preferential adsorption of HMF over fructose, implying rapid rehydration of the former into levulinic acid. Furthermore, they evidenced a remarkable contribution of an unknown compound in the chromatograms with a tripled area of that of levulinic acid. They attributed this compound to oligomers of HMF which can be once again catalyzed by zeolites. Another interesting point derived from their study is the dissolution of zeolite by acids formed as by-products, mainly levulinic and formic acids. They observed a considerable zeolite dissolution mostly *via* Al leaching, however Si leaching was also proven.

3.2. *MOFs*

MOFs have been progressively used as solid acid catalysts in fructose dehydration. This includes dehydration in different media and batch conditions, Table I.5. Thus, one of the first works on the one pot fructose dehydration over MOFs was published by Chen *et al.* [98]. In their work, the authors performed framework functionalization *via* post-synthetic modification route in order to generate Brønsted acid sites on several known MOFs including Cr-based MIL-101, Zr-based UiO-66 and Al-based MIL-53.

Table I.5 – List of MOFs applied in fructose dehydration under different conditions.

Catalyst [▲]	m _{fruc} /m _{cat} , mg/mg	Solvent	T, °C	t, h	Fructose conv., %	HMF yield (selec.), %	Ref
UiO-66-SO ₃ H (50 %)*	300/10	H ₂ O	140	3	48	23 (48)	[111]
UiO-66-NH ₂	300/10	H ₂ O	140	3	40	29 (73)	[111]
UiO-66-NO ₂	300/10	H ₂ O	140	3	48	31 (65)	[111]
UiO-66-(OH) ₂	300/10	H ₂ O	140	3	32	21 (66)	[111]
UiO-66-(COOH) ₂	300/10	H ₂ O	140	3	60	41 (68)	[111]
MIL-101(Cr)	500/300	DMSO	120	1	45	24 (53)	[98]
MIL-101(Cr)-SO ₃ H (3.0 %)	500/300	DMSO	120	1	83	63 (76)	[98]
MIL-101(Cr)-SO ₃ H (6.2 %)	500/300	DMSO	120	1	91	71 (78)	[98]
MIL-101(Cr)-SO ₃ H (15.0 %)	500/300	DMSO	120	1	>99	90 (91)	[98]
MIL-53(Al)-SO ₃ H (8.2 %)	500/300	DMSO	120	1	>99	79 (80)	[98]
UiO-66(Zr)-SO ₃ H (9.5 %)	500/300	DMSO	120	1	>99	85 (86)	[98]
UiO-66(Zr)	50/35	DMSO	100	1	5	- (-)	[112]
UiO-66(Hf)	50/50	DMSO	100	1	12	8 (67)	[112]
NUS-6(Zr)	50/35	DMSO	100	1	>99	84 (85)	[112]
NUS-6(Hf)	50/50	DMSO	100	1	>99	98 (99)	[112]
MIL-101(Cr)	250/100	DMSO	120	2	~39	~27 (69)	[113]
MIL-101(Cr)-SO ₃ H (2.32 %)	250/100	DMSO	120	2	~73	~50 (68)	[113]
MIL-101(Cr)-PhSO ₃ H	250/100	DMSO	120	2	~99	~98 (99)	[113]

[▲] Powder catalyst dispersed in a batch reactor;

* Numbers in brackets correspond to the degree of functionalization.

The modification process implied grafting of acidic -SO₃H groups onto a MOF surface using a strong oxidizing agent such as chlorosulfuric acid, ClSO₃H. This yielded acidic MOFs with various grafting degrees: 3 %, 6 % and 15 % for MIL-101(Cr)-SO₃H as well as 9.5 % for UiO-66(Zr)-SO₃H and 8.2 % for MIL-53(Al)-SO₃H as confirmed *via* elemental analysis. As a consequence, this led to an increased number of Brønsted acid sites as estimated by acid-base titration and therefore to an increased activity in fructose dehydration into HMF. Thus, the series of MIL-

MIL-101(Cr)-SO₃H resulted in a progressive increase of fructose conversion and HMF yield after 1 h of reaction at 120 °C in DMSO. More precisely, the pristine MIL-101(Cr) converted 45 % fructose with 24 % HMF yield as compared to respectively 83 % and 63 % over MIL-101(Cr)-SO₃H (3.0 %), 91 % and 71 % over MIL-101(Cr)-SO₃H (6.2 %) and >99 % and 90 % over MIL-101(Cr)-SO₃H (15.0 %). This underlines the positive effect of grafting -SO₃H groups on the MOF surface on their catalytic performance. Similarly, MIL-53(Al)-SO₃H (8.2 %) and UiO-66-SO₃H (9.5 %) converted >99 % fructose each and yielded 79 % and 85 % HMF, respectively. However, no data on the performance of the pristine MIL-53(Al) and UiO-66(Zr) as well as the blank test was given.

Zhong *et al.* [113] showed the possibility to graft -SO₃H acidic groups to yield MIL-101(Cr)-SO₃H with high hydrophobicity. They found that insertion of benzenesulfonic or naphthalenesulfonic acid could increase both the number of Brønsted acid sites and hydrophobicity of the modified MOF. This was done in order to increase HMF selectivity by preventing its rehydration into levulinic acid by water released as a by-product upon fructose dehydration. Thus, fructose conversion after 2 h of reaction at 120 °C in DMSO reached ~73 % with approximate 50 % HMF yield over MIL-101(Cr)-SO₃H (2.32 %) prepared in the same way as in the work by Chen *et al.* [98]. The yield of levulinic acid and humins made up 5 % and 18 %, respectively. At the same time, grafting of -SO₃H groups *via* benzenesulfonic acid increased the number of acid sites from 0.77 mmol·g⁻¹ in MIL-101(Cr)-SO₃H (2.32 %) to 1.17 mmol·g⁻¹ in MIL-101(Cr)-PhSO₃H (3.68 %). Besides, increased hydrophobicity of the latter was proven by a wider contact angle of H₂O 114 ° vs 99 ° with MIL-101(Cr)-SO₃H (2.32 %). Consequently, fructose conversion and HMF yield reached 99 % and 98 %, respectively boosting selectivity towards HMF up to nearly 100 %.

Hu and coworkers [112] reported fructose dehydration over NUS-6(Zr) and NUS-6(Hf) which can be basically considered as highly defective UiO-66(Zr)-SO₃H and UiO-66(Hf)-SO₃H,

respectively. Indeed, the presence of the bulky $-\text{SO}_3\text{H}$ groups causes structural defects mainly due to steric hindrance and therefore leading to a change of intrinsic structural properties of the parent UiO-66 topology. Nevertheless, both solids demonstrated good activity towards fructose dehydration. Thus, after 1 h of reaction at $100\text{ }^\circ\text{C}$ in DMSO, NUS-6(Zr) reached complete fructose conversion ($>99\%$) yielding 84% HMF while its Hf counterpart, NUS-6(Hf), yielded 98% HMF at the complete fructose conversion reaching an excellent 98% selectivity. Besides, they found that the latter provides higher acid sites density *i.e.* 13.9 mol of H^+ per mol of MOF than NUS-6(Zr) with its $12.9\text{ mol}\cdot\text{mol}^{-1}$. This was also given as a possible explanation of the increased HMF selectivity over NUS-6(Hf). In turn, it was attributed to an easier dissociation of $\mu_3\text{-OH}$ groups and therefore more acidic nature of the proton in the Hf-oxocluster due to the higher oxophilic nature of Hf^{4+} as compared to Zr^{4+} . This was further proven by the catalytic tests over the non-functionalized MOFs *i.e.* UiO-66(Zr) and UiO-66(Hf). Accordingly, the former showed $\sim 5\%$ fructose conversion with no HMF yield while UiO-66(Hf) converted $\sim 12\%$ with $\sim 8\%$ HMF yield. Recently, Oozeerally *et al.* [111] reported an extensive study on performance of the functionalized UiO-66-based MOFs in fructose dehydration. The list of studied MOFs includes remarkable UiO-66- SO_3H , UiO-66- NO_2 , UiO-66- $(\text{COOH})_2$ and UiO-66- $(\text{OH})_2$. The results suggested the highest fructose conversion of 60% and HMF yield of 41% after 3 h of reaction at $140\text{ }^\circ\text{C}$ in water over UiO-66- $(\text{COOH})_2$. These relatively modest results at high temperature and long reaction time as well as unpredictable results are probably due to the chosen solvent as water does not favor dehydration reactions.

Summing up, fructose dehydration is a simple one step Brønsted acid-catalyzed reaction. The present studies showed a decent catalytic performance of zeolites in their acidic H-form with activity correlated to their acid site strength and textural properties based on pore size dimensions.

Different approaches to facilitate diffusion of the reactant within the pores were shown to increase both fructose conversion and HMF yield. At the same time, the catalytic activity of MOFs strongly depends on insertion of Brønsted acid functional groups as they originally exhibit pronounced Lewis acidity. It was shown that strong $-\text{SO}_3\text{H}$ groups were capable to increase catalytic performances of original MOFs.

4. Glucose Isomerization on Solid Catalysts

4.1. Basic Zeolites

Among the first published studies on basic zeolites applied in glucose isomerization, Moreau *et al.* [114] studied a wide variety of cation-exchanged A, X and Y zeolites (Table I.6). They found that the parent zeolites exhibited different catalytic activities which they attributed to differences in basic site strength. Briefly, it can be concluded that the basicity decreases in the following order: $\text{Y} < \text{A} < \text{X}$. This statement was further supported by the increased fructose selectivity (62 %, 72 % and 86 %) obtained at 95 °C in H_2O over NaY, NaA and NaX zeolites, respectively. The glucose overall conversion accounted for 9 %, 26 %, and 20 %, respectively. Importantly, they stated that the selectivity towards fructose also increased as the basic nature of the cation increased. Thus, LiX, NaX, KX and CsX exchanged zeolites resulted in fructose selectivities of 85 %, 86 %, 80 % and 77 %, respectively. Of note, K and Cs were prone to a more drastic leaching than Li and Na.

Table I.6 – Glucose isomerization over basic zeolites.

Catalyst [▲]	m _{glu} /m _{cat} , mg/mg	Solvent	T, °C	t, h	Glucose conv., %	Fruc. yield (selec.), %	Ref
NaY	5000/1000	H ₂ O	95	-	9	<6 (62)	[114]
NaA	5000/1000	H ₂ O	95	-	26	<19 (72)	[114]
NaX	5000/1000	H ₂ O	95	-	20	<18 (86)	[114]
LiX	5000/1000	H ₂ O	95	-	19	<17 (85)	[114]
KX	5000/1000	H ₂ O	95	-	23	<19 (80)	[114]
CsX	5000/1000	H ₂ O	95	-	25	<20 (77)	[114]
NaX	50/20	H ₂ O	100	2	27	<21 (76)	[115]
Na-ETS-10	50/20	H ₂ O	100	2	33	<25 (74)	[115]
K-ETS-10	50/20	H ₂ O	100	2	31	<21 (66)	[115]
5wt.% Mg/NaY	500/100	H ₂ O	100	2	28	<23 (82)	[116]
10wt.% Mg/NaY	500/100	H ₂ O	100	2	45	<33 (73)	[117]
15wt.% Mg/NaY	500/100	H ₂ O	100	2	49	<33 (66)	[117]
5wt.% Mg/NaMOR	500/100	H ₂ O	100	2	37	<29 (76)	[116]
5wt.% Mg/Na*BEA	500/100	H ₂ O	100	2	39	<25 (64)	[116]
5wt.% Mg/NaZSM-5	500/100	H ₂ O	100	2	38	<34 (88)	[116]
5wt.% Mg/NaFER	500/100	H ₂ O	100	2	27	<24 (86)	[116]
5wt.% Mg/NaY, hierar	500/100	H ₂ O	100	2	34	34 (100)	[118]
2.5wt.% Ca/Na*BEA, hierar	50/20	H ₂ O	100	0.5	39	<32 (80)	[119]
2.5wt.% Mg/Na*BEA, hierar	50/20	H ₂ O	100	0.5	42	<30 (70)	[119]

[▲] Powder catalyst dispersed in a batch reactor.

Lima *et al.* [115] showed the possibility to convert glucose into fructose over basic microporous titanosilicates (SiO₂/TiO₂): ETS-10 and ETS-4. The former has 12-membered ring channel system with aperture diameter of around 0.8 nm while the latter possesses 8-membered rings with a smaller pore diameter of around 0.5 nm. They found that Na-ETS-10 converted 33 % glucose with

74 % fructose selectivity after 2 h at 100 °C, which is comparable to the commercial NaX zeolite (27 % and 76 %, respectively). Also, they demonstrated that the catalytic activity can be altered upon replacement of Na⁺ cations by K⁺ as the latter is considered to generate stronger basic sites. Nevertheless, K-exchanged ETS-10 exhibited lower conversion (31 %) and selectivity (66 %), attributed to the incomplete or inefficient ion-exchange. Lastly, Na-ETS-4 outperformed Na-ETS-10 converting 48 % (*vs* 33 %) glucose with 84 % (*vs* 74 %) fructose selectivity. The authors attributed this to different basic properties originating from structural features of each solid.

Graça *et al.* [116]. conducted an extensive study on a series of Mg-impregnated zeolites which include NaY, NaMOR, Na*BEA, NaZSM-5 and NaFER. First, they found a negligible (<6 %) glucose conversion after 2 h at 100 °C over each of the examined solids before impregnation. Low conversion over NaY was also observed by Moreau *et al.* [114] and this is probably due to its weak basic sites. Nevertheless, once impregnated with 5 wt.% Mg, glucose conversion accounted for 28 %, 37 %, 39 %, 38 % and 27 % with fructose selectivity 82 %, 76 %, 64 %, 88 % and 86 % respectively over Mg/NaY, Mg/NaMOR, Mg/Na*BEA, Mg/NaZSM-5 and Mg/NaFER. Despite its modest activity, Mg/NaY was chosen as the most promising catalyst due to the less pronounced leaching of Mg upon glucose isomerization as well as less coke formed on its surface. The latter is probably due to larger pores of the parent Y zeolite (~0.74 nm).

Therefore, the authors further continued the study on Mg/NaY [117], examining the effect of Mg loading on the zeolite support gradually increasing it from 5 wt.% up to 15 wt.% under the same conditions, 2 h at 100 °C. They established a correlation between the Mg loading on catalyst activity. While the parent NaY exhibited around 6 % glucose conversion, the impregnated zeolites showed a consistent increase in conversion reaching 28 %, 45 % and 49 % over 5 wt.%Mg/NaY, 10 wt.%Mg/NaY and 15 wt.%Mg/NaY, respectively. Interestingly the corresponding fructose

selectivities made up 82 %, 73 % and 66 %, respectively, indicating nearly similar performance of 10 wt.%Mg/NaY and 15 wt.%Mg/NaY. This was explained by the considerable growth of MgO particles upon increasing the Mg loading which causes a partial pore blocking. This subsequently leads to an increased residence time of fructose within the catalyst's pores and therefore to its further condensation into undesirable oligomers. Furthermore, 10 wt.%Mg/NaY was considered preferential due to the lesser Mg leaching upon glucose conversion (0.8 % against 2.8 % in 15 wt.%Mg/NaY). Importantly, bulk MgO itself showed 66 % glucose conversion at 42 % fructose selectivity demonstrating an increased conversion but decreased selectivity as compared to 5 wt.%Mg/NaY and 10 wt.%Mg/NaY. This was attributed to a higher number of strong basic sites on MgO which favor side reactions. Therefore, Mg loadings between 5 wt.% and 10 wt.% were found to be optimal to provide a decent catalytic activity.

Finally, the authors completed the study on the 5 wt.%Mg/NaY by creating mesopores in the parent zeolite support *via* partial desilication [118]. Mild desilication in 0.01 % NaOH solution increased mesoporous volume from $0.045 \text{ cm}^3 \cdot \text{g}^{-1}$ to $0.055 \text{ cm}^3 \cdot \text{g}^{-1}$. The generation of a hierarchical micro/mesoporosity should improve the diffusion of molecules within the pores of the catalyst, and hence the conversion of glucose and yield of fructose. Indeed, the hierarchical zeolite reached 34 % glucose conversion with a remarkable 100 % fructose selectivity, as compared to respectively 28 % and 82 % over its microporous analogue.

One of the recent works was done by Antunes *et al.* [119] who also applied desilication on Na*BEA zeolite to improve its textural properties, before subsequent impregnation with Mg or Ca (2.5 wt.%). They found that desilication with NaOH resulted in higher mesopore volume of $0.33 \text{ cm}^3 \cdot \text{g}^{-1}$, as compared to $0.09 \text{ cm}^3 \cdot \text{g}^{-1}$ for the pristine Na*BEA zeolite. This had a positive effect on the catalyst performance, converting 32 % glucose at 85 % fructose yield whereas the

pristine *BEA zeolite only converted 12 % glucose with no fructose after 30 min at 100 °C. Furthermore, upon Ca and Mg impregnation, the glucose conversion increased further to 39 % and 42 %, respectively, however, the selectivity decreased to ~80 % and ~70 %, respectively. This agrees well with the other reported results mentioning a certain decrease of fructose selectivity upon generation of strong basic sites *via* impregnation which leads to partial pore blocking. Importantly, the authors found severe metal leaching from both the charge-compensating cation and the impregnated metal oxide. Thus, upon lowering the reaction temperature from 100 °C to 75 °C, Na leaching decreased from 61 % to 38 % while Mg – from 14 % to 4 %. Further decrease to 35 % and 3 %, respectively, was reached by applying ultrasonic irradiation as the activation source instead of conventional conductive heating.

4.2. Lewis Acid Zeolites

Studies on glucose isomerization over Lewis acid zeolites had their debut in 2010 with the work of Moliner *et al.* [120]. They showed the possibility of a complete isomorphous substitution of Al by Sn in *BEA zeolite framework to result in Sn-silicate. The insertion of the tetravalent Sn causes a neutral framework *i.e.* no negative charge as in the case of the trivalent Al atoms. Thus, no compensation by cations or H⁺ is needed, therefore no intrinsic Brønsted acidity is generated allowing to consider Sn-beta zeotype as a pure Lewis solid acid (Table I.7).

Table I.7 – Glucose isomerization over Lewis acid zeolites.

Catalyst [▲]	m _{glu} /m _{cat} , mg/mg	Solvent	T, °C	t, h	Glucose conv., %	Fruc. yield (selec.), %	Ref
Ti-Beta (100)*	120/150	H ₂ O	110	1.5	26	14 (54)	[120]
Sn-Beta (100)	120/150	H ₂ O	110	0.5	55	32 (58)	[120]
Sn-Beta (100) cycle 1	120/150	H ₂ O	110	0.5	59	32 (54)	[120]
Sn-Beta (100) cycle 2	120/150	H ₂ O	110	0.5	55	30 (55)	[120]
Sn-Beta (100) cycle 3	120/150	H ₂ O	110	0.5	53	29 (55)	[120]
Sn-Beta (100) cycle 4 [×]	120/150	H ₂ O	110	0.5	55	32 (59)	[120]
Sn-Beta (100)	30/150	H ₂ O	110	1	54	29 (54)	[120]

[▲] Powder catalyst dispersed in a batch reactor;

* Numbers in brackets correspond to the Si/Sn or Si/Ti ratios.

[×] After calcination at 540 °C

Indeed, when applied in glucose isomerization, it showed a decent activity exhibiting 55 % glucose conversion with 32 % fructose yield after 30 min of reaction at 110 °C in water. Catalyst recycling test performed under the same conditions revealed the preservation of its initial activity after 3 cycles. Calcination at 540 °C thereafter (after the 3rd cycle) did not alter the initial activity meaning that Sn-beta zeotype can easily withstand a typical zeolite regeneration procedure. Importantly, there was no Sn leaching observed during catalytic tests as it was the case for the alkali metal-impregnated basic zeolites discussed above. At the same time, no glucose conversion took place once the catalyst was removed from the reaction mixture meaning that the catalytic performance of Sn-beta is of heterogeneous nature. Besides, when applying SnO₂ or SnCl₄ no fructose was observed among the products implying that the catalytically active species is the Sn coordinated in beta framework alongside Si atoms. Interestingly, the Ti-incorporated analogue, Ti-beta, demonstrated a 26 % glucose conversion with 14 % fructose yield after 90 min at 110 °C, while Sn-beta reached respectively 55 % and 32 % already after 30 min. This might serve as a hint

towards the difference in acid site strength, however, this remained beyond the scope of this study. Of note, it was shown that Sn-beta exhibited the same performance in the presence of HCl (pH = 2) which is critically important as it allows for coupling glucose isomerization with fructose dehydration step to produce HMF *via* cascade reaction. Indeed, glucose isomerization/dehydration *via* intermediate fructose over Sn-beta + HCl catalyst system resulted in 72 % glucose conversion with 18 % fructose and 11 % HMF yields after 2 h of reaction at 140 °C. In comparison, such coupling with basic zeolites is impossible due to neutralization of basic sites by inorganic acids. The authors further proposed a mechanism of glucose isomerization to fructose based on computational studies and confirmed the metal-assisted intramolecular hydride shift catalyzed on Lewis acid sites [121]. They further claimed that not only fully incorporated framework Sn species are responsible for glucose isomerization but also extra-framework SnO₂ particles could isomerize glucose [122]. The latter, however, proceeds *via* the base-assisted proton transfer as confirmed *via* ¹H and ¹³C NMR spectroscopic studies using deuterium-labelled glucose. At this point, the authors suggested that activity in glucose isomerization towards fructose cannot be attributed only to the Lewis acid sites generated by framework Sn species. Therefore, conclusions on the complete or incomplete Sn incorporation into a zeolite framework based on its activity in glucose isomerization to fructose is impossible. Rather, detailed studies involving deuterium or ¹³C labelled glucose is recommended in order to fully understand the mechanism and therefore the active sites responsible for glucose isomerization.

In addition to that, the authors investigated the mechanism of glucose isomerization [123]. They confirmed that the formation of fructose is favored by silanol groups (-SiOH) *via* 1,2-intramolecular hydride shift, as seen by ¹H and ¹³C NMR experiments on the ¹³C-labelled glucose.

To sum up, glucose isomerization is a simple one step reaction which can be catalyzed by both Lewis solid acids and solid bases. Its mechanism is strongly defined by the catalyst used: Lewis acids rather transform glucose *via* the so-called intramolecular hydride shift, whereas solid bases preferably *via* proton transfer. Glucose isomerization over basic zeolites is enabled due to their cationic (mainly Na, K)-exchanged forms. In order to further improve their catalytic performance, deposition of basic metal oxides (such as CaO or MgO) *via* classical impregnation is possible. In that case, a special attention should be given to the total content of deposited metal oxide in order to avoid particle agglomeration and therefore pore blocking. As for the textural properties of the parent zeolites, generation of hierarchical micro/mesoporosity improves the diffusion of glucose and fructose within the pores therefore improving the overall catalytic performance by avoiding the formation of by-products. However, considerable leaching of both impregnated metal oxides and charge-compensating cations remains a problem. At the same time, the purely Lewis acidic Sn-beta zeolite is considered as a benchmark solid catalyst for glucose isomerization into fructose and was shown to actively form fructose even at low reaction durations. Its stability against metal leaching and therefore high capacity of reusability was demonstrated after the corresponding catalytic tests. Potential coupling of glucose isomerization and fructose dehydration steps to yield HMF as the targeted product was demonstrated as well.

4.3. MOFs

The pioneering work on glucose isomerization on MOFs was done by Akiyama *et al.* [124]. They did a comparative study between two Cr-based MOFs: MIL-100 and MIL-101, which have 1,3,5-benzenetricarboxylate and 1,4-benzenedicarboxylate linkers, respectively (Table I.8).

Table I.8 – Glucose isomerization over MOFs.

Catalyst [▲]	m _{glu} /m _{cat} , mg/mg	Solvent	T, °C	t, h	Glucose conv., %	Fruc. yield (selec.), %	Ref
MIL-100(Cr)	25/200	H ₂ O	100	24	7	4 (57)	[124]
MIL-101(Cr)	25/200	H ₂ O	100	24	22	13 (59)	[124]
MIL-101(Cr)-NH ₂	25/200	H ₂ O	100	24	55	11 (20)	[124]
MIL-101(Cr)-NO ₂	25/200	H ₂ O	100	24	42	18 (43)	[124]
MIL-101(Cr)-SO ₃ H	25/200	H ₂ O	100	24	22	22 (100)	[124]
NU-1000(Zr)	30/12	E+H*	90	70	63	30 (46)	[125]
UiO-66(Zr)	40/7	P+H*	90	24	48	33 (69)	[126]
UiO-66(Zr)	40/7	E+H*	90	24	35	10 (29)	[126]
UiO-66(Zr)	40/7	M+H*	90	24	55	2 (4)	[126]
MIL-101(Cr)	36/18	E+H*	100	24	39	24 (62)	[127]
Cr(OH) ₃ /MIL-101(Cr)	36/18	E+H*	100	24	77	59 (77)	[127]
MIL-101(Cr)	36/50	H ₂ O	100	24	14	12 (86)	[128]
UiO-66(Zr)	36/50	H ₂ O	100	24	37	5 (14)	[128]
UiO-66(Zr)-NH ₂	36/50	H ₂ O	100	24	59	4 (7)	[128]
MIL-101(Cr)	50/80	H ₂ O	140	0.5	<5	- (-)	[129]
MIL-101(Cr)	50/80	H+G ^x	140	0.5	67	22 (33)	[129]

[▲] Powder catalyst dispersed in a batch reactor;

*Two-step glucose isomerization in EtOH, PrOH or MeOH followed by hydrolysis in H₂O (E+H), (P+H) or (M+H), respectively.

Thus, MIL-101 exhibits a larger surface area and, most importantly, a larger pores size as compared to MIL-100 (1.2 nm x 1.6 nm vs 0.55 nm x 0.86 nm, respectively). Thus, the latter exhibited only 7 % glucose conversion with 4 % fructose yield after 24 h of reaction at 100 °C in H₂O. At the same time, under the same conditions MIL-101 demonstrated higher glucose conversion (22 %) and fructose yield (13 %) originated from an easier diffusion of the reactants through its larger pores. Further, they found that introduction of functional groups (-NH₂, -NO₂

and -SO₃H) onto MIL-101 considerably improved its catalytic activity. Thus, glucose conversion on MIL-101-NH₂ increased up to 55 %, however yielding only 11 % fructose. This was attributed to the strong interaction of glucose with the basic amino groups. However, MIL-101-NO₂ and MIL-101-SO₃H each converted 42 % and 22 % glucose with 18 % and 22 % fructose yield, respectively, with the latter exhibiting the remarkable 100 % fructose selectivity.

Among other early works on glucose isomerization into fructose over MOFs, there is the study published by D. Malonzo *et al.* [125]. The authors examined the catalytic activity of NU-1000, a MOF composed of Zr-oxoclusters ([Zr₆(μ₃-O)₄(μ₃-OH)₄(OH)₄(H₂O)₄]⁸⁺). The latter, as stated by the authors, serves as Lewis acid sites required for glucose isomerization upon dehydration at high temperatures (300 °C). Indeed, once dehydrated, it yielded 30 % fructose at 65 % glucose conversion at 90 °C in ethanol after 70 h, following hydrolysis in water at 90 °C for 2 days, thus following a “two-step” isomerization process (figure I-8).

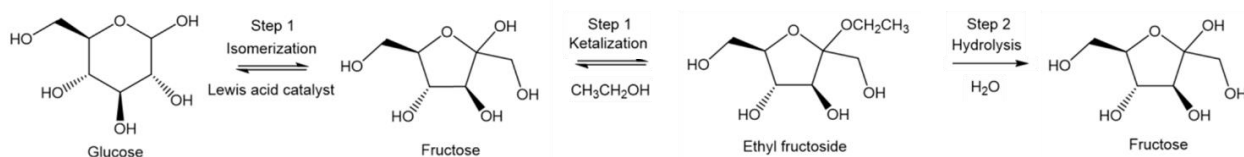


Figure I-8. Proposed mechanism of the “two-step” glucose isomerization into fructose. Adapted from [125].

When NU-1000 was calcined, giving pure Zr-oxoclusters, no activity at the given conditions was observed due to their agglomeration upon thermal treatment. However, Zr₆@SiO₂ obtained *via* a nanocasting approach through creating SiO₂ layer within the inner walls of the parent NU-1000, and subsequent calcination, showed a comparable catalytic activity yielding 23 % fructose at 50 % glucose conversion under the same conditions. The authors attributed this activity to the isolated Zr-oxoclusters on SiO₂ matrix therefore enabling the so-called single-site catalyst as a result of the nanocasting procedure.

De Mello *et al.* [126] examined the performance of UiO-66 MOF both modulated and defect-free in different solvents: methanol, ethanol, 1-propanol. They found that the modulated *i.e.* defect-containing UiO-66 outperformed its defect-free counterpart in each of the tested solvents. They attributed that to the presence of larger (~1.5 nm) pores induced by the structural defects in UiO-66 which favor hosting glucose molecules. Of note, defects in UiO-66 MOFs generate open metal sites and thus Lewis acidity, which was not quantified herein. Besides, they demonstrated that 1-propanol was the best solvent to provide higher fructose yields. After 24 h of reaction at 90 °C in 1-propanol and subsequent hydrolysis step as described above, the modulated UiO-66 yielded ~33 % fructose at ~48 % glucose conversion. At the same time, 35 % glucose conversion with 10 % fructose yield and 55 % glucose conversion with <2% fructose yield were reported in ethanol and methanol, respectively. The decreased fructose yield with an increase of the alkyl chain of the solvent was attributed to formation of alkyl fructoside by-products. This was explained by higher fructose-framework interaction in methanol and ethanol as compared to 1-propanol.

Guo and co-workers [127] examined the activity of the Cr(OH)₃/MIL-101(Cr) MOF-based catalyst. Notably, they found that the synergetic effect of both phases greatly improves glucose conversion and fructose yield. Indeed, this catalyst is composed of the basic Cr(OH)₃ hydroxide deposited on the surface of MIL-101(Cr) exhibiting predominantly Lewis acid sites. The authors performed the catalytic tests in the same “two-step” fashion as in the works mentioned above [125,126]. After 24 h of reaction at 100 °C in ethanol, followed by hydrolysis in water at 100 °C for another 24 h, 77 % glucose conversion with 59 % fructose yield were obtained over Cr(OH)₃/MIL-101(Cr). This is for now the highest activity demonstrated by a MOF or a MOF-derived catalyst in similar conditions. Interestingly, MIL-101(Cr) MOF alone converted 39 % glucose with 24 % fructose yield whereas Cr(OH)₃ alone converted 49 % glucose yielding 24 %

fructose under the same conditions. Thus, the authors showed the positive dual effect of basic and Lewis acid sites in glucose isomerization into fructose.

Luo *et al.* [128] extensively studied two MOFs: MIL-101(Cr) and UiO-66(Zr) applied in glucose isomerization. First, the former showed similar results as in the work by Akiyama *et al.* [124] converting 14 % glucose and yielding 12 % fructose after 24 h of reaction at 100 °C in H₂O. Under the same conditions, UiO-66 reached 37 % glucose conversion and 5 % fructose yield. The remarkable difference in conversion and yield might be originated from stronger Lewis acid sites generated by open metal sites on Zr atoms in the cluster. Indeed, this might be explained by the larger atomic radius and therefore higher polarizability of Zr as compared to Cr. Further, upon introduction of basic -NH₂ groups onto the UiO-66 surface, fructose conversion increased even more up to 59 %, but yielding only 4 % fructose. This agrees well with the results reported by Akiyama *et al.* [124] who also stated a considerable decrease in fructose selectivity over MIL-101(Cr)-NH₂ as compared to the parent MIL-101(Cr).

Oozeerally *et al.* [130] also reported on functionalized MOFs, namely UiO-66-SO₃H, applied in glucose isomerization. Thus, the classical UiO-66 reached 17 % glucose conversion yielding 7 % fructose after 3 h of reaction at 140 °C in H₂O confirming once again a lowered selectivity over UiO-66 as in the work by Luo *et al.* [128]. Upon insertion of 10 % and 20 % -SO₃H groups onto the parent UiO-66, glucose conversion increased up to 30 % and 32 % with fructose yields reaching 16 % and 21 %, respectively. The increase of the catalytic activity upon insertion of -SO₃H functional groups is in a good agreement with the results reported by Akiyama *et al.* [124].

Recently, Lara-Serrano *et al.* [129] reported on a comparative study on different MOFs' activities towards glucose isomerization in a GVL:water binary solvent system (90:10, wt.:%wt.%). They stated that aprotic solvents such as GVL do not tend to ligate to metal centers as protic ones such

as water, therefore maintaining the open metal sites available as source of Lewis acidity. They supported their statement by catalytic tests over MIL-101(Cr) MOF which demonstrated negligible (<5 %) glucose conversion and fructose yield after 30 min at 140 °C in water, whereas upon using of GVL:water mixture, the MOF showed considerable 22 % fructose yield at 67 % glucose conversion. Besides, they found that among the tested MOFs MIL-101(Cr) showed superior catalytic activity due to its larger pores as compared to the other tested MOFs MIL-53(Al), HKUST-1, MIL-53(Cr) and MIL-100(Fe).

To sum up, in order to catalyze glucose isomerization into fructose over MOFs, several conditions must be fulfilled: first, the MOF should exhibit pore diameters large enough to host glucose molecules with the kinetic diameter around 0.8 nm and decrease diffusion limitation. Second, they should possess Lewis acid sites provided by open metal sites in the cluster or basic sites provided by a functionalized linker. Third, they should be thermally stable in order to withstand hydrothermal conditions applied ($T > 100$ °C, few bars). The present studies showed that a large number of MOFs exhibited high capacities towards glucose isomerization due to their pronounced Lewis acid features. It should be noted as well that MOFs exhibit not only tunable acidic properties *via* framework functionalization but also tunable textural properties *via* structural defects due to missing linkers.

5. Upscaling and Limitations

5.1. Large Scale Synthesis

Transition from the small laboratory scale to the large-scale production (upscaling) of materials such as MOFs is a critical step towards their implementation in real industrial applications. This transition is possible due to technologies and equipment enabling MOFs manufacture at the required scale, purity and price. Such commercialization of zeolites was done decades ago and nowadays the list of commercially available zeolites includes MFI, FAU, MOR, CHA, BEA and others provided by CLARIANT, Zeolyst, and BASF. On the other hand, MOFs are still making their way towards the industrial production and up to now a few MOFs are commercially available and provided by major chemical actors including BASF (HKUST-1/Basolite C300, ZIF-8/Basolite Z1200, Fe-BTC/Basolite F300), and Strem Chemicals (MIL-53(Al), MIL-101(Cr), UiO-66). Several start-ups also emerged on this specific topic, counting MOFapps, MOFgen Ltd, MOF Technologies, novoMOF AG, Framergy, MOFWORX, Mosaic Materials, ProfMOF, Water Harvesting Inc, PrometheanParticles, and NuMat Technologies.

There are a few challenges associated with upscaling of MOFs which are based on:

- 1) Use of toxic, hazardous and flammable organic solvents;
- 2) Metal precursors as generally-employed nitrate and chloride salts generally provoke a safety hazard and corrosion, respectively;
- 3) Linker accessibility as many MOFs oftentimes require the use of sophisticated linkers;
- 4) Activation *i.e.* removal of the unreacted species and the solvent;
- 5) Shaping which is required for the final industrial application of MOFs.

Thus, upscaling strongly relies on optimization of the synthesis at small scale in order to establish the appropriate conditions. This includes the possible replacement of hazardous and toxic solvents by less dangerous analogues. Indeed, synthesis of many MOFs oftentimes requires the use of toxic for health and environmentally non-friendly solvents such as *N,N*-dimethylformamide (DMF) and *N,N*-dimethylacetamide (DMA) as well as aggressive mineral and organic acids such as hydrochloric, acetic, formic acid and so on. Besides, optimization should include suitable metal precursors (oxides or sulfates) and available linkers as well as the reasonable activation and purification steps to ensure a product with a high yield and purity. Novel synthetic routes of MOFs manufacturing were extensively reviewed by Maspoch *et al.* [131] who outlined a few production techniques with a high space-time yield (STY). The latter is the key parameter which implies the amount of MOFs possible to produce per unit volume of reactor per unit of time. Thus, among others, MOF synthesis by means of mechanochemistry, spray-drying and continuous flow methods were stated to be capable of high STYs.

5.2. Shaping

Lastly, as seen above shaping is a crucial step towards the industrial implementation of MOFs. Usually, powders are not convenient to use in big industrial reactors as they cause several difficulties from the process point of view. They induce, for example, consequent pressure drops within the reactor bed. In addition to that, powders can induce clogging and are generally complicated to handle and recover, involving additional costly separation steps. In order to overcome these issues and enable industrial implementation of solid catalysts, powders should be formulated into packed objects with defined size and dimensions. This process is called “shaping” and generally represents the compaction of individual crystallites into millimeter-sized objects.

Shaping allows for production of easily-handled objects required for industrial processes and generally has a few objectives:

- 1) Formulation of powders into mechanically stable objects to withstand a variety of process conditions (elevated pressure, gas/liquid flow, mixing);
- 2) Reduction of mass transfer limitation within the reactor volume;
- 3) Preservation of the physico-chemical properties of the pristine powder.

The latter represents the major challenge especially for MOFs as they are prone to drastic losses in available surface area and pore volume upon formulation process. Oftentimes, shaping implies the use of binders to enhance the mechanical stability of the shaped objects. Generally, they are classified into organic such as starch, cellulose or polyvinyl alcohol (PVA) and inorganic such as clays, silica or graphite. Nowadays, there are plenty of available shaping techniques which enable the formulation of powders into shaped bodies for the use in different types of reactors (Table I.9).

Table I.9 – Shaped bodies for different types of reactors. Adapted from [132].

Shaping technique	Object dimensions	Shape	Type of reactor
Pelletization	d = 3 – 15 mm h = 3 – 15 mm	Pellet	Fixed bed reactor
Extrusion	d = 1 – 20 mm h = 3 – 50 mm	Extrudate	Fixed bed reactor
Granulation	d = 1 – 20 mm	Bead	Fixed bed reactor
Spray-Drying	d = 0.02 – 0.2 mm	Microspheres	Fluidized bed reactor

Therefore, each of the shaping techniques provides unique features to the final objects in terms of size and appearance for a defined application. Thus, pelletization is one of the most widely used shaping technique and represents compaction of powder particles by applying pressure [133,134]. Owing to its simplicity, pelletization is the first shaping technique to have been applied at industrial scale. Extrusion is nowadays considered the most commonly used technique for shaping of catalysts or adsorbents for industrial applications in fixed-bed reactors. As the main principle, extrusion relies on passing the pre-formed paste inside an extruder through a die. Depending on the form of the die, the final objects can have different shapes: hollow tubes, sheets, strips, cylinders with various cross-sections and others [135,136]. Granulation is another commonly-used shaping process which is based on size enlargement of a parent powder material into an assembly of bigger agglomerates *via* adhesion with a solvent. A typical body shaped *via* granulation is referred as a “granule” with an average size range of 2-20 mm [137,138]. Spray-drying relies on atomization of a solution (MOF precursor) into micron-sized droplets within a heated chamber. During this process, the precursors rapidly react thus forming MOF particles inside droplets replicating their shape and size. Eventually, the droplets are completely evaporated and freshly formed MOF beads are collected leaving the dried powder to be further captured and collected. Therefore, the entire spray-drying process can be viewed as a technique for simultaneous synthesis and shaping of MOF particles into micron-sized spherical agglomerates [139,140].

These represent the so-called conventional shaping techniques already implemented in industry. Instead, the 3D printing method is a newly-emerged type of extrusion with controlled deposition of the forming paste in three dimensions in space [141,142]. Therefore, 3D printing allows shaping powders with desired shapes and dimensions for a wide variety of applications. Recently, shaping of MOF powders into solid objects was extensively reviewed by our team, outlining positive and

Chapter I – Upscaling and Limitations

negative sides of each technique when applied on typical MOFs [143]. Thus, it was concluded that MOFs in general are prone to remarkable changes of structural and textural properties upon shaping. There are MOFs such as HKUST-1 and MOF-5 which exhibit lower tolerance for high pressures, formulation or binders and therefore suffer significantly structural and textural collapse. On the other hand, MOFs such as ZIF-8, UiO-66, MIL-101 are generally less affected by shaping and therefore considered more appropriate and appealing for shaping.

References:

- [1] N.L. Panwar, S.C. Kaushik, S. Kothari, Role of renewable energy sources in environmental protection: A review, *Renew. Sustain. Energy Rev.* 15 (2011) 1513–1524. <https://doi.org/10.1016/j.rser.2010.11.037>.
- [2] A. Tursi, A review on biomass: Importance, chemistry, classification, and conversion, *Biofuel Res. J.* 6 (2019) 962–979. <https://doi.org/10.18331/BRJ2019.6.2.3>.
- [3] M. Guo, W. Song, J. Buhain, Bioenergy and biofuels: History, status and perspective, *Renew. Sustain. Energy Rev.* 42 (2015) 712–725. <https://doi.org/10.1016/j.rser.2014.10.013>.
- [4] D.M. Alonso, J.Q. Bond, J.A. Dumesic, Catalytic conversion of biomass to biofuels, *Green Chem.* 12 (2010) 1493–1513. <https://doi.org/10.1039/c004654j>.
- [5] F.R. Amin, H. Khalid, H. Zhang, S. Rahman, R. Zhang, G. Liu, C. Chen, Pretreatment methods of lignocellulosic biomass for anaerobic digestion, *AMB Express.* 7 (2017) 72. <https://doi.org/10.1186/s13568-017-0375-4>.
- [6] R. Rinaldi, F. Schüth, Acid Hydrolysis of Cellulose as the Entry Point into Biorefinery Schemes, *ChemSusChem.* 2 (2009) 1096–1107. <https://doi.org/10.1002/cssc.200900188>.
- [7] S. Kang, J. Fu, G. Zhang, From lignocellulosic biomass to levulinic acid: A review on acid-catalyzed hydrolysis, *Renew. Sustain. Energy Rev.* 94 (2018) 340–362. <https://doi.org/10.1016/j.rser.2018.06.016>.
- [8] G. Dedes, A. Karnaouri, E. Topakas, Novel Routes in Transformation of Lignocellulosic Biomass to Furan Platform Chemicals: From Pretreatment to Enzyme Catalysis, *Catalysts.* 10 (2020) 743.
- [9] J.U. Hernández-Beltrán, I.O. Hernández-De Lira, M.M. Cruz-Santos, A. Saucedo-Luevanos, F. Hernández-Terán, N. Balagurusamy, Insight into Pretreatment Methods of Lignocellulosic Biomass to Increase Biogas Yield: Current State, Challenges, and Opportunities, *Appl. Sci.* 9 (2019) 3721.
- [10] R.P. John, K.M. Nampoothiri, A. Pandey, Fermentative production of lactic acid from biomass: an overview on process developments and future perspectives, *Appl. Microbiol. Biotechnol.* 74 (2007) 524–534. <https://doi.org/10.1007/s00253-006-0779-6>.
- [11] C. Lavinia-florina, D. Cristian, G. Adrian, Trends in Food Science & Technology Bio-vanillin: Towards a sustainable industrial production, *Trends Food Sci. Technol.* 109 (2021) 579–592. <https://doi.org/10.1016/j.tifs.2021.01.059>.
- [12] M. Fache, B. Boutevin, S. Caillol, Vanillin production from lignin and its use as a renewable chemical, *ACS Sustain. Chem. Eng.* 4 (2016) 35–46. <https://doi.org/10.1021/acssuschemeng.5b01344>.
- [13] J. Esteban, P. Yustos, M. Ladero, Catalytic Processes from Biomass-Derived Hexoses and Pentoses: A Recent Literature Overview, *Catalysts.* 8 (2018) 1–39. <https://doi.org/10.3390/catal8120637>.

Chapter I – References

- [14] P. Hull, Glucose syrup manufacture 3.1, in: *Glucose Syrups Technol. Appl.*, 2010: pp. 19–44.
- [15] J. Wang, J. Xi, Y. Wang, Recent advances in the catalytic production of glucose from lignocellulosic biomass, *Green Chem.* 17 (2015) 737–751. <https://doi.org/10.1039/c4gc02034k>.
- [16] P. Gallezot, P.J. Cerino, B. Blanc, G. Flèche, P. Fuertes, Glucose Hydrogenation on Promoted Raney-Nickel Catalysts, *J. Catal.* 146 (1994) 93–102.
- [17] M. Rose, R. Palkovits, Isosorbide as a Renewable Platform chemical for Versatile Applications — Quo Vadis?, *ChemSusChem.* 5 (2012) 167–176. <https://doi.org/10.1002/cssc.201100580>.
- [18] J. Tang, X. Guo, L. Zhu, C. Hu, Mechanistic Study of Glucose-to-Fructose Isomerization in Water Catalyzed by $[Al(OH)_2(aq)]^+$, *ACS Catal.* 5 (2015) 5097–5103.
- [19] I. Delidovich, R. Palkovits, Catalytic Isomerization of Biomass-Derived Aldoses: A Review, *ChemSusChem.* 9 (2016) 547–561. <https://doi.org/10.1002/cssc.201501577>.
- [20] H. Li, S. Yang, S. Saravanamurugan, A. Riisager, Glucose isomerization by enzymes and chemo-catalysts: Status and current advances, *ACS Catal.* 7 (2017) 3010–3029. <https://doi.org/10.1021/acscatal.6b03625>.
- [21] I. Delidovich, Green and Sustainable Chemistry Recent progress in base-catalyzed isomerization of D-glucose into D-fructose, *Curr. Opin. Green Sustain. Chem.* 27 (2021) 100414. <https://doi.org/10.1016/j.cogsc.2020.100414>.
- [22] S.S. Chen, Y. Cao, D.C.W. Tsang, J. Tessonier, J. Shang, D. Hou, Z. Shen, S. Zhang, Y.S. Ok, K.C. Wu, Effective dispersion of MgO nanostructure on biochar support as a basic catalyst for glucose isomerization, *ACS Sustain. Chem. Eng.* 8 (2020) 6990–7001. <https://doi.org/10.1021/acssuschemeng.0c00278>.
- [23] M. Ventura, J.A. Cecilia, M.E. Rodríguez-Castelló, Enrique Domine, Tuning Ca–Al-based catalysts' composition to isomerize or epimerize glucose and other sugars, *Green Chem.* 22 (2020) 1393–1405. <https://doi.org/10.1039/C9GC02823D>.
- [24] A. Marianou, C. Michailof, S. Karakoulia, D. Ipsakis, H. Yiannoulakis, K.S. Triantafyllidis, A.A. Lappas, Isomerization of glucose into fructose over natural and synthetic MgO catalysts, *ACS Sustain. Chem. Eng.* 6 (2018) 16459–16470. <https://doi.org/10.1021/acssuschemeng.8b03570>.
- [25] H. Kitajima, Y. Higashino, S. Matsuda, H. Zhong, M. Watanabe, T.M. Aida, R.L. Smith, Isomerization of glucose at hydrothermal condition with TiO₂, ZrO₂, CaO-doped ZrO₂ or TiO₂-doped ZrO₂, Lee, Richard Jr., 274 (2016) 67–72. <https://doi.org/10.1016/j.cattod.2016.01.049>.
- [26] J.M. Carraher, C.N. Fleitman, J. Tessonier, Kinetic and Mechanistic Study of Glucose Isomerization Using Homogeneous Organic Brønsted Base Catalysts in Water, *ACS Catal.* 5 (2015) 3162–3173. <https://doi.org/10.1021/acscatal.5b00316>.
- [27] L. Zhang, B. Deng, N. Li, H. Zhong, Isomerization of glucose into fructose with

- homogenous amine-type base catalysts: amine structure, chain length, and kinetics, *Bioresour. Bioprocess.* 6 (2019) 35. <https://doi.org/10.1186/s40643-019-0271-7>.
- [28] A.A. Marianou, C.M. Michailof, A. Pineda, E.F. Iliopoulou, K.S. Triantafyllidis, A.A. Lappas, Glucose to Fructose Isomerization in Aqueous Media over Homogeneous and Heterogeneous Catalysts, *ChemCatChem.* 8 (2016) 1100–1110. <https://doi.org/10.1002/cctc.201501203>.
- [29] Y. Romun-leshkov, M. Moliner, J.A. Labinger, M.E. Davis, Mechanism of Glucose Isomerization Using a Solid Lewis Acid Catalyst in Water, *Angew. Chemie Int. Ed.* 49 (2010) 8954–8957. <https://doi.org/10.1002/ange.201004689>.
- [30] T. Shintani, Food Industrial Production of Monosaccharides Using Microbial, Enzymatic, and Chemical Methods, *Fermentation.* 5 (2019) 47.
- [31] R. Van Putten, J.C. Van Der Waal, E. De Jong, C.B. Rasrendra, H.J. Heeres, J.G. De Vries, Hydroxymethylfurfural, A Versatile Platform Chemical Made from Renewable Resources, *Chem. Rev.* 113 (2013) 1499–1597.
- [32] A.A. Rosatella, S.P. Simeonov, R.F.M. Frade, C.A.M. Afonso, 5-Hydroxymethylfurfural (HMF) as a building block platform: Biological properties, synthesis and synthetic applications, *Green Chem.* (2011) 754–793. <https://doi.org/10.1039/c0gc00401d>.
- [33] G.P. Perez, A. Mukherjee, M. Dumont, Insights into HMF catalysis, *J. Ind. Eng. Chem.* 70 (2019) 1–34. <https://doi.org/10.1016/j.jiec.2018.10.002>.
- [34] B. Agarwal, K. Kailasam, R. Singh, Traversing the history of solid catalysts for heterogeneous synthesis of 5-hydroxymethylfurfural from carbohydrate sugars: A review, *Renew. Sustain. Energy Rev.* 82 (2018) 2408–2425. <https://doi.org/10.1016/j.rser.2017.08.088>.
- [35] T. Wang, W. Nolte, B.H. Shanks, Catalytic dehydration of C6 carbohydrates for the production of hydroxymethylfurfural (HMF) as a versatile platform chemical, *Green Chem.* 16 (2014) 548–572. <https://doi.org/10.1039/c3gc41365a>.
- [36] S.P. Teong, G. Yi, Y. Zhang, Hydroxymethylfurfural production from bioresources: past, present and future, *Green Chem.* 16 (2014) 2015–2026. <https://doi.org/10.1039/c3gc42018c>.
- [37] C. Sievers, I. Musin, T. Marzalletti, M.B.V. Olarte, P.K. Agrawal, C.W. Jones, Acid-Catalyzed Conversion of Sugars and Furfurals in an Ionic-Liquid Phase, *ChemSusChem.* 2 (2009) 665–671. <https://doi.org/10.1002/cssc.200900092>.
- [38] T. Tuercke, S. Panic, S. Loebbecke, Microreactor Process for the Optimized Synthesis of 5-Hydroxymethylfurfural: A Promising Building Block Obtained by Catalytic Dehydration of Fructose, *Chem. Eng. Technol.* 32 (2009) 1815–1822. <https://doi.org/10.1002/ceat.200900427>.
- [39] Y. Roman-Leshkov, J.A. Dumesic, Solvent Effects on Fructose Dehydration to 5-Hydroxymethylfurfural in Biphasic Systems Saturated with Inorganic Salts, *Top. Catal.* 52 (2009) 297–303. <https://doi.org/10.1007/s11244-008-9166-0>.

- [40] Z. Huang, Y. Pan, Y. Chao, W. Shen, C. Wang, H. Xu, Triazaheterocyclic compound as an efficient catalyst for dehydration of fructose into 5-hydroxymethylfurfural, *RSC Adv.* 4 (2014) 13434. <https://doi.org/10.1039/c4ra00534a>.
- [41] J. Lu, Y. Yan, Y. Zhang, Y. Tang, Microwave-assisted high efficient transformation of ketose/aldose to 5- hydroxymethylfurfural (5-HMF) in a simple phosphate buffer system, *RSC Adv.* 2 (2012) 7652–7655. <https://doi.org/10.1039/b000000x>.
- [42] S.L. Barbosa, M.D.S. Freitas, W.T.P. Santos, D.L. Nelson, S.I. Klein, G.C. Clososki, F.J. Caires, A.C.M. Baroni, A.P. Wentz, Dehydration of D-fructose in DMSO using a hydrophilic sulfonated silica catalyst in a process promoted by microwave irradiation, *Sci. Rep.* 11 (2021) 1919. <https://doi.org/10.1038/s41598-020-80285-2>.
- [43] V. V Ordonsky, J. Van Der Schaaf, J.C. Schouten, T.A. Nijhuis, Fructose Dehydration to 5-Hydroxymethylfurfural over Solid Acid Catalysts in a Biphasic System, *ChemSusChem.* 5 (2012) 1–9. <https://doi.org/10.1002/cssc.201200072>.
- [44] G. Morales, J.A. Melero, M. Paniagua, J. Iglesias, B. Hernández, M. Sanz, Sulfonic acid heterogeneous catalysts for dehydration of C6-monosaccharides to 5-hydroxymethylfurfural in dimethyl sulfoxide, *Chinese J. Catal.* 35 (2014) 644–655. [https://doi.org/10.1016/S1872-2067\(14\)60020-6](https://doi.org/10.1016/S1872-2067(14)60020-6).
- [45] J. Jeong, C.A. Antonyraj, S. Shin, S. Kim, B. Kim, K. Lee, J. Ku, Commercially attractive process for production of 5-hydroxymethyl-2-furfural from high fructose corn syrup, *J. Ind. Eng. Chem.* 19 (2013) 1106–1111. <https://doi.org/10.1016/j.jiec.2012.12.004>.
- [46] L. Wang, J. Zhang, L. Zhu, X. Meng, F.-S. Xiao, Efficient conversion of fructose to 5-hydroxymethylfurfural over sulfated porous carbon catalyst, *J. Energy Chem.* 22 (2013) 241–244. [https://doi.org/10.1016/S2095-4956\(13\)60029-7](https://doi.org/10.1016/S2095-4956(13)60029-7).
- [47] X. Guo, Q. Cao, Y. Jiang, J. Guan, X. Wang, X. Mu, Selective dehydration of fructose to 5-hydroxymethylfurfural catalyzed by mesoporous SBA-15-SO₃H in ionic liquid BmimCl, *Carbohydr. Res.* 351 (2012) 35–41. <https://doi.org/10.1016/j.carres.2012.01.003>.
- [48] F.N.D.C. Gomes, F.M.T. Mendes, M.M.V.M. Souza, Synthesis of 5-hydroxymethylfurfural from fructose catalyzed by phosphotungstic acid, *Catal. Today.* 279 (2017) 296–304. <https://doi.org/10.1016/j.cattod.2016.02.018>.
- [49] J.C. Serrano-ruiz, A. Sepu, J.C. Serrano-ruiz, Transformations of biomass-derived platform molecules: from high added-value chemicals to fuels *via* aqueous-phase processing, *Chem. Soc. Rev.* 40 (2011) 5266–5281. <https://doi.org/10.1039/c1cs15131b>.
- [50] M. Ventura, A. Marinas, M.E. Domine, Catalytic Processes for Biomass - Derived Platform Molecules Valorisation, *Top. Catal.* 63 (2020) 846–865. <https://doi.org/10.1007/s11244-020-01309-9>.
- [51] D.M. Alonso, S.G. Wettstein, J.A. Dumesic, Gamma-valerolactone, a sustainable platform molecule derived from lignocellulosic biomass, *Green Chem.* 15 (2013) 584–595. <https://doi.org/10.1039/b000000x>.
- [52] K. Yan, Y. Yang, J. Chai, Y. Lu, Catalytic reactions of gamma-valerolactone: A platform to fuels and value-added chemicals, *Appl. Catal. B Environ.* 179 (2015) 292–304.

- <https://doi.org/10.1016/j.apcatb.2015.04.030>.
- [53] C.H.L. Tempelman, R. Oozeerally, V. Degirmenci, Heterogeneous Catalysts for the Conversion of Glucose into 5-Hydroxymethyl Furfural, *Catalysts*. 11 (2021) 861.
- [54] C. Megías-Sayago, S. Navarro-Jaén, F. Drault, S. Ivanova, Recent Advances in the Brønsted/Lewis Acid Catalyzed Conversion of Glucose to HMF and Lactic Acid: Pathways toward Bio-Based Plastics, *Catalysts*. 11 (2021) 1395.
- [55] Database of Zeolite Structures, (n.d.). <http://www.iza-structure.org/databases/>.
- [56] F.C. Hendriks, D. Valencia, P.C.A. Bruijninx, B.M. Weckhuysen, Zeolite molecular accessibility and host–guest interactions studied by adsorption of organic probes of tunable size, *Phys. Chem. Chem. Phys.* 19 (2017) 1857–1867. <https://doi.org/10.1039/c6cp07572j>.
- [57] J. Hagen, Shape-Selective Catalysis : Zeolites, in: *Ind. Catal. A Pract. Approach*, 2015: pp. 239–260.
- [58] R.P. Townsend, E.N. Coker, Ion exchange in zeolites, in: *Introd. to Zeolite Sci. Pract.*, 2001: pp. 467–524.
- [59] Y. Li, J. Yu, Emerging applications of zeolites in catalysis, separation and host–guest assembly, *Nat. Rev. Mater.* 6 (2021) 1156–1174. <https://doi.org/10.1038/s41578-021-00347-3>.
- [60] L.-H. Chen, M.-H. Sun, Z. Wang, W. Yang, Z. Xie, B.-L. Su, Hierarchically Structured Zeolites: From Design to Application, *Chem. Rev.* 120 (202AD) 11194–11294. <https://doi.org/10.1021/acs.chemrev.0c00016>.
- [61] C.S. Triantafillidis, N.P. Evmiridis, L. Nalbandian, I.A. Vasalos, Performance of ZSM-5 as a Fluid Catalytic Cracking Catalyst Additive: Effect of the Total Number of Acid Sites and Particle Size, *Ind. Eng. Chem. Res.* 38 (1999) 916–927.
- [62] P.J. Smeets, J.S. Woertink, B.F. Sels, E.I. Solomon, R.A. Schoonheydt, Transition-Metal Ions in Zeolites: Coordination and Activation of Oxygen, *Inorg. Chem.* 49 (2010) 3573–3583. <https://doi.org/10.1021/ic901814f>.
- [63] M. Dusselier, M.E. Davis, Small-Pore Zeolites: Synthesis and Catalysis, *Chem. Rev.* 118 (2018) 5265–5329. <https://doi.org/10.1021/acs.chemrev.7b00738>.
- [64] A. Sachse, J. Garcia-Martinez, Surfactant-Templating of Zeolites: From Design to Application, *Chem. Mater.* 29 (2017) 3827–3853. <https://doi.org/10.1021/acs.chemmater.7b00599>.
- [65] Z. Mo, Q. Li, Y. Qin, L. Duan, X. Zhang, L. Song, A DFT study of the effect of NNN Al atom on strength of Brønsted acid sites of HY zeolite, *Mol. Simul.* 42 (2016) 986–992. <https://doi.org/10.1080/08927022.2015.1135332>.
- [66] S. Mintova, V. Valtchev, T. Onfroy, C. Marichal, H. Knozinger, T. Bein, Variation of the Si/Al ratio in nanosized zeolite Beta crystals, *Microporous Mesoporous Mater.* 90 (2006) 237–245. <https://doi.org/10.1016/j.micromeso.2005.11.026>.
- [67] A. Janda, A.T. Bell, Effects of Si/Al Ratio on the Distribution of Framework Al and on the

- Rates of Alkane Monomolecular Cracking and Dehydrogenation in H-MFI, *J. Am. Chem. Soc.* 135 (2013) 19193–19207.
- [68] T. Crémoux, I. Batonneau-Gener, A. Moissette, J.-L. Paillaud, M. Hureau, E. Ligner, C. Morais, S. Laforge, C. Marichal, H. Nouali, Influence of framework Si/Al ratio and topology on electron transfers in zeolites, *Phys. Chem. Chem. Phys.* 21 (2019) 14892–14903. <https://doi.org/10.1039/C9CP01166H>.
- [69] A. Fink, H. Gierlich, I. Delidovich, R. Palkovits, Systematic Catalyst Screening of Zeolites with Various Frameworks and Si/Al Ratios to Identify Optimum Acid Strength in OME Synthesis, *ChemCatChem*. 12 (2020) 5710–5719. <https://doi.org/10.1002/cctc.202000972>.
- [70] T. Pang, X. Yang, C. Yuan, A.A. Elzatahry, A. Alghamdi, X. He, X. Cheng, Y. Deng, Recent advance in synthesis and application of heteroatom zeolites, *Chinese Chem. Lett.* 32 (2021) 328–338. <https://doi.org/10.1016/j.cclet.2020.04.018>.
- [71] X. Fang, Q. Wang, A. Zheng, Y. Liu, Y. Wang, X. Deng, H. Wu, F. Deng, M. He, P. Wu, Fluorine-planted titanosilicate with enhanced catalytic activity in alkene epoxidation with hydrogen peroxide, *Catal. Sci. Technol.* 2 (2012) 2433–2435. <https://doi.org/10.1039/c2cy20446k>.
- [72] G. Energy, R. Bai, Y. Song, G. Tian, F. Wang, A. Corma, J. Yu, Titanium-rich TS-1 zeolite for highly efficient oxidative desulfurization, *Green Energy Environ.* (2021) 1–10. <https://doi.org/10.1016/j.gee.2021.03.006>.
- [73] C.T.-W. Chu, C.D. Chang, Isomorphous Substitution in Zeolite Frameworks. 1. Acidity of Surface Hydroxyls in [B]-, [Fe]-, [Ga]-, and [Al]-ZSM-5, *J. Phys. Chem.* 89 (1985) 1569–1571.
- [74] R.E. Patet, M. Koehle, R.F. Lobo, S. Caratzoulas, D.G. Vlachos, General Acid-Type Catalysis in the Dehydrative Aromatization of Furans to Aromatics in H-[Al]-BEA, H-[Fe]-BEA, H-[Ga]-BEA, and H-[B]- BEA Zeolites, *J. Phys. Chem. C*. 121 (2017) 13666–13679. <https://doi.org/10.1021/acs.jpcc.7b02344>.
- [75] H. Bemdt, A. Martin, H. Kosslick, B. Lücke, Comparison of the acidic properties of ZSM-5 zeolites isomorphously substituted by Ga, In, B and Fe, *Microporous Mater.* 2 (1994) 197–204.
- [76] C. Altintas, O.F. Altundal, S. Keskin, R. Yildirim, Machine Learning Meets with Metal Organic Frameworks for Gas Storage and Separation, *J. Chem. Inf. Model.* 61 (2021) 2131–2146. <https://doi.org/10.1021/acs.jcim.1c00191>.
- [77] H. Li, L. Li, R.-B. Lin, W. Zhou, S. Xiang, B. Chen, Porous metal-organic frameworks for gas storage and separation: Status and challenges, *EnergyChem.* 1 (2019) 100006. <https://doi.org/10.1016/j.enchem.2019.100006>.
- [78] A. Bavykina, N. Kolobov, I.S. Khan, J.A. Bau, A. Ramirez, J. Gascon, Metal – Organic Frameworks in Heterogeneous Catalysis: Recent Progress, New Trends, and Future Perspectives, *Chem. Rev.* 120 (2020) 8468–8535. <https://doi.org/10.1021/acs.chemrev.9b00685>.
- [79] B. Jun, Y.A.J. Al-hamadani, A. Son, C.M. Park, M. Jang, A. Jang, N.C. Kim, Y. Yoon,

- Applications of metal-organic framework based membranes in water purification: A review, *Sep. Purif. Technol.* 247 (2020) 116947. <https://doi.org/10.1016/j.seppur.2020.116947>.
- [80] E. Barea, C. Montoro, J.A.R. Navarro, Toxic gas removal – metal–organic frameworks for the capture and degradation of toxic gases and vapours, *Chem. Soc. Rev.* 43 (2014) 5419. <https://doi.org/10.1039/c3cs60475f>.
- [81] S.M. Moosavi, A. Nandy, K.M. Jablonka, D. Ongari, J.P. Janet, P.G. Boyd, Y. Lee, B. Smit, H.J. Kulik, Understanding the diversity of the metal-organic framework ecosystem, *Nat. Commun.* 11 (2020) 1–10. <https://doi.org/10.1038/s41467-020-17755-8>.
- [82] S.S.-Y. Chui, S.M.-F. Lo, J.P.H. Charmant, A.G. Orpen, I.D. Williams, A Chemically Functionalizable Nanoporous Material $[\text{Cu}_3(\text{TMA})_2(\text{H}_2\text{O})_3]_n$, *Science* (80-.). 283 (1999) 1148–1151. <https://doi.org/10.1126/science.283.5405.1148>.
- [83] J. Huo, M. Brightwell, S. El Hankari, A. Garai, D. Bradshaw, A versatile, industrially relevant, aqueous room temperature synthesis of HKUST-1 with high space-time yield, *J. Mater. Chem. A.* 1 (2013) 15220–15223. <https://doi.org/10.1039/C3TA14409G>.
- [84] M. Todaro, G. Buscarino, L. Sciortino, A. Alessi, M. Fabrizio, M. Taddei, M. Ranocchiarì, M. Cannas, F.M. Gelardi, Decomposition Process of Carboxylate MOF HKUST-1 Unveiled at the Atomic Scale Level, *J. Phys. Chem. C.* 120 (2016) 12879–12889. <https://doi.org/10.1021/acs.jpcc.6b03237>.
- [85] H. Li, M. Eddaoudi, M. O’Keeffe, O.M. Yaghi, Design and synthesis of an exceptionally stable and highly porous metal-organic framework, *Nature.* 402 (1999) 276–279.
- [86] D. Saha, Z. Bao, F. Jia, S. Deng, Adsorption of CO_2 , CH_4 , N_2O , and N_2 on MOF-5, MOF-177, and Zeolite 5A, *Environ. Sci. Technol.* 44 (2010) 1820–1826.
- [87] J.A. Greathouse, M.D. Allendorf, The Interaction of Water with MOF-5 Simulated by Molecular Dynamics, *J. Am. Chem. Soc.* 128 (2006) 10678–10679.
- [88] Y. Ming, N. Kumar, D.J. Siegel, Water Adsorption and Insertion in MOF-5, *ACS Omega.* 2 (2017) 4921–4928. <https://doi.org/10.1021/acsomega.7b01129>.
- [89] J.Y. Choi, R. Huang, F.J. Uribe-romo, H.K. Chae, K.S. Park, Z. Ni, A.P. Co, M.O. Keeffe, O.M. Yaghi, Exceptional chemical and thermal stability of zeolitic imidazolate frameworks, *PNAS.* 103 (2006) 10186–10191. <https://doi.org/10.1073/pnas.0602439103>.
- [90] H. Yin, H. Kim, J. Choi, A.C.K. Yip, Thermal stability of ZIF-8 under oxidative and inert environments: A practical perspective on using ZIF-8 as a catalyst support, *Chem. Eng. J.* 278 (2015) 293–300. <https://doi.org/10.1016/j.cej.2014.08.075>.
- [91] F. Millange, C. Serre, G. Férey, Synthesis, structure determination and properties of MIL-53as and MIL-53ht: the first Crⁱⁱⁱ hybrid inorganic–organic microporous solids: $\text{Cr}^{\text{iii}}(\text{OH}) \cdot \{\text{O}_2\text{C}-\text{C}_6\text{H}_4-\text{CO}_2\} \cdot \{\text{HO}_2\text{C}-\text{C}_6\text{H}_4-\text{CO}_2\text{H}\}_x$, *Chem. Commun.* (2002) 822–823.
- [92] T. Loiseau, C. Serre, C. Huguenard, G. Fink, F. Taulelle, M. Henry, T. Bataille, G. Férey, A Rationale for the Large Breathing of the Porous Aluminum Terephthalate (MIL-53) Upon Hydration, *Chem. Eur. J.* 10 (2004) 1373–1382. <https://doi.org/10.1002/chem.200305413>.

- [93] J.H. Cavka, S. Jakobsen, U. Olsbye, N. Guillou, C. Lamberti, S. Bordiga, K.P. Lillerud, A New Zirconium Inorganic Building Brick Forming Metal Organic Frameworks with Exceptional Stability, *J. Am. Chem. Soc.* 130 (2008) 13850–13851. <https://doi.org/10.1021/ja8057953>.
- [94] C.G. Piscopo, A. Polyzoidis, M. Schwarzer, S. Loebbecke, Stability of UiO-66 under acidic treatment: Opportunities and limitations for post-synthetic modifications, *Microporous Mesoporous Mater.* 208 (2015) 30–35. <https://doi.org/10.1016/j.micromeso.2015.01.032>.
- [95] M.J. Katz, Z.J. Brown, Y.J. Colon, P.W. Siu, K.A. Scheidt, R.Q. Snurr, J.T. Hupp, O.K. Farha, A facile synthesis of UiO-66, UiO-67 and their derivatives, *Chem. Commun.* 49 (2013) 9449–9451. <https://doi.org/10.1039/C3CC46105J>.
- [96] D. Kim, H. Kim, D. Cho, Catalytic performance of MIL-100 (Fe, Cr) and MIL-101 (Fe, Cr) in the isomerization of Endo- to exo-dicyclopentadiene, *CATCOM.* 73 (2016) 69–73. <https://doi.org/10.1016/j.catcom.2015.10.006>.
- [97] V.R. Bakuru, S.R. Churapird, S.P. Maradur, S.B. Kalidindi, Exploring the Brønsted Acidity of UiO-66 (Zr, Ce, Hf) Metal-Organic Frameworks for Efficient Solketal Synthesis from Glycerol Acetalization, *Dalt. Trans.* 48 (2019) 843–847. <https://doi.org/10.1039/C8DT03512A>.
- [98] J. Chen, K. Li, L. Chen, R. Liu, X. Huang, D. Ye, Conversion of fructose into 5-hydroxymethylfurfural catalyzed by recyclable sulfonic acid-functionalized metal-organic frameworks, *Green Chem.* 16 (2014) 2490. <https://doi.org/10.1039/c3gc42414f>.
- [99] M.L. Foo, S. Horike, T. Fukushima, Y. Hijikata, Y. Kubota, M. Takata, S. Kitagawa, Ligand-based solid solution approach to stabilisation of sulphonic acid groups in porous coordination polymer $Zr_6O_4(OH)_4(BDC)_6$ (UiO-66), *Dalt. Trans.* 41 (2012) 13791–13794. <https://doi.org/10.1039/c2dt31195j>.
- [100] L. Ma, L. Xu, X. Yuan, Comparative research on three types of MIL-101(Cr)-SO₃H for esterification of cyclohexene with formic acid, *RSC Adv.* 9 (2019) 5692. <https://doi.org/10.1039/c8ra10366f>.
- [101] J.-M. Yang, R.-Z. Zhang, Y.-Y. Liu, Superior adsorptive removal of anionic dyes by MIL-101 analogues: the effect of free carboxylic acid groups in the pore channels, *CrystEngComm.* 21 (2019) 5824–5833. <https://doi.org/10.1039/C9CE01224A>.
- [102] L. Zhang, J. Wang, T. Du, W. Zhang, W. Zhu, C. Yang, T. Yue, J. Sun, T. Li, J. Wang, NH₂-MIL-53(Al) Metal-Organic Framework as the Smart Platform for Simultaneous High-Performance Detection and Removal of Hg²⁺, *Inorg. Chem.* 58 (2019) 12573–12581. <https://doi.org/10.1021/acs.inorgchem.9b01242>.
- [103] Z. Zhang, X. Li, B. Liu, Q. Zhao, G. Chen, Hexagonal microspindle of NH₂-MIL-101(Fe) metal-organic frameworks with visible-light-induced photocatalytic activity for the degradation of toluene, *RSC Adv.* 6 (2016) 4289. <https://doi.org/10.1039/C5RA23154J>.
- [104] C. Moreau, R. Durand, C. Pourcheron, S. Razigade, Preparation of 5-hydroxymethylfurfural from fructose and precursors over H-form zeolites, *Ind. Crops Prod.* 3 (1994) 85–90.
- [105] V. V. Ordonsky, J. Van Der Schaaf, J.C. Schouten, T.A. Nijhuis, The effect of solvent

- addition on fructose dehydration to 5-hydroxymethylfurfural in biphasic system over zeolites, *J. Catal.* 287 (2012) 68–75. <https://doi.org/10.1016/j.jcat.2011.12.002>.
- [106] V. Rac, V. Rakic, D. Stošić, O. Otman, A. Auroux, Hierarchical ZSM-5, Beta and USY zeolites: Acidity assessment by gas and aqueous phase calorimetry and catalytic activity in fructose dehydration reaction, *Microporous Mesoporous Mater.* 194 (2014) 126–134. <https://doi.org/10.1016/j.micromeso.2014.04.003>.
- [107] P. Dornath, W. Fan, Dehydration of fructose into furans over zeolite catalyst using carbon black as adsorbent, *Microporous Mesoporous Mater.* 191 (2014) 10–17. <https://doi.org/10.1016/j.micromeso.2014.02.031>.
- [108] Y. Shi, X. Li, J. Hu, J. Lu, Y. Ma, Y. Zhang, Y. Tang, Zeolite microspheres with hierarchical structures: formation, mechanism and catalytic performance, *J. Mater. Chem.* 21 (2011) 16223. <https://doi.org/10.1039/c1jm11669j>.
- [109] C. Moreau, R. Durand, S. Razigade, J. Duhamet, P. Faugeras, P. Rivalier, P. Ros, G. Avignon, Dehydration of fructose to 5-hydroxymethylfurfural over H-mordenites, *Appl. Catal. A Gen.* 145 (1996) 211–224.
- [110] J.S. Kruger, V. Choudhary, V. Nikolakis, D.G. Vlachos, Elucidating the Roles of Zeolite H-BEA in Aqueous-Phase Fructose Dehydration and HMF Rehydration, *ACS Catal.* 3 (2013) 1279–1291.
- [111] R. Oozeerally, D.L. Burnett, T.W. Chamberlain, R.J. Kashtiban, S. Huband, R.I. Walton, V. Degirmenci, Systematic Modification of UiO-66 Metal-Organic Frameworks for Glucose Conversion into 5-Hydroxymethyl Furfural in Water, *ChemCatChem.* 13 (2021) 2517–2529. <https://doi.org/10.1002/cctc.202001989>.
- [112] Z. Hu, Y. Peng, Y. Gao, Y. Qian, S. Ying, D. Yuan, S. Horike, N. Ogiwara, R. Babarao, Y. Wang, N. Yan, D. Zhao, Direct Synthesis of Hierarchically Porous Metal – Organic Frameworks with High Stability and Strong Brønsted Acidity: The Decisive Role of Hafnium in Efficient and Selective Fructose Dehydration, *Chem. Mater.* 28 (2016) 2659–2667. <https://doi.org/10.1021/acs.chemmater.6b00139>.
- [113] Y. Zhong, Q. Yao, P. Zhang, H. Li, Q. Deng, J. Wang, Z. Zeng, S. Deng, Preparation of Hydrophobic Acidic Metal–Organic Frameworks and Their Application for 5-Hydroxymethylfurfural Synthesis, *Ind. Eng. Chem. Res.* 59 (2020) 22068–22078. <https://doi.org/10.1021/acs.iecr.0c04798>.
- [114] C. Moreau, R. Durand, A. Roux, D. Tichit, Isomerization of glucose into fructose in the presence of cation-exchanged zeolites and hydrotalcites, *Appl. Catal. A Gen.* 193 (2000) 257–264.
- [115] S. Lima, A.S. Dias, Z. Lin, P. Brandao, P. Ferreira, M. Pillinger, J. Rocha, V. Calvino-Casilda, A. A. Valente, Isomerization of D -glucose to D -fructose over metallosilicate solid bases, *Anabela.* 339 (2008) 21–27. <https://doi.org/10.1016/j.apcata.2007.12.030>.
- [116] I. Graça, M.C. Bacariza, D. Chadwick, Glucose isomerisation into fructose over Mg-impregnated Na-zeolites: Influence of zeolite structure, *Microporous Mesoporous Mater.* 255 (2018) 130–139. <https://doi.org/10.1016/j.micromeso.2017.07.015>.

- [117] I. Graça, D. Iruretagoyena, D. Chadwick, Glucose isomerisation into fructose over magnesium-impregnated NaY zeolite catalysts, *Appl. Catal. B Environ.* 206 (2017) 434–443. <https://doi.org/10.1016/j.apcatb.2017.01.037>.
- [118] I. Graça, M.C. Bacariza, A. Fernandes, D. Chadwick, Desilicated NaY zeolites impregnated with magnesium as catalysts for glucose isomerisation into fructose, *Appl. Catal. B Environ.* 224 (2018) 660–670. <https://doi.org/10.1016/j.apcatb.2017.11.009>.
- [119] M.M. Antunes, D. Falcão, A. Fernandes, F. Ribeiro, M. Pillinger, J. Rocha, A.A. Valente, Catalytic isomerization of d-glucose to d-fructose over BEA base zeotypes using different energy supply methods, *Catal. Today.* 362 (2021) 162–174. <https://doi.org/10.1016/j.cattod.2020.03.024>.
- [120] M. Moliner, Y. Román-leshkov, M.E. Davis, Tin-containing zeolites are highly active catalysts for the isomerization of glucose in water, *PNAS.* 107 (2010) 6164–6168. <https://doi.org/10.1073/pnas.1002358107>.
- [121] R. Bermejo-deval, R.S. Assary, E. Nikolla, M. Moliner, Y. Román-leshkov, S.-J. Hwang, A. Palsdottir, D. Silverman, R.F. Lobo, L.A. Curtiss, M.E. Davis, Metalloenzyme-like catalyzed isomerizations of sugars by Lewis acid zeolites, *PNAS.* 109 (2012) 9727–9732. <https://doi.org/10.1073/pnas.1206708109>.
- [122] R. Bermejo-deval, R. Gounder, M.E. Davis, Framework and Extraframework Tin Sites in Zeolite Beta React Glucose Differently, *ACS Catal.* 2 (2012) 2705–2713.
- [123] R. Bermejo-deval, M. Orazov, R. Gounder, S. Hwang, M.E. Davis, Active Sites in Sn-Beta for Glucose Isomerization to Fructose and Epimerization to Mannose, *ACS Catal.* 4 (2014) 2288–2297.
- [124] G. Akiyama, R. Matsuda, H. Sato, S. Kitagawa, Catalytic glucose isomerization by porous coordination polymers with open metal sites, *Chem. Asian J.* 9 (2014) 2772–7. <https://doi.org/10.1002/asia.201402119>.
- [125] C.D. Malonzo, S.M. Shaker, L. Ren, S.D. Prinslow, A.E. Platero-Prats, L.C. Gallington, J. Borycz, A.B. Thompson, T.C. Wang, O.K. Farha, J.T. Hupp, C.C. Lu, K.W. Chapman, C. Myers, R.L. Penn, L. Gagliardi, M. Tsapatsis, A. Stein, Thermal Stabilization of Metal-Organic Framework-Derived Single-Site Catalytic Clusters through Nanocasting, *J. Am. Chem. Soc.* 138 (2016) 2739–2748. <https://doi.org/10.1021/jacs.5b12688>.
- [126] M. Dorneles de Mello, M. Tsapatsis, Selective glucose to fructose isomerization over modified zirconium UiO-66 in alcohol media, *ChemCatChem.* 10 (2018) 2417–2423. <https://doi.org/10.1002/cctc.201800371>.
- [127] Q. Guo, L. Ren, P. Kumar, V.J. Cybulskis, K.A. Mkhoyan, M.E. Davis, M. Tsapatsis, A Chromium Hydroxide/MIL-101(Cr) MOF Composite Catalyst and Its Use for the Selective Isomerization of Glucose to Fructose, *Angew. Chem. Int. Ed.* 57 (2018) 4926–4930. <https://doi.org/10.1002/ange.201712818>.
- [128] Q.-X. Luo, Y. Zhang, L. Qi, L. Susannah, Glucose Isomerization and Epimerization over Metal-Organic Frameworks with Single-Site Active Centers, *ChemCatChem.* 11 (2019) 1903–1909. <https://doi.org/10.1002/cctc.201801889>.

- [129] M. Lara-Serrano, S. Morales-delarosa, J.M. Campos-martin, V.K. Abdelkader-Fernández, L. Cunha-Silva, S.S. Balula, Isomerization of glucose to fructose catalyzed by metal–organic frameworks, *Sustain. Energy Fuels*. 5 (2021) 3847–3857. <https://doi.org/10.1039/d1se00771h>.
- [130] A.R. Oozeerally, D.L. Burnett, T.W. Chamberlain, R.I. Walton, V. Degirmenci, Exceptionally Efficient and Recyclable Heterogeneous Metal–Organic Framework Catalyst for Glucose Isomerization in Water, *ChemCatChem*. 10 (2018) 706–709. <https://doi.org/10.1002/cctc.201701825>.
- [131] M. Rubio-martinez, C. Avci-Camur, A.W. Thornton, I. Imaz, D. Maspoch, M.R. Hill, M. Rubio-martinez, New synthetic routes towards MOF production at scale, *Chem. Soc. Rev.* 46 (2017) 3453–3480. <https://doi.org/10.1039/C7CS00109F>.
- [132] C. Perego, P. Villa, Catalyst preparation methods, *Catal. Today*. 34 (1997) 281–305. [https://doi.org/10.1016/S0920-5861\(96\)00055-7](https://doi.org/10.1016/S0920-5861(96)00055-7).
- [133] D. Bazer-bachi, L. Assié, V. Lecocq, B. Harbuzaru, V. Falk, Towards industrial use of metal-organic framework : Impact of shaping on the MOF properties, *Powder Technol.* 255 (2014) 52–59. <https://doi.org/10.1016/j.powtec.2013.09.013>.
- [134] O. Ardelean, G. Blanita, G. Borodi, M.D. Lazar, I. Misan, I. Coldea, D. Lupu, Volumetric hydrogen adsorption capacity of densified MIL-101 monoliths, *Int. J. Hydrogen Energy*. 38 (2013) 7046–7055. <https://doi.org/10.1016/j.ijhydene.2013.03.161>.
- [135] G. Majano, J. Pérez-ramírez, Scalable Room-Temperature Conversion of Copper (II) Hydroxide into HKUST-1 ($\text{Cu}_3(\text{btc})_2$), *Adv. Mater.* 25 (2013) 1052–1057. <https://doi.org/10.1002/adma.201203664>.
- [136] W.Y. Hong, S.P. Perera, A.D. Burrows, Manufacturing of metal-organic framework monoliths and their application in CO₂ adsorption, *Microporous Mesoporous Mater.* 214 (2015) 149–155. <https://doi.org/10.1016/j.micromeso.2015.05.014>.
- [137] A.H. Valekar, K. Cho, U. Lee, S. Lee, W. Yoon, Y.K. Hwang, G. Lee, J. Cho, J. Chang, RSC Advances granules using mesoporous r-alumina as a binder, *RSC Adv.* 7 (2017) 55767–55777. <https://doi.org/10.1039/C7RA11764G>.
- [138] N. Chanut, A.D. Wiersum, U. Lee, K. Hwang, F. Ragon, H. Chevreau, S. Bourrelly, B. Kuchta, J. Chang, C. Serre, P.L. Llewellyn, Observing the Effects of Shaping on Gas Adsorption in Metal- Organic Frameworks, *Eur. J. Inorg. Chem.* 2016 (2016) 4416–4423. <https://doi.org/10.1002/ejic.201600410>.
- [139] A. Carne-Sanchez, I. Imaz, M. Cano-Sarabia, D. Maspoch, A spray-drying strategy for synthesis of nanoscale metal–organic frameworks and their assembly into hollow superstructures, *Nat. Chem.* 5 (2013) 203–211. <https://doi.org/10.1038/nchem.1569>.
- [140] A. Carné-Sánchez, K.C. Stylianou, C. Carbonell, M. Naderi, I. Imaz, D. Maspoch, Protecting Metal – Organic Framework Crystals from Hydrolytic Degradation by Spray-Dry Encapsulating Them into Polystyrene Microspheres, *Adv. Mater.* 27 (2015) 869–873. <https://doi.org/10.1002/adma.201403827>.
- [141] J. Lefevre, B. Claessens, S. Mullens, G. Baron, J. Cousin-saint-remi, J.F.M. Denayer, 3D-

Chapter I – References

- Printed Zeolitic Imidazolate Framework Structures for Adsorptive Separations, *ACS Appl. Nano Mater.* 2 (2019) 4991–4999. <https://doi.org/10.1021/acsanm.9b00934>.
- [142] J. Dhainaut, M. Bonneau, R. Ueoka, K. Kanamori, S. Furukawa, Formulation of Metal-Organic Framework Inks for the 3D Printing of Robust Microporous Solids Towards High-Pressure Gas Storage and Separation, *ACS Appl. Mater. Interfaces.* 12 (2020) 10983–10992. <https://doi.org/10.1021/acсами.9b22257>.
- [143] B. Yeskendir, J. Dacquin, Y. Lorgouilloux, C. Courtois, S. Royer, J. Dhainaut, From metal-organic framework powders to shaped solids: recent developments and challenges, *Mater. Adv.* 2 (2021) 7139–7186. <https://doi.org/10.1039/d1ma00630d>.

Chapter II

Experimental Part

Chapter II

This chapter includes a detailed description of the materials and methods applied to accomplish synthesis, characterization and catalytic performance of zeolitic materials and MOFs. It is therefore divided into three parts with the first containing full information on the synthesis methodologies. The second part comprises specification of the applied characterization techniques with the information derived thereof. And finally, the last part concerns the catalytic performance of the synthesized solids with illustrations of the employed equipment.

1. Materials and Synthesis

Zirconium chloride (99.5 %, Alfa Aesar), zirconium sulfate tetrahydrate (98 %, Alfa Aesar), terephthalic acid (99 %, Acros Organics), monosodium 2-sulfoterephthalate (98 %, TCI Chemicals), 2-aminoterephthalic acid (99 %, Thermo Scientific), 1,2,4-benzenetricarboxylic acid (>99 % Sigma-Aldrich), 2-hydroxyterephthalic acid (97 % Sigma-Aldrich) D-fructose (99 %, Acros Organics), N,N-dimethylformamide (pure, Carlo Erba Reagents), dimethyl sulfoxide (99.7 %, Fisher BioReagents), acetic acid (100 %, VWR), ethanol (96 %, VWR), 5-(hydroxymethyl)furfural (98 %, Acros Organics), Ludox HS-40 colloidal silica (Sigma-Aldrich); zirconium sulfate tetrahydrate (98 %, Alfa Aesar); Tetrapropylammonium hydroxide, TPAOH 25% aqueous solution (Sigma-Aldrich); tetraethyl orthosilicate, TEOS (98%, Sigma-Aldrich) were used as-received in this work

1.1. Synthesis of UiO-66-based MOFs

1.1.1. UiO-66

UiO-66 was synthesized following a method issued from the literature [1,2]. Accordingly, 0.32 g $ZrCl_4$ and 0.22 g terephthalic acid, TA (molar ratio of 1:1) were dissolved in 100 mL DMF. Upon

dissolution, 3 mL acetic acid were added and thereafter the solution was placed in oven to crystallize at 120 °C for 24 h. The white precipitate was recovered by centrifugation at 10 000 rpm for 15 min and washed thoroughly in fresh DMF at 50 °C to dissolve unreacted species. This was followed by 3 consecutive washing and centrifugation steps in ethanol at 50 °C, with the last washing step lasting overnight. Eventually, the product was recovered and dried overnight at 100 °C.

1.1.2. UiO-66-SO₃H Traditional Approach

The preparation of UiO-66-SO₃H-D following the so-called traditional “DMF” approach was done by dissolving 0.31 g ZrCl₄ and 0.35 g monosodium 2-sulfoterephthalate (molar ratio of 1:1) in 100 mL DMF as described in the literature [3]. Upon addition of 3 mL acetic acid, the resulting solution was left to crystallize at 120 °C for 24 h. In the same manner, UiO-66-SO₃H-D containing 25 %, 50 % and 75 % of monosodium 2-sulfoterephthalate linker were prepared, with the rest of the composition corresponding to terephthalic acid linker. The recovering and washing steps were identical as in the case of the classical UiO-66 described above.

1.1.3. UiO-66-SO₃H Green Approach

For UiO-66-SO₃H-W prepared in a green way, a modified synthesis protocol was applied [4]. Namely, 1 g Zr(SO₄)₂·4H₂O and 1.44 g monosodium 2-sulfoterephthalate (molar ratio of 1:2) were dissolved in 100 mL water. The resulting solution was heated up to 100 °C in a round-bottom flask supplied with a condenser to crystallize for various durations (from 2 h to 24 h) in oil bath. The resulting white solid was recovered by centrifugation and washed 3 times with fresh H₂O at 50 °C until neutral pH as well as with ethanol at 50 °C overnight. Upon washing, the product was dried at 100 °C overnight.

1.1.4. UiO-66-OH

For a typical preparation of UiO-66-OH, 1 g $\text{Zr}(\text{SO}_4)_2 \cdot 4\text{H}_2\text{O}$ and 1 g 2-hydroxyterephthalic acid (molar ratio of 1:2) were dissolved in 100 mL water. Upon addition of 3 mL acetic acid, the resulting pale brown turbid suspension was heated up to 100 °C in a round-bottom flask supplied with a condenser to crystallize for 24 h in oil bath. The resulting white solid was recovered by centrifugation and washed 3 times with fresh H_2O at 50 °C until neutral pH as well as with ethanol at 50 °C overnight. Upon washing, the product was dried at 100 °C overnight.

1.1.5. UiO-66-COOH

UiO-66-COOH was prepared following the procedure described by [5] with slight modifications. Thus, 1 g $\text{Zr}(\text{SO}_4)_2 \cdot 4\text{H}_2\text{O}$ and 1.2 g 1,2,4-benzenetricarboxylic acid (molar ratio of 1:2) were dissolved in 100 mL water. Thus-formed white suspension was heated up to 100 °C in a round-bottom flask supplied with a condenser to crystallize for 3 h in oil bath. After that, the resulting white solid was recovered by centrifugation and washed 3 times with fresh H_2O at 50 °C until neutral pH as well as with ethanol at 50 °C overnight. Upon washing, the product was dried at 100 °C overnight.

1.1.6. UiO-66-NH₂

For a typical preparation of UiO-66-NH₂, 1 g $\text{Zr}(\text{SO}_4)_2 \cdot 4\text{H}_2\text{O}$ and 1 g 2-aminoterephthalic acid (molar ratio of 1:2) were dissolved in 100 mL water. Upon addition of 3 mL acetic acid, the resulting yellow turbid suspension was heated up to 100 °C in a round-bottom flask supplied with a condenser to crystallize for 24 h in oil bath. The resulting white solid was recovered by centrifugation and washed 3 times with fresh H_2O at 50 °C until neutral pH as well as with ethanol at 50 °C overnight. Upon washing, the product was dried at 100 °C overnight.

The recapitulation of the synthesized MOFs is given in Table II.1 with the linkers depicted in figure II-1.

Table II.1 – UiO-66 and UiO-66-based MOFs prepared in this work.

MOF	Zr-source	Ligand	Modulator	Solvent
UiO-66	ZrCl ₄	BDC (TA)	AA	DMF
UiO-66-SO ₃ H-D-25	ZrCl ₄	TA-SO ₃ Na (25%) + TA (75%)	AA	DMF
UiO-66-SO ₃ H-D-50	ZrCl ₄	TA-SO ₃ Na (50%) + TA (50%)	AA	DMF
UiO-66-SO ₃ H-D-75	ZrCl ₄	TA-SO ₃ Na (75 %) + TA (25 %)	AA	DMF
UiO-66-SO ₃ H-D-100	ZrCl ₄	TA-SO ₃ Na	AA	DMF
UiO-66-SO ₃ H-W	Zr(SO ₄) ₂ .4H ₂ O	TA-SO ₃ Na	None	H ₂ O
UiO-66-OH	Zr(SO ₄) ₂ .4H ₂ O	TA-OH	AA	H ₂ O
UiO-66-COOH	Zr(SO ₄) ₂ .4H ₂ O	1,2,4-BTC	None	H ₂ O
UiO-66-NH ₂	Zr(SO ₄) ₂ .4H ₂ O	TA-NH ₂	AA	H ₂ O

Linker abbreviations: BDC (TA) – 1,4-benzenedicarboxylic acid, TA-SO₃Na – monosodium 2-sulfoterephthalate, TA-OH – 2-hydroxyterephthalic acid, 1,2,4-BTC – 1,2,4-benzenetricarboxylic acid, TA-NH₂ – 2-aminoterephthalic acid;

Modulator: AA – acetic acid;

Solvent: DMF – N,N-dimethylformamide.

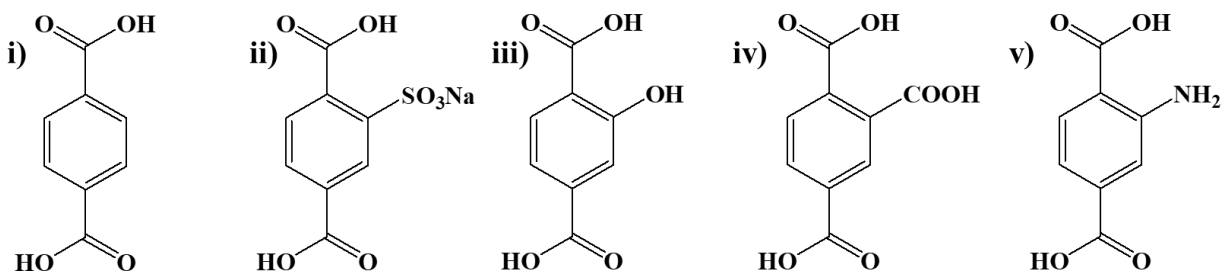


Figure II-1. Linkers used to prepare UiO-66 MOF and its derivatives: i) BDC (or TA) – 1,4-benzenedicarboxylic acid, ii) TA-SO₃Na – monosodium 2-sulfoterephthalate, iii) TA-OH – 2-hydroxyterephthalic acid, iv) 1,2,4-BTC – 1,2,4-benzenetricarboxylic acid, v) TA-NH₂ – 2-aminoterephthalic acid.

1.2. MFI Zeolitic Materials

For simplicity, in this chapter and further on, the elements comprising an MFI-type material will be given in square brackets prior to the framework name. A short summary of the synthesized zeolitic materials is given in Table II.2.

Table II.2 – MFI-type materials prepared in this work.

Zeolite	Si-precursor	Al-precursor	Zr-precursor	Si/Al ratio	Si/Zr ratio
[Si]-MFI	TEOS	-	-	-	-
[Si,Al]-MFI	TEOS	NaAlO ₂	-	30	-
[Si,Zr]-MFI-in	TEOS	-	Zr-propoxide	-	30
[Si,Zr]-MFI-ex	Ludox	-	Zr(SO ₄) ₂ ·4H ₂ O	-	30

TEOS – Tetraethyl orthosilicate; Ludox HS-40: colloidal silica, 40 wt.% SiO₂ in water.

1.2.1. [Si]-MFI

For a typical synthesis of the reference [Si]-MFI, a starting gel with a molar composition of 30 SiO₂ : 850 H₂O : 12 TPAOH was prepared by mixing TEOS with TPAOH (Tetrapropylammonium hydroxide, 25 wt.%) aqueous solution. Then, the mixture was transferred into a 250 mL PTFE (polytetrafluoroethylene)-lined autoclave for crystallization under autogenous pressure and static conditions at 180 °C for 72 h. Upon this treatment, a white solid product was recovered by filtration, washed with a decent amount of distilled water to lower pH until ~7, dried at 120 °C overnight and calcined in air at 550 °C for 8 h at 0.5 °C·min⁻¹.

1.2.2. [Si,Al]-MFI

For a typical synthesis of the reference [Si,Al]-MFI, a starting gel with a molar composition of 30 SiO₂ : 0.5 Al₂O₃ : 850 H₂O : 12 TPAOH was prepared by mixing TEOS with TPAOH aqueous

solution with pre-dissolved NaAlO_2 . Then, the mixture was transferred into a 250 mL PTFE-lined autoclave for crystallization under autogenous pressure and static conditions at $180\text{ }^\circ\text{C}$ for 72 h. Upon this treatment, a white solid product was recovered by filtration, washed with a decent amount of distilled water to lower pH until ~ 7 , dried at $120\text{ }^\circ\text{C}$ overnight and calcined in air at $550\text{ }^\circ\text{C}$ for 8 h at $0.5\text{ }^\circ\text{C}\cdot\text{min}^{-1}$.

Ion-exchange to replace Na^+ by H^+ was performed on the calcined [Si,Al]-MFI. Typically, 1 g of the powder was immersed into a 100 mL of 1M NH_4NO_3 aqueous solution. This was followed by stirring the suspension for 24 h at $40\text{ }^\circ\text{C}$. After that, the solid was separated by centrifugation and immersed into a fresh 1M NH_4NO_3 aqueous solution and stirred for another 24 h at $40\text{ }^\circ\text{C}$. Upon 3 consecutive ion-exchange steps, the solid was recovered, dried at $120\text{ }^\circ\text{C}$ for 24 h and calcined in air at $550\text{ }^\circ\text{C}$ for 4 h ($0.5\text{ }^\circ\text{C}\cdot\text{min}^{-1}$) to convert the NH_4^+ into H^+ -form.

1.2.3. [Si,Zr]-MFI-in

Synthesis of Zr-substituted MFI zeolites was adapted from [6]. For a typical synthesis, a starting gel with a molar composition of $30\text{ SiO}_2 : 1\text{ ZrO}_2 : 850\text{ H}_2\text{O} : 12\text{ TPAOH}$ was prepared by mixing Zr-propoxide and TEOS with TPAOH aqueous solution. Then, the mixture was transferred into a 250 mL PTFE-lined autoclave for crystallization under autogenous pressure and static conditions at $180\text{ }^\circ\text{C}$ for 72 h. Upon this treatment, a white solid product was recovered by filtration, washed with a decent amount of distilled water to lower pH until ~ 7 , dried at $120\text{ }^\circ\text{C}$ overnight and calcined in air at $550\text{ }^\circ\text{C}$ for 8 h at $0.5\text{ }^\circ\text{C}\cdot\text{min}^{-1}$.

1.2.4. [Si,Zr]-MFI-ex

An alternative method to prepare the Zr-substituted MFI zeolite was employed. A starting gel with a molar composition of $30\text{ SiO}_2 : 1\text{ ZrO}_2 : 900\text{ H}_2\text{O} : 15\text{ TPAOH} : 40\text{ NaOH}$ was prepared by adding Ludox HS-40 to an aqueous solution containing NaOH and TPAOH. This was followed by

addition of a pre-dissolved Zr-sulfate solution. Then, the mixture was transferred into a 250 mL PTFE-lined autoclave for crystallization under autogenous pressure and static conditions at 180 °C for 72 h. Upon this treatment, a white solid product was recovered by filtration, washed with a decent amount of distilled water to lower pH until ~7, dried at 120 °C overnight and calcined in air at 550 °C for 8 h at 0.5 °C·min⁻¹.

1.3. Upscaling

Upscaling or large-scale synthesis was performed in a Reactor-Ready double-wall reactor of 3 L capacity from Radley equipped with a PTFE stirrer and a thermocouple as well as a condenser and a silicon oil circulating system (figure II-2.). This setup was used to scale-up the preparation of UiO-66-SO₃H-W owing to its superior catalytic activity in fructose dehydration as compared to other MOFs from Table II.1. Typically, 30 g Zr(SO₄)₂·4H₂O and 45 g monosodium 2-sulfoterephthalate (molar ratio of 1:2) were dissolved in 1200 mL water and poured into the double-wall reactor. The synthesis temperature was set to 100 °C and stirring speed to 300 rpm. After 24 h under these conditions, the white solid product was recovered, washed thoroughly with fresh water to lower pH until ~7 and solvent-exchanged with ethanol at 50 °C overnight. Thereafter, the solid was separated by centrifugation and dried at 100 °C for 15 h.

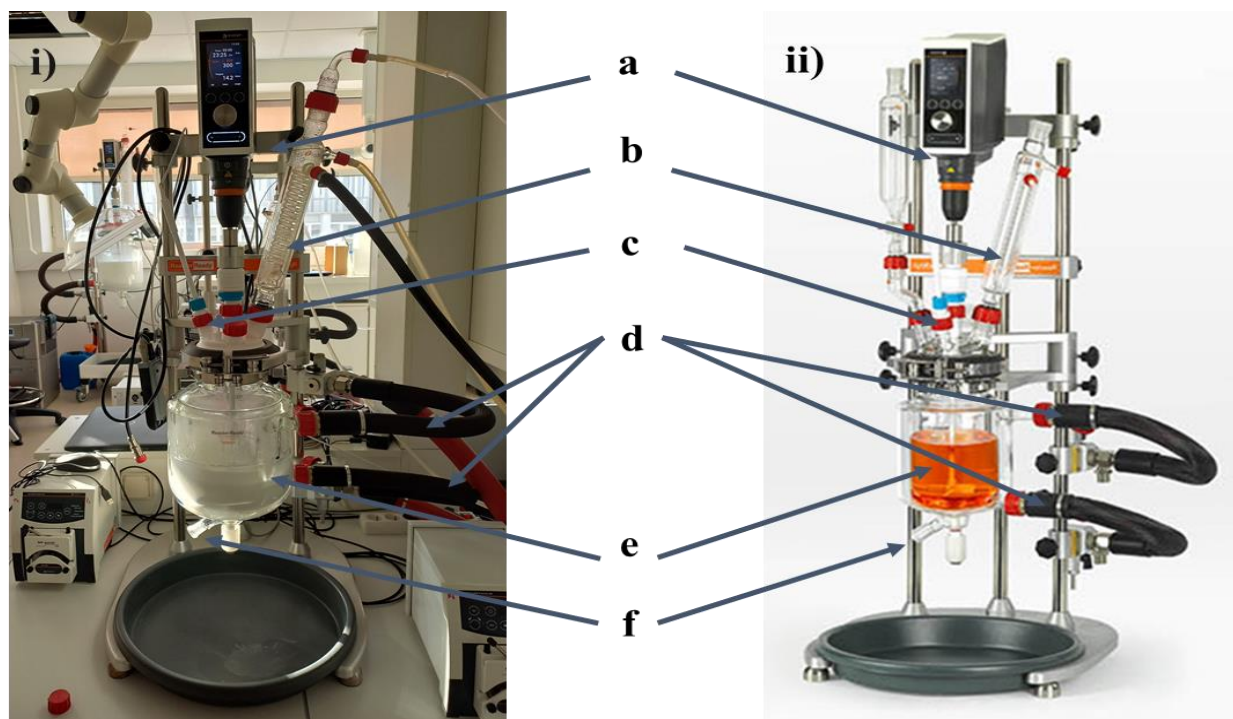


Figure II-2. Images of the 3 L double-wall reactor used for upscaling (i) and the one from the provider's official website (ii, <https://www.radleys.com/range/reactor-ready-lab-reactor/>) demonstrating the stirring controller (a), condenser (b), thermocouple (c), silicon oil circulating system (d), double-wall reactor with a stirrer inside (e), reactor exit for product recovery (f).

1.4. Shaping

1.4.1. Extrusion

Extrusion was carried out with the scaled-up amounts of UiO-66-SO₃H-W MOF using a Caleva Multi Lab equipment. Typically, prior to extrusion, a MOF-based paste was prepared as follows: 150 mL of deionized water was heated up to 80 °C in oil bath under stirring. Then, ~6 g of HEC (2-hydroxyethylcellulose used as a binder) were slowly added to the heated water. The stirring was stopped at some point due to the increase of viscosity. Thus-formed HEC gel was left to cool down and placed in a fridge at 4 °C overnight prior using. Then, 8 g of UiO-66-SO₃H-W were mixed with about 8 g of HEC gel for the final binder content of 4 wt.% (or with about 4 g of HEC gel for the binder content of 2 wt.%) at 150 rpm for 1 h. The paste was further recovered and pushed by

Chapter II – Characterization

a single screw through a 3 mm die at the rotation speed of 90 rpm. Thereafter, the extrudates were cut into 1 cm length cylinders and subsequently dried overnight at 120 °C.

1.4.2. Pelletization

Densification of UiO-66-SO₃H-W powder into pellets was performed on a Eurolabo hydraulic press (figure II-3). A force of ~2 tons was applied for ~10-15 seconds.

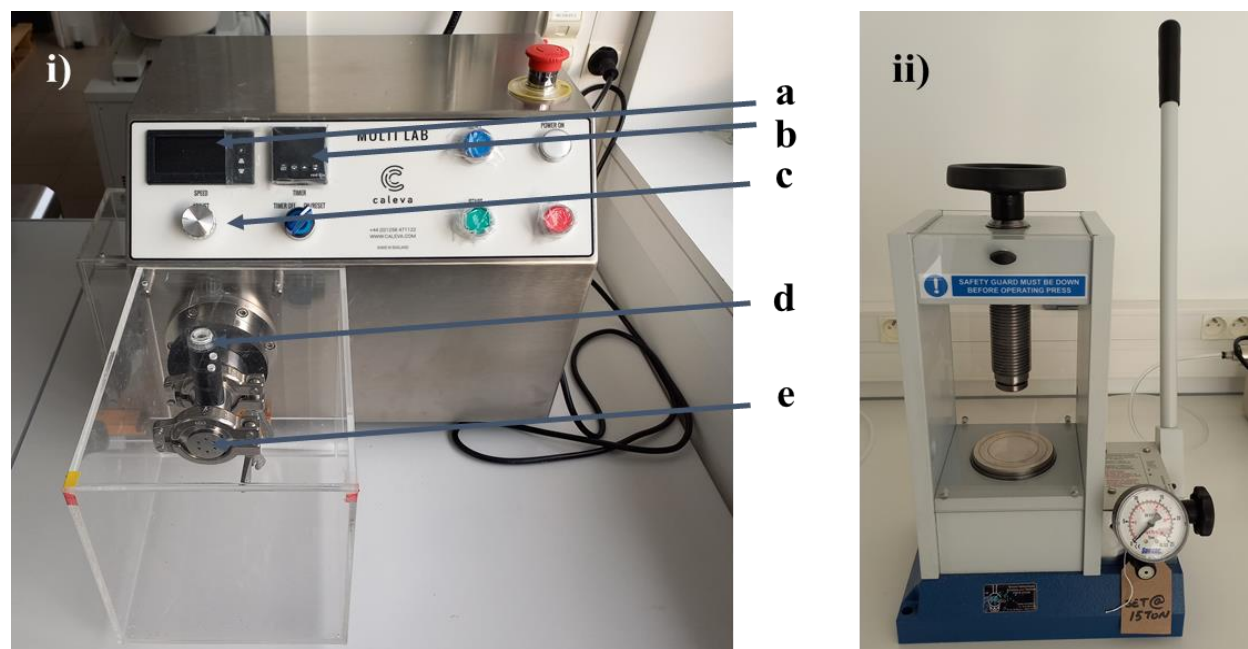


Figure II-3. The extruder (i) with speed (a) and time (b) indicator panels, speed controller (c), paste feed-port (d) and die (e) as well as the hydraulic press (ii) used for shaping in this work.

2. Characterization

2.1. Structural Properties

2.1.1. Powder X-Ray Diffraction (PXRD)

PXRD is a technique that allows to examine the crystal structure of powdery materials. It allows the identification of crystalline phases *via* determination of lattice structural parameters, as well as an estimation of crystallite size. Typically, X-Rays have short wavelengths in the range of

Ångstroms *i.e.* are highly energetic and therefore have high penetration depth into a matter's bulk. They are generated within the X-Ray source (also called X-Ray tube) due to the bombardment of a target (anode, usually Cu) by high-energy electrons. Apart from a continuous background spectrum called Bremsstrahlung, this process allows for generation of the characteristic X-Rays, Cu K α lines, having an energy (E) of ~8.04 keV and a wavelength (λ) of 1.54 Å. This radiation is used for typical X-Ray analysis and is generated due to filling a core hole in the K-shell, produced upon electron bombardment, by an electron from the L-shell.

It is essential to note that X-Ray diffraction is based on the elastic scattering of X-Rays by atoms that compose a matter's periodic lattice structure (figure II-4, i). Thus, constructive interference takes place once the scattered X-Ray photons become “in phase” which further enables their detection (figure II-4, ii). Therefore, diffraction of X-Rays by crystal planes allows to determine interplanar lattice distance (d) by applying the Bragg's law: $n\lambda = 2d\sin\theta$; where n is an integer describing the “order” of reflection; λ is the X-Ray wavelength, d is the interplanar lattice distance and θ is the angle of incidence.

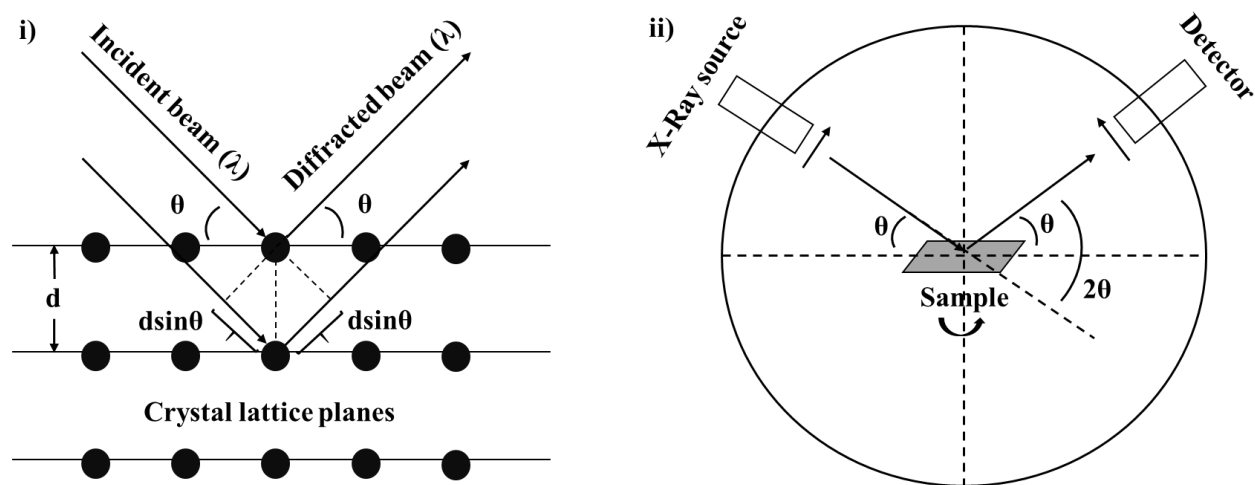


Figure II-4. Schematic representation of X-Ray photons diffracted from a crystalline matter (i) as well as a representation of a typical XRD measurement on the widely used Bragg-Brentano geometry equipment with a rotating sample holder (ii).

Chapter II – Characterization

Upon measuring 2θ which is the angle between the incident and the diffracted beam, one can derive the corresponding interplanar distances d which are characteristic of a certain given compound. In this work, powder XRD patterns were recorded on a D8 Advance instrument from Bruker, equipped with a $\text{CuK}\alpha$ X-ray source ($\lambda = 1.54184 \text{ \AA}$) and a LynxEye XE-T detector, using the following acquisition parameters: 2θ range between $5\text{--}80^\circ$, scan rate of 0.02° per step and acquisition time of 1 s per step.

2.1.2. ATR-IR (Attenuated Total Reflectance-Infrared Spectroscopy)

Infrared spectroscopy is a universal and the most prevailing type of vibrational spectroscopy. Vibrations in molecules or solids are generally excited by absorption of infrared radiation and allow to describe structural properties of a specimen *via* its characteristic vibrations. Currently, there are a few methodologies to perform an infrared spectroscopy in general use operating in different modes such as Attenuated Total Reflectance (ATR), transmission and Diffuse Reflectance (DRIFTS), figure II-5.

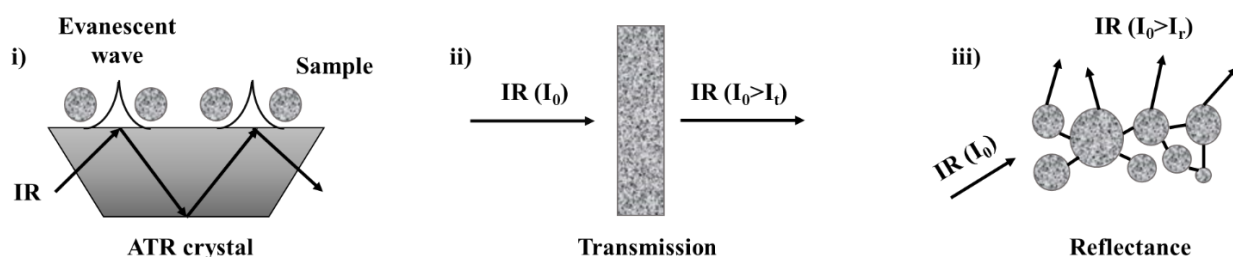


Figure II-5. The most common modes of IR spectroscopy: ATR (i), transmission (ii) and reflectance (iii).

The choice of the operating mode strongly depends on the nature of the material under study and defines the sample preparation. Among the mentioned types of infrared spectroscopy, ATR has become one of the most used techniques nowadays. Specifically, it implies the interaction of the studied material with the so-called evanescent wave. The latter is the result of reflection of IR light

Chapter II – Characterization

within a crystal (usually diamond or germanium) having a high refractive index and high robustness. This evanescent wave protrudes outside the crystal and usually has a penetrating depth of $\sim 2 \mu\text{m}$ which enables interaction with the sample and therefore excites its characteristic vibrational modes. Particularly in this work, IR spectra were recorded in ATR mode using a Nicolet iS50 FT-IR spectrometer from Thermo-Fisher equipped with a diamond crystal, an iS50 ATR sampling station and a DTGS detector. Typically, a small amount of a powdery sample was deposited on the sampling station and 50 scans over a scanning range from 4000 cm^{-1} to 400 cm^{-1} with a resolution of 2 cm^{-1} were recorded.

2.1.3. Raman Spectroscopy

Similar to IR, Raman spectroscopy allows to probe structural properties of materials *via* examining their characteristic vibrations. While the former is based on the absorption of photons to excite characteristic vibrations requiring specific energies, Raman spectroscopy is based on inelastic scattering of photons which occurs with a certain change of their primary energy. During this inelastic scattering process, a monochromatic light (usually sourced from a laser) interacts with a sample in several different ways (figure II-6, i).

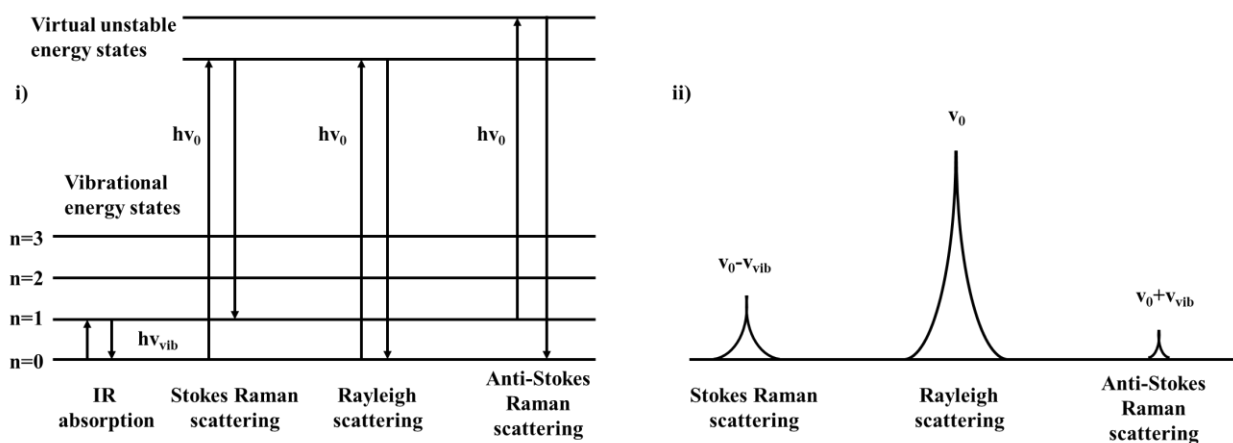


Figure II-6. Schematic representation of the processes behind a typical IR and Raman measurements (i) and the bands resulted upon an inelastic scattering of photons from a sample (ii).

Chapter II – Characterization

As evident from figure II-6 (ii), the majority of the photons are scattered elastically (Rayleigh scattering) *i.e.* with no loss of their initial energy as if they excite molecules in the sample to an unstable state with a subsequent decay back to the ground vibrational state ($n=0$). However, once the decay takes place to the first vibrational level ($n=1$) at the frequency ν_{vib} , a part of the initial energy ($h\nu_0 - h\nu_{\text{vib}}$) is lost upon scattering. Such decay provokes appearance of a Raman active band which is called the “Stokes band” in the spectrum, at the frequency corresponding to $\nu_0 - \nu_{\text{vib}}$. At the same time, light scattering might cause a transition in the sample from the excited vibrational state ($n=1$) to an unstable energy state with a subsequent relaxation back to the ground vibrational state ($n=0$). This process gives rise to a total energy gain of $h\nu_0 + h\nu_{\text{vib}}$ of the scattered photons and therefore generates bands at a higher frequency ($\nu_0 + \nu_{\text{vib}}$). These bands are referred to as the “anti-Stokes bands” and usually have much lower intensity than the Stokes bands due to the lower population of excited vibrational states. In general, Raman spectroscopy employs a higher energy visible or near IR radiation as compared to the mid-IR radiation used in IR spectroscopy and therefore both techniques complement each other. In this work, typical Raman spectra were recorded on a XPlora Plus Horiba Scientific micro-spectrometer equipped with a 50X focal length objective. The acquisition of spectra was performed using a laser excitation wavelength of 532 nm or 785 nm and a filter (up to 50 %) to avoid possible sample degradation under the laser beam especially in the case of MOFs.

2.2. Textural Properties

2.2.1. N₂ Physisorption

Nitrogen physisorption is a typical analysis done to probe the textural properties of porous materials at N₂ liquefaction temperature, 77 K. The most useful characteristics quantified by N₂ physisorption include surface area (SA), total pore volume (V_t) and pore size distribution (PSD).

Chapter II – Characterization

The critical step prior to a measurement is the sample preparation, done by outgassing it under vacuum at elevated temperatures to liberate its surface from pre-adsorbed molecules. Once outgassed, the sample is exposed to N₂ gas which is adsorbed onto the sample's surface through van der Waals-type weak physical interactions. The quantity of adsorbed gas progressively increases with N₂ pressure therefore yielding a typical adsorption isotherm, while the reverse process results in a desorption isotherm. The resulting adsorption-desorption isotherm serves as a fingerprint of the porous nature of a material indicating its micro (<2 nm), meso (2-50 nm), macro (>50 nm) or non-porous features. The most used way to assess the surface area of a porous material is *via* the so-called “Brunauer-Emmett-Teller method” or simply “B.E.T. method”. It is based on the multi-layer model of adsorption and allows estimation of the surface area by considering the monolayer capacity or the gas quantity in the monolayer and the cross-sectional area of the gas molecule (~0.162 nm² for N₂). At the same time, the total pore volume is estimated using the gas quantity at relative pressure close to 1 *i.e.* ~0.99, where it is mostly converted to liquid. The pore size distribution in microporous materials is nowadays mostly estimated by using computational approaches such as the Density Functional theory (DFT). In this work, textural properties of the synthesized materials were measured by N₂ physisorption experiments performed at 77 K using a Micromeritics Tristar II instrument. Before analysis, a known mass (~50 mg) of solid was treated at 120 °C under vacuum for 15 h in the case of MOFs and at 250 °C for 4-6 h in the case of zeolites. The specific surface area (S_{BET}) was calculated using the B.E.T. method, on the linear part of the B.E.T. plot ($p/p_0 < 0.3$). The total pore volume was calculated using the adsorption branch of the isotherms at a p/p_0 value of 0.99.

2.3. Morphological Properties

The size and shape of solid particles are routinely examined *via* various types of electron microscopy techniques. Interaction of the matter with high-energy electrons having wavelengths in the range of interatomic distances or even smaller causes a variety of phenomena (figure II-7, i). Thus-produced electrons are used to further derive valuable information on the chemical composition or internal structure of a sample under study therefore greatly expanding the application of electron microscopy.

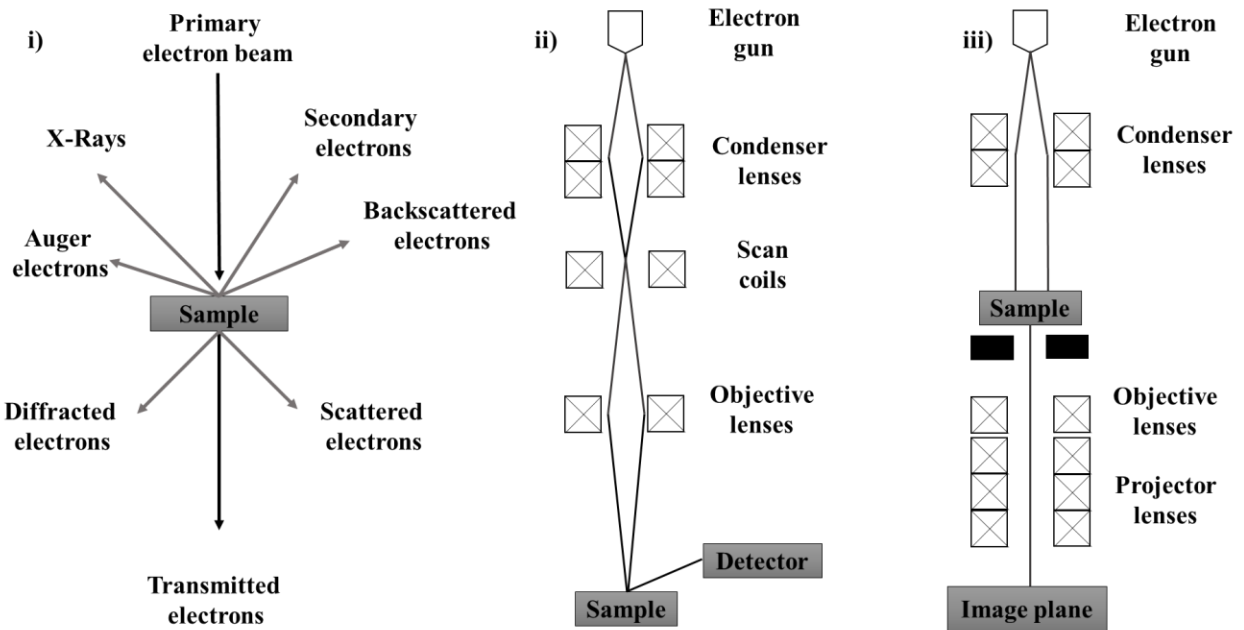


Figure II-7. Schematic representation of the detectable signals upon the interaction between the primary electron beam and the sample (i) as well as the simplified configurations of SEM (ii) and TEM (iii).

Chapter II – Characterization

As depicted in figure II-7 (i), the electron-sample interaction causes the formation of the following species:

- secondary electrons (SE) which are emitted by the sample due to inelastic scattering of the primary electron beam and originate from the surface region, thus providing information on its topology;
- backscattered electrons (BSE) which are the result of collisions of the primary electrons with the atoms in the sample. They originate from a deeper part than SE and are sensible to the atomic mass. Therefore, heavier atoms appear brighter in a resulting image due to a higher yield of BSE;
- X-rays which are generated in the same way as in XRD experiments *i.e.* due to ejection of an electron from an inner atomic shell, leaving the atom in an ionized state, followed by the filling of the vacancy by an electron from an outer shell. This process generates X-ray photons characteristic to a certain element, which are further used for its identification;
- Auger electrons are produced following the interaction of X-rays, generated as described above, with electrons from other shells. They are typically used in Auger Electron Spectroscopy (AES);
- diffracted electrons which can be used to further derive crystallographic information *i.e.* orientation of diffracting planes and interplanar distance (d);
- transmitted electrons which are a fraction of electrons passing through the sample without energy loss. Transmission strongly depends on the energy carried by the primary electrons as well as the thickness of the sample. Higher electron energies and thinner samples favor transmission.

Chapter II – Characterization

2.3.1. Scanning Electron Microscopy (SEM)

SEM (figure II-7, ii) typically uses low-energy electrons of up to 15-20 keV, which are focused on the sample by a series of lenses. This causes generation of secondary electrons, backscattered electrons, X-rays and a small portion of diffracted electrons which are used to derive information on surface topology, particle size and shape (SE), contrast topographic imaging (BSE), elemental analysis and mapping (X-Rays) and atomic planes orientation (diffraction) with a typical resolution of 5-10 nm. In this work, SEM micrographs were registered on a JEOL JSM 7800F microscope using an electron beam energy in the range of 5-10 keV. Before observation, the samples were covered with a thin layer of Cr (150 Å). When SEM was coupled with EDS (Energy Dispersive X-Ray Spectroscopy) for elemental analysis, the samples were covered with a thin carbon layer (~200 Å) and were observed under an applied electron beam energy of 15 keV.

2.3.2. High Resolution Transmission Electron Microscopy (HRTEM)

HRTEM usually employs higher-energy electrons of up to 300 keV which are directed onto the sample following a parallel beam (figure II-7, iii). Under these conditions transmission and diffraction dominate the electron-sample interaction which allow for images with high resolution of up to 0.3-0.5 nm as well as diffraction patterns and elemental analysis. Herein, HRTEM images were taken on a FEI TITAN Themis 300 microscope using an electron beam energy in the range of 80-200 keV. Prior to observation, powdered samples were deposited directly on a copper grid covered with a carbon film.

2.4. Surface Properties

2.4.1. X-Ray Photoelectron Spectroscopy (XPS)

XPS is a frequently used analytical technique which provides information on the chemical composition, oxidation state and therefore the chemical environment of the elements composing a

Chapter II – Characterization

material. XPS is based on the photoelectric effect during which an atom absorbs a photon energy ($h\nu$) which forces a valence electron with a binding energy (BE) to be ejected with a kinetic energy (KE). Typically, an XPS spectrum represents the intensity of thus-ejected photoelectrons plotted as a function of the binding energy. The latter can be calculated by a simplified equation: $BE = h\nu - KE$. In this work, XPS analysis was performed on a Kratos Axis Ultra DLD instrument equipped with a monochromatized AlK_{α} X-ray source at 1486.6 eV. The base pressure in the analysis chamber was lower than 5.10^{-9} Torr. General survey spectra were recorded at a 160 eV pass energy and Zr 3d, C 1s, O 1s, S 2p and Si 2p core level spectra were recorded at a 20 eV pass energy. The Kratos charge compensation system was used during all analysis and binding energy scales were adjusted according to the Zr 3d_{5/2} peak placed at 182.8 eV.

2.4.2. ToF-SIMS (Time-of-Flight – Secondary Ion Mass Spectrometry)

ToF-SIMS is another widely known surface technique with surface sensitivity surpassing that of XPS. The principle behind ToF-SIMS is based on the sputtering of atoms, ions or molecular fragments from the surface *via* a bombardment with a primary ion beam, usually Ar^{+} with 0.5-5 keV or Bi_3^{+} with ~25 keV. Secondary ions produced as a result of such sputtering are directed into the ToF mass spectrometer where they are analyzed and quantified. Thus, the obtained results represent a typical mass spectrum representing the intensity of ions plotted against their mass-to-charge (m/z) ratio. In this work, the samples were analyzed using a ToF.SIMS 5 spectrometer (ION TOF GmbH, Germany) equipped with a pulsed bismuth liquid metal ion gun and Bi_3^{+} as the primary ion source (25 keV, 1 pA current). The analyzed sample area was $500 \mu m \times 500 \mu m$ for spectral analyses while maintaining static conditions.

2.5. Elemental Analysis

2.5.1. Inductively Coupled Plasma – Optical Emission Spectroscopy (ICP-OES)

ICP-OES is a routine and yet powerful analytical technique used to qualitatively and quantitatively determine elements composing a sample under study. The principle behind this technique is based on excitation of electrons from the ground state to an excited state using a hot plasma as an energy source. As electrons return back to the ground state they emit light at a specific wavelength which is analyzed by means of optical emission spectroscopy. By measuring the intensity of each wavelength, it is possible to calculate the proportion of each element in a sample. Therefore, in this thesis, chemical composition of the synthesized materials was determined by means of ICP-OES. Analyses were performed on a Perkin Elmer Optima 2000 DV instrument to determine the chemical composition of the solids based on Zr, S and Na for MOFs and Si, Al and Zr for zeolites. Before analysis, a known amount of sample was dissolved in a diluted HF-HCl solution, and then heated under microwave until complete dissolution before exposition to the plasma.

2.5.2. Carbon, Hydrogen, Nitrogen and Sulfur (CHNS) Analysis

CHNS is a routine technique to qualitatively and quantitatively analyze the organic matter in a solid sample. The principle behind the analysis lies in combustion of the specimen followed by determination and quantification of the combustion products. In this thesis, the CHNS compounds were determined using the thermo scientific FlashSmart automated elemental analyzer. The samples (~10 mg) were weighed in tin (Sn) containers and introduced into the combustion reactor maintained at 950 °C and promoting dynamic flash combustion of the sample. The products are then directed into the column reactor filled with copper oxide for their oxidation and pass through the nickel reducer. The N, C, H and S were therefore detected as N₂, CO₂, H₂O and SO₂, respectively. The resulted gases were separated in a packed column heated at 65°C and detected

by a thermal conductivity detector. The analysis duration was 10 min with 3 repetitions performed for each sample.

2.6. Chemical Properties

2.6.1. Temperature-Programmed Desorption (TPD)

TPD is an analytical technique that allows examining the strength of interaction of the adsorption gases with the material's surface. It is based on a progressive desorption of a pre-adsorbed gas from a surface upon gradual temperature increase. Quantification of the desorbed gas by means of mass spectrometry as a function of temperature allows one to derive information on surface chemical properties (acidity or basicity) and their related strength.

Thus, in this thesis, acidic properties of the synthesized materials were probed by means of NH₃-TPD. Typical experiments were performed on a Micromeritics Autochem II 2920 instrument. Ammonia concentration in the outlet mixture was monitored using an OmnistarTM Pfeiffer mass spectrometer. Prior to the desorption, the samples (~100 mg) were outgassed under helium flow at 250 °C in the case of MOFs and at 500 °C in the case of zeolites (60 min, 10 °C·min⁻¹). Sample saturation was performed at 10 % NH₃ in He (30 mL·min⁻¹) at 100 °C for 30 min and the sample was then purged under He flow (50 mL·min⁻¹) for 2 h at 100 °C to remove physisorbed NH₃. The desorption experiment was performed following a heating ramp of 2 °C·min⁻¹ from 100 °C to 250 °C for MOFs, and following a ramp of 5 °C·min⁻¹ from 100 °C to 700 °C for zeolites. Similar conditions were applied to study surface basicity by changing the probe gas from NH₃ to CO₂ (CO₂-TPD).

Chapter II – Characterization

2.6.2. Pyridine Adsorbed Infrared Spectroscopy (Py-FTIR)

Py-FTIR spectroscopy allows the qualitative and quantitative analysis of acid sites of both Lewis and Brønsted nature present in a solid sample. The latter is possible because pyridine complexes formed with Lewis and Brønsted acid sites can be easily distinguished in an IR spectrum and therefore acid site strength and density can be deduced. The principle behind this technique lies in a gradual desorption of the pre-adsorbed pyridine molecules from a solid's surface. This is followed by examining the evolution (progressive decrease) of the IR bands corresponding to the pyridine complexes (with Lewis and Brønsted acid sites) as a function of the applied desorption temperature. Thus, in this thesis, infrared spectra were recorded during pyridine adsorption–desorption experiments using a Nicolet Protege 460 infrared spectrometer equipped with an MCT detector. Prior to each experiment, samples were activated at 450 °C in the case of zeolites and at 150 °C in the case of MOFs under high vacuum (10^{-6} mbar) overnight. Pyridine adsorption took place at room temperature until saturation coverage at the equilibrium (1.2 mbar). Desorption under vacuum was performed at 150 °C, 250 °C, 350 °C and 450 °C. Qualitative and quantitative analyses of acidic sites were done by examination and integration of the bands at $\sim 1450\text{ cm}^{-1}$ and $\sim 1550\text{ cm}^{-1}$ for Lewis and Brønsted acid sites, respectively.

2.7. Thermal Stability Properties

2.7.1. Thermogravimetric Analysis with Differential Scanning Calorimetry (TGA-DSC)

TGA is an analytical technique of thermal analysis during which the mass of a sample is continuously measured as a function of increasing temperature. Coupled with DTA (Differential Thermal Analysis) or DSC, it allows identification of the phenomena taking place at different temperatures and including combustion, desorption, phase transition, and others. Importantly, TGA enables establishing the thermal stability of materials by quantifying, for example, the

organic fraction in them and the temperature at which its combustion starts. Therefore, in this work thermal stability properties were evaluated by recording the TG and DSC profiles with a thermal analyzer instrument Q600 from TA Instrument within the temperature range 25-800 °C at a heating rate of 5 °C·min⁻¹ under air flow (100 mL·min⁻¹).

3. Catalytic Tests

3.1. Fructose Dehydration

Fructose dehydration tests were performed in a Carousel 12 Plus Reaction Station (Radleys) (figure II-8, i) under atmospheric pressure, using 1.2 mmol of fructose, 2 mL of solvent (dimethyl sulfoxide, DMSO) and 20 mg of catalyst. The reaction mixture and the catalyst were stirred at 600 rpm and heated to the desired reaction temperature (80-120 °C) for a reaction duration up to 6 h. At the end of the reaction, the reactors were cooled to room temperature by quenching in cold water and the products were removed with a syringe, filtered and diluted 10 times with 5 mM sulfuric acid solution. The products were analyzed in high-performance liquid chromatography (HPLC) equipped with UV-vis and refractive index (RID) detectors and a Rezex ROA-Organic Acid column using sulfuric acid (5 mM, 0.6 mL·min⁻¹) as a mobile phase. For the recycling experiment, the catalyst was separated by centrifugation and then reused directly for the next run with a fresh fructose solution in DMSO. The fructose conversion and 5-HMF yield were defined as:

$$\text{Conversion (\%)} = \frac{\text{mol of Fructose}_0 - \text{mol of Fructose}_{\text{end}}}{\text{mol of Fructose}_0} * 100 \%$$

$$\text{Yield (\%)} = \frac{\text{mol of HMF}}{\text{mol of Fructose}_0} * 100 \%$$

$$\text{Selectivity (\%)} = \frac{\text{mol of HMF}}{\text{mol of Fructose}_0 - \text{mol of Fructose}_{\text{end}}} * 100 \%$$

3.2. Fructose Dehydration on Shaped MOFs

Fructose dehydration over shaped MOFs was performed in a batch stainless steel reactor of 250 mL provided by Anton Paar and equipped with a stirrer, a thermocouple and a catalyst basket (figure II-8, ii and iii). The round, metallic catalyst basket presents aperture dimensions of 1.5 cm x 0.5 cm to insert a catalyst. The applied reaction conditions were similar to the ones applied for the tests in the Carousel station. In the same way, products identification and quantification were done by HPLC as described above.

3.3. Glucose Isomerization

Glucose isomerization tests were performed in a Carousel 12 Plus Reaction Station (Radleys) working at atmospheric pressure, using 1.2 mmol of glucose, 2 mL of solvent (water) and 20 mg of catalyst. The reaction mixture and the catalyst were stirred at 600 rpm and heated to 120 °C for a reaction time of 3 h. At the end of the reaction, the reactors were cooled to room temperature by quenching in cold water and the products were removed with a syringe, filtered and diluted 10 times with 5 mM sulfuric acid solution. The products were analyzed in high-performance liquid chromatography (HPLC) equipped with a refractive index (RID) detector and a Rezex ROA-Organic Acid column using sulfuric acid (5 mM, 0.6 mL·min⁻¹) as a mobile phase. Glucose conversion and fructose yield were defined as:

$$\text{Conversion (\%)} = \frac{\text{mol of Glucose}_0 - \text{mol of Glucose}_{\text{end}}}{\text{mol of Glucose}_0} * 100 \%$$

$$\text{Yield (\%)} = \frac{\text{mol of Fructose}}{\text{mol of Glucose}_0} * 100 \%$$

$$\text{Selectivity (\%)} = \frac{\text{mol of Fructose}}{\text{mol of Glucose}_0 - \text{mol of Glucose}_{\text{end}}} * 100 \%$$



Figure II-8. Setups used to perform catalytic tests: Carousel Station (i) as well as the catalyst basket with the catalyst inside (ii), and the batch reactor Paar (iii).

4. References:

- [1] J.H. Cavka, S. Jakobsen, U. Olsbye, N. Guillou, C. Lamberti, S. Bordiga, K.P. Lillerud, A New Zirconium Inorganic Building Brick Forming Metal Organic Frameworks with Exceptional Stability, *J. Am. Chem. Soc.* 130 (2008) 13850–13851. <https://doi.org/10.1021/ja8057953>.
- [2] M.J. Katz, Z.J. Brown, Y.J. Colon, P.W. Siu, K.A. Scheidt, R.Q. Snurr, J.T. Hupp, O.K. Farha, A facile synthesis of UiO-66, UiO-67 and their derivatives, *Chem. Commun.* 49 (2013) 9449–9451. <https://doi.org/10.1039/C3CC46105J>.
- [3] M.L. Foo, S. Horike, T. Fukushima, Y. Hijikata, Y. Kubota, M. Takata, S. Kitagawa, Ligand-based solid solution approach to stabilisation of sulphonic acid groups in porous coordination polymer $Zr_6O_4(OH)_4(BDC)_6$ (UiO-66), *Dalt. Trans.* 41 (2012) 13791–13794. <https://doi.org/10.1039/c2dt31195j>.
- [4] J.M. Taylor, T. Komatsu, S. Dekura, K. Otsubo, M. Takata, H. Kitagawa, The Role of a Three Dimensionally Ordered Defect Sublattice on the Acidity of a Sulfonated Metal-Organic Framework, *J. Am. Chem. Soc.* 137 (2015) 11498–11506. <https://doi.org/10.1021/jacs.5b07267>.
- [5] Y. Khabzina, J. Dhainaut, M. Ahlhelm, H. Richter, H. Reinsch, N. Stock, D. Farrusseng, Synthesis and Shaping Scale-up Study of Functionalized UiO-66 MOF for Ammonia Air Purification Filters, *Ind. Eng. Chem. Res.* 57 (2018) 8200–8208. <https://doi.org/10.1021/acs.iecr.8b00808>.
- [6] M.K. Dongare, P. Singh, P.P. Moghe, P. Ratnasamy, Synthesis, characterization, and catalytic properties of [Zr]-ZSM-5, *Zeolites.* 11 (1991) 690–693.

Chapter III

Properties and Catalytic Performance of

Zeolites

Chapter III

As it was discussed in chapter I, isomorphous substitution of Al by another element is a classical approach for tuning acid properties of zeolites resulting in the so-called metallosilicates. With this in mind, this chapter is focused on the characterization of the zeolitic materials prepared according to the procedures described in the section 1.2 of chapter II and presented in Table II.2. This includes basic techniques applied for routine characterization such as XRD, N₂ physisorption, ATR-IR spectroscopy and others as well as advanced spectroscopic techniques: XPS and ToF-SIMS. The two latter are less often used for characterization of zeolitic materials and therefore the information they provide are of particular interest. A special attention will be given to the MFI type Zr-containing metallosilicates *i.e.* [Si,Zr]-MFI-in and [Si,Zr]-MFI-ex which, to the best of the manuscript's author knowledge, are poorly described in the literature.

Finally, catalytic performances of the prepared zeolitic materials in fructose dehydration to HMF and glucose isomerization to fructose is discussed.

1. Characterization of Zeolitic Materials

1.1. Structural Properties

1.1.2. XRD

Characterization of a solid product often starts by examining its structure to establish whether it is crystalline or amorphous. As discussed in the previous chapter, XRD is the ultimate technique to probe crystallographic properties of solids. Figure III-1 demonstrates the diffractograms of the zeolitic materials prepared in this work.

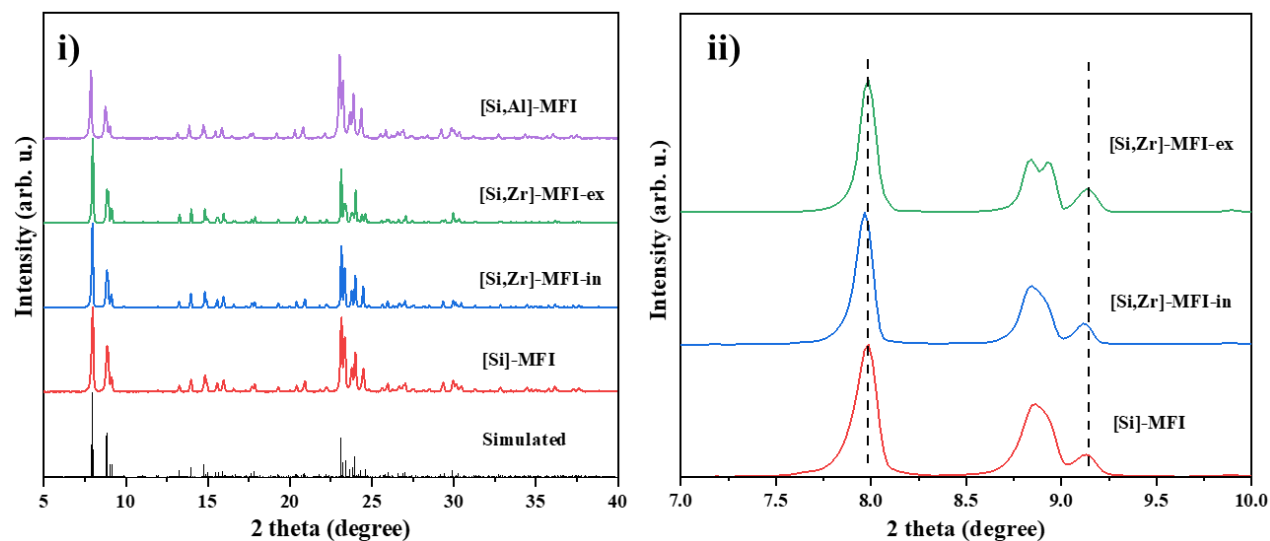


Figure III-1. XRD patterns of the synthesized solids as compared to the simulated diffractogram of a MFI-type zeolite with a Si/Al of 300 (i), and magnification into the 7-10 ° region to evidence a small shift of reflections in [Si,Zr]-MFI-in as compared to the pure siliceous [Si]-MFI (ii). The pattern simulation was done using the corresponding CIF file [1]. The intensities are normalized to the intensity of the reflection at ~8 °.

First of all, all the synthesized solids exhibit the typical diffraction pattern of the MFI topology with a monoclinic symmetry organization, as in the case of the simulated pattern (figure III-1, i). Of note, MFI-type materials are oftentimes described by the principle reflections at 7-9 ° and 23-25 ° two theta values, representing a combination of families of the diffraction planes [1].

Interestingly, [Si,Zr]-MFI-in experienced a small shift of its reflections towards smaller 2 theta values when compared to a pure siliceous Silicalite-1, named [Si]-MFI hereafter (Figure III-1, ii). This might serve as a first indication of the introduction of bigger ions in the MFI framework. Indeed, according to the existing databases [2,3] Zr^{4+} ionic radius (0.59 Å) in tetrahedral coordination is much bigger than that of Si^{4+} (0.26 Å). In contrast, there is no perceptible shift in the diffractogram of [Si,Zr]-MFI-ex, indicating that tetrahedral Zr^{4+} might not be present in the MFI structure and that the diffraction pattern is related to a Silicalite-1-like material. At the same time there is no evidence of a secondary crystalline phase neither in [Si,Zr]-MFI-in nor in [Si,Zr]-

MFI-ex, despite possible crystallization of ZrO_2 phases upon hydrothermal treatment in basic medium [4,5]. Therefore, this might suggest either the presence of ZrO_2 nanocrystals non-detectable by XRD and/or simply amorphous ZrO_2 phase.

Overall, XRD confirms the successful crystallization of the synthesized solids into MFI-type zeolitic materials. In the case of [Si,Zr]-MFI-in and [Si,Zr]-MFI-ex, it is possible to hypothesize that the former contains framework-incorporated Zr atoms within the MFI lattice resulting in a shift of the reflections, whereas in the latter the Zr species are mostly extra-framework. The corresponding prefixes “in” and “ex” in the solids’ names are thus related to this hypothesis. Nevertheless, further characterization is needed to support or deny these results.

1.1.3. ATR-FTIR and Raman Spectroscopy

Structural properties *via* examining characteristic vibrations of the MFI-type solids were probed by ATR-FTIR and are revealed in the spectra presented in figure III-2 (i).

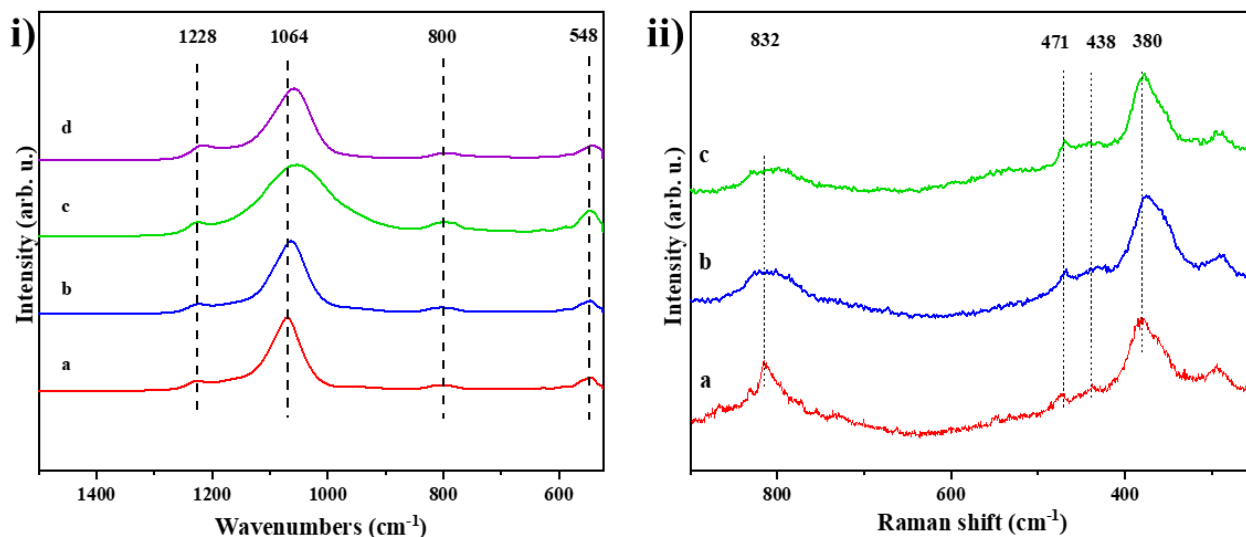


Figure III-2. ATR-IR spectra (i) of [Si]-MFI (a), [Si,Zr]-MFI-in (b), [Si,Zr]-MFI-ex (c) and [Si,Al]-MFI (d) and their corresponding Raman spectra (ii). The intensities are normalized to the intensity of the band at 1064 cm^{-1} (ATR-IR) and at 380 cm^{-1} (Raman).

By a careful look at the presented zone, one can distinguish the bands originated from several vibrations that include: external asymmetric Si-O-Si stretching ($\sim 1228\text{ cm}^{-1}$), internal asymmetric Si-O-Si stretching ($\sim 1064\text{ cm}^{-1}$), internal symmetric Si-O-Si stretching ($\sim 800\text{ cm}^{-1}$) and the double ring vibration ($\sim 548\text{ cm}^{-1}$). The latter represents the characteristic vibration of the MFI framework and therefore serves as its fingerprint in IR spectra [6–8]. Once again, a small shift towards lower wavenumbers, when compared to [Si]-MFI, is attributed to the presence of heteroatoms in SiO_2 framework *i.e.* Al and Zr which require higher energy to excite the corresponding vibrational states upon binding to Si atoms. For example, the band at $\sim 1064\text{ cm}^{-1}$ is observed at $\sim 1060\text{ cm}^{-1}$ in [Si,Zr]-MFI-in and at $\sim 1055\text{ cm}^{-1}$ in [Si,Al]-MFI.

In addition, Raman spectroscopy is a powerful and sensitive tool to distinguish all the three existing ZrO_2 phases: cubic, monoclinic, and tetragonal [9]. Therefore, it was used in this work to probe possible ZrO_2 phases formed upon hydrothermal syntheses of [Si,Zr]-MFI-in and [Si,Zr]-MFI-ex, by comparison to the spectrum of [Si]-MFI. The Raman spectra are depicted in figure III-2 (ii) in which the characteristic vibrations can be distinguished. The latter include: Si-O-Si symmetric stretching ($\sim 832\text{ cm}^{-1}$), Si-O-Si bending ($\sim 471\text{ cm}^{-1}$), Si-O-Si asymmetric stretching ($\sim 438\text{ cm}^{-1}$) and the characteristic vibration of the MFI framework ($\sim 380\text{ cm}^{-1}$) [10]. Importantly, there is no evidence of any crystalline ZrO_2 phase which, according to the literature, all present an intense band at $\sim 650\text{ cm}^{-1}$ [9]. This correlates with the XRD results obtained for [Si,Zr]-MFI-in and [Si,Zr]-MFI-ex. The latter, however, exhibits a weak, broad band in the range of $520\text{--}630\text{ cm}^{-1}$ which corresponds to amorphous ZrO_2 [11].

Hence, [Si,Zr]-MFI-in is expected to mostly contain framework-inserted Zr^{4+} species owing to XRD and spectroscopic results. In the case of [Si,Zr]-MFI-ex, however, Zr-species not inserted in

the framework might be only of amorphous nature as-evidenced by Raman analysis. Nevertheless, further assessment of the presence of Zr heteroatoms in MFI-type zeolitic materials is needed.

1.2. Textural Properties

1.2.1. N₂ Physisorption

Figure III-3 shows the adsorption/desorption isotherms recorded upon N₂ physisorption analyses. All the solids are represented by a classical type I isotherm, which is defined by a sharp gas uptake at low relative N₂ pressures. Usually, this uptake is associated with a consequent filling of micropores by the sorbent until a plateau is reached, usually below 0.3. This monolayer corresponds to the formation of the N₂ monolayer which is at the basis of the BET equation, allowing one to calculate the surface area (Table III.1). Accordingly, all the synthesized materials exhibit similar surface areas which are consistent with MFI-type ZSM-5 zeolites [12,13].

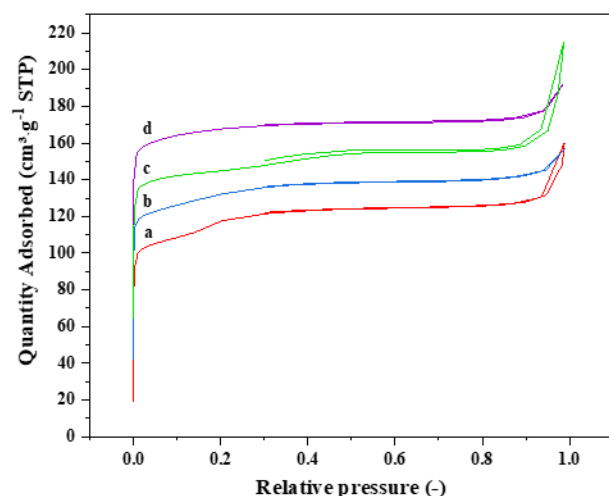


Table III.1 – Textural properties of the synthesized solids.

Sample	S _{BET} , m ² g ⁻¹	Pore volume, cm ³ g ⁻¹	
		Micro ^a	Total ^b
[Si,Al]-MFI	419	0.17	0.20
[Si,Zr]-MFI-ex	394	0.14	0.25
[Si,Zr]-MFI-in	421	0.18	0.21
[Si]-MFI	438	0.19	0.24

a – calculated by the *t*-plot method;

b – using the adsorption branch at $p/p_0 \sim 0.99$.

Figure III-3. N₂ physisorption isotherms of [Si]-MFI (a, offset y-axis: 0), [Si,Zr]-MFI-in (b, offset y-axis: +20 cm³·g⁻¹ STP), [Si,Zr]-MFI-ex (c, offset y-axis: +35 cm³·g⁻¹ STP) and [Si,Al]-MFI (d, offset y-axis: +60 cm³·g⁻¹ STP).

Upon further increase of relative pressure, gas adsorption is considerably slowed down as the interaction of N₂ molecules with the surface becomes weaker. This plateau region continues until

$p/p_0 < 0.9$, above which a subsequent uptake is often associated with gas adsorption on the external surface of particles and therefore might provide valuable information on their size and homogeneity. Thus, the open character of adsorption/desorption branches of the isotherm of [Si,Zr]-MFI-ex implies a strong inhomogeneity of its surface as compared to the other solids. Based on the results obtained from Raman spectroscopy, it might originate from the external ZrO_2 amorphous phase and should be further studied by electron microscopy. Lastly, the region at $p/p_0 > 0.9$ is associated with complete condensation of liquid N_2 in the pores and therefore the quantity of adsorbed gas at $p/p_0 \sim 0.99$ is typically used to calculate the total pore volume (Table III.1). The latter agrees well with the values reported elsewhere [12,13].

1.3. Elemental Analysis

1.3.1. ICP-OES

The elemental analysis was performed according to the theoretical chemical composition of the synthesized solids, with the quantified elements presented in Table III.2.

Table III.2 – Elemental composition of the synthesized solids.

Sample	Elements for quantification							
	Si, wt.%		Zr, wt.%		Al, wt.%		Na, wt.%	
	Theor*	Exp	Theor*	Exp	Theor*	Exp	Theor*	Exp
[Si,Zr]-MFI-in	43.7	36.1	4.7	2.7	-	-	-	-
[Si,Zr]-MFI-ex	43.7	38.0	4.7	3.4	-	-	< 1.2	0.3
[Si,Al]-MFI [♦]	44.6	38.0	-	-	1.4	1.3	< 1.2	<< 0.1

* calculated from the composition of gels considering pure non-hydrated oxide forms;

♦ after ion-exchange.

As seen from Table III.2, all the synthesized solids are composed of the targeted elements within the desired percentage range. The theoretical values were calculated from the pure oxide forms

without considering water molecules and therefore it can explain the remarkable difference between theoretical and experimental values especially in the case of Si and Zr. The ion-exchange step performed on [Si,Al]-MFI to convert Na⁺ to H⁺-form was successful as the amount of Na present in the solid is negligibly small. As for [Si,Zr]-MFI-in and [Si,Zr]-MFI-ex, both exhibited comparable Si (36.1 wt.% and 38.0 wt.%) and Zr (2.7 wt.% and 3.4 wt.%) experimental contents, respectively. Of note, some Na⁺ cations remain present in [Si,Zr]-MFI-ex, while the framework should be electroneutral. This could be due to insufficient washing of the sample after synthesis.

1.4. Chemical Properties

1.4.1. TPD and Py-FTIR

Prior to use in catalysis, it is crucial to determine the acid-base properties of the synthesized solids. They were evaluated by means of NH₃-TPD, CO₂-TPD, Py-FTIR and the results are depicted in Table III.3.

Table III.3 – Acidic and basic properties of the synthesized solids

Sample	Acidic properties						Basic prop.	
	Py-FTIR, $\mu\text{mol}\cdot\text{g}^{-1}$						NH ₃ -TPD, $\mu\text{mol}\cdot\text{g}^{-1}$	CO ₂ -TPD, $\mu\text{mol}\cdot\text{g}^{-1}$
	Weak, <250 °C		Med-strong, 250-350 °C		Strong, >350 °C			
	B	L	B	L	B	L		
[Si]-MFI	-	-	-	-	-	-	10	-
[Si,Zr]-MFI-in	10	48	-	-	-	-	109	-
[Si,Zr]-MFI-ex	-	19	-	-	-	-	65	34
[Si,Al]-MFI	398	104	166	23	79	23	684	-
[Si,Al]-MFI-c*	834	216	292	84	104	73	1983	-
t-ZrO ₂ †	-	201	-	9	-	-	not meas-d	-

B - *Brønsted*;

L - *Lewis*;

* - *commercial H-ZSM-5 (MFI) zeolite with a Si/Al molar ratio of 11*;

♦ - *commercial tetragonal ZrO₂*.

According to Table III.3, both synthesized [Si,Zr]-MFI-in and [Si,Zr]-MFI-ex exhibit acidic properties confirmed by NH₃-TPD as well as Py-FTIR. Both techniques suggested a doubled amount of acid sites in [Si,Zr]-MFI-in (109 μmol·g⁻¹ by NH₃-TPD) as compared to [Si,Zr]-MFI-ex (65 μmol·g⁻¹ by NH₃-TPD). At the same time, Py-FTIR suggested the presence of rather weak Lewis acid sites which are more pronounced in [Si,Zr]-MFI-in (48 μmol·g⁻¹) than in [Si,Zr]-MFI-ex (19 μmol·g⁻¹). This agrees well with the acidic properties of the commercial t-ZrO₂ which possesses mainly weak Lewis acid sites (201 μmol·g⁻¹) as suggested by Py-FTIR. This implies that Zr introduction into the MFI framework generates mainly weak Lewis acid sites.

Notably, [Si,Al]-MFI synthesized in this work with a Si/Al molar ratio of 30 exhibits three times less acid sites probed by NH₃-TPD when compared to its commercial analogue with a Si/Al molar ratio of 11 (684 μmol·g⁻¹ vs 1983 μmol·g⁻¹), while as seen in Table III.2 complete sodium-to-proton ion-exchange was obtained. This difference in the amount of acid sites agrees with the nearly 3 times less amount of Al in the synthesized [Si,Al]-MFI. Besides, both solids mainly exhibit Brønsted acid sites as probed by Py-FTIR as the result of the ion-exchange procedure. Interestingly, the percentage of strong Brønsted acid sites in the synthesized [Si,Al]-MFI represents nearly 12 % of the total Brønsted acid sites, whereas it represents about 8% in its commercial counterpart. This supports the NNN theory briefly discussed in chapter I according to which a smaller number of Al atoms results in stronger (but lesser) Brønsted acid sites.

Importantly, there is a certain amount of basic acid sites in [Si,Zr]-MFI-ex as probed by CO₂-TPD. This might be due to the presence of trace amounts of Na⁺ as suggested by the ICP-OES elemental analysis.

1.5. Morphological Properties

1.5.1. SEM

SEM micrographs of representative crystal morphologies of the synthesized solids are displayed in figure III-4. Accordingly, [Si]-MFI is composed of coffin-shaped crystals of different size ranging from ~200 nm up to ~2 μm, as described in the literature [14,15]. Similar crystal morphology, *i.e.* coffin shape but rather rounded crystals, is observed for [Si,Zr]-MFI-in, along with a considerably smaller and homogeneous crystal size distribution of around 200 nm, as also described previously [16]. Importantly, particles in [Si,Zr]-MFI-ex exhibit rather a complex morphology. They are composed of large cross-shaped crystals of around 7 μm with a visible secondary phase deposited on their surface. This secondary phase is represented by fine particles whose size and shape are difficult to evaluate by SEM due to its limited resolution. Therefore, further assessment by TEM is necessary. Nevertheless, this remarkable inhomogeneity of crystal size is probably at the origin of the open N₂ adsorption-desorption isotherm shown in figure III-3 and increased N₂ uptake at p/p₀>0.9 due to liquid N₂ condensation in inter-particle space. Finally, [Si,Al]-MFI consists of aggregates of small coffin-shaped crystals of around 200 nm [17,18].

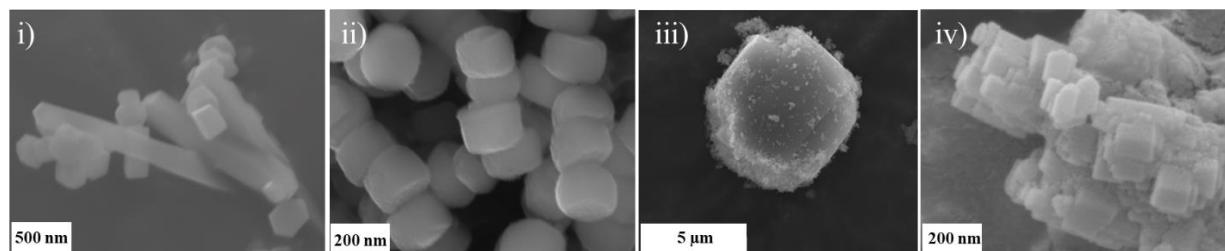


Figure III-4. SEM images of [Si]-MFI (i, scale bar: 500 nm), [Si,Zr]-MFI-in (ii, scale bar: 200 nm), [Si,Zr]-MFI-ex (iii, scale bar: 5 μm) and [Si,Al]-MFI (iv, scale bar: 200 nm).

As [Si]-MFI and [Si,Al]-MFI have been extensively described in the literature, more emphasis has been put on the investigation of [Si,Zr]-MFI-in and [Si,Zr]-MFI-ex. Consequently, the elemental composition of both solids was evaluated by the coupled SEM-EDS analysis (figure III-5). [Si,Zr]-MFI-in exhibits rather a homogeneous distribution of the elements across the particles with Zr being less detectable due to its lowered percentage. At the same time, when examining [Si,Zr]-MFI-ex, one can notice that the large cross-shaped crystals are mainly composed of pure SiO_2 according to the elemental mapping, while the fine particles at the surface of these crystals are rich in Zr. Therefore, at this point it is possible to conclude that [Si,Zr]-MFI-ex is mainly composed of large Si-rich MFI crystals along with a secondary phase containing fine particles of zirconium oxide species.

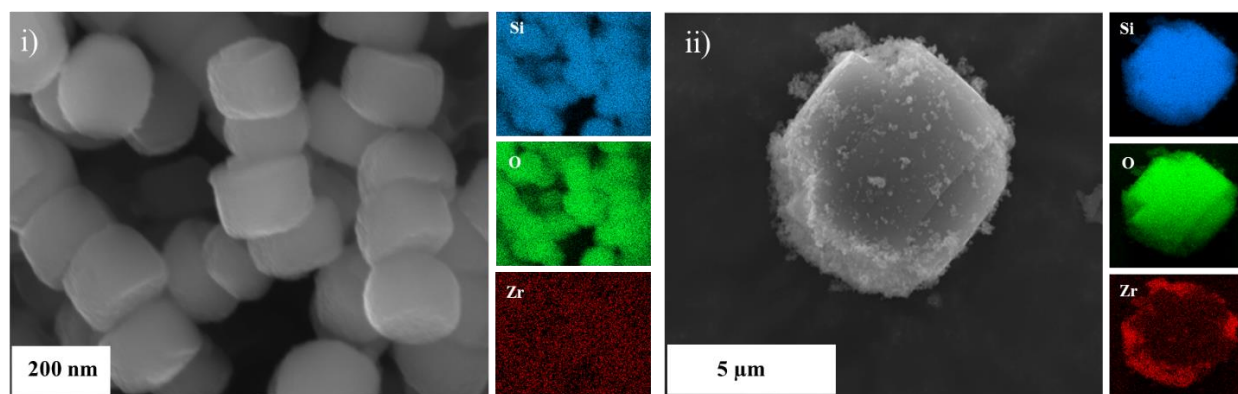


Figure III-5. SEM images and EDS mapping of the targeted elements of [Si,Zr]-MFI-in (i, scale bar: 200 nm) and [Si,Zr]-MFI-ex (ii, scale bar: 5 μm).

1.5.2. HRTEM

HRTEM reveals the crystalline nature of the particles composing [Si,Zr]-MFI-in (figure III-6, a and b insets) represented by electron diffraction patterns collected on selected areas (SAED) thus confirming the XRD data. Similar to SEM-EDS, high-angle annular dark-field (HAADF) imaging made on scanning transmission (STEM) mode (figure III-6, iii) followed by elemental mapping (figure III-6, iv-vi) confirms a homogeneous distribution of the elements within the crystals. The

latter is critical in the case of Zr to understand its localization and therefore one can observe no surface saturation with Zr as also confirmed by SEM-EDS.

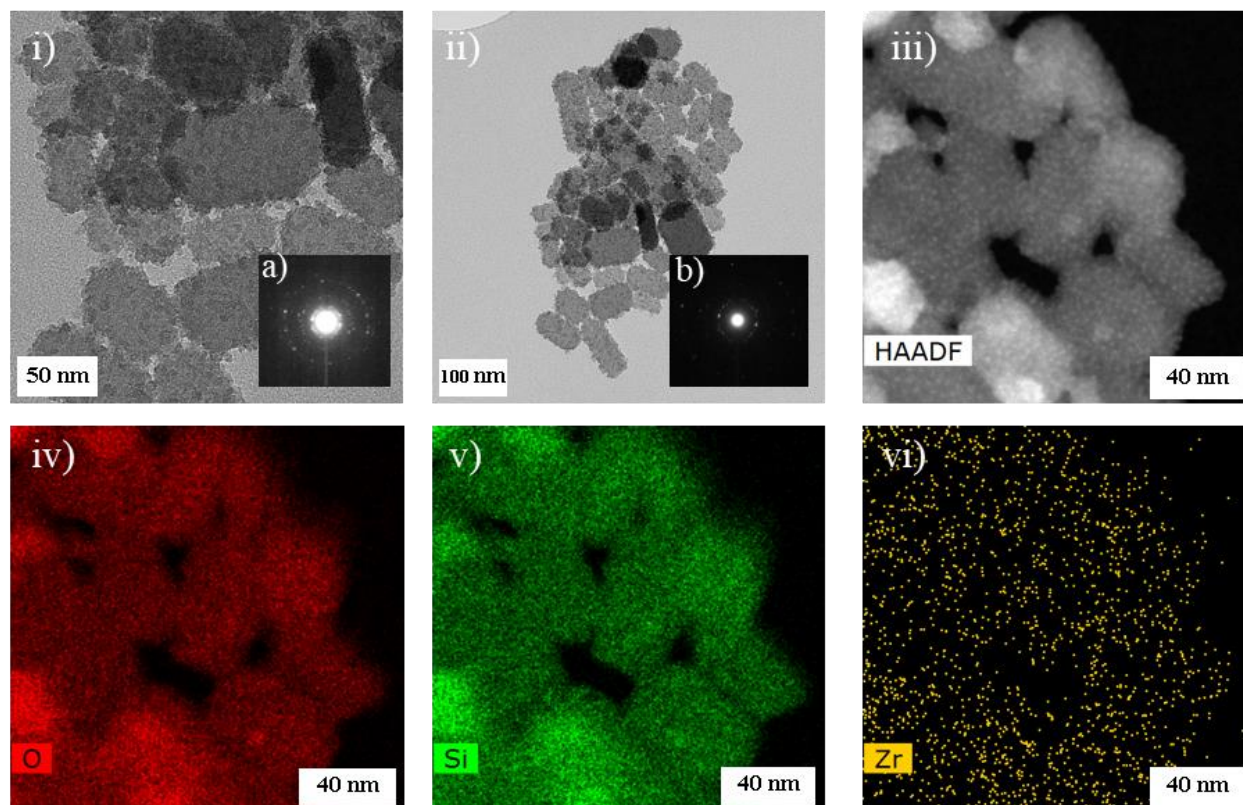


Figure III-6. HRTEM images (i and ii) of [Si,Zr]-MFI-in with the insets (a and b) corresponding to SAED; HAADF-STEM image (iii) and elemental mapping (iv-vi) of the area shown in (iii).

When examining the two phases present in [Si,Zr]-MFI-ex, the amorphous nature of the fine ZrO_2 aggregates on top of SiO_2 crystals can be deduced from the absence of a diffraction pattern in the SAED image (figure III-7, a). In contrast, the large crystals yielded a diffraction pattern viewed as the dots in its SAED image (figure III-7, b). This allows to prove the results obtained by XRD and Raman spectroscopy which suggested that the diffraction originated mostly from the crystalline SiO_2 phase with the presence of amorphous ZrO_2 .

In order to investigate whether or not Zr atoms are also present within the zeolite framework, [Si,Zr]-MFI-ex was cut into small (50-100 nm) slices prior to observation as shown in figure III-7

(iii). Further elemental analysis on this area (figure III-7, iv-vi) confirmed that the crystals are purely composed of SiO_2 , whereas the secondary phase is mainly composed of ZrO_2 with a negligible percentage of SiO_2 which may be assigned to the formation of amorphous $\text{ZrO}_2\text{-SiO}_2$ mixed oxide.

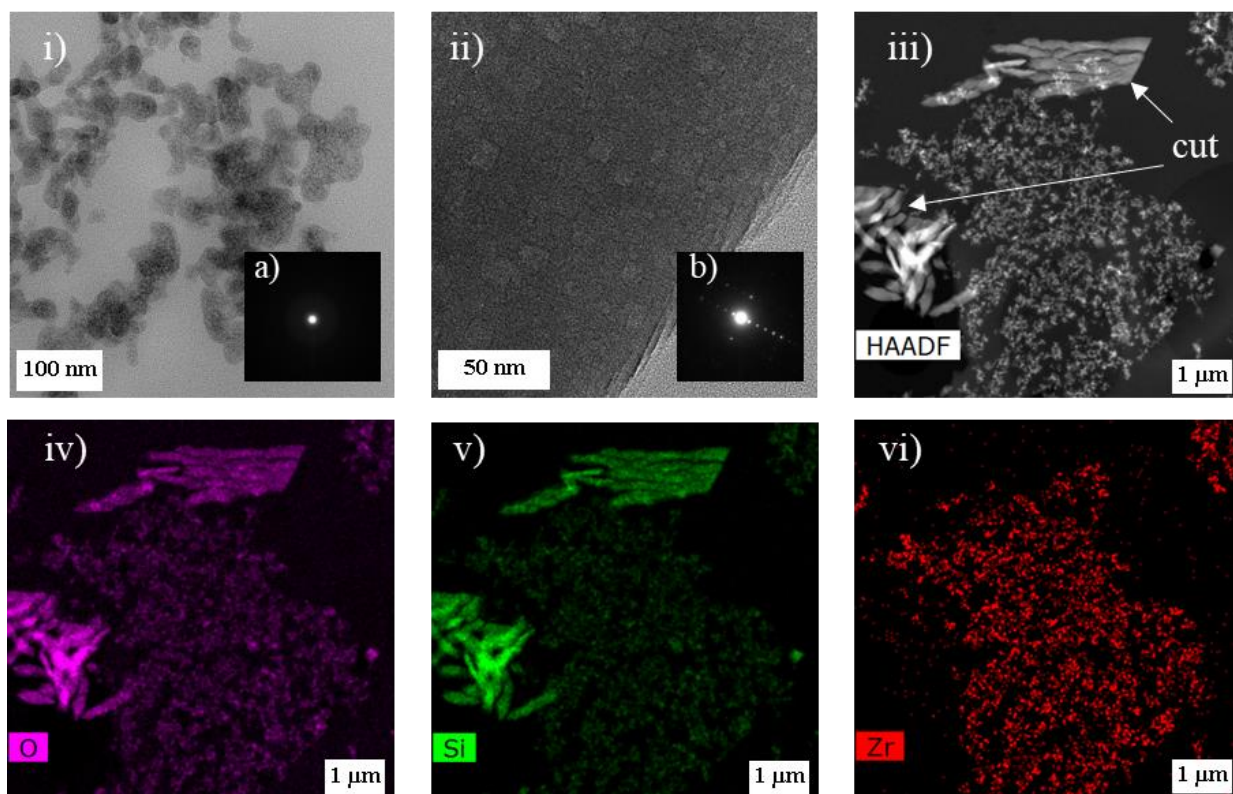


Figure III-7. HRTEM images of the secondary phase located on the large cross-shaped crystals of [Si,Zr]-MFI-ex (i-ii), with inserts corresponding to SAED (a-b). HAADF-STEM image where “cut” represents smaller slices of the large cross-shaped crystals (iii), and related elemental mapping (iv-vi).

1.6. Surface Properties

1.6.1. ToF-SIMS

To further investigate the effective insertion of Zr species within the zeolite frameworks, the surface composition of [Si,Zr]-MFI-ex and [Si,Zr]-MFI-in were examined by ToF-SIMS and the related spectra are presented in figure III-8.

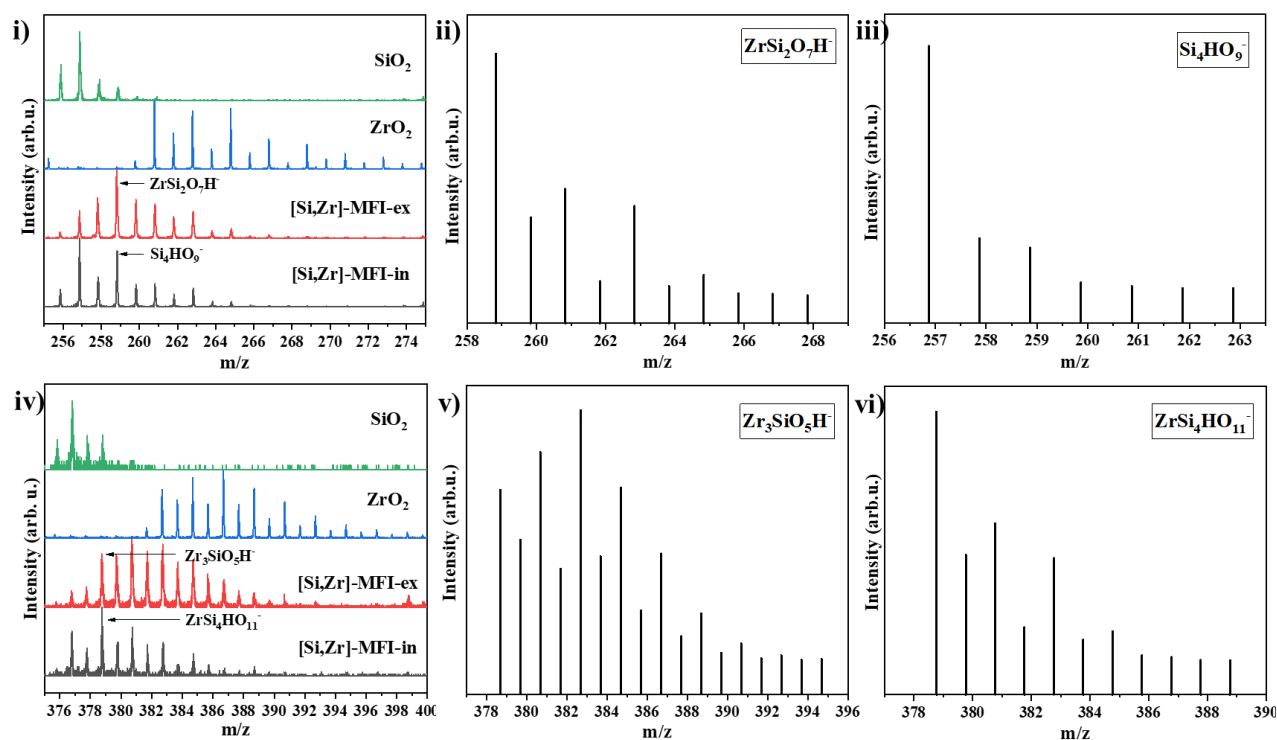


Figure III-8. Global ToF-SIMS spectra of [Si,Zr]-MFI-ex and [Si,Zr]-MFI-in as compared to SiO₂ and ZrO₂ references over the m/z range of 255-275 (i) and 375-400 (iv) as well as the simulated spectra of the fragments: ZrSi₂O₇H⁻ (ii), Si₄HO₉⁻ (iii), Zr₃SiO₅H⁻ (v) and ZrSi₄HO₁₁⁻ (vi).

As it is evident, both solids exhibit fragments corresponding to mixed SiO₂/ZrO₂ as compared to the spectra of pure ZrO₂ and SiO₂. Critically, when examining the m/z range between 256 and 276 (figure III-8, i), one can notice that [Si,Zr]-MFI-ex spectrum reveals fragments with higher Zr content, by comparison with the simulated pattern of ZrSi₂O₇H⁻. Indeed, they share the same most

intense peak at 259 m/z. On the other hand, [Si,Zr]-MFI-in exhibits more pronounced Si-containing fragments, deduced by comparison with the simulation of Si_4HO_9^- and their common most intense peak at 257 m/z. At the first glance, this suggests Zr-enrichment of [Si,Zr]-MFI-ex surface and can be further confirmed by studying the m/z range of 376-400 (figure III-8, iv). In this region, the results once again point at a majority of Zr-rich fragments such as $\text{Zr}_3\text{SiO}_5\text{H}^-$ from [Si,Zr]-MFI-ex as confirmed by the good match between the experimental spectrum of the solid and the simulated pattern of the fragment. This clearly shows the qualitative evidence of surface saturation with Zr. Also, it agrees well with the presence of an amorphous ZrO_x phase deposited on pure SiO_2 crystals as seen in SEM and TEM micrographs. In contrast, [Si,Zr]-MFI-in is composed of Si-rich fragments such as $\text{ZrSi}_4\text{HO}_{11}^-$ peaking at m/z of 379, which interestingly can serve as a fingerprint of a tetrahedral Zr atom surrounded by 4 Si atoms. In fact, this corresponds well to the configuration that Zr atoms would have in the MFI framework and therefore can be used as a proof of the successful introduction of Zr atoms in the MFI framework. Once again, this can be supported by the SEM and TEM images which suggest rather a homogeneous composition with Zr atoms evenly distributed across the crystals.

1.6.2. XPS

Although the surface sensitivity of XPS is somewhat less than that of ToF-SIMS, the former is a quantitative technique and therefore allows obtaining both qualitative and quantitative information. Figure III-9 represents the spectra of [Si,Zr]-MFI-ex and [Si,Zr]-MFI-in.

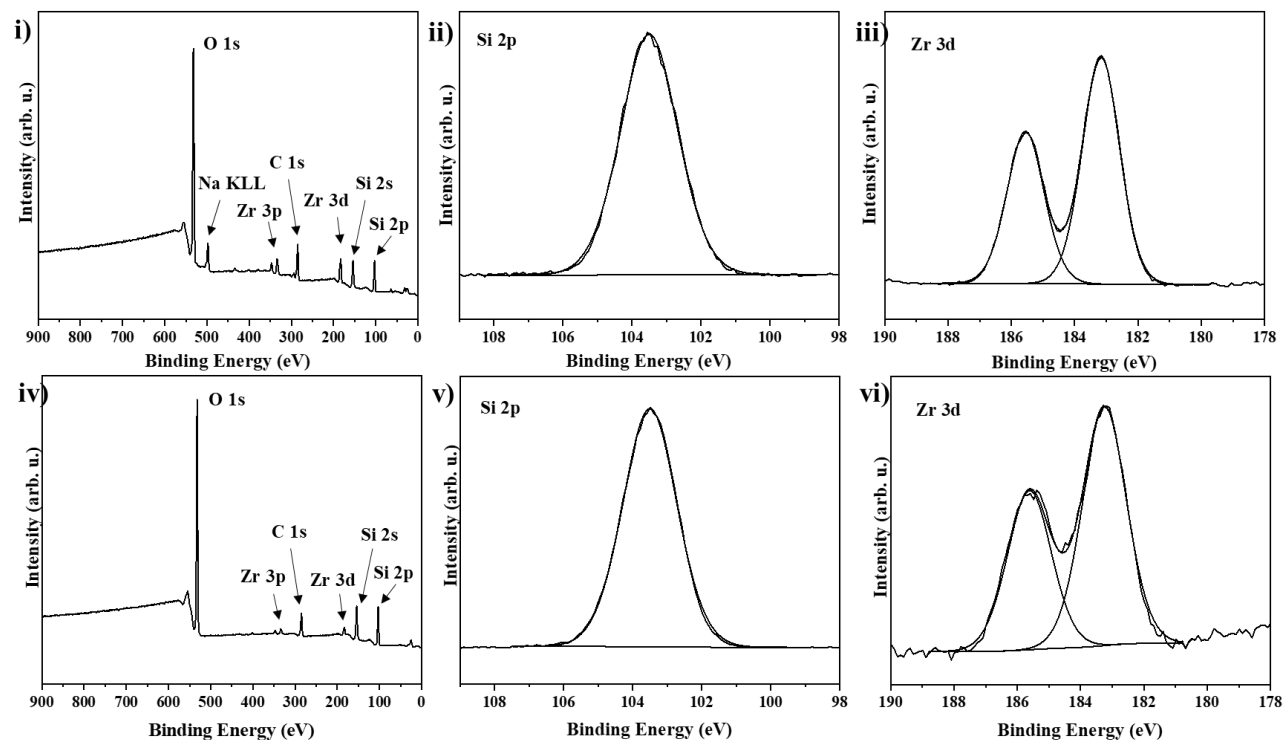


Figure III-9. XPS surveys of [Si,Zr]-MFI-ex (i) and [Si,Zr]-MFI-in (iv) with the assigned elements as well as the spectra of their respective Si 2p (ii and v) and Zr 3d (iii and vi) contributions used for establishing the Si/Zr ratios.

Once again, the global surveys suggest the presence of the targeted elements. Interestingly, the Zr 2p and Zr 3d peaks have higher apparent relative intensities in [Si,Zr]-MFI-ex than in [Si,Zr]-MFI-in (figure III-9, i and iv) confirming once again the surface enrichment of the former with Zr. Further integration of Si 2p and Zr 3d contributions allows quantifying the elements and therefore establishing the corresponding Si/Zr ratios (Table III.4).

Table III.4 – Surface fragments and Si/Zr ratios in the bulk and on the surface.

Sample	Si/Zr ratio			Key fragment (ToF-SIMS)
	Theor.	Experim.	Experim.	
	(Synthesis gel)	ICP-OES (bulk)	XPS (surface)	
[Si,Zr]-MFI-ex	30	36	8	Zr ₃ SiO ₅ H ⁻
[Si,Zr]-MFI-in	30	40	29	ZrSi ₄ HO ₁₁ ⁻

Accordingly, [Si,Zr]-MFI-ex exhibits a low Si/Zr molar ratio of ~8 which is considerably lower than the theoretical value (30) and the value derived from ICP-OES elemental analysis (36), which is a bulk analytical technique. This again confirms the surface enrichment of Zr species. At the same time, [Si,Zr]-MFI-in exhibits a Si/Zr molar ratio of ~29 which is close to the theoretical value (30) and not largely different from the one suggested by the ICP-OES analysis (40). Thus, it is possible to conclude that Zr distribution is rather homogeneous within [Si,Zr]-MFI-in as both the bulk and the surface Si/Zr ratios are somewhat comparable, on the contrary to [Si,Zr]-MFI-ex.

2. Catalytic Tests

2.1. Fructose Dehydration to HMF

Following previous works dedicated on fructose dehydration on solid acid catalysts, 3 different solvent compositions were studied in order to test their suitability with respect to catalysts. This includes the following solvent systems: water, water:ethanol (v:v, 1:1) and DMSO (figure III-10).

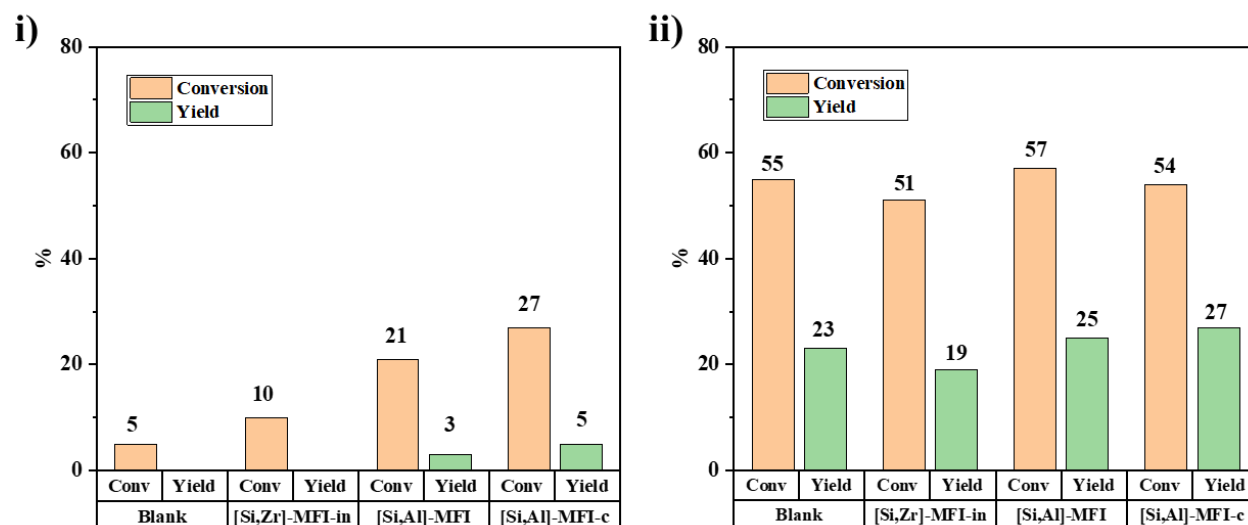


Figure III-10. Fructose conversion and HMF yield over a series of tested catalysts compared to blank tests. Reaction conditions: $T = 100\text{ }^{\circ}\text{C}$, $P_{\text{atm.}}$, $m(\text{catalyst}) = 20\text{ mg}$, $c(\text{fructose}) = 0.6\text{ mM}$, $V(\text{solvent}) = 2\text{ mL}$, 600 rpm, solvents: H_2O (after $t = 2\text{ h}$) (i) and DMSO (after $t = 1\text{ h}$) (ii).

First of all, [Si]-MFI and [Si,Zr]-MFI-ex showed no conversion in water under these conditions. Therefore, these two catalysts were not plotted. As seen in figure III-10 (i), water does not seem to be an appropriate choice for the targeted dehydration reaction, as briefly discussed in chapter I. It shifts the chemical equilibrium towards the reactant *i.e.* fructose and thus does not favor its conversion. In this regard, no HMF was detected after 2 h of reaction in water, without catalyst (blank test) or with [Si,Zr]-MFI-in. The detected conversions of 5 % (blank) and 10 % ([Si,Zr]-MFI-in) might be attributed to the formation of fructose oligomers as well as to fructose adsorption on [Si,Zr]-MFI-in surface. When [Si,Al]-MFI was used as the catalyst, fructose conversion reached 21 % with only traces of HMF (~3 % yield) observed after 2 h, while it increased to 27 % and ~5 %, respectively, using the commercial [Si,Al]-MFI-c. The slight difference might be attributed to the higher number of Brønsted acid sites, as confirmed by Py-FTIR analyses (Table III.3). Additionally, in terms of selectivity the results shown by both [Si,Al]-MFI and [Si,Al]-MFI-c are somewhat in agreement with the ones reported elsewhere [19–21]. Indeed, they both demonstrated considerably low HMF selectivities of 14 % and 19 %, respectively, with a small amount of levulinic acid as the major by-product in both cases.

In order to increase the HMF selectivity, one can use a biphasic solvent system such as H₂O/MIBK. Upon formation, HMF would be preferentially solubilized by the MIBK phase, preventing its further rehydration into by-products as discussed in chapter I. In this work, the mentioned biphasic system was also applied as solvent. However, due to certain difficulties with the analytical instrumentation, originated from the used HPLC equipment, a reasonable analysis of the MIBK phase, rich in HMF, was not possible. Another binary solvent system *i.e.* H₂O/ethanol was attempted with the same intention to increase the HMF selectivity. However, such system did not

show any fructose conversion under the same reaction conditions used with water. Therefore, the last solvent considered in this work was DMSO.

Figure III-10 (ii) illustrates the results of fructose dehydration in DMSO. Accordingly, one can notice a decent performance of DMSO alone, without catalyst (blank test), converting 55 % fructose and yielding 23 % HMF after 1 h at 100 °C (selectivity = 42 %). Thus, DMSO itself outperforms all the catalysts tested in water at 100 °C for 2 h and underlines its positive catalytic effect. Indeed, its activity towards fructose dehydration is well known and therefore it has been considered as an optimal solvent for a long time [22,23]. However, when examining the performance of the tested catalysts, it is clear that fructose conversion and HMF yield are comparable to those of the blank test and remain around 55 % and 23 % on average, respectively. It is critically important to note that all the catalysts were found dissolved after the catalytic tests. After 1 h of reaction at 100 °C, the reaction mixture turned from a turbid suspension into a clear solution (figure III-11).

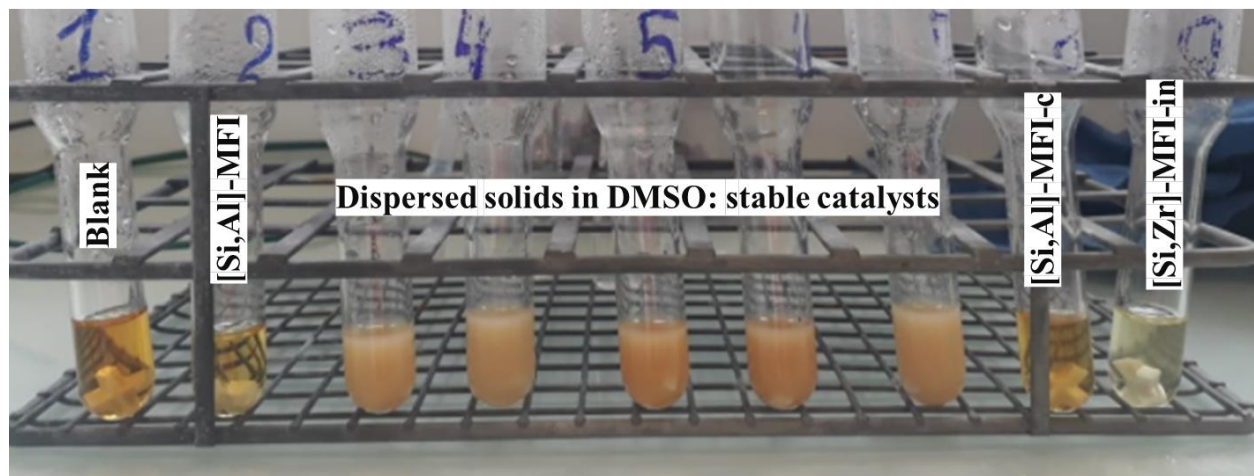


Figure III-11. Illustration of the reaction mixtures after 1 h of catalytic test at 100 °C in DMSO. The tests run with the zeolitic solids yielded clear solutions with colors similar to that of the blank test. Dispersed MOF-based solids after catalytic tests shown for comparison (reactors 3 to 7).

Partial dissolution of zeolites during fructose dehydration by the side products was shown before [24–26]. It implies mostly Al-leaching induced by levulinic and formic acid attacks on the zeolite framework, which also provoke Si-leaching to some extent. In this work, however, the dissolution was rather remarkable as the catalysts were impossible to recover by filtration or centrifugation. This might explain the similar performance of the tested catalysts relative to the blank test, implying no heterogeneous catalytic activity provided. It is possible to increase a zeolite's stability under solvothermal conditions by grafting hydrophobic groups onto its surface [27,28]. However, this is beyond the scope of the present work.

Therefore, considering the results presented above *i.e.* low selectivity of zeolites towards HMF in water and their complete dissolution in DMSO during fructose dehydration, it was decided to move to the one-step glucose isomerization into fructose in aqueous medium. The corresponding results will be discussed below.

2.2. Glucose Isomerization to Fructose

The reaction conditions for glucose isomerization were similar to those applied in fructose dehydration in water. The temperature, however, was increased from 100 °C to 120 °C. The list of the applied catalysts and their corresponding performances are presented in Table III.5.

Table III.5 – Glucose conversion and fructose yield over the series of zeolitic catalysts under the following reaction conditions: P_{atm} , 600 rpm, $c(\text{glucose}) = 0.6 \text{ mM}$, $m(\text{catalyst}) = 20 \text{ mg}$, $V(\text{H}_2\text{O}) = 2 \text{ mL}$, $T = 120 \text{ }^\circ\text{C}$, $t = 3 \text{ h}$.

Catalyst	Gl. conv., %	Fr. yield, %	Fr. sel., %
Blank	0	0	0
[Si]-MFI	0	0	0
[Si,Al]-MFI	0	0	0
[Si,Al]-MFI-c*	0	0	0

Table III.5 continued

t-ZrO ₂ [♦]	<5	0	0
[Si,Zr]-MFI-in	0	0	0
[Si,Zr]-MFI-ex	26	25	96

* - commercial [Si,Al]-MFI with Si/Al = 11;

♦ - commercial tetragonal ZrO₂.

As seen from Table III.5, in the applied conditions without catalyst (blank test) there is no glucose conversion. Therefore, they are appropriate to evaluate the catalytic activity of the applied solids. Similarly, commercial [Si,Al]-MFI-c and synthesized [Si,Al]-MFI showed no glucose conversion even though both exhibited considerable amount of weak, medium-strong and even strong Lewis acid sites as seen in Table III.3. This might be originated from the synergetic effect of Brønsted-Lewis acid sites which apparently limits glucose isomerization in water. Nevertheless, similar negligible results over ZSM-5 zeolites in H⁺-form were reported by other authors [29,30].

Interestingly, the commercial tetragonal ZrO₂ was found to be also inactive for glucose isomerization, showing insignificant glucose conversion and no fructose formation under the applied conditions. As reported in Table III.3, t-ZrO₂ possesses mostly weak Lewis acid sites with a negligible number of medium-strong sites. As discussed in chapter I, glucose isomerization proceeds *via* the intramolecular hydride shift mechanism over Lewis acids. Therefore, this allows to make an intermediate conclusion that weak Lewis acid sites are incapable of this transfer. This could also explain the complete inactivity of the synthesized [Si,Zr]-MFI-in towards glucose isomerization. Indeed, once incorporated in the MFI framework, Zr generates weak Lewis acid sites which can be visualized when comparing [Si]-MFI and [Si,Zr]-MFI-in (Table III.3).

As it was discussed in chapter I, the average pore size associated with the MFI framework is around 0.51 nm x 0.55 nm which is somewhat smaller than the reported kinetic diameter of a glucose

molecule of ~0.8 nm [31]. Therefore, glucose transformation over MFI-type materials takes place mostly on the surface. Also, since Zr incorporation into the MFI framework does not favor glucose isomerization, it was decided to look for an alternative approach to make [Si,Zr]-MFI type catalyst active in the given reaction. The idea is built around the proton transfer mechanism catalyzed by basic sites to form fructose from glucose. In this regard, [Si,Zr]-MFI-ex could be a good catalyst for glucose isomerization due to its basic characteristics. As was discussed above (figure III-7), this solid mostly consists of pure SiO₂ crystals with an amorphous zirconium oxide phase deposited on its surface. In terms of its chemical properties, it has around two times less amount of Lewis acid sites (19 μmol·g⁻¹ vs 48 μmol·g⁻¹) as compared to [Si,Zr]-MFI-in. However, [Si,Zr]-MFI-ex exhibits a certain number of basic sites (34 μmol·g⁻¹) as confirmed by the CO₂-TPD measurement, being the only zeolitic material with basic properties presented in this work. This explains its high catalytic activity in the given conditions which is provided both by its basicity and the accessibility of its active sites for glucose molecules. The latter can be confirmed by the SEM-EDS elemental mapping presented in the figure annex-1 which clearly shows the presence of Na together with ZrO₂ amorphous phase on the surface of the SiO₂ crystals.

With this being said, [Si,Zr]-MFI-ex demonstrated 26 % glucose conversion and 25 % fructose yield (selectivity = 96 %) after 3 h of reaction at 120 °C. This agrees well with the results reported over cation-exchanged zeolites [32–35]. Also, it is comparable to the results published on the hierarchical micro/mesoporous NaY zeolites impregnated with 5 wt.% MgO, which showed a remarkable 100 % fructose selectivity at 34 % glucose conversion after 2 h of reaction at 100 °C [34]. So far, it is the highest reported activity among zeolites with basic sites. Although the applied temperature and reaction duration were higher in the present work, the catalyst-to-glucose ratio was considerably higher *i.e.* 1:11 vs 1:5 in the reference work [34]. Thus, there is still room to

further optimize the reaction conditions and therefore to increase glucose conversion and fructose yield over [Si,Zr]-MFI-ex. Additionally, the reported catalyst, 5 wt.% MgO impregnated NaY, exhibited $98 \mu\text{mol}\cdot\text{g}^{-1}$ basic sites as compared to the nearly 3 times less $34 \mu\text{mol}\cdot\text{g}^{-1}$ in [Si,Zr]-MFI-ex. This might indicate an easier accessibility of the active sites on the surface of the latter rather than in the micro/mesopores of 5 wt.%MgO/NaY.

Importantly, after the first catalytic run, [Si,Zr]-MFI-ex was recovered from the reaction mixture and regenerated by calcination at $550 \text{ }^\circ\text{C}$ for 3 hours. Upon such regeneration, the catalyst converted 24 % glucose and yielded $\sim 23 \%$ fructose (selectivity = 95 %) under the same reaction conditions. This suggests a good recyclability of the catalyst as well as a presumably low Na leaching from the composition. As shown before, Na is less prone to leaching as compared to other alkali and alkali-earth metals [32]. Although a long-run capability of regeneration is necessary to adequately assess the catalyst's reusability *i.e.* after at least 3 and ideally after 5 runs, the obtained results are promising and therefore should be further addressed. In the meantime, the structural integrity of [Si,Zr]-MFI-ex upon the first catalytic run and catalyst regeneration is retained as confirmed by XRD and ATR-IR spectroscopic analyses (figure III-12).

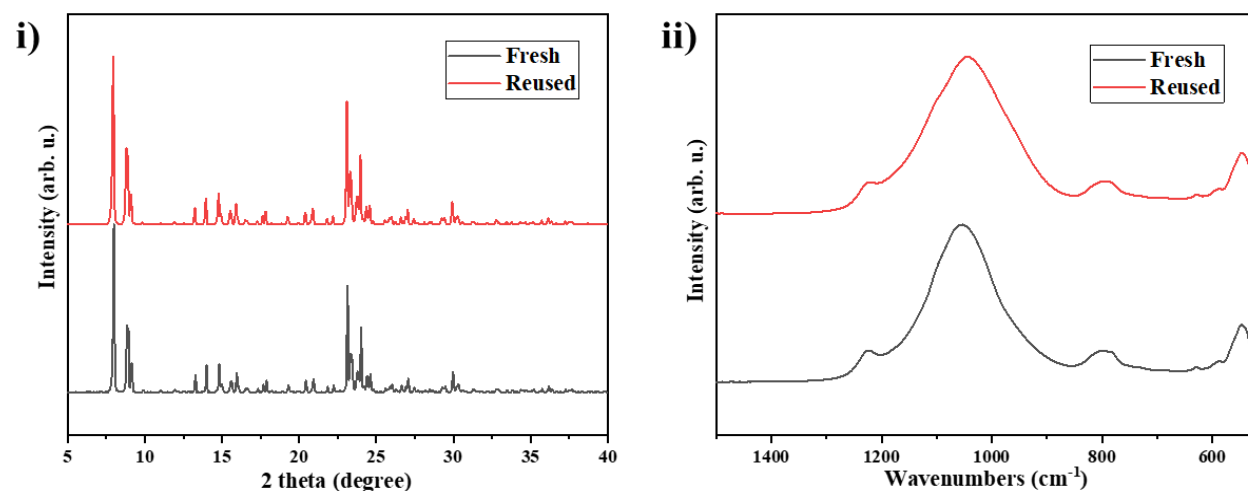


Figure III-12. XRD patterns (i) and ATR-IR spectra (ii) of the fresh and the reused [Si,Zr]-MFI-ex after regeneration at $550 \text{ }^\circ\text{C}$.

Considering the discussions above in this chapter, it is possible at this point to provide a hypothetical glucose isomerization scheme over [Si,Zr]-MFI-ex (figure III-13).

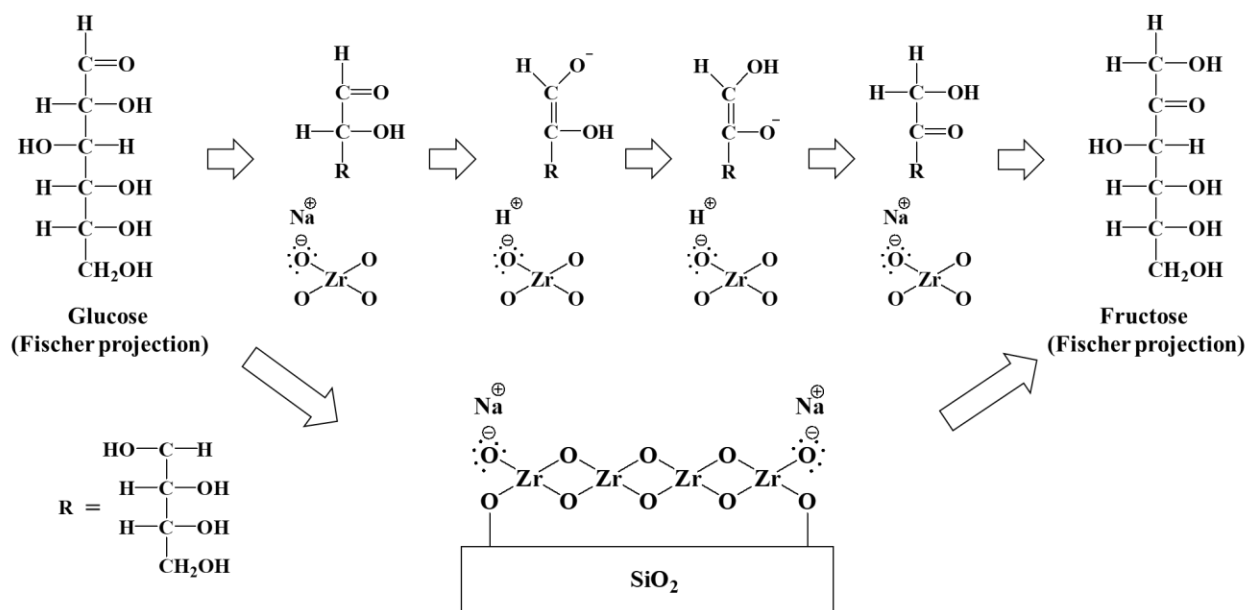


Figure III-13. Schematic representation of the proposed mechanism of glucose isomerization to fructose over [Si,Zr]-MFI-ex *via* the base-catalyzed "proton transfer" route.

Accordingly, the generation of basic sites is conditioned by the presence of Na⁺ which provides a saturation of lone pairs of electrons on oxygen atoms. The latter are readily available to be donated to a typical electron pair acceptor *i.e.* H⁺ originated from the C₂ of glucose in this case. This provokes a chain of intramolecular transformations leading to the displacement of the double bond from C₁ to C₂ position. In turn, this is followed by the H⁺ positioning at C₁ eventually leading to fructose formation. Lastly, the catalyst is recovered *via* the charge recompensation by Na⁺.

3. Conclusion

In summary, the zeolitic materials synthesized in this work exhibit structural, textural and morphological properties characteristic of MFI-type materials. Indeed, it is the case for [Si]-MFI and [Si,Al]-MFI known in the literature as Silicalite-1 and ZSM-5 zeolites, respectively. The latter, with a Si/Al molar ratio of 30, demonstrates three times lesser acid sites than the commercial ZSM-5 with a Si/Al molar ratio of 11, while their acid strength is proportionally higher. Besides, all characterization performed on [Si,Zr]-MFI-in suggest successful and homogeneous insertion of Zr heteroatoms within Si,Zr-MFI-in. [Si,Zr]-MFI-ex, however, is composed of amorphous ZrO₂ nanoparticles deposited on the surface of SiO₂ crystals. Indeed, the combination of bulk and surface characterization techniques provides valuable qualitative and quantitative information on heteroatoms in MFI-type zeolitic materials, including their location and distribution within the solids. For atoms such as Zr which present a challenging nucleus for solid-state NMR, such combination could be a possible way to examine whether or not the heteroatom is present in the MFI framework in a tetrahedral coordination. Importantly, it was shown that the presence of Zr in the MFI structure, indeed, generates weak Lewis acid sites when compared to [Si]-MFI. Thus, [Si,Zr]-MFI-in resulted in a higher amount of these weak Lewis sites as compared to [Si,Zr]-MFI-ex. The latter, in turn, additionally exhibited a certain number of basic sites due to the presence of Na used for its synthesis.

The catalytic performance of the synthesized zeolitic materials was investigated as well. This included the Brønsted acid catalyzed fructose dehydration to HMF and the Lewis acid (or base) catalyzed glucose isomerization to fructose. In accordance with the results reported in the literature, it was shown that the classical [Si,Al]-MFI zeolites exhibiting dual Brønsted-Lewis acid properties have considerably low activity towards fructose dehydration to HMF especially in

Chapter III – Conclusion

water. Same applies to the Zr-incorporated [Si,Zr]-MFI zeolites which is explained by the absence of Brønsted acid sites necessary for dehydration. Besides, the zeolite dissolution *via* acidic attack of the framework by side products, notably levulinic and formic acids, remains a problem. The latter is more pronounced when performing fructose dehydration in DMSO, a conventional solvent, leading to the complete zeolite dissolution. Besides, upon catalytic tests in DMSO, the activity of the zeolitic materials was found to be similar to the one shown by the solvent itself. This implies a negligible catalytic impact of the tested solids in the applied conditions. Therefore, the zeolitic materials examined in this thesis were found to be inappropriate for the use as solid catalysts for fructose dehydration.

In this regard, glucose isomerization into fructose seemed a better way to avoid the formation of aggressive side products as well as the dissolving effect of DMSO. As expected, the conventional [Si,Al]-MFI zeolites demonstrated no activity regardless of their considerable amount of strong Lewis acid sites. Interestingly, it was shown that Lewis acidic [Si,Zr]-MFI-in had insufficient acid strength to isomerize glucose, which can also be supported by the catalytic inactivity of the reference t-ZrO₂. Of note, the bulky glucose molecules can hardly diffuse within the porosity of the zeolite, thus making the active sites hardly reachable. Thus, a pertinent way to make the Zr presence in MFI zeolitic materials beneficial for isomerization is to generate basic sites which would be accessible for bulky glucose molecules. Indeed, such strategy resulted in [Si,Al]-MFI-ex which exhibited high activity in glucose isomerization with a remarkable 96 % fructose selectivity. Nevertheless, further optimization of the reaction conditions as well as the complete evaluation of its long-term activity should be critically studied. This needs to include more recycling tests (up to 5 cycles or until complete catalyst deactivation) with further characterization of structural and chemical integrity.

4. References:

- [1] Database of Zeolite Structures, (n.d.). <http://www.iza-structure.org/databases/>.
- [2] M. Rahm, R. Hoffmann, N.W. Ashcroft, Atomic and Ionic Radii of Elements 1 – 96, *Chem. Eur. J.* 22 (2016) 1–9. <https://doi.org/10.1002/chem.201602949>.
- [3] Database of Ionic Radii, (n.d.). <http://abulafia.mt.ic.ac.uk/shannon/ptable.php>.
- [4] D.H. Aguilar, L.C. Torres-Gonzalez, L.M. Torres-Martinez, A Study of the Crystallization of ZrO₂ in the Sol+Gel System: ZrO₂+SiO₂, *J. Solid State Chem.* 158 (2000) 349–357. <https://doi.org/10.1006/jssc.2001.9126>.
- [5] L. Kumari, W.Z. Li, Controlled Hydrothermal Synthesis of Zirconium Oxide Nanostructures and Their Optical Properties, *Cryst. Growth Des.* 9 (2009) 3874–3880. <https://doi.org/10.1021/cg800711m>.
- [6] Y. Tao, H. Kanoh, K. Kaneko, ZSM-5 Monolith of Uniform Mesoporous Channels, *J. Am. Chem. Soc.* 125 (2003) 6044–6045.
- [7] H. Zhang, L. Han, A. Duan, C. Xu, Z. Zhao, Y. Wei, G. Jiang, J. Liu, D. Wang, Z. Xia, Synthesis of micro-mesoporous materials ZSM-5/ FDU-12 and the performance of dibenzothiophene hydrodesulfurization, *RSC Adv.* 7 (2017) 28038. <https://doi.org/10.1039/C7RA03679E>.
- [8] J. Jiang, Y. Yang, C. Duanmu, Y. Xu, L. Feng, X. Gu, J. Chen, Preparation of hollow ZSM-5 crystals in the presence of polyacrylamide, *Microporous Mesoporous Mater.* 163 (2012) 11–20. <https://doi.org/10.1016/j.micromeso.2012.06.048>.
- [9] S.N. Basahel, T. Ali, M. Mokhtar, K. Narasimharao, Influence of crystal structure of nanosized ZrO₂ on photocatalytic degradation of methyl orange, *Nanoscale Res. Lett.* (2015) 73. <https://doi.org/10.1186/s11671-015-0780-z>.
- [10] Y. Yu, G. Xiong, C. Li, F. Xiao, Characterization of aluminosilicate zeolites by UV Raman spectroscopy, *Microporous Mesoporous Mater.* 46 (2001) 23–34.
- [11] C.G. Kontoyannis, M. Orkoulas, Quantitative determination of the cubic, tetragonal and monoclinic phases in partially stabilized zirconias by Raman spectroscopy, *J. Mater. Sci.* 29 (1994) 5316–5320.
- [12] M.G. Nijkamp, J.E.M.J. Raaymakers, A.J. Van Dillen, K.P. de Jong, Hydrogen storage using physisorption –materials demands, *Appl. Phys. A.* 72 (2001) 619–623.
- [13] X. Du, E. Wu, Porosity of microporous zeolites A, X and ZSM-5 studied by small angle X-ray scattering and nitrogen adsorption, *J. Phys. Chem. Solids.* 68 (2007) 1692–1699. <https://doi.org/10.1016/j.jpcs.2007.04.013>.
- [14] X. Huang, R. Wang, X. Pan, C. Wang, M. Fan, Y. Zhu, Y. Wang, J. Peng, Catalyst design strategies towards highly shape-selective HZSM-5 for para-xylene through toluene alkylation, *Green Energy Environ.* 5 (2020) 385–393. <https://doi.org/10.1016/j.gee.2019.12.001>.
- [15] C. Shao, X. Li, S. Qiu, F. Xiao, O. Terasaki, Size-controlled synthesis of silicalite-1 single

- crystals in the presence of benzene-1,2-diol, *Microporous Mesoporous Mater.* 39 (2000) 117–123.
- [16] M.K. Dongare, P. Singh, P.P. Moghe, P. Ratnasamy, Synthesis, characterization, and catalytic properties of [Zr]-ZSM-5, *Zeolites*. 11 (1991) 690–693.
- [17] X. Liu, Y. Sun, Effect of Ethanol on the Morphology and Textual Properties of ZSM-5 Zeolite, *Catalysts*. 10 (2020) 198.
- [18] Y. Xu, W. Lai, Y. Dong, Z. Chen, X. Yi, W. Fang, Internal defects-oriented dissolution: controllable evolution of hollow ZSM-5 nano-structures, *CrystEngComm*. 20 (2018) 5625–5631. <https://doi.org/10.1039/C8CE01105B>.
- [19] V. V Ordonsky, J. Van Der Schaaf, J.C. Schouten, T.A. Nijhuis, The effect of solvent addition on fructose dehydration to 5-hydroxymethylfurfural in biphasic system over zeolites, *J. Catal.* 287 (2012) 68–75. <https://doi.org/10.1016/j.jcat.2011.12.002>.
- [20] V. Rac, V. Rakic, D. Stošić, O. Otman, A. Auroux, Hierarchical ZSM-5, Beta and USY zeolites: Acidity assessment by gas and aqueous phase calorimetry and catalytic activity in fructose dehydration reaction, *Microporous Mesoporous Mater.* 194 (2014) 126–134. <https://doi.org/10.1016/j.micromeso.2014.04.003>.
- [21] P. Dornath, W. Fan, Dehydration of fructose into furans over zeolite catalyst using carbon black as adsorbent, *Microporous Mesoporous Mater.* 191 (2014) 10–17. <https://doi.org/10.1016/j.micromeso.2014.02.031>.
- [22] S. Despax, C. Maurer, B. Estrine, J. Le, N. Hoffmann, S. Marinkovic, J. Muzart, Fast and efficient DMSO-mediated dehydration of carbohydrates into 5-hydroxymethylfurfural, *Catal. Commun.* 51 (2014) 5–9. <https://doi.org/10.1016/j.catcom.2014.03.009>.
- [23] J. Zhao, C. Zhou, C. He, Y. Dai, X. Jia, Y. Yang, Efficient dehydration of fructose to 5-hydroxymethylfurfural over sulfonated carbon sphere solid acid catalysts, *Catal. Today*. 264 (2016) 123–130. <https://doi.org/10.1016/j.cattod.2015.07.005>.
- [24] J.S. Kruger, V. Choudhary, V. Nikolakis, D.G. Vlachos, Elucidating the Roles of Zeolite H-BEA in Aqueous-Phase Fructose Dehydration and HMF Rehydration, *ACS Catal.* 3 (2013) 1279–1291.
- [25] J.S. Kruger, V. Nikolakis, D.G. Vlachos, Aqueous-phase fructose dehydration using Brønsted acid zeolites: Catalytic activity of dissolved aluminosilicate species, *Appl. Catal. A, Gen.* 469 (2014) 116–123. <https://doi.org/10.1016/j.apcata.2013.09.030>.
- [26] R. Gounder, Hydrophobic microporous and mesoporous oxides as Brønsted and Lewis acid catalysts for biomass conversion in liquid water, *Catal. Sci. Technology*. 4 (2014) 2877. <https://doi.org/10.1039/c4cy00712c>.
- [27] P.A. Zapata, Y. Huang, M.A. Gonzalez-borja, D.E. Resasco, Silylated hydrophobic zeolites with enhanced tolerance to hot liquid water, *J. Catal.* 308 (2013) 82–97. <https://doi.org/10.1016/j.jcat.2013.05.024>.
- [28] L. Zhang, K. Chen, B. Chen, J.L. White, D.E. Resasco, Factors that Determine Zeolite Stability in Hot Liquid Water, *J. Am. Chem. Soc.* 137 (2015) 11810–11819. <https://doi.org/10.1021/jacs.5b07398>.

- [29] A.A. Marianou, C.M. Michailof, A. Pineda, E.F. Iliopoulou, K.S. Triantafyllidis, A.A. Lappas, Glucose to Fructose Isomerization in Aqueous Media over Homogeneous and Heterogeneous Catalysts, *ChemCatChem*. 8 (2016) 1100–1110. <https://doi.org/10.1002/cctc.201501203>.
- [30] S. Saravanamurugan, M. Paniagua, J.A. Melero, A. Riisager, Efficient Isomerization of Glucose to Fructose over Zeolites in Consecutive Reactions in Alcohol and Aqueous Media, *J. Am. Chem. Soc.* 135 (2013) 5246–5249.
- [31] S. Li, V.A. Tuan, J.L. Falconer, R.D. Noble, Separation of 1,3-propanediol from glycerol and glucose using a ZSM-5 zeolite membrane Shiguang, *J. Memb. Sci.* 191 (2001) 53–59.
- [32] C. Moreau, R. Durand, A. Roux, D. Tichit, Isomerization of glucose into fructose in the presence of cation-exchanged zeolites and hydrotalcites, *Appl. Catal. A Gen.* 193 (2000) 257–264.
- [33] I. Graça, D. Iruretagoyena, D. Chadwick, Glucose isomerisation into fructose over magnesium-impregnated NaY zeolite catalysts, *Appl. Catal. B Environ.* 206 (2017) 434–443. <https://doi.org/10.1016/j.apcatb.2017.01.037>.
- [34] I. Graça, M.C. Bacariza, A. Fernandes, D. Chadwick, Desilicated NaY zeolites impregnated with magnesium as catalysts for glucose isomerisation into fructose, *Appl. Catal. B Environ.* 224 (2018) 660–670. <https://doi.org/10.1016/j.apcatb.2017.11.009>.
- [35] I. Graça, M.C. Bacariza, D. Chadwick, Glucose isomerisation into fructose over Mg-impregnated Na-zeolites: Influence of zeolite structure, *Microporous Mesoporous Mater.* 255 (2018) 130–139. <https://doi.org/10.1016/j.micromeso.2017.07.015>.

Chapter IV
Properties and Catalytic Performance
of MOFs

Chapter IV

The present chapter concerns the results on characterization of the synthesized MOFs including the classical UiO-66 and its functionalized analogues: UiO-66-SO₃H, UiO-66-COOH, UiO-66-OH and UiO-66-NH₂. As it was briefly mentioned in chapter I, UiO-66 and its functionalized analogues are oftentimes synthesized in aggressive and toxic solvents such as DMF (*N,N*-dimethylformamide) and DMA (*N,N*-dimethylacetamide). This is especially the case of UiO-66 since its linker, terephthalic acid, is insoluble in most conventional solvents, therefore the use of either DMF or DMA is, for the moment, unavoidable for its synthesis. However, the direct synthesis of functionalized UiO-66 implies using functionalized linkers, for instance monosodium 2-sulfoterephthalic acid or 2-aminoterephthalic acid to insert sulfonic acid (-SO₃H) or amino (-NH₂) groups, respectively. These linkers are usually water-soluble and thus make possible the preparation of UiO-66-SO₃H and UiO-66-NH₂ without using aggressive solvents. Nevertheless, still, up to this point, DMF and DMA are oftentimes used for synthesis in most of the publications on functionalized UiO-66 MOFs. Therefore, in this chapter, a special care was given to establish green and reproducible routes towards the synthesis of functionalized UiO-66 MOFs, and to compare them to the traditional “DMF” route providing a detailed characterization and a further perspective to facilitate upscaling and shaping of the resulting solids.

Eventually, all synthesized MOFs were applied as solid catalysts in fructose dehydration to HMF and glucose isomerization to fructose and their performances were discussed accordingly.

1. Characterization of the Synthesized MOFs

1.1. UiO-66 and UiO-66-SO₃H by Traditional Way

1.1.1. Structural Properties (XRD)

As described in chapter II, UiO-66 and UiO-66-SO₃H were prepared following similar synthesis protocols, with the only difference being the linker used for preparation: terephthalic acid and monosodium 2-sulfoterephthalate, respectively [1–4]. Figure IV-1 (i) demonstrates the XRD patterns derived from the as-synthesized solids. It is clear that all of them exhibit well-distinguished reflections corresponding well to that of the simulated pattern. These include reflections at $\sim 7.4^\circ$ (111), $\sim 8.5^\circ$ (002), $\sim 12.0^\circ$ (022) and $\sim 25.7^\circ$ (006) [5,6]. Importantly, all reflections are retained upon functionalization of UiO-66 with monosodium 2-sulfoterephthalic acid with its content progressively increasing from 25 % (UiO-66-SO₃H-D-25) to 100 % (UiO-66-SO₃H-D-100). This suggests the preservation of the crystalline structure *i.e.* the UiO-66 framework topology upon insertion of -SO₃H groups as already reported [2,3]. Also, as described in the literature, the classical UiO-66 MOF exhibits a face-centered cubic (FCC) crystal system belonging to *Fm-3m* space group with $a = 20.7551(5) \text{ \AA}$ [1,7].

1.1.2. Structural Properties (ATR-IR)

Direct evidence of -SO₃H groups presence on the surface of MOFs is given by ATR-IR and shown in figure IV-1 (ii).

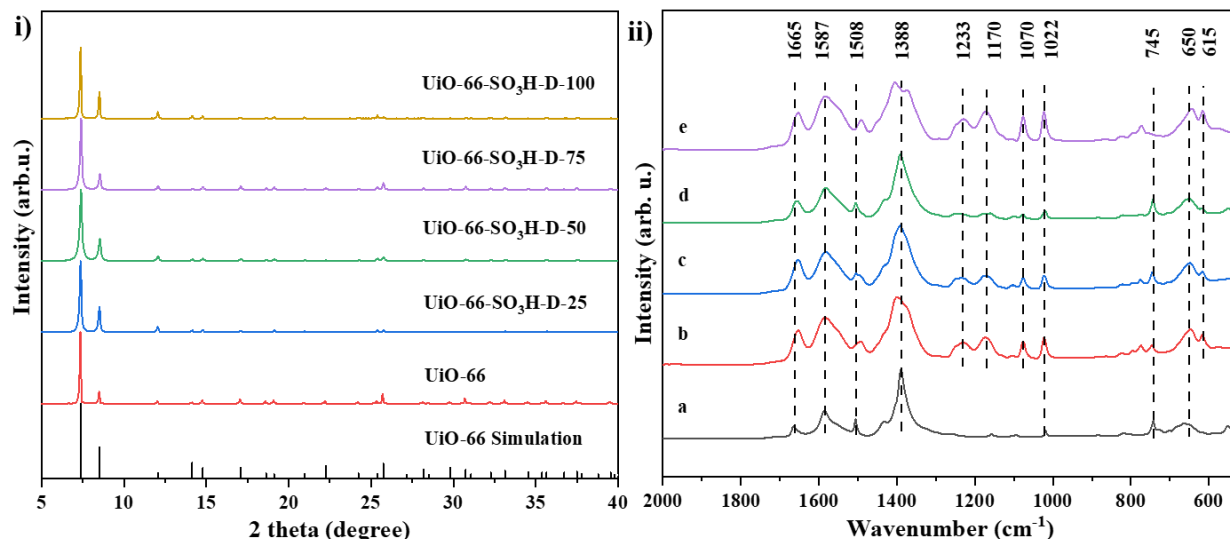


Figure IV-1. XRD patterns (i) of the as-synthesized UiO-66 and its sulfonic acid functionalized analogues as well as the simulated pattern of UiO-66 for comparison. Simulation was performed using the CIF file of UiO-66 provided in [7]. The intensities were normalized to the intensity of the reflection at $\sim 7.4^\circ$. ATR-IR spectra (ii) of the synthesized MOFs: UiO-66 (a), UiO-66-SO₃H-D-25 (b), UiO-66-SO₃H-D-50 (c), UiO-66-SO₃H-D-75 (d) and UiO-66-SO₃H-D-100 (e). The band intensities were normalized to the intensity of the band at ~ 1388 cm⁻¹.

Firstly, the bands corresponding to the principal vibrations of the UiO-66 framework are present in all the studied solids. Namely, the IR bands at ~ 1388 cm⁻¹ and ~ 1587 cm⁻¹ are characteristic of symmetric and asymmetric stretching mode of $\nu(\text{O-C-O})$ in the terephthalate linker, respectively. The small IR band at ~ 1508 cm⁻¹ stem from $\nu(\text{C=C})$ of the benzene ring while the band at ~ 1022 cm⁻¹ is originated from the aromatic ring breathing. Moreover, the bands below 1000 cm⁻¹ correspond to a combination of vibrations: C-H (~ 745 cm⁻¹) and $\mu_3\text{-O}$ (~ 650 cm⁻¹) stretching [1,8–10]. Importantly, all the functionalized UiO-66-SO₃H-D exhibit additional IR bands that correspond to S-O vibrations (~ 615 cm⁻¹ and ~ 1070 cm⁻¹) and S=O vibrations (~ 1170 cm⁻¹ and 1233 cm⁻¹) which provide a clear evidence of the framework functionalization [2,11]. Importantly, there is also an IR band corresponding to C=O stretching (~ 1665 cm⁻¹) in all synthesized MOFs. Despite a rigorous activation step, carbonyl groups are typically associated with the presence of residual DMF in the pores [9].

1.1.3. Textural Properties (N₂ physisorption)

Figure IV-2 represents the N₂ physisorption isotherms recorded for the series of as-synthesized solids. As evident, UiO-66 and UiO-66-SO₃H-D-100 exhibit classical Type I isotherms with a characteristic sharp N₂ uptake at low relative pressures ($p/p_0 < 0.2-0.3$) and a pronounced plateau region at higher relative pressures ($p/p_0 > 0.3$). This plateau region is more evident in UiO-66 and UiO-66-SO₃H-D-100 whereas UiO-66-SO₃H-D-25, UiO-66-SO₃H-D-50 and UiO-66-SO₃H-D-75 exhibit a hysteresis of type H4 taking place at $p/p_0 > 0.45$. Usually, the presence of the latter is an indication of mesoporosity *i.e.* the pores with a diameter between 2 and 50 nm [12]. This can be attributed to structural defects within the framework originated from missing linkers for which UiO-66 is well-known [13,14]. The exclusive presence of such hysteresis in the partially functionalized UiO-66-SO₃H-D (with 25 %, 50% and 75 % loading) might be explained by the presence of both linkers: terephthalate and 2-sulfoterephthalate which apparently provide different crystallization rates resulting in more defective frameworks. Nevertheless, all the five synthesized solids exhibit large surface areas which decreases with increasing the sulfonic acid groups loading. The latter is well explained by the volume occupied by the bulky -SO₃H groups within the porosity (Table IV.1).

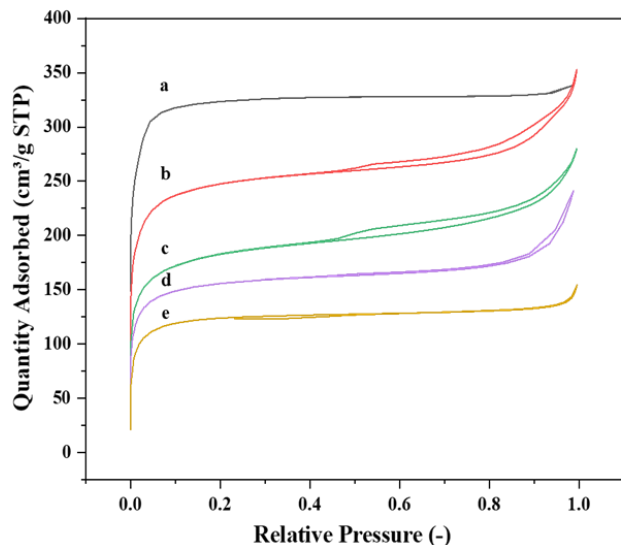


Table IV.1 – Textural properties of the synthesized MOFs.

Sample	S_{BET} , $\text{m}^2\cdot\text{g}^{-1}$	Pore volume, $\text{cm}^3\cdot\text{g}^{-1}$	
		Micro ^a	Total ^b
UiO-66	1287	0.53	0.54
UiO-66-SO ₃ H-D-25	935	0.37	0.49
UiO-66-SO ₃ H-D-50	670	0.25	0.40
UiO-66-SO ₃ H-D-75	592	0.20	0.24
UiO-66-SO ₃ H-D-100	474	0.13	0.16

a – calculated by the *t*-plot method;

b – using the adsorption branch at $p/p_0 \sim 0.99$.

Figure IV-2. N₂ physisorption isotherms of the synthesized MOFs: UiO-66 (a), UiO-66-SO₃H-D-25 (b), UiO-66-SO₃H-D-50 (c), UiO-66-SO₃H-D-75 (d) and UiO-66-SO₃H-D-100 (e).

1.1.4. Morphological Properties (SEM)

The shape and size of the synthesized MOF crystals were evaluated by SEM, and representative micrographs are depicted in figure IV-3. Accordingly, the classical UiO-66 exhibits well defined octahedrally shaped crystals with a mean size of ~200 nm (figure IV-3, a) in agreement with other reports [15,16]. It is clear that upon insertion of sulfonic acid groups the crystals undergo shape distortion which can be seen in figure IV-3 (b) for UiO-66-SO₃H-D-25. This becomes more evident upon further increase of the functionalization degree from 25 % to 100 %, as the crystals lose completely their shape and grow into aggregates of various size and shape (figure IV-3, c-e). In turn, this once again might suggest a different nucleation and crystal growth mechanism of the functionalized UiO-66 when using monosodium 2-sulfoterephthalate linker as compared to the classical UiO-66 with terephthalic acid [2,4].

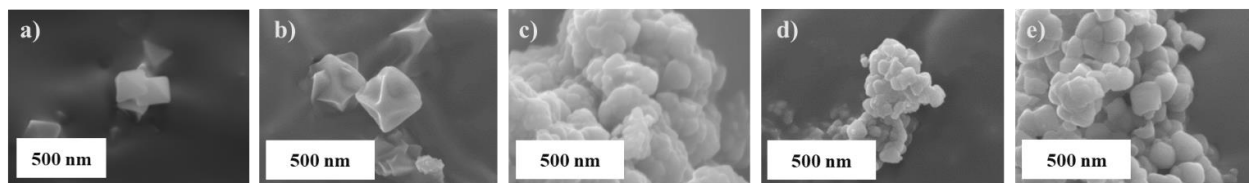


Figure IV-3. SEM images of UiO-66 (a), UiO-66-SO₃H-D-25 (b), UiO-66-SO₃H-D-50 (c), UiO-66-SO₃H-D-75 (d) and UiO-66-SO₃H-D-100 (e); scale bars: 500 nm.

At the light of these first characterizations, it is possible to conclude that functionalization of the UiO-66 framework with -SO₃H sulfonic acid groups leads to preservation of the crystallographic properties of the pristine UiO-66. Additionally, it was shown that insertion of bulky -SO₃H groups leads to a drastic decrease of the textural properties of the microporous hybrid solids. Besides, we clearly observe a modification of the crystal morphology, from an octahedral shape to aggregated particles poorly defined. Critically, in spite of several consecutive solvent exchange steps to wash away residual DMF, it is still found in all synthesized solids. As will be discussed in the next chapter, it could negatively affect the catalytic performance of the functionalized MOFs and therefore alternative routes without using DMF are of particular interest.

1.2. UiO-66-SO₃H, UiO-66-COOH, UiO-66-OH and UiO-66-NH₂ Green Way

The use of aggressive and toxic solvents such as DMF have considerable negative impact on the environment and public health. Specifically, DMF is classified as toxic to reproduction, acute toxicant (inhalation and dermal route) and as an eye irritant in accordance with Regulation (EC) No 1272/2008 of the European Parliament and of the Council of 16 December 2008. Moreover, there are studies claiming that DMF is responsible for severe liver damages upon exposure provoking hepatitis and cancer [17]. In 2021, the European Commission adopted a regulation amending Annex XVII of REACH (Registration, Evaluation, Authorisation and Restriction of Chemicals) to ban DMF from the EU market starting from December 2023. Therefore, there is an

urgent need to find replacements of solvents as DMF in order to enable sustainable MOF production.

In response to this need for avoiding the use of DMF, a series of functionalized MOFs were synthesized using water as the solvent. This includes UiO-66-SO₃H-W (“W” standing for “water”), UiO-66-COOH, UiO-66-OH, and UiO-66-NH₂. Detailed characterization of these MOFs is presented below.

1.2.1. Structural Properties (XRD)

Figure IV-4 demonstrates the XRD patterns of the synthesized functionalized MOFs. As one can notice, they are all well crystallized solids exhibiting well-defined reflections. More precisely: UiO-66-COOH, UiO-66-OH and UiO-66-NH₂ exhibit similar diffraction patterns which correspond to the one of the simulated UiO-66 (figure IV-4, i). This suggests preservation of the UiO-66 framework topology upon functionalization under the given conditions with -COOH, -OH and -NH₂ groups, respectively. At a closer look on the principle reflections at ~7.4 ° and ~8.5 °, one can notice their certain broadening in UiO-66-OH and UiO-66-NH₂ which might suggest a smaller crystal size as compared to UiO-66-COOH. Interestingly, UiO-66-SO₃H-W demonstrated a variety of newly observed reflections in addition to the ones present in the simulated pattern of the classical UiO-66, especially at 2 theta angles lower than 8 ° (figure IV-4, ii). This phenomenon implies certain changes of the crystallographic properties and originates from X-Rays diffracted from planes with a large interplanar distance, d . Indeed, according to the Bragg's law ($n\lambda = 2d\sin\theta$ *i.e.* $2d = n\lambda \cdot \sin^{-1}\theta$), higher values of d causes smaller θ angles.

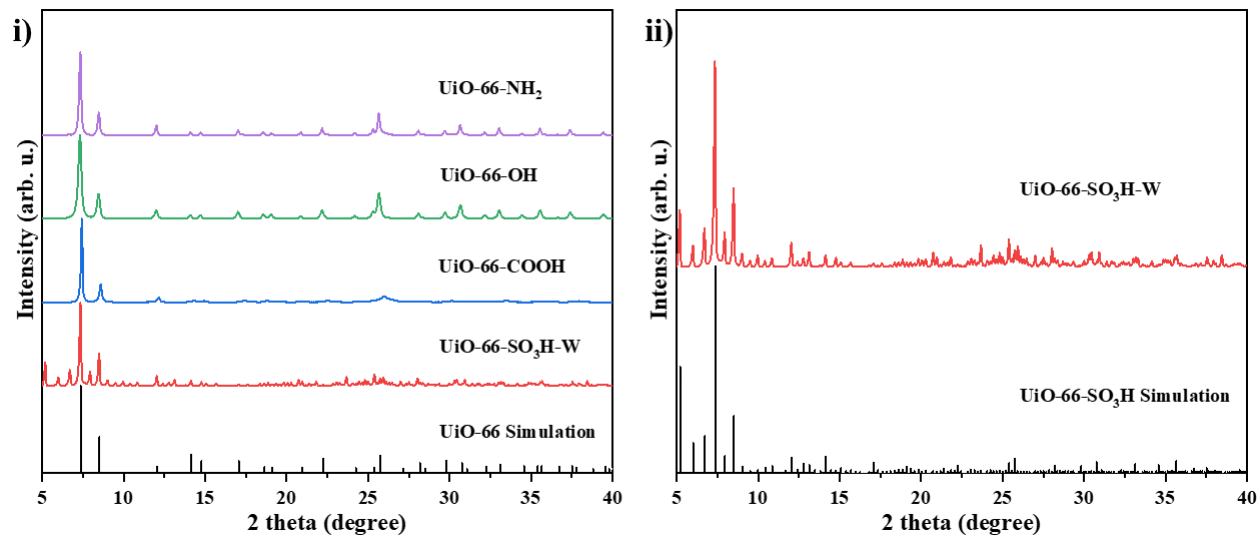


Figure IV-4. XRD patterns (i) of a series of MOFs synthesized in water as compared to the simulated pattern of UiO-66; simulation was performed using the CIF file of UiO-66 provided in [7]. XRD patterns (ii) of UiO-66-SO₃H-W and its simulation made using the CIF file provided in [18]. The intensities were normalized to the intensity of the reflection at ~7.4 °.

In other words, when prepared in water, UiO-66-SO₃H-W exhibits increased unit cell parameters as compared to UiO-66-SO₃H-D and the classical UiO-66. This was first mentioned a few years ago by Juan-Alcaniz *et al.* [19] and studied in more detail by Taylor *et al.* [18]. Accordingly, it was shown that UiO-66-SO₃H-W experienced remarkable structural defects viewed as a high number of missing linkers resulting in Zr-clusters connected mostly by 8 linkers and not 12 as in the case of the classical UiO-66 (figure IV-5). Importantly, 12 and 8 linkers in UiO-66-SO₃H-W result in $Zr_6O_4(OH)_4[C_6H_3(COO)_2SO_3H]_6$ and $Zr_6O_4(OH)_4[C_6H_3(COO)_2SO_3H]_4$ molecular formulas, respectively, as each linker coordinates to 2 neighboring $Zr_6O_4(OH)_4$ clusters.

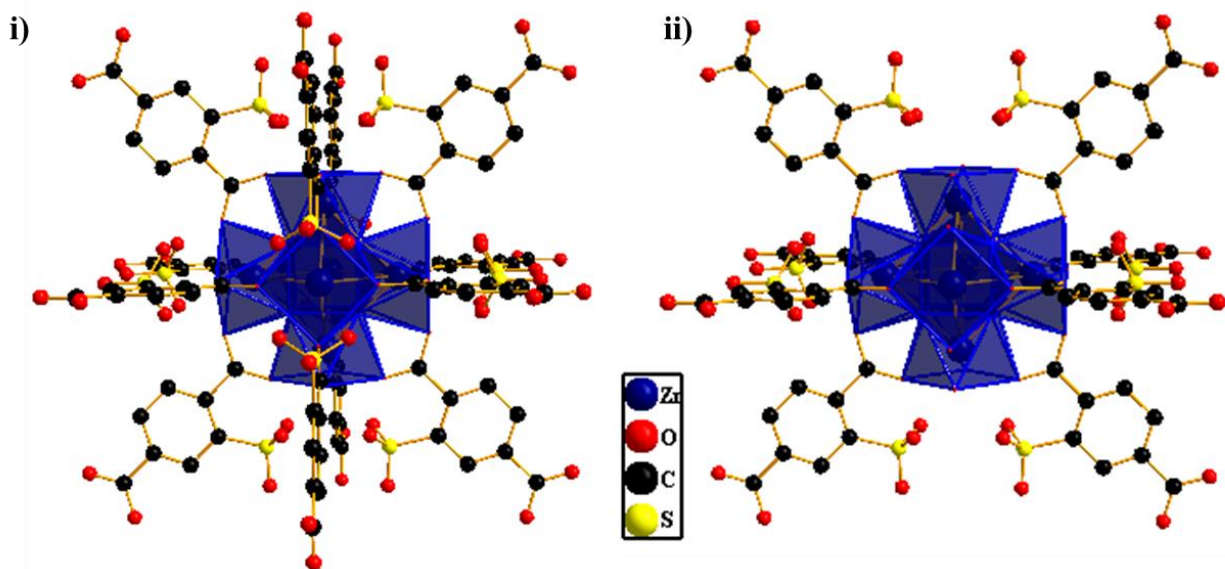


Figure IV-5. Schematic representation of the Zr-cluster (blue polyhedra) connected by 12 (i) and 8 (ii) sulfoterephthalic acid linkers in UiO-66-SO₃H. Hydrogen atoms are omitted for simplicity.

These structural defects are at the origin of a twofold increase of the unit cell volume and therefore lowering the crystallographic symmetry resulting in a body-centered cubic system ($Im-3$ with $a = 41.4440(8)$ Å) as compared to the face-centered cubic system in UiO-66 made in DMF ($Fm-3m$ with $a = 20.7809(3)$ Å) as depicted in figure annex-2. Indeed, as seen in figure IV-4 (ii), the experimental pattern of UiO-66-SO₃H-W fits well the one simulated for the $Im-3$ system with the doubled unit cell parameter, a . This suggests that UiO-66-SO₃H-W undergoes a structural change and does not preserve the intrinsic framework topology of UiO-66. Therefore, some authors attributed a different name to UiO-66-SO₃H-W: NUS-6 (National University of Singapore) [20]. Nevertheless, this particular MOF is surprisingly rarely described in the literature therefore underlining the need to contribute to its study.

1.2.2. Structural Properties (ATR-IR Spectroscopy)

The ATR-IR spectra collected on the synthesized solids are depicted in figure IV-6. As it can be seen, all the bands characteristic of the UiO-66 framework are present in all the 4 depicted spectra

as it was discussed in more detail above. Briefly, these include the bands at 652 cm^{-1} , 766 cm^{-1} , 1392 cm^{-1} , 1502 cm^{-1} and 1595 cm^{-1} (figure IV-6, i). Clearly, UiO-66-SO₃H-W exhibits S-O ($\sim 615\text{ cm}^{-1}$ and $\sim 1070\text{ cm}^{-1}$) and S=O vibrations ($\sim 1170\text{ cm}^{-1}$ and 1233 cm^{-1}) confirming the presence of -SO₃H groups. In contrast, functionalization in UiO-66-COOH and UiO-66-OH is somewhat less evident as both -COOH and -OH groups are present in the classical *i.e.* non-functionalized UiO-66 and represent a broad band at $>3000\text{ cm}^{-1}$ (figure IV-6, ii). In this region, two weak contributions from -NH₂ (at $\sim 3375\text{ cm}^{-1}$ and $\sim 3480\text{ cm}^{-1}$) can be seen in the spectrum of UiO-66-NH₂ which demonstrates its functionalization.

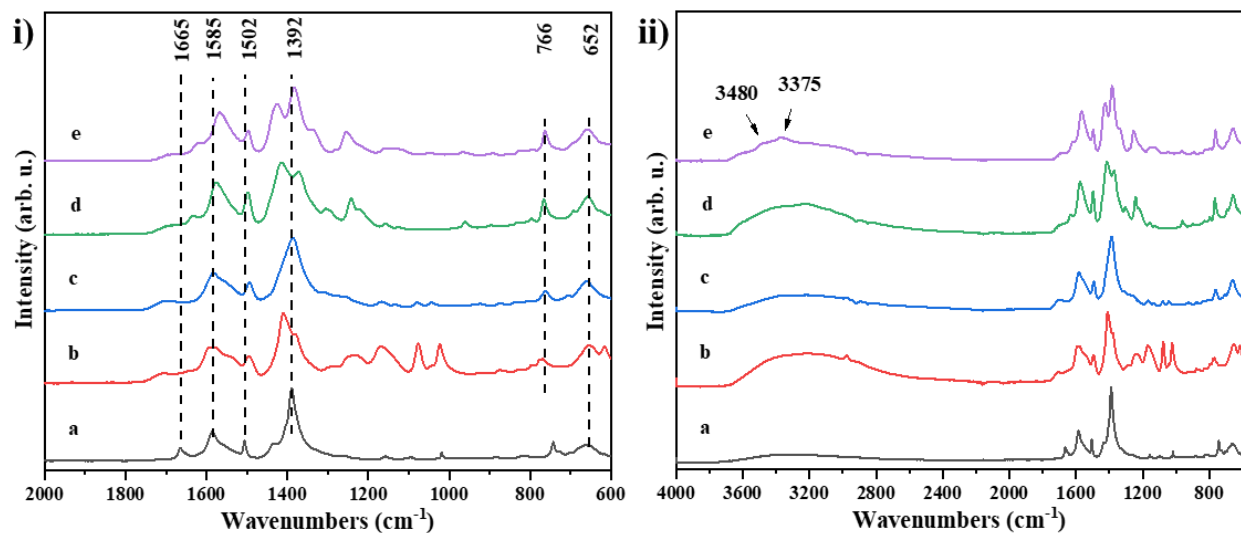


Figure IV-6. ATR-IR spectra of a zoomed (i) and the global area (ii) recorded for UiO-66 (a), UiO-66-SO₃H-W (b), UiO-66-COOH (c), UiO-66-OH (d) and UiO-66-NH₂ (e).

Importantly, the band at $\sim 1665\text{ cm}^{-1}$ attributed to the carbonyl group in DMF is logically absent in all MOFs prepared in water.

1.2.3. Textural Properties (*N*₂ physisorption)

Figure IV-7 depicts the N₂ physisorption isotherms recorded on the synthesized MOFs and representing their porous nature. Accordingly, all 4 solids exhibit Type I isotherms characterizing

purely microporous materials. An increased N_2 uptake at relative pressure above 0.9 represent nitrogen condensation in interparticle voids. As a result, all studied solids possess high surface area and micropore volume (Table IV.2) which, however, experienced a considerable drop as compared to the classical UiO-66 ($1287 \text{ m}^2 \cdot \text{g}^{-1}$ and $0.53 \text{ cm}^3 \cdot \text{g}^{-1}$, Table IV-1). Once again, this drop is due to the presence of functional groups ($-\text{SO}_3\text{H}$, $-\text{COOH}$, $-\text{OH}$ and NH_2) in the framework causing a partial pore blocking.

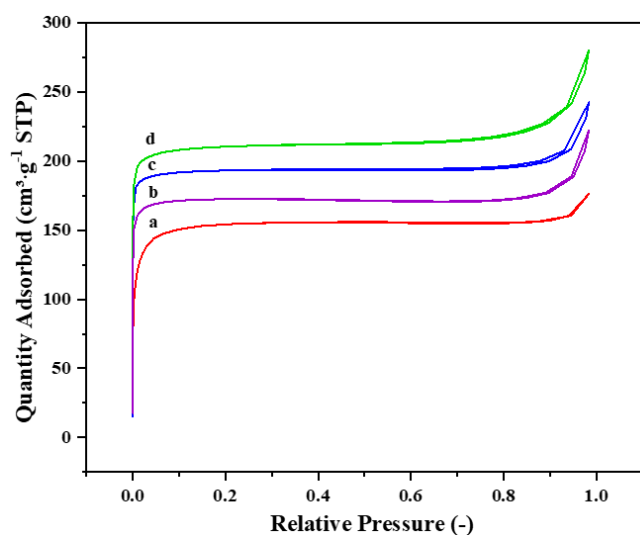


Table IV.2 – Textural properties of the synthesized MOFs.

Sample	S_{BET} , $\text{m}^2 \cdot \text{g}^{-1}$	Pore volume, $\text{cm}^3 \cdot \text{g}^{-1}$	
		Micro ^a	Total ^b
UiO-66- SO_3H -W	639	0.26	0.27
UiO-66-COOH	773	0.29	0.38
UiO-66-OH	709	0.26	0.34
UiO-66- NH_2	797	0.31	0.42

a – calculated by the *t*-plot method;

b – using the adsorption branch at $p/p_0 \sim 0.99$.

Figure IV-7. N_2 physisorption isotherms of the synthesized MOFs: UiO-66- SO_3H -W (a, offset: 0), UiO-66- NH_2 (b, offset 0), UiO-66-COOH (c, offset: $+5 \text{ cm}^3 \cdot \text{g}^{-1}$ STP), UiO-66-OH (d, offset: $+10 \text{ cm}^3 \cdot \text{g}^{-1}$ STP).

Of note, UiO-66- SO_3H -W prepared in water exhibited higher surface area and micropore volume ($639 \text{ m}^2 \cdot \text{g}^{-1}$ and $0.26 \text{ cm}^3 \cdot \text{g}^{-1}$) as compared to its analogue prepared in DMF ($474 \text{ m}^2 \cdot \text{g}^{-1}$ and $0.13 \text{ cm}^3 \cdot \text{g}^{-1}$) showing also the positive impact of the structural changes implied by water as solvent on the textural properties of the resulted MOFs.

1.2.4. Thermal Stability (TGA)

Thermal stability of MOFs is a crucial feature oftentimes defining their final application.

Figure IV-8 (i) represents the TGA profiles of the synthesized MOFs, which correspond well to

the ones reported in the literature [21,22]. It is evident that all of them exhibit a similar behavior characterized by the following steps: 1) loss of the solvent and physisorbed species up to 100-150 °C; 2) loss of chemisorbed molecules *i.e.* cluster dehydration between 150 °C and 300 °C and 3) linker decomposition above 300 °C leading to a residual zirconium oxide-like compound at temperatures above 500 °C (figure IV-8, ii). As evident, the sharp weight decrease associated with linker decomposition starts at relatively lower temperature (~350 °C) in UiO-66-OH and UiO-66-NH₂ as compared to ~400 °C, 450 °C and ~500 °C in UiO-66-COOH, UiO-66-SO₃H-W and UiO-66, respectively. This is due to the lower decomposition temperatures of the corresponding functionalized linkers as compared to terephthalic acid [21].

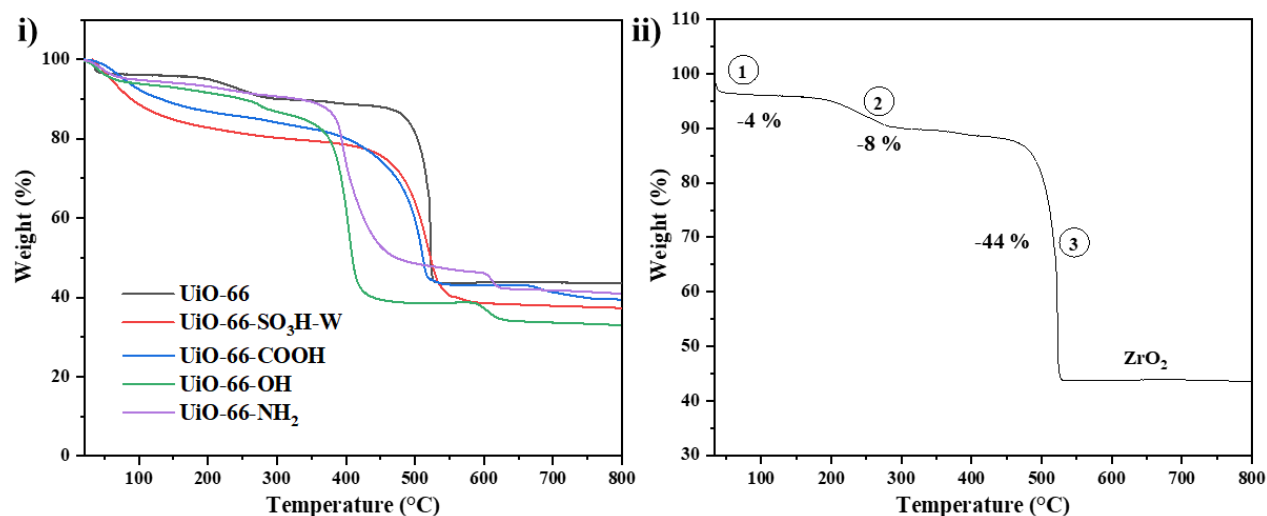


Figure IV-8. TGA profiles of the synthesized MOFs (i) and UiO-66 (ii) to demonstrate the typical decompositions steps.

With this being said, it is possible to establish thermal stability of the MOFs increasing in the following order: UiO-66-OH < UiO-66-NH₂ < UiO-66-COOH < UiO-66-SO₃H-W < UiO-66. Lastly, TGA allows for an estimation of the number of missing linkers by examining the weight loss corresponding to the linker's decomposition as described by Shearer *et al.* [23,24]. As an example, this concerns the area in the TGA profile of UiO-66 (figure IV-8, ii) from ~475 °C to

550 °C and represents ~44 % weight loss. Based on $Zr_6O_4(OH)_4[C_6H_4(COO)_2]_6$ molecular formula, one terephthalate linker represents ~10 % of the total mass while 6 of them represent ~59 %. Therefore, the difference of ~15 % (59 % - 44 %) allows to estimate around 1 missing linker in UiO-66 (Table IV.3).

Table IV.3 – Number of missing linkers estimated by TGA and Zr/S ratio in UiO-66-SO₃H-W.

Sample	Zr/S atomic ratio		Missing linkers per Zr-cluster ^c
	ICP ^a	XPS ^b	
UiO-66	-	-	0.9
UiO-66-SO ₃ H-W	1.41	1.46	2.3
UiO-66-COOH	-	-	1.5
UiO-66-OH	-	-	0.7
UiO-66-NH ₂	-	-	1.0

a – derived from ICP-OES;

b – derived from XPS using Zr 3d and -SO₃H component from S 2p spectra.

c – estimated by TGA.

1.2.5. Elemental Analysis (CHNS)

Table IV.4 represents the composition of the organic part constituting the synthesized MOFs. As can be seen, the analyzed amount of C is somewhat less than the theoretical ones thus suggesting missing linkers correlating with the TGA results. The latter is more pronounced in UiO-66-SO₃H-W (experimental 20.6 wt.% vs theoretical 26.9 wt.%) which implies a more drastic number of missing linkers. This statement can be further supported by the decreased amount of sulfur which is 1.5 times lower than expected (6.2 wt.% vs 9.0 wt.%). At the same time, an increased percentage of H in all solids might be due to the presence of physisorbed water, as they were not thermally treated prior to the experiment.

Table IV.4 – Elemental analysis of the organic part of the synthesized MOFs.

Sample	Elements for quantification							
	C, wt.%		H, wt.%		N, wt.%		S, wt.%	
	Th.	Exp.	Th.	Exp.	Th.	Exp.	Th.	Exp.
UiO-66*	34.6	33.2	1.7	2.1	-	-	-	-
UiO-66-SO ₃ H-W [♦]	26.9	20.6	1.3	3.2	-	-	9.0	6.2
UiO-66-COOH [•]	33.6	29.5	1.3	3.6	-	-	-	0.3
UiO-66-OH [■]	32.8	30.7	1.4	2.8	-	-	-	0.3
UiO-66-NH ₂ [▲]	32.9	29.0	1.7	3.1	4.8	3.9	-	0.2

* based on $Zr_6O_4(OH)_4[C_6H_4(COO)_2]_6$ molecular formula;

♦ based on $Zr_6O_4(OH)_4[C_6H_3(COO)_2SO_3H]_6$ molecular formula;

• based on $Zr_6O_4(OH)_4[C_6H_3(COO)_2COOH]_6$ molecular formula;

■ based on $Zr_6O_4(OH)_4[C_6H_3(COO)_2OH]_6$ molecular formula;

▲ based on $Zr_6O_4(OH)_4[C_6H_3(COO)_2NH_2]_6$ molecular formula.

Lastly, a certain amount of sulfur observed in UiO-66-COOH, UiO-66-OH and UiO-66-NH₂ is due to the Zr-sulfate used for the synthesis and probably still present in the cluster.

1.2.6. Surface Properties and Elemental Composition (XPS)

Complementary analysis of the elemental composition of UiO-66-SO₃H-W was performed by means of XPS (figure IV-9). As indicated by the positions of the photopeaks, one can clearly see the presence of all the targeted elements in UiO-66-SO₃H-W (figure IV-9, i). Interestingly, there are two contributions to the S 2p signal (figure IV-9, iii). One of them is shifted towards lower binding energies with its 2p_{3/2} signal centered at 166 eV and the other exhibits a shift towards higher binding energies with the 2p_{3/2} signal centered at 168 eV. The latter can be attributed to the sulfur species originated from the linker and therefore constituting the -SO₃H groups of interest (noted “Link” in the spectra) [25]. This signal was therefore used for quantification to estimate the Zr/S atomic ratios (Table IV.3). Concerning the S 2p signal with lowered binding energy, this might be due to S species bound directly to the Zr-clusters (noted “Clus” in the spectra) and related to the S found in UiO-66-COOH, UiO-66-OH and UiO-66-NH₂ after the CHNS analyses as mentioned above. The presence of such “cluster” S-species is observed in small amounts in the

spectra of UiO-66 (figure annex-3) although no sulfoterephthalate linker nor Zr-sulfate precursor were used. Hence, they are considered as an impurity.

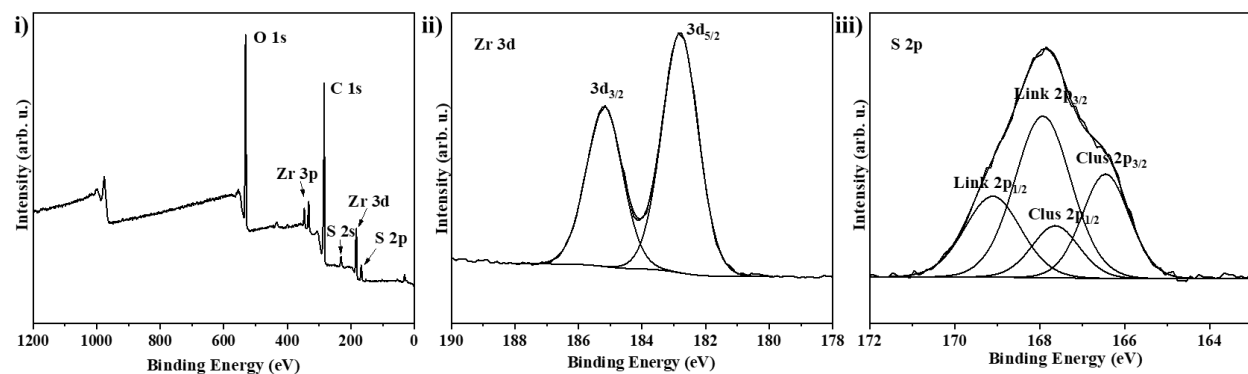


Figure IV-9. XPS survey spectrum (i) of UiO-66-SO₃H-W as well as its Zr 3d (ii) and S 2p (iii) signals.

Lastly, no sodium was detected in UiO-66-SO₃H-W implying the complete *in-situ* -SO₃Na to -SO₃H ion-exchange during synthesis generating Brønsted acid sites.

According to Table IV.3, the classical UiO-66 exhibited around one missing terephthalate linker per Zr-cluster. This observation is also valid for UiO-66-OH and UiO-66-NH₂, while UiO-66-COOH presents a slightly more defective framework with 1.5 (25 %) missing linkers. Importantly, UiO-66-SO₃H-W exhibits approximately 2.3 (38 %) missing ligands per cluster as estimated by TGA, suggesting that less than 4 coordinated sulfoterephthalate linkers per Zr₆O₄(OH)₄ cluster. The latter is further supported by ICP elemental analysis according to which UiO-66-SO₃H-W exhibits 1.41 zirconium atoms per sulfur atom, which implies approximately 4 sulfoterephthalate linkers per Zr₆O₄(OH)₄ cluster. Similarly, XPS suggests a Zr/S atomic ratio of 1.46 which is in good accordance with that derived from ICP. All of these observations are in line with previous reports [18]. With this being said, it is possible to derive the simplified Zr₆O₄(OH)₄[C₆H₃(COO)₂SO₃H]₄ molecular formula for UiO-66-SO₃H-W as compared to the theoretical Zr₆O₄(OH)₄[C₆H₃(COO)₂SO₃H]₆.

2. Catalytic Tests

2.1. Fructose Dehydration on MOFs

As in the case of zeolites discussed in chapter III, the evaluation of activities of MOFs in fructose dehydration started with establishing the appropriate conditions. Hence, Table IV.5 demonstrates preliminary results of the tests performed over a series of MOFs in water. As can be seen, after 2 h of reaction, no considerable fructose conversion was observed with the maximum reached over UiO-66-SO₃H-W providing rather a low selectivity towards HMF of (~13 %) at 23 % fructose conversion. The other examined MOFs resulted in poor performances which are well in line with the low conversion and selectivity obtained over zeolites discussed in chapter III, confirming the inhibiting role of water in fructose dehydration.

Table IV.5 – Fructose conversion and HMF yield over a series of MOFs.

Catalyst	T, °C	t, h	Solvent	Fr. conv., %	HMF y-d, %	HMF sel., %
Blank	100	2	H ₂ O	5	0	0
UiO-66	100	2	H ₂ O	0	0	0
UiO-66-SO ₃ H-D-100	100	2	H ₂ O	15	<2	<13
UiO-66-SO ₃ H-W	100	2	H ₂ O	23	<3	<13
UiO-66-COOH	100	2	H ₂ O	0	0	0

Reaction conditions: P_{atm}, 600 rpm, V_{solv} = 2 mL, C_{fructose} = 0.6 mM, m_{cat} = 20 mg.

As reported in chapter I (Table I.5), several functionalized Zr-based MOFs exhibit a good activity in water solvent. For instance, UiO-66-(COOH)₂ demonstrate 60 % fructose conversion with 68 % HMF selectivity after 3 h, however at 140 °C [26]. Thus, the relatively weak performance of the MOFs examined above might be explained by the lower applied temperature.

H₂O/ethanol solvent system was then employed in attempt to increase HMF selectivity and therefore find a more appropriate solvent. The results were similar to the ones obtained over the zeolites demonstrating no fructose conversion and HMF yield after 2 h of reaction at 100 °C. Following these first negative results, DMSO was further used as the solvent to evaluate catalytic performance of the synthesized MOFs. Table IV.6 shows the preliminary results upon tests for 2 h at 100 °C.

Table IV.6 – Fructose conversion and HMF yield over a series of functionalized MOFs.

Catalyst	T, °C	t, h	Solvent	Fr. conv., %	HMF y-d, %	HMF sel., %
Blank	100	2	DMSO	82	45	54
UiO-66	100	2	DMSO	87	51	59
UiO-66-SO ₃ H-D-25	100	2	DMSO	74	43	58
UiO-66-SO ₃ H-D-50	100	2	DMSO	75	38	51
UiO-66-SO ₃ H-D-75	100	2	DMSO	85	43	51
UiO-66-SO ₃ H-D-100	100	2	DMSO	97	64	66
UiO-66-SO ₃ H-W	100	2	DMSO	>99	73	73
UiO-66-COOH	100	2	DMSO	82	43	52

Reaction conditions: P_{atm}, 600 rpm, V_{solv} = 2 mL, C_{fructose} = 0.6 mM, m_{cat} = 20 mg.

As mentioned briefly in chapter III, DMSO is well known for its activity in fructose dehydration [27–30]. In the applied conditions, DMSO alone (blank test) yields 45 % HMF at 82 % fructose conversion after 2 h of reaction at 100 °C. Indeed, recent studies showed that its catalytic activity is provided by the valence unsaturation of both S and O atoms resulting in an electron-rich double bond [31]. The latter acts as a donor of an electron pair and therefore enables fructose dehydration *via* deprotonation. The activity of DMSO is even higher in the presence of oxygen due to formation of the [O₂ : DMSO] complex as compared to the inert N₂ atmosphere. Therefore, the results obtained herein are in line with the reported 70 % fructose conversion after 3 h at 100 °C in DMSO

alone [32]. This underlines the positive effect of the latter in the presence of O₂ at 100 °C and higher.

In the presence of an acid catalyst, DMSO preferably interacts with the latter forming the [DMSOH]⁺ complex which further increases its activity [31]. Thus, both DMSO as solvent and Brønsted acid sites on a catalyst surface (such as sulfonic acid groups) are able to convert fructose to HMF [33,34]. The UiO-66-assisted reaction gave 87 % fructose conversion and 51 % HMF yield, comparable to that of the blank test therefore allowing to attribute such activity to the presence of the reactive solvent and not to the MOF. In fact, the same conclusion can be made with UiO-66-COOH, which converted 82 % fructose yielding 43 % HMF under the same conditions. This suggests that insertion of carboxylic groups into the UiO-66 framework is insufficient to improve fructose conversion. This, in turn, might be originated from the weak Brønsted acid sites generated by -COOH (pK_{a(-COOH)} ~5).

At the same time, the series of UiO-66-SO₃H-D-x (x = 25 to 100) prepared in DMF demonstrated an irregular conversion pattern. First of all, the addition of UiO-66-SO₃H-D-25, UiO-66-SO₃H-D-50 and UiO-66-SO₃H-D-75 led comparable results to the ones obtained with the blank test in spite of the increasing functionalization degree and therefore the increasing number of Brønsted acid sites. This remains unclear and the only explanation can be derived from the fact that all these MOFs were synthesized in DMF. Indeed, it was shown that it is still found trapped in the pores of MOFs as confirmed previously by ATR-IR studies. There is, however, no clear explanation of the hindering effect of DMF on fructose dehydration particularly in DMSO. On the other hand, studies on binary mixtures showed that there is a complexation behavior of DMSO-DMF mixture *via* H-bond interactions through H and O atoms both in DMSO and DMF over a wide range of concentrations [35]. This might explain the decreased conversion over UiO-66-SO₃H-D with

residual DMF which is prone to complexation with DMSO inhibiting formation of the $[\text{DMSOH}]^+$ and $[\text{O}_2:\text{DMSO}]$ complexes therefore decreasing its dehydration capacity.

It is worth mentioning that UiO-66-SO₃H-D-100 showed the highest activity among the MOFs prepared in DMF under the given conditions, converting 97 % fructose with 64 % HMF yield. This is in line with the previously reported activities of functionalized MOFs and even surpasses that of MIL-101(Cr)-SO₃H at 120 °C [33,36]. This suggests that -SO₃H groups provide Brønsted acidity of sufficient strength ($\text{pK}_{\text{a}}(-\text{SO}_3\text{H}) \sim -7$) to deprotonate and hence favor fructose dehydration, contrary to -COOH.

Same applies to UiO-66-SO₃H-W which demonstrated the highest activity in the given reaction conditions among all tested MOFs in this work. After 2 h of reaction at 100 °C, complete fructose conversion was obtained with an HMF yield of 73 %. The latter is higher than that of UiO-66-SO₃H-D-100 (73 % *vs* 64 %) and agrees well with that over NUS-6(Zr) reported by Hu *et al.* [20]. This also underlines the positive effect of framework functionalization with strong acidic -SO₃H groups.

At first glance, both solids exhibit comparable catalytic performance in fructose dehydration. Further investigations were conducted to understand the solvent effect during the preparation of sulfonic acid MOFs and its subsequent impact on the catalytic performance

2.1.1. Kinetic Profiles

In order to examine the catalytic activity of our catalysts throughout a certain reaction duration, a kinetic study was performed under the conditions applied in the screening test (Table IV.6). For this, the two most active solids that are UiO-66-SO₃H-W and UiO-66-SO₃H-D-100 were chosen

and further compared to the reference UiO-66 and blank tests. Figure IV-10 represents the kinetic profiles of fructose conversion performed at 100 °C from 30 min to 6 h.

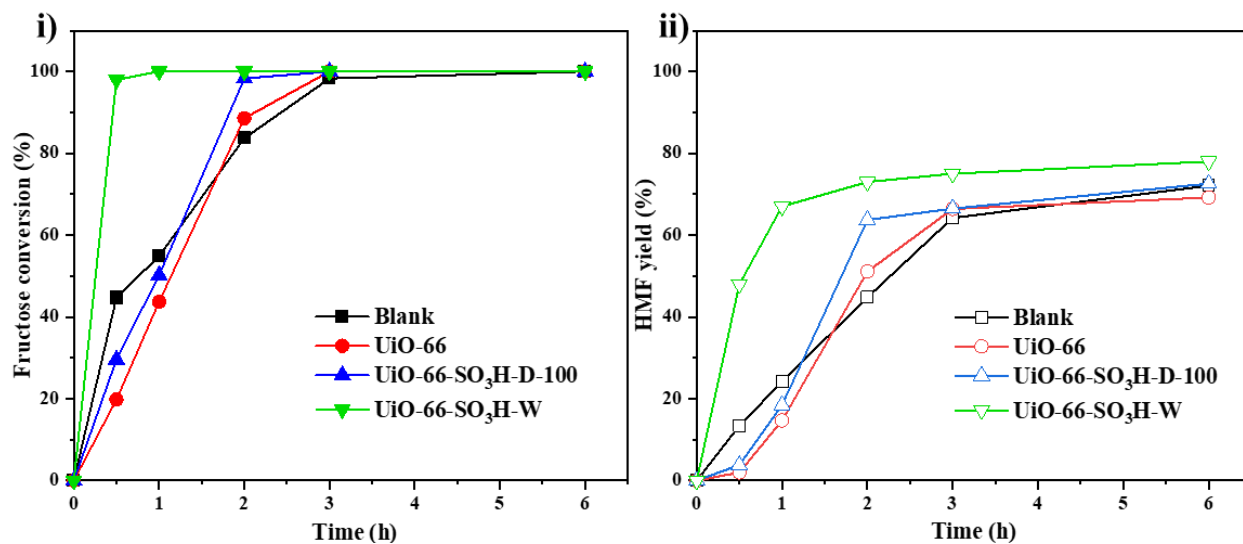


Figure IV-10. Kinetic profiles of fructose conversion (i) and HMF yield (ii) in blank tests as well as over UiO-66, UiO-66-SO₃H-D-100 and UiO-66-SO₃H-W. Reaction conditions: T = 100 °C, P_{atm}, 600 rpm, solvent – DMSO, V_{DMSO} = 2 mL, C_{fructose} = 0.6 mM, m_{cat} = 20 mg.

As illustrated, all tested catalysts as well as the blank test demonstrated activity starting already from 30 min with the latter converting 45 % fructose and yielding 13 % HMF. At the same time, UiO-66 and UiO-66-SO₃H-D-100 follow the same conversion and yield curves characterized by a progressive increase and finally reaching total conversion after 3 h, yielding approximately 66 % HMF. Importantly, UiO-66 and UiO-66-SO₃H-D-100 both exhibited slower conversion and HMF formation rates as compared to the blank test up to 1 h of reaction. This might be attributed to the presence of residual DMF as discussed above which might hinder formation of the active [DMSOH]⁺ and [O₂: DMSO] species by forming the DMSO-DMF complex. This statement was further supported by the blank tests run in DMSO alone and DMSO/DMF 3:1 v/v mixture. As a result, fructose conversion in DMSO reached 80 % after 2 h at 100 °C yielding a light-brown colored solution characteristic of HMF and indicating its presence (figure annex-4), whereas no

fructose conversion was observed for the reaction in DMSO/DMF mixture under the same conditions as well as no HMF formed which was supported by the colorless reaction solution after 2 h.

Therefore, it can be hypothesized that DMSO takes initial time to wash away the DMF adsorbed on the surface of the catalyst and form the DMSO-DMF complex to further liberate the active sites for interaction with fructose. Indeed, almost total fructose conversion (>98 %) with 64 % HMF yield over UiO-66-SO₃H-D-100 was reached in 2 h thus suggesting an enhanced activity as opposed to the blank test. As for UiO-66, its overall performance matches well with the one of the blank test with an insignificant improvement in fructose conversion after 2 h (87 % vs 82 %) and HMF yield (51 % vs 41 %), which could originate from the presence of a low amount of Brønsted sites in its Zr-clusters.

At the same time, fructose conversion over UiO-66-SO₃H-W was almost quantitative (~98 %) already after 30 min of reaction, yielding 48 % HMF and confirming its superior catalytic activity as compared to the blank test and the other catalysts mentioned above. It suggests that the active sites in UiO-66-SO₃H-W are readily available for interaction with the solvent and fructose without the hindering effect of DMF as it was the case in UiO-66-SO₃H-D-100. Not only UiO-66-SO₃H-W allows the fastest fructose conversion but also the highest overall HMF yield of 78 % after 6 h as compared to 72 % over UiO-66-SO₃H-D-100. Of note, all the examined catalysts remained stable and are easily recovered after the catalytic tests suggesting no structural damage in DMSO as it was the case of zeolites.

Overall, the kinetic tests suggest the superior performance of UiO-66-SO₃H-W as compared to the other tested MOFs and the blank test, demonstrating almost the complete (>98 %) fructose conversion after 30 min. In the work reported by Hu *et al.* [20], NUS-6(Zr), which is essentially

UiO-66-SO₃H-W, reached the complete fructose conversion after 1 h at 100 °C yielding 84 % HMF. In this work, UiO-66-SO₃H-W exhibited as well the full fructose conversion after 1 h but with 68 % HMF yield. This difference might be attributed to the relatively low amount of catalyst with a fructose-to-catalyst ratio of 11:1, as compared to the work of Hu *et al.* with 2:1 [20].

These results allow to underline the positive impact of the synthesis procedure in green conditions resulting in UiO-66-SO₃H-W, a highly active catalyst with readily available acid sites. In contrast, the traditional “DMF” route resulted in UiO-66-SO₃H-D-100 which exhibited overall better performance than the blank test but poorer than that of UiO-66-SO₃H-W.

2.1.2. Temperature Effect

The performance of the most active UiO-66-SO₃H-W was further evaluated at decreased (80 °C) and increased (120 °C) temperatures. Figure IV-11 represents the corresponding kinetic profiles. Accordingly, after 6 h at 80 °C (figure IV-11, i) UiO-66-SO₃H-W converted remarkable 93 % fructose yielding 65 % HMF while the blank test revealed 40 % conversion with 13 % HMF yield. Interestingly, after 3 h there was no fructose conversion observed in the blank test whereas UiO-66-SO₃H-W exhibited 81 % conversion with 52 % HMF yield. This shows that the latter exhibits a high catalytic activity even when there is no contribution from DMSO.

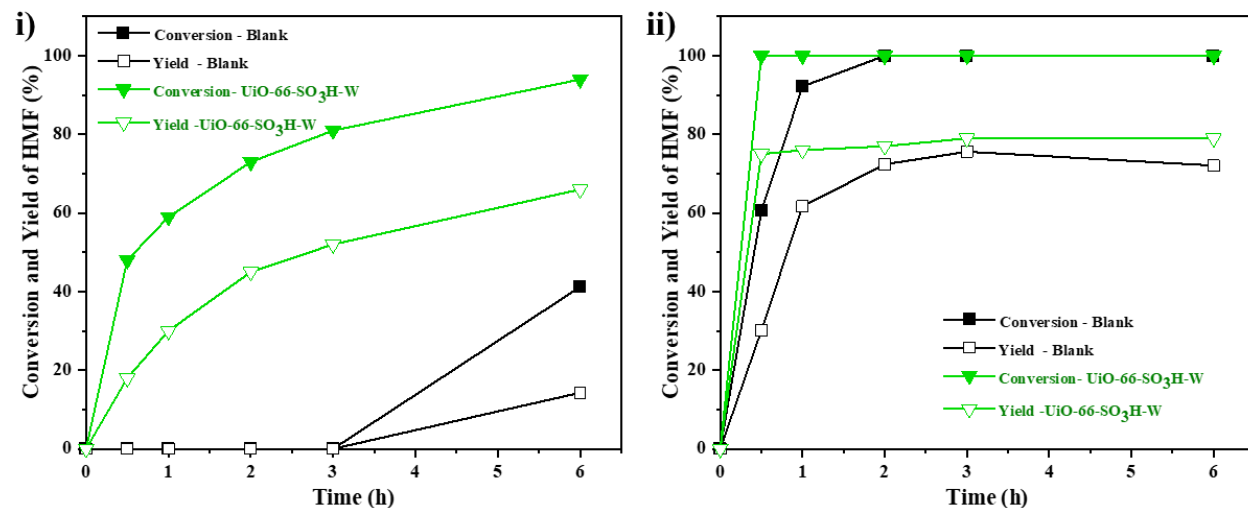


Figure IV-11. Kinetic profiles of fructose conversion and HMF yield at 80 °C (i) and 120 °C (ii) in blank test and over UiO-66-SO₃H-W. Reaction conditions: P_{atm} , 600 rpm, solvent – DMSO, $V_{\text{DMSO}} = 2 \text{ mL}$, $C_{\text{fructose}} = 0.6 \text{ mM}$, $m_{\text{cat}} = 20 \text{ mg}$.

At the same time, when tested at 120 °C, UiO-66-SO₃H-W reached complete fructose conversion already after 30 min yielding 75 % HMF. This is considerably higher than 60 % fructose conversion and 30 % HMF yield upon the blank test. Additionally, the blank test demonstrated the complete fructose conversion only after 2 h of reaction yielding 71 % HMF. Nevertheless, the maximum HMF yield accounts for 78 % and is obtained over UiO-66-SO₃H-W after 3 h, which is the same observed at 100 °C but after 6 h (figure IV-10, ii).

2.1.3. Catalyst Reusability

In order to probe the durability and reusability of UiO-66-SO₃H-W, a series of recycling tests were done. Briefly, recycling in this work implies catalyst recovery by centrifugation after the first run and, without further washing, immersing it into a fresh fructose solution in DMSO for the subsequent second run. Thus, 9 runs in total were performed at 80 °C and 100 °C with a 30 min duration of each run (figure IV-12). As seen previously (figure IV-11, i) after 30 min at 80 °C,

DMSO has no contribution to fructose conversion therefore providing good conditions to tests the reusability of UiO-66-SO₃H-W.

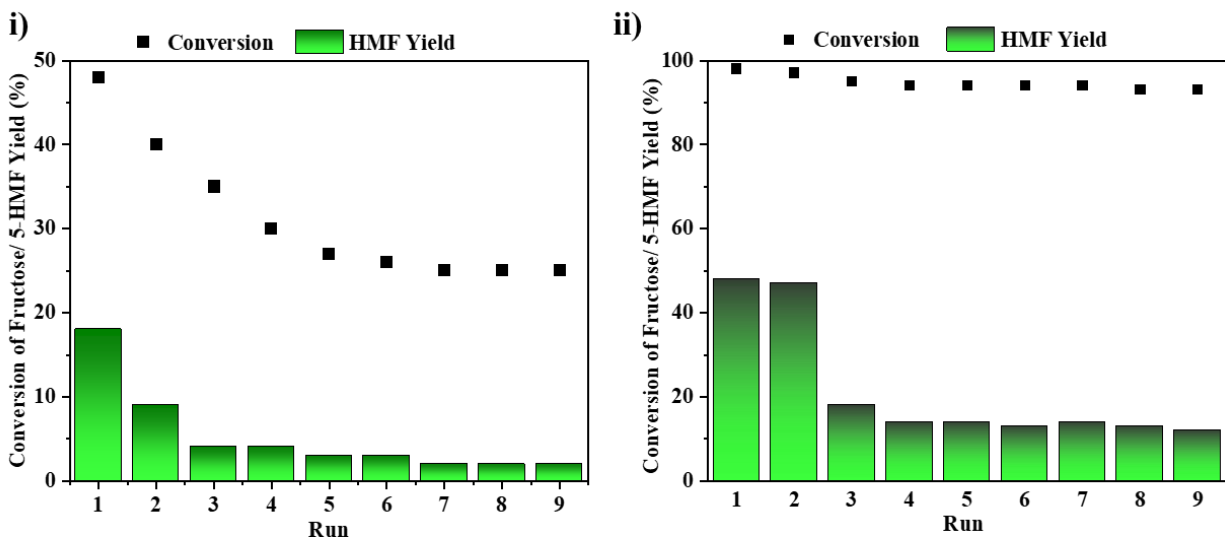


Figure IV-12. Fructose conversion and HMF yield upon 9 consecutive catalytic runs over UiO-66-SO₃H-W at 80 °C (i) and 100 °C (ii). Reaction conditions: $t_{\text{run}} = 30$ min, P_{atm} , 600 rpm, solvent – DMSO, $V_{\text{DMSO}} = 2$ mL, $C_{\text{fructose}} = 0.6$ mM, $m_{\text{cat}} = 20$ mg.

Therefore, at 80 °C (figure IV-12, i), UiO-66-SO₃H-W demonstrated 48 % fructose conversion and 18 % HMF yield upon the 1st run and a gradual decrease of its performance over the following runs. The apparent loss of its activity is observed after the 3rd run with the negligible 3 % HMF yield which is probably originated from considerable humin deposition on the active sites of the catalyst, a known phenomenon in biomass conversion [37–39]. The latter can be easily confirmed by TGA and ATR-IR experiments (figure IV-13). Accordingly, upon 9 cycles, UiO-66-SO₃H-W exhibited a 10 % weight increase as confirmed by TGA (figure IV-13, i). Furthermore, it is supported by the new broad IR band at ~ 1668 cm⁻¹ (figure IV-13, ii) which corresponds to C=C bond stretching in a furanic ring implying humins formed from HMF. Additionally, the new bands at ~ 951 cm⁻¹ and 1004 cm⁻¹ might be indicative of unwashed and therefore adsorbed HMF species on the catalyst surface [40].

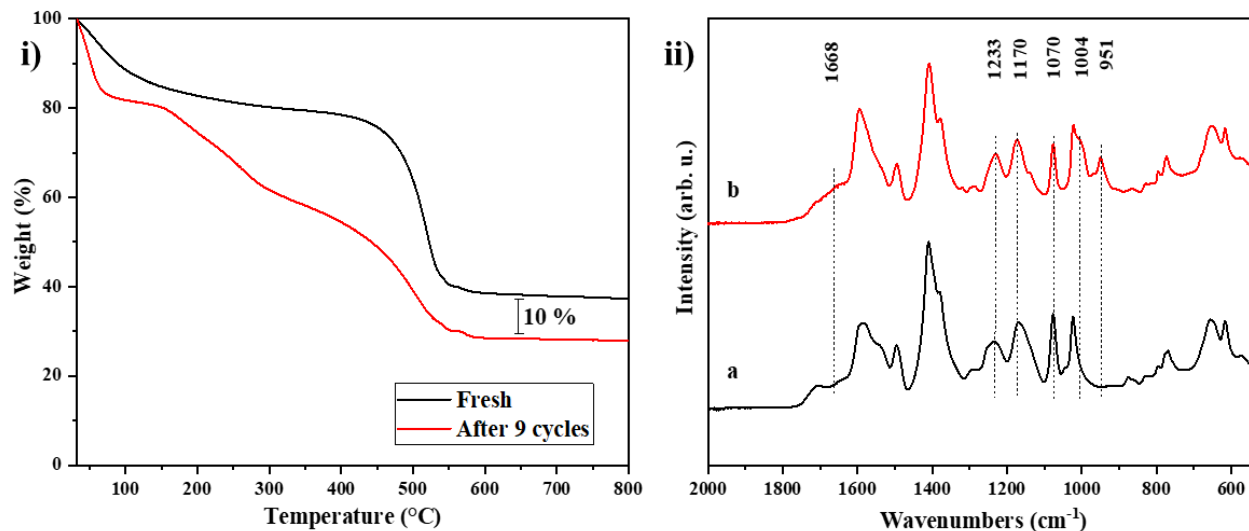


Figure IV-13. TGA profiles (i) and ATR-IR spectra (ii) of UiO-66-SO₃H-W before (fresh, a) and after 9 consecutive catalytic runs (b).

Importantly, one can notice that the bands originated from -SO₃H functional group *i.e.* 615 cm⁻¹ and 1070 cm⁻¹ (S-O stretching) as well as 1170 cm⁻¹ and 1233 cm⁻¹ (S=O stretching) are still present in the MOF after 9 cycles [2,11]. This suggests the retaining of -SO₃H functional groups in UiO-66-SO₃H-W upon reuse.

At the same time, fructose conversion still takes place after the 3rd run accounting for 35 % and remains at 25 % upon the last 9th run. This is probably due to the presence of Lewis acid sites which are responsible of ongoing fructose conversion into longer-chain oligomers non-detectable by HPLC [41,42]. The trends observed upon catalyst recycling at 100 °C for 30 min (figure IV-12, ii) follow a similar pattern as at 80 °C. Namely, after the 1st run, UiO-66-SO₃H-W demonstrated almost complete (>98 %) fructose conversion with 48 % HMF yield after 30 min which gradually diminished upon the subsequent runs. Namely, upon the 3rd run, HMF yield dropped to 16 % and hereafter it dropped even further to 13 % making up the value of the blank test at 100 °C after 30 min (13 %, figure IV-10, ii). This allows to conclude that after the 3rd run, the catalyst is deactivated and that the observed HMF formation is due to DMSO alone. The high

fructose conversion throughout the 9 cycles at 100 °C is again attributed to the reactive solvent which converts up to 45 % fructose at the given conditions (figure IV-10, i) and also to the Lewis acid sites in UiO-66-SO₃H-W.

Importantly, UiO-66-SO₃H-W preserves its structural integrity upon 9 runs at both 80 °C and 100 °C as described by the XRD reflections remaining intact before and after recycling. The same applies to the tests done at 80 °C, 100 °C and 120 °C after 6 h (figure IV-14).

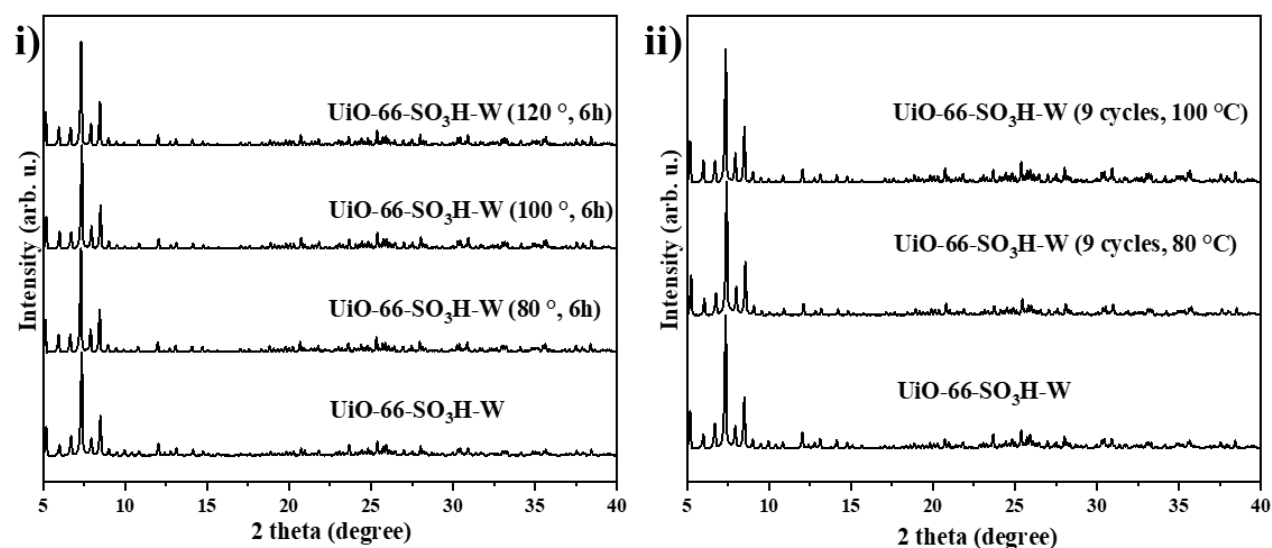


Figure IV-14. XRD patterns of UiO-66-SO₃H-W after 6 h of reaction at 80 °C, 100 °C and 120 °C (i) as well as after 9 consecutive catalytic runs at 80 °C and 100 °C (ii) as compared to the pristine UiO-66-SO₃H-W.

With this being said, one can notice that the observed catalyst deactivation is not due to structural collapse of the MOF structure but rather to inaccessibility of the sulfonic acid groups due to the remarkable humin deposition.

2.1.4. Comparison with a Commercial Solid Acid Catalyst

Lastly, since UiO-66-SO₃H-W can convert fructose into HMF at 80 °C thus avoiding the solvent effect, further decrease down to 60 °C was attempted to confirm its usability at even lower temperatures. As expected, there was no fructose conversion observed in the blank test even after 24 h at 60°C. At the same time, UiO-66-SO₃H-W demonstrated decent 68 % fructose conversion with 39 % HMF after 24 h further confirming its strong acidic nature. Interestingly, both UiO-66-SO₃H-W and Amberlyst-15©, a commercial solid catalyst with sulfonic acid functions, demonstrated surprisingly similar performances (Table IV.7). The latter was not the case for UiO-66-COOH and UiO-66-OH.

Table IV.7 – Fructose conversion and HMF yield over a series of functionalized MOFs as compared to Amberlyst-15©.

Catalyst	T, °C	t, h	Solvent	Fr. conv., %	HMF yield, %	HMF sel., %
Blank	60	24	DMSO	0	0	0
UiO-66-COOH	60	24	DMSO	0	0	0
UiO-66-OH	60	24	DMSO	23	5	22
Amberlyst-15©	60	24	DMSO	69	41	59
UiO-66-SO ₃ H-W	60	24	DMSO	68	39	57

Reaction conditions: P_{atm} , 600 rpm, $V_{DMSO} = 2 \text{ mL}$, $C_{fructose} = 0.6 \text{ mM}$, $m_{cat} = 20 \text{ mg}$.

This allows to predict that UiO-66-SO₃H-W could, in some time, extend the list of benchmark solid acid catalysts and become a promising candidate supported by its easily scalable green synthesis. The latter will be discussed in more detail in the following chapter.

To conclude this section, it was shown that the functionalized MOFs are active catalysts towards fructose dehydration to HMF. Using UiO-66-SO₃H synthesized traditionally in DMF, it was shown that it was difficult to evaluate their catalytic performance due to the unavoidable effect of the residual DMF. It was clearly seen that upon increasing the functionalization degree from 25 %

to 100 %, both fructose conversion and HMF yield over UiO-66-SO₃H-D followed a non-traceable trend. Therefore, it underlines the need for the complete elimination of DMF from their structure.

Hence, a series of functionalized acidic MOFs were prepared in water and their intrinsic catalytic activity was studied. Thus, UiO-66-COOH showed no enhancement of fructose conversion neither at 100 °C nor at 60 °C, related to its rather weak acidic properties. On the other hand, UiO-66-SO₃H-W demonstrated superior catalytic performance over the temperature window comprised between 80 °C and 120 °C and reaction durations up to 6 h, as compared to all tested MOFs in this work. This is related to its strong acidic nature comparable to a commercial solid acid catalyst, Amberlyst-15®.

2.2. Glucose Isomerization

The series of functionalized MOFs was also examined in glucose isomerization to fructose (Table IV.8) under the same conditions as for the zeolites discussed in chapter III.

Table IV.8 – Glucose conversion as well as fructose and HMF yields over functionalized MOFs.

Catalyst	T, °C	t, h	Solvent	Gl. conv., %	Fr. yield, %	HMF yield, %
Blank	120	3	H ₂ O	0	0	0
UiO-66	120	3	H ₂ O	5	0	0
UiO-66-NH ₂	120	3	H ₂ O	11	2	0
UiO-66-SO ₃ H-W	120	3	H ₂ O	13	0	7

Reaction conditions: P_{atm}, 600 rpm, V_{solv} = 2 mL, C_{glucose} = 0.6 mM, m_{cat} = 20 mg.

As evidenced, UiO-66 exhibits negligible glucose conversion of 5 % with no traces of fructose or HMF. This probably originates from the short reaction duration of only 3 h as compared to 24 h in the reference works [43,44]. Nevertheless, UiO-66 is stated to possess a low selectivity towards fructose. At the same time, UiO-66-NH₂ exhibited 11 % glucose conversion with only 2 % fructose

yield making up 18 % selectivity. In spite of such low conversion and yield, the results are in line with those obtained over MIL-101-NH₂ by Akiyama *et al.* [43]. Indeed, they stated that insertion of amino groups leads to an increase of basic sites in MOFs and therefore positively impacts glucose conversion. However, NH₂ functional groups provide rather strong basic sites causing a strong interaction with glucose which therefore remains adsorbed on the surface after reaction. As a consequence, this leads to a lowered selectivity towards fructose which explains the low selectivity of 18 % observed over UiO-66-NH₂ in this work.

Alternatively, UiO-66-SO₃H-W demonstrated the comparable 13 % glucose conversion, however with only traces of fructose. This is somewhat different from the results obtained by Akiyama *et al.* [43] and Oozeerally *et al.* [45] who suggested an increase of fructose yield over MOFs functionalized with -SO₃H groups. The absence of fructose could be explained in the same manner as in the case of UiO-66-NH₂, however, HMF yield is surprisingly considerable and accounts for 7 % giving 54 % selectivity. This might indicate the further fructose dehydration to HMF therefore suggesting a cascade reaction implying glucose isomerization to fructose on Lewis acid sites with its subsequent dehydration to HMF on Brønsted acid sites. Indeed, it is possible as UiO-66-SO₃H-W, apart from -SO₃H groups, exhibits a high number of structural defects as discussed above therefore providing a high number of open metal sites in Zr-clusters. Thus, this MOF exhibits dual Brønsted/Lewis acid sites whose synergy enables the direct one-pot HMF formation from glucose. In this regard, further evaluation of UiO-66-SO₃H-W catalytic system could be a promising candidate for glucose conversion into HMF it poorly performed in dehydration of fructose in water.

3. Conclusion

A series of functionalized UiO-66-based MOFs was prepared and characterized. It was shown that upon synthesis in DMF, UiO-66-SO₃H and UiO-66 with mixed terephthalate and sulfoterephthalate linkers retain the framework topology of the parent UiO-66. While the presence of sulfonic acid groups was qualitatively proven, the textural properties of the resulting MOFs experienced a certain drop both in available surface area and micropore volume due to partial pore occupancy. To avoid the use of DMF and thus its presence within the porosity of the MOF, UiO-66-SO₃H was also prepared in water owing to the solubility of the sulfoterephthalate linker. Nevertheless, it was demonstrated that its water-based preparation results in a highly defective framework leading to a change of framework topology from the UiO-66 face-centered cubic system (*Fm-3m* with $a = 20.7809(3)$ Å) to a body-centered cubic system (*Im-3* with $a = 41.4440(8)$ Å). Further qualitative and quantitative elemental analyses revealed lower amounts of carbon and sulfur than expected in UiO-66-SO₃H-W confirming its higher number of missing linkers. Despite that, the thus-formed MOF exhibits surface area and micropore volume higher than its counterpart prepared in DMF. A “green” water-based synthesis was further applied to UiO-66-COOH, UiO-66-OH and UiO-66-NH₂ MOFs also resulting in highly porous crystalline solids but with preserved UiO-66 topology. Further in this work, the catalytic performances of a number of acid- and base-functionalized UiO-66-based MOFs were evaluated. When applied in fructose dehydration, sulfonic acid functionalized UiO-66-SO₃H showed superior activity as opposed to UiO-66-COOH, in line with the stronger Brønsted acid sites generated by -SO₃H groups. It was shown that the preparation method of UiO-66-SO₃H had a clear impact on its performance. Thus, when prepared *via* traditional DMF-involved route, UiO-66-SO₃H-D suffered from an inhibiting effect of DMF resulting in slower conversion rates. In contrast, UiO-66-SO₃H-W, the product of a water-based

Chapter IV – Conclusion

preparation route, demonstrated the highest catalytic activity among all tested MOFs and retained its exceptional activity over a wide range of applied temperatures. At 60 °C and 80 °C, solvent (DMSO) has no impact on fructose dehydration, however UiO-66-SO₃H-W showed a decent performance comparable to that of Amberlyst-15©, a commercial acidic solid catalyst.

Furthermore, a few MOFs were capable of glucose isomerization to fructose. Thus, UiO-66-NH₂ showed a certain activity due to its basic sites generated by amino groups. The strength of the latter is responsible for the increased interaction with glucose and therefore its adsorption on the surface of the catalyst. This unavoidably leads to the low fructose selectivity that is reported in this work. In contrast, UiO-66-SO₃H-W once again demonstrates its relevance by favoring direct glucose conversion to HMF through the glucose-to-fructose isomerization intermediate step. This is possible due to the structural specificities of UiO-66-SO₃H-W which exhibits both Lewis and Brønsted acid sites originated from structural defects and -SO₃H groups, respectively. Further study of the direct glucose conversion to HMF over UiO-66-SO₃H-W should be addressed in more detail as it provides promising results.

4. References:

- [1] J.H. Cavka, S. Jakobsen, U. Olsbye, N. Guillou, C. Lamberti, S. Bordiga, K.P. Lillerud, A New Zirconium Inorganic Building Brick Forming Metal Organic Frameworks with Exceptional Stability, *J. Am. Chem. Soc.* 130 (2008) 13850–13851. <https://doi.org/10.1021/ja8057953>.
- [2] M.L. Foo, S. Horike, T. Fukushima, Y. Hijikata, Y. Kubota, M. Takata, S. Kitagawa, Ligand-based solid solution approach to stabilisation of sulphonic acid groups in porous coordination polymer $Zr_6O_4(OH)_4(BDC)_6$ (UiO-66), *Dalt. Trans.* 41 (2012) 13791–13794. <https://doi.org/10.1039/c2dt31195j>.
- [3] S. Biswas, J. Zhang, Z. Li, Y. Liu, M. Grzywa, L. Sun, D. Volkmer, P. Van Der Voort, Enhanced selectivity of CO₂ over CH₄ in sulphonate-, carboxylate- and iodo-functionalized UiO-66 frameworks, *Dalt. Trans.* 42 (2013) 4730–4737. <https://doi.org/10.1039/c3dt32288b>.
- [4] T. Xu, M.A. Shehzad, X. Wang, B. Wu, L. Ge, T. Xu, Engineering Leaf-Like UiO-66 -SO₃H Membranes for Selective Transport of Cations, *Nano-Micro Lett.* 12 (2020) 51. <https://doi.org/10.1007/s40820-020-0386-6>.
- [5] G.Y. Shangkum, P. Chammingkwan, D.X. Trinh, T. Taniike, Design of a Semi-Continuous Selective Layer Based on Deposition of UiO-66 Nanoparticles for Nanofiltration, *Membranes (Basel)*. 8 (2018) 129. <https://doi.org/10.3390/membranes8040129>.
- [6] R. Wu, X. Qian, K. Zhou, H. Liu, B. Yadian, J. Wei, H. Zhu, Y. Huang, Highly dispersed Au nanoparticles immobilized on Zr-based metal–organic frameworks as heterostructured catalyst for CO oxidation, *J. Mater. Chem. A*. 1 (2013) 14294. <https://doi.org/10.1039/C3TA13114A>.
- [7] S. Øien, D. Wragg, H. Reinsch, S. Svelle, S. Bordiga, C. Lamberti, K.P. Lillerud, Detailed Structure Analysis of Atomic Positions and Defects in Zirconium Metal–Organic Frameworks, *Cryst. Growth Des.* 14 (2014) 5370–5372.
- [8] S.M. Chavan, G.C. Shearer, S. Svelle, U. Olsbye, F. Bonino, J. Ethiraj, K.P. Lillerud, S. Bordiga, Synthesis and Characterization of Amine-Functionalized Mixed- Ligand Metal – Organic Frameworks of UiO-66 Topology, *Inorg. Chem.* 53 (2014) 9509–9515.
- [9] Y. Han, M. Liu, K. Li, Y. Zuo, Y. Wei, S. Xu, G. Zhang, C. Song, Z. Zhang, X. Guo, Facile synthesis of morphology and size-controlled zirconium metal–organic framework UiO-66: the role of hydrofluoric acid in crystallization, *CrystEngComm*. 17 (2015) 6434. <https://doi.org/10.1039/C5CE00729A>.
- [10] D.M. Driscoll, D. Troya, P.M. Usov, A.J. Maynes, A.J. Morris, J.R. Morris, Geometry and Energetics of CO Adsorption on Hydroxylated UiO-66, *Phys. Chem. Chem. Phys.* 21 (2019) 5078–5085.
- [11] C.G. Piscopo, A. Polyzoidis, M. Schwarzer, S. Loebbecke, Stability of UiO-66 under acidic treatment: Opportunities and limitations for post-synthetic modifications, *Microporous Mesoporous Mater.* 208 (2015) 30–35. <https://doi.org/10.1016/j.micromeso.2015.01.032>.
- [12] K. Sing, R. Williams, Physisorption Hysteresis Loops and the Characterization of

- Nanoporous Materials Kenneth, *Adsorpt. Sci. Technol.* 22 (2004) 773–782. <https://doi.org/10.1260/0263617053499032>.
- [13] H. Wu, Y.S. Chua, V. Krungleviciute, M. Tyagi, P. Chen, T. Yildirim, W. Zhou, Unusual and Highly Tunable Missing-Linker Defects in Zirconium Metal -Organic Framework UiO-66 and Their Important Effects on Gas Adsorption, *J. Am. Chem. Soc.* 135 (2013) 10525–10532. <https://doi.org/10.1021/ja404514r>.
- [14] W. Xiang, J. Ren, S. Chen, C. Shen, Y. Chen, M. Zhang, The metal–organic framework UiO-66 with missing-linker defects: A highly active catalyst for carbon dioxide cycloaddition, *Appl. Energy.* 277 (2020) 115560. <https://doi.org/10.1016/j.apenergy.2020.115560>.
- [15] Q. Zhao, W. Yuan, J. Liang, J. Li, Synthesis and hydrogen storage studies of metal-organic framework UiO-66, *Int. J. Hydrogen Energy.* 38 (2013) 13104–13109. <https://doi.org/10.1016/j.ijhydene.2013.01.163>.
- [16] R. Wei, J. Fan, X. Qu, L. Gao, Y. Wu, Z. Zhang, F. Hu, G. Xiao, Tuning the Catalytic Activity of UiO-66 via Modulated Synthesis : Esterification of Levulinic Acid as A Test Reaction, *Eur. J. Inorg. Chem.* 2020 (2020) 833–840. <https://doi.org/10.1002/ejic.202000031>.
- [17] T.H. Kim, S.G. Kim, Clinical Outcomes of Occupational Exposure to N,N - Dimethylformamide: Perspectives from Experimental Toxicology, *Saf. Health Work.* 2 (2011) 97–104. <https://doi.org/10.5491/SHAW.2011.2.2.97>.
- [18] J.M. Taylor, T. Komatsu, S. Dekura, K. Otsubo, M. Takata, H. Kitagawa, The Role of a Three Dimensionally Ordered Defect Sublattice on the Acidity of a Sulfonated Metal-Organic Framework, *J. Am. Chem. Soc.* 137 (2015) 11498–11506. <https://doi.org/10.1021/jacs.5b07267>.
- [19] J. Juan-Alcaniz, R. Gielisse, A.B. Lago, E. V Ramos-Fernandez, P. Serra-Crespo, T. Devic, N. Guillou, C. Serre, F. Kapteijn, J. Gascon, Towards acid MOFs – catalytic performance of sulfonic acid functionalized architectures, *Catal. Sci. Technol.* 3 (2013) 2311–2318. <https://doi.org/10.1039/c3cy00272a>.
- [20] Z. Hu, Y. Peng, Y. Gao, Y. Qian, S. Ying, D. Yuan, S. Horike, N. Ogiwara, R. Babarao, Y. Wang, N. Yan, D. Zhao, Direct Synthesis of Hierarchically Porous Metal – Organic Frameworks with High Stability and Strong Brønsted Acidity: The Decisive Role of Hafnium in Efficient and Selective Fructose Dehydration, *Chem. Mater.* 28 (2016) 2659–2667. <https://doi.org/10.1021/acs.chemmater.6b00139>.
- [21] M. Kandiah, M.H. Nilsen, S. Usseglio, S. Jakobsen, U. Olsbye, M. Tilset, C. Larabi, E.A. Quadrelli, F. Bonino, K.P. Lillerud, D. Lyon, Synthesis and Stability of Tagged UiO-66 Zr-MOFs, *Chem. Mater.* 22 (2010) 6632–6640. <https://doi.org/10.1021/cm102601v>.
- [22] J. Winarta, B. Shan, S.M. McIntyre, L. Ye, C. Wang, J. Liu, B. Mu, A Decade of UiO-66 Research: A Historic Review of Dynamic Structure, Synthesis Mechanisms, and Characterization Techniques of an Archetypal Metal–Organic Framework, *Cryst. Growth Des.* 20 (2020) 1347–1362. <https://doi.org/10.1021/acs.cgd.9b00955>.
- [23] G.C. Shearer, S. Chavan, S. Bordiga, S. Svelle, U. Olsbye, K.P. Lillerud, Defect Engineering: Tuning the Porosity and Composition of the Metal – Organic Framework UiO-

- 66 via Modulated Synthesis, *Chem. Mater.* 28 (2016) 3749–3761. <https://doi.org/10.1021/acs.chemmater.6b00602>.
- [24] S. Gökpınar, S. Ernst, E. Hastürk, M. Möllers, E. Aita, R. Wiedey, N. Tannert, S. Nießing, S. Abdpour, J. Quodbach, G. Földner, S.K. Henninger, C. Janiak, Air-con Metal–Organic Frameworks in Binder Composites for Water Adsorption Heat Transformation Systems, *Ind. Eng. Chem. Res.* 58 (2019) 21493–21503. <https://doi.org/10.1021/acs.iecr.9b04394>.
- [25] W. Zhang, W. Ji, L. Li, P. Qin, I.E. Khalil, Z. Gu, P. Wang, H. Li, Y. Fan, Z. Ren, Y. Shen, W. Zhang, Y. Fu, F. Huo, Exploring the Fundamental Roles of Functionalized Ligands in Platinum@Metal–Organic Framework Catalysts, *ACS Appl. Mater. Interfaces.* 12 (2020) 52660–52667. <https://doi.org/10.1021/acsami.0c15340>.
- [26] R. Oozeerally, D.L. Burnett, T.W. Chamberlain, R.J. Kashtiban, S. Huband, R.I. Walton, V. Degirmenci, Systematic Modification of UiO-66 Metal–Organic Frameworks for Glucose Conversion into 5-Hydroxymethyl Furfural in Water, *ChemCatChem.* 13 (2021) 2517–2529. <https://doi.org/10.1002/cctc.202001989>.
- [27] S. Despax, C. Maurer, B. Estrine, J. Le, N. Hoffmann, S. Marinkovic, J. Muzart, Fast and efficient DMSO-mediated dehydration of carbohydrates into 5-hydroxymethylfurfural, *Catal. Commun.* 51 (2014) 5–9. <https://doi.org/10.1016/j.catcom.2014.03.009>.
- [28] L. Hu, X. Tang, Z. Wu, L. Lin, J. Xu, N. Xu, B. Dai, Magnetic lignin-derived carbonaceous catalyst for the dehydration of fructose into 5-hydroxymethylfurfural in dimethylsulfoxide, *Chem. Eng. J.* 263 (2015) 299–308. <https://doi.org/10.1016/j.cej.2014.11.044>.
- [29] H. Wang, Q. Kong, Y. Wang, T. Deng, C. Chen, X. Hou, Y. Zhu, Graphene Oxide Catalyzed Dehydration of Fructose into 5-Hydroxymethylfurfural with Isopropanol as Cosolvent, *ChemCatChem.* 6 (2014) 728–732. <https://doi.org/10.1002/cctc.201301067>.
- [30] J. Wang, W. Xu, J. Ren, X. Liu, G. Lu, Y. Wang, Efficient catalytic conversion of fructose into hydroxymethylfurfural by a novel carbon-based solid acid, *Green Chem.* 13 (2011) 2678–2681. <https://doi.org/10.1039/c1gc15306d>.
- [31] L.-K. Ren, L. Zhu, T. Qi, J. Tang, H. Yang, C. Hu, Performance of Dimethylsulfoxide and Brønsted Acid Catalysts in Fructose Conversion to 5-Hydroxymethylfurfural, *ACS Catal.* 7 (2017) 2199–2212. <https://doi.org/10.1021/acscatal.6b01802>.
- [32] T.C. Tudino, R.S. Nunes, D. Mandelli, W.A. Carvalho, Influence of Dimethylsulfoxide and Dioxygen in the Fructose Conversion to 5-Hydroxymethylfurfural Mediated by Glycerol's Acidic Carbon, *Front. Chem.* 8 (2020) 1–11. <https://doi.org/10.3389/fchem.2020.00263>.
- [33] J. Chen, K. Li, L. Chen, R. Liu, X. Huang, D. Ye, Conversion of fructose into 5-hydroxymethylfurfural catalyzed by recyclable sulfonic acid-functionalized metal–organic frameworks, *Green Chem.* 16 (2014) 2490. <https://doi.org/10.1039/c3gc42414f>.
- [34] E. Kılıç, S. Yılmaz, Fructose Dehydration to 5-Hydroxymethylfurfural over Sulfated TiO₂–SiO₂, Ti-SBA-15, ZrO₂, SiO₂, and Activated Carbon Catalysts, *Ind. Eng. Chem. Res.* 54 (2015) 5220–5225. <https://doi.org/10.1021/acs.iecr.5b00628>.
- [35] R.J. Sengwa, S. Sankhla, V. Khatri, Dielectric characterization and molecular interaction behaviour in binary mixtures of amides with dimethylsulphoxide and 1,4-dioxane, *J. Mol. Liq.* 151 (2010) 17–22. <https://doi.org/10.1016/j.molliq.2009.10.011>.

- [36] Y. Zhong, Q. Yao, P. Zhang, H. Li, Q. Deng, J. Wang, Z. Zeng, S. Deng, Preparation of Hydrophobic Acidic Metal–Organic Frameworks and Their Application for 5-Hydroxymethylfurfural Synthesis, *Ind. Eng. Chem. Res.* 59 (2020) 22068–22078. <https://doi.org/10.1021/acs.iecr.0c04798>.
- [37] I. Van Zandvoort, Y. Wang, C.B. Rasrendra, E.R.H. Van Eck, P.C.A. Bruijninx, H.J. Heeres, B.M. Weckhuysen, Formation, Molecular Structure, and Morphology of Humins in Biomass Conversion: Influence of Feedstock and Processing Conditions, *ChemSusChem*. 6 (2013) 1745–1758. <https://doi.org/10.1002/cssc.201300332>.
- [38] M. Bosilj, J. Schmidt, A. Fischer, R.J. White, One pot conversion of glucose to ethyl levulinate over a porous hydrothermal acid catalyst in green solvents, *RSC Adv.* 9 (2019) 20341. <https://doi.org/10.1039/c9ra03902c>.
- [39] H.C. Genuino, H.H. Van De Bovenkamp, E. Wilbers, J.G.M. Winkelman, A. Goryachev, J.P. Hofmann, E.J.M. Hensen, B.M. Weckhuysen, P.C.A. Bruijninx, H.J. Heeres, Catalytic Hydrogenation of Renewable Levulinic Acid to γ -Valerolactone: Insights into the Influence of Feed Impurities on Catalyst Performance in Batch and Flow Reactors, *ACS Sustain. Chem. Eng.* 8 (2020) 5903–5919. <https://doi.org/10.1021/acssuschemeng.9b07678>.
- [40] G. Tsilomelekis, M.J. Orella, Z. Lin, Z. Cheng, W. Zheng, V. Nikolakis, D.G. Vlachos, Molecular structure, morphology and growth mechanisms and rates of 5-hydroxymethyl furfural (HMF) derived humins, *Green Chem.* 18 (2016) 1983–1993. <https://doi.org/10.1039/c5gc01938a>.
- [41] V. V Ordonsky, J. Van Der Schaaf, J.C. Schouten, T.A. Nijhuis, Fructose Dehydration to 5-Hydroxymethylfurfural over Solid Acid Catalysts in a Biphasic System, *ChemSusChem*. 5 (2012) 1–9. <https://doi.org/10.1002/cssc.201200072>.
- [42] X. Li, K. Peng, X. Liu, Q. Xia, Y. Wang, Comprehensive understanding the role of Brønsted and Lewis acid sites in glucose conversion to 5-hydroxymethylfurfural, *ChemCatChem*. 9 (2017) 2739–2746.
- [43] G. Akiyama, R. Matsuda, H. Sato, S. Kitagawa, Catalytic glucose isomerization by porous coordination polymers with open metal sites, *Chem. Asian J.* 9 (2014) 2772–7. <https://doi.org/10.1002/asia.201402119>.
- [44] Q.-X. Luo, Y. Zhang, L. Qi, L. Susannah, Glucose Isomerization and Epimerization over Metal–Organic Frameworks with Single-Site Active Centers, *ChemCatChem*. 11 (2019) 1903–1909. <https://doi.org/10.1002/cctc.201801889>.
- [45] A.R. Oozeerally, D.L. Burnett, T.W. Chamberlain, R.I. Walton, V. Degirmenci, Exceptionally Efficient and Recyclable Heterogeneous Metal–Organic Framework Catalyst for Glucose Isomerization in Water, *ChemCatChem*. 10 (2018) 706–709. <https://doi.org/10.1002/cctc.201701825>.

Chapter V

Upscaling and Shaping of

UiO-66-SO₃H MOF

Chapter V

This final chapter is dedicated to the large-scale synthesis of UiO-66-SO₃H-W to ensure its further shaping into solid objects by providing sufficient amounts of powdery MOF. As was discussed in chapter I, the list of existing commercialized MOFs includes HKUST-1, MIL-53(Al), MIL-100(Fe), UiO-66(Zr) and continues to grow. It is important to mention that industrial production of any material should proceed with the least possible impact on the environment and public health. Therefore, the green route for MOFs synthesis established *via* replacing the toxic DMF by water and discussed in the previous chapter is beneficial for upscaling and further shaping.

As briefly discussed in chapter I, the major challenge associated with shaping of MOFs is preservation of their intrinsic physico-chemical properties. It was the principle goal of the systematic review conducted recently in our team [1]. Accordingly, it was concluded that some MOFs experience more pronounced changes of their initial properties upon shaping. This is directly linked to the nature of the parent MOFs *i.e.* their structural and chemical stabilities which define their tolerance towards, for instance, compaction pressure or binder presence. Therefore, it was underlined that UiO-66-based MOFs experience less dramatic physico-chemical properties upon shaping as compared to the other reviewed MOFs.

Thus, in this chapter, we will only consider MOFs produced in water solvent *via* upscaling and shaping. In this line, UiO-66-SO₃H-W was selected as our best active solid acid catalyst. Thus, the scaling-up of the initial batch synthesis includes a 30-times synthesis upscaling by using a 3 L double-wall process reactor and subsequent shaping of the resulting powder by extrusion and pelletization, as discussed in chapter II.

1. Upscaling and Shaping

1.1. Powder vs Shaped Object: Characterization

As mentioned in chapter I, upscaling should be performed on an optimized synthesis protocol applied at small scale by possibly avoiding the use of aggressive solvents. Therefore, sulfonic acid functionalized UiO-66-SO₃H-W produced in water as the solvent seems pertinent for scaling-up. The results of the optimization of the synthesis duration (from 2 h to 120 h) on its structural and textural properties are depicted in figure V-1.

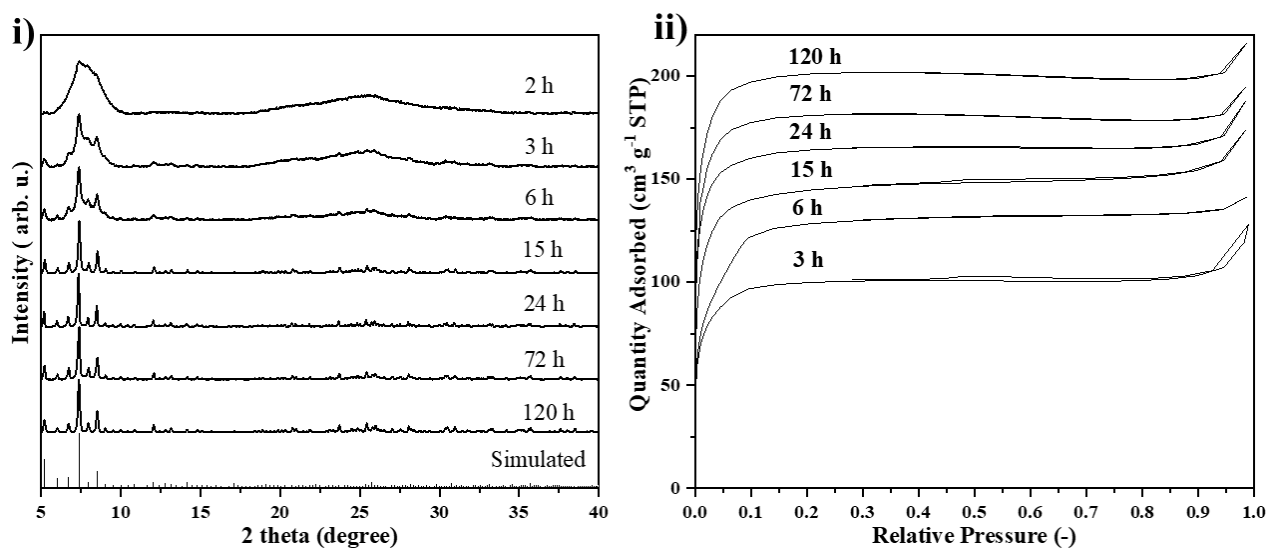


Figure V-1. XRD patterns (i) and N₂ isotherms (ii) of UiO-66-SO₃H-W obtained after various synthesis durations. The isotherms were adjusted by applying the following offset functions: 15 h offset - 10 cm³·g⁻¹ STP, 72 h offset + 10 cm³·g⁻¹ STP and 120 h offset +20 cm³·g⁻¹ STP.

Accordingly, synthesis duration seems to play a key factor determining the quality of the final product. Thus, UiO-66-SO₃H-W gradually turns into a crystalline solid within the applied synthesis durations (figure V-1, i). Thus, a considerable fraction of amorphous matter is observed up to 6 h. Then, it becomes negligible after 15 h yielding a crystalline solid with well-defined

reflections. This agrees well with the continuous increase of the surface areas (figure V-1 (ii) and Table V.1)

Table V.1 – Surface areas and yields of UiO-66-SO₃H-W at various synthesis durations.

Synthesis duration, h	2	3	6	15	24	72	120
Yield, %	35	41	55	68	78	81	83
S _{BET} , m ² ·g ⁻¹	-	376	492	596	639	630	691

Yields are based on Zr₆O₄(OH)₄[C₆H₃(COO)₂SO₃H]₆ molecular formula.

Therefore, owing to the structural and textural properties as well as the decent yield, the optimal synthesis duration for scaling-up the synthesis of UiO-66-SO₃H-W in a 3 L double reactor was defined as 24 h.

Thereafter, the amount of the up-scaled MOF (23 g with an approximate yield of 76 %) was sufficient to perform several shaping experiments. Table V.2 presents the different solids including the extruded, the pelletized and the up-scaled powdery UiO-66-SO₃H-W as well as their available surface areas.

Table V.2 – Short summary of the shaped UiO-66-SO₃H-W and their surface areas.

Solid	Extrusion		Pelletization	S _{BET} , m ² ·g ⁻¹
	Binder, wt. %	Plasticizer	Pressure, MPa	
Powder	-	-	-	600 (=)
Extrudate2	HEC, 2	H ₂ O	-	192 (-68 %)
Extrudate4	HEC, 4	H ₂ O	-	7 (-99 %)
Pellet	-	-	62	150 (-75 %)

HEC – 2-hydroxyethylcellulose.

Chapter V – Upscaling and Shaping

As evidenced, the upscaling of UiO-66-SO₃H-W resulted in a porous solid displaying a surface area of 600 m²·g⁻¹ which agrees well with the 639 m²·g⁻¹ of the powder obtained at small scale (chapter IV, Table IV.2). It is clear that upon compression, the UiO-66-SO₃H-W pellet underwent a dramatic loss in surface area exhibiting 150 m²·g⁻¹ which is 75 % less than that of the pristine powder. Indeed, such decrease is expected due to the destructive impact of the applied pressure and was previously observed for a wide variety of MOFs [1–5]. Specifically, UiO-66 possesses high structural stability against elevated pressure and therefore can handle a considerable pressure up to 665 MPa while preserving its surface area [6]. At the same time, its functionalized analogues such as UiO-66-NH₂ and UiO-66-COOH experienced a considerable loss of their porosity upon pelletization at lower pressures, underlining their less stable frameworks [7–9]. Nevertheless, there is no data on pelletized UiO-66-SO₃H so far and the mild pressure applied (62 MPa) on UiO-66-SO₃H-W in this work led to the remarkable loss of its textural properties. This might originate from the highly defective framework of UiO-66-SO₃H-W as discussed in chapter IV.

On the other hand, extrusion is a shaping technique which requires fewer pressure but necessitates the formation of a paste composed of the parent powder, a binder and a plasticizer. Such paste is further drawn through a narrow nozzle of few millimeters and subsequently cut into smaller cylinders (extrudates) and dried [1]. The total HEC contents of 2 wt.% and 4 wt.% were chosen as an average of what is used in the literature for organic polymers as the binder [10–12]. Thus-prepared extrudates are depicted in figure V-2 (iii).



Figure V-2. Photographs of the pelletized (i) and extruded UiO-66-SO₃H-W before (ii) and after cutting and drying (iii).

As evident from figure V-3 (i), upon shaping the N₂ isotherms underwent a certain change in their shape along with a considerable drop of adsorbed nitrogen over the whole range of pressures. Notably, the pelletized UiO-66-SO₃H-W presents a decreased N₂ uptake at relative pressure >0.90 and a small hysteresis between 0.45 and 0.80 as compared to the pristine powdery UiO-66-SO₃H-W. This indicates a loss of macroporous volume and creation of mesopores upon pelletization following reduction of the free void space between individual crystals. Some mesopores could also be created following a partial framework degradation. At the same time, Extrudate2 exhibits a remarkable increase of adsorbed N₂ at relative pressure >0.9 contrary to the pelletized MOF. This might suggest that the binder is responsible for the generation of additional macroporous void space between the crystals.

The loss in surface area upon extrusion usually comes from pore blocking effect by the binder and strongly depends on its nature and percentage in the final extrudates. Mostly, organic polymers are used as binders (polyvinyl alcohol or methyl cellulose) therefore providing H-bonding with the parent powder through their functional groups. The latter ensures mechanical stability of extrudates. HEC has been used as a binder in several previous works and led to a certain decrease of surface area [8,12–14]. In this work, however, addition of relatively small quantities of HEC

(2 wt.% to 4 wt.%) led to a surprisingly high drop of surface areas (from 68 % to 99 %, respectively).

So far, there is no report on the extrusion of UiO-66-SO₃H and therefore no reference is available. Nevertheless, it is possible to hypothesize that the severe pore blocking in Extrudate2 and Extrudate4 in spite of the low amounts of binder is due to the specifics of the MOF itself. In particular, sulfonic acid groups, -SO₃H, serve as a great source of hydrogen bonding due to their saturation with oxygen. When contacted with hydrogen-rich HEC, -SO₃H might establish numerous H-bonds which would be strong enough to cause a partial framework collapse. This can be visualized by examining their XRD patterns (figure V-3, ii).

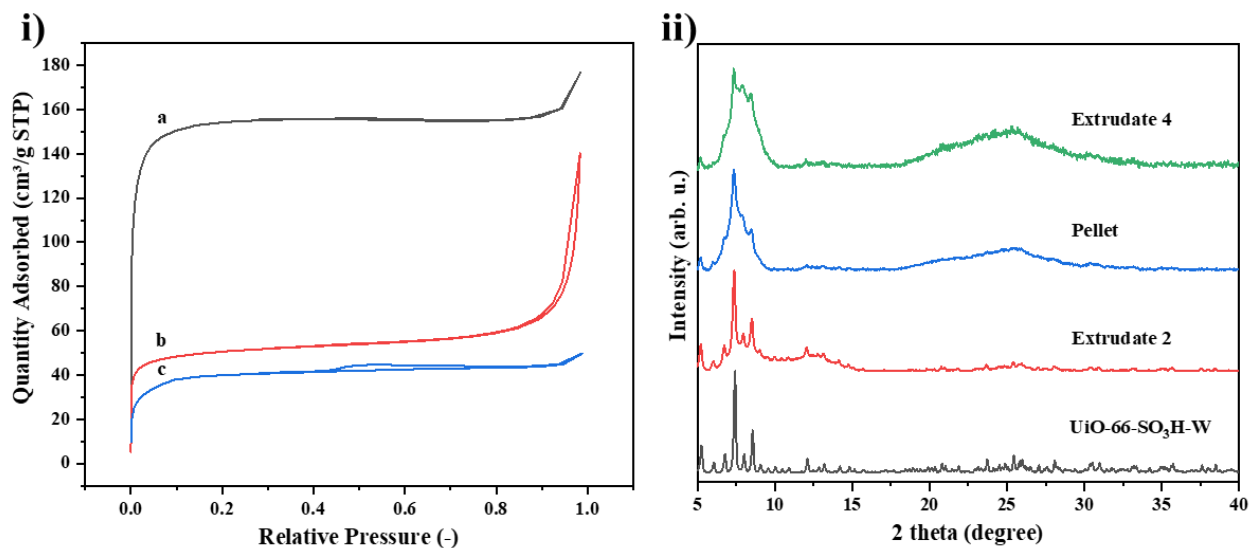


Figure V-3. N₂ isotherms (i) of powdery UiO-66-SO₃H-W (a), Extrudate2 (b) and pellet (c) as well as their corresponding XRD patterns (ii).

Accordingly, all the shaped solids underwent amorphization to a certain extent as compared to the pristine UiO-66-SO₃H-W, viewed as the remarkable broadening of the reflections at 5-10 ° and 20-30 °. MOF amorphization is the result of bond breakage between the Zr-clusters and the linkers and it can be the result of sufficient applied pressures as already reported in several studies [2, 4,

7]. In the case of extrudates, amorphization is suspected to be due to the presence of HEC forming strong H-bonding with the MOF linkers (HEC)-O-H \cdots O-(MOF) due to the high electronegativity of oxygen. Therefore, the observed amorphization can take place as a consequence of the participation of neighboring -SO₃H groups in H-bonding with the same HEC molecule thus causing framework distortion and finally amorphization. Moreover, Hu *et al.* [15] showed that UiO-66-SO₃H can even undergo amorphization due to the H-bonding formed between -SO₃H groups located in close proximity to one another. The reverse recrystallization of the framework was achieved by elimination of the H-bonding *via* H⁺ to Na⁺ ion-exchange.

This hypothesis can be further supported by the fact that both extrudates preserved the positions and intensity of the principal framework vibrations in their IR spectra suggesting framework integrity, contrary to the XRD patterns (figure V-4).

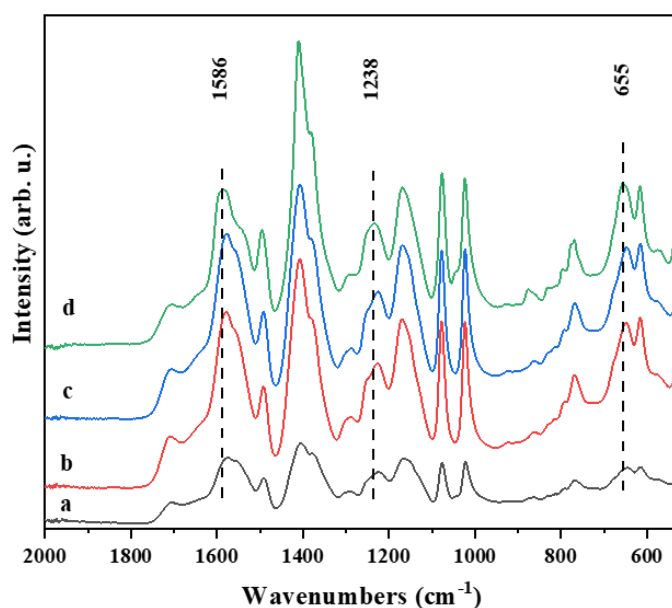


Figure V-4. ATR-IR bands of the pellet (a), Extrudate2 (b), Extrudate4 (c) and pristine UiO-66-SO₃H-W (d).

Thus, a certain shift towards lower wavenumbers is observed for the bands at 655 cm^{-1} (shifted to 651 cm^{-1}), 1238 cm^{-1} (shifted to 1230 cm^{-1}), and 1586 cm^{-1} (shifted to 1582 cm^{-1}) as compared to the pristine powder. This is due to formation of the H-bonding as predicted by Hu *et al.* [15]. Importantly, the pelletized UiO-66-SO₃H-W experienced a remarkable loss in intensity of its IR bands suggesting a partial framework degradation also suggested by its XRD pattern.

1.2. Powder vs Shaped Object: Catalytic Performance

The catalytic performance of the shaped solids was evaluated in fructose dehydration and compared to the parent powdered solids. Batch reactions were conducted in a 250-mL reactor equipped with a catalyst basket as described in chapter II. The reaction conditions were chosen to eliminate the solvent effect on fructose dehydration. Table V.3 represents thus-obtained results.

Table V.3 - Fructose conversion and HMF yield over a series of powdery and shaped UiO-66-SO₃H-W.

Catalyst	T, °C	t, h	Solvent	Fr. conv., %	HMF y-d, %	Δm_{cat} , % ^a
Blank	60	24	DMSO	0	0	-
UiO-66-SO ₃ H-W ^b	60	24	DMSO	68	39	-
UiO-66-SO ₃ H-W ^c	60	24	DMSO	43	17	-
Extrudate2	60	24	DMSO	14	3	14
Extrudate4	60	24	DMSO	0	0	8
Pellet	60	24	DMSO	20	6	27

Reaction conditions: P_{atm} , 300 rpm, $V_{\text{DMSO}} = 150\text{ mL}$, $C_{\text{fruc}} = 0.6\text{ mM}$, $m_{\text{cat}} = 1.5\text{ g}$ (on MOF basis).

a – mass loss of the shaped catalyst after the reaction;

b – powdery UiO-66-SO₃H-W tested in 2 mL reaction volume;

c – powdery UiO-66-SO₃H-W tested in 150 mL reaction volume.

As evident, DMSO has no contribution to fructose conversion at 60 °C as confirmed by the blank test. Once again, UiO-66-SO₃H-W demonstrated its superior catalytic activity converting 43 % fructose and yielding 17 % HMF at such low temperature. Interestingly, it is somewhat lower than

when the test was performed in small carousel-type reactors under the same conditions, which showed 68 % conversion and 39 % HMF yield. The difference in reaction volumes (2 mL vs 150 mL) and related stirring inhomogeneity could be at the origin of the decreased reaction kinetics due to diffusion limitations in the 250-mL reactor. The extruded MOFs exhibited a poor performance with Extrudate4 being completely inactive. As described in the characterization part, it was expected as this extrudate composition led to a severe structural collapse viewed as amorphization. At the same time, its analogue *i.e.* Extrudate2 demonstrated 14 % fructose conversion with 3 % HMF yield. This can be explained by the lowered binder amount in Extrudate2 as opposed to Extrudate4 which led to less drastic structural collapse viewed as a partial preservation of the surface area. Nevertheless, as it was hypothesized a part of acid $-SO_3H$ sites remain unavailable due to the H-bonding with the binder thus explaining negligible 3 % HMF yield. Additionally, the presence of the binder can greatly limit the diffusion of fructose/HMF onto/from the active sites as polymeric HEC covers the UiO-66- SO_3H -W crystals (figure V-5).

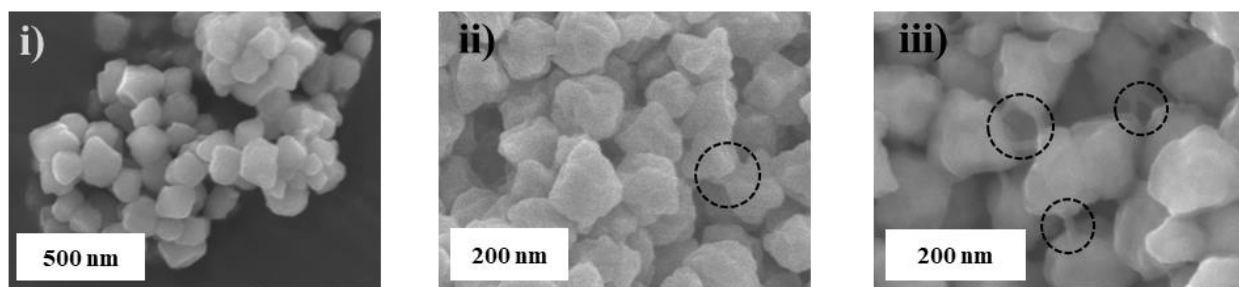


Figure V-5. SEM micrographs of UiO-66- SO_3H -W (i), Extrudate2 (ii) and Extrudate4 (iii); HEC binder is shown in dashed circles.

At the same time, the pellet demonstrated 20 % fructose conversion with 6 % HMF yield which rather suggests an enhanced performance with respect to Extrudate2. It can be speculated that in spite of the considerable framework amorphization under the applied pressure, the active $-SO_3H$ sites are still available and not blocked by a binder.

Chapter V – Upscaling and Shaping

Lastly, mechanical stability of shaped solids is an important parameter to consider in order to provide an adequate performance in a targeted application. Nowadays, there are numerous ways to probe the mechanical stability from sophisticated compression and attrition tests to simple crush or drop-tests [16–20]. In this work, attrition was estimated by simply weighing the shaped solids after 24 h of reaction and comparing to their starting mass. For this, each solid was filtered, washed properly in ethanol and dried before weighing. Thus, the pelletized UiO-66-SO₃H-W experienced the most dramatic mass loss of 27 % which is considerably higher than that of Extrudate2 (14 %) and Extrudate4 (8 %). This highlights the reinforcing effect of the binder as a function of its content.

2. Conclusion

To sum up this chapter, the synthesis of UiO-66-SO₃H-W produced in water was demonstrated to be easily scalable by a factor of 30. Structural and textural properties of thus-produced powder agree well with those observed for the small-scale synthesis. Further shaping *via* pelletization at 62 MPa, revealed a considerable framework amorphization along with a remarkable 77 % loss in surface area. Still, the pellets demonstrated a certain catalytic activity in fructose dehydration meaning that in spite of the severe framework collapse, the active sites were still accessible. On the other hand, extrusion with HEC as the binder displayed as well consequent structural degradation, which was more remarkable with the highest binder content (4 wt.%). The latter is thought to be responsible of complete pore blocking. It was hypothesized that strong H-bonding formed between the MOF linker and the binder is at the origin of this degradation. This can be supported by the fact that upon reduction of the binder content down to 2 wt.% the extrudates exhibited less structural collapse and therefore larger available surface area than that with 4 wt.% binder. As a result, it showed a certain activity in fructose dehydration therefore implying a partial availability of the active sites. Importantly, it was shown that the binder content defines the mechanical stability towards attrition of the shaped objects estimated as a percentage of the recoverable part of the solid after application. Therefore, it is possible to state that a higher binder content provides a higher mechanical stability but deteriorated textural/structural properties and therefore worse catalytic performance. With this being said, a further optimization of the shaping of UiO-66-SO₃H-W should be considered with a certain stress on the binder choice. Replacement of the polymeric organic compound used in this work by an inorganic binder (silica or alumina) might seem pertinent.

3. References:

- [1] B. Yeskendir, J. Dacquin, Y. Lorgouilloux, C. Courtois, S. Royer, J. Dhainaut, From metal–organic framework powders to shaped solids: recent developments and challenges, *Mater. Adv.* 2 (2021) 7139–7186. <https://doi.org/10.1039/d1ma00630d>.
- [2] J. Alcañiz-Monge, G. Trautwein, M. Pérez-Cadenas, M.C. Román-Martínez, Effects of compression on the textural properties of porous solids, *Microporous Mesoporous Mater.* 126 (2009) 291–301. <https://doi.org/10.1016/j.micromeso.2009.06.020>.
- [3] R.P.P.L. Ribeiro, C.L. Antunes, A.U. Garate, A.F. Portela, M.G. Plaza, J.P.B. Mota, I.A.A.C. Esteves, Binderless shaped metal-organic framework particles: Impact on carbon dioxide adsorption, *Microporous Mesoporous Mater.* 275 (2018) 111–121. <https://doi.org/10.1016/j.micromeso.2018.08.002>.
- [4] D. Bazer-bachi, L. Assié, V. Lecocq, B. Harbuzaru, V. Falk, Towards industrial use of metal-organic framework : Impact of shaping on the MOF properties, *Powder Technol.* 255 (2014) 52–59. <https://doi.org/10.1016/j.powtec.2013.09.013>.
- [5] T. Remy, S.A. Peter, S. Van Der Perre, D.E. De Vos, G. V Baron, J.F.M. Denayer, Selective Dynamic CO₂ Separations on Mg-MOF-74 at Low Pressures : A Detailed Comparison with 13X, *J. Phys. Chem. C.* 117 (2013) 9301–9310. <https://doi.org/10.1021/jp401923v>.
- [6] S.E. Bambalaza, H.W. Langmi, R. Mokaya, N.M. Musyoka, L.E. Khotseng, Compaction of a zirconium metal–organic framework (UiO-66) for high density hydrogen storage applications, *J. Mater. Chem. A.* 6 (2018) 23569–23577. <https://doi.org/10.1039/C8TA09227C>.
- [7] J. Dhainaut, J. Troyano, A. Legrand, J. Canivet, I. Imaz, D. MasPOCH, H. Reinsch, D. Farrusseng, Systematic study of the impact of MOF densification into tablets on textural and mechanical properties, *CrystEngComm.* 19 (2017) 4211–4218. <https://doi.org/10.1039/C7CE00338B>.
- [8] Y. Khabzina, J. Dhainaut, M. Ahlhelm, H. Richter, H. Reinsch, N. Stock, D. Farrusseng, Synthesis and Shaping Scale-up Study of Functionalized UiO-66 MOF for Ammonia Air Purification Filters, *Ind. Eng. Chem. Res.* 57 (2018) 8200–8208. <https://doi.org/10.1021/acs.iecr.8b00808>.
- [9] G.W. Peterson, J.B. Decoste, F. Fatollahi-fard, D.K. Britt, Engineering UiO-66-NH₂ for Toxic Gas Removal, *Ind. Eng. Chem. Res.* 53 (2014) 701–707. <https://doi.org/10.1021/ie403366d>.
- [10] J.A. Delgado, V.I. Águeda, M.A. Uguina, P. Brea, C.A. Grande, Comparison and evaluation of agglomerated MOFs in biohydrogen purification by means of pressure swing adsorption (PSA), *Chem. Eng. J.* 326 (2017) 117–129. <https://doi.org/10.1016/j.cej.2017.05.144>.
- [11] C.A. Grande, V.I. Águeda, A. Spjelkavik, R. Blom, An efficient recipe for formulation of metal-organic Frameworks, *Chem. Eng. Sci.* 124 (2015) 154–158. <https://doi.org/10.1016/j.ces.2014.06.048>.
- [12] M. Kriesten, V. Schmitz, J. Siegel, C.E. Smith, M. Kaspereit, M. Hartmann, Shaping of

- Flexible Metal-Organic Frameworks: Combining Macroscopic Stability and Framework Flexibility, *Eur. J. Inorg. Chem.* 2019 (2019) 4700–4709. <https://doi.org/10.1002/ejic.201901100>.
- [13] J. Kim, S. Kim, S. Yang, W. Ahn, Materials Bench-scale preparation of Cu₃(BTC)₂ by ethanol reflux: Synthesis optimization and adsorption / catalytic applications, *Microporous Mesoporous Mater.* 161 (2012) 48–55. <https://doi.org/10.1016/j.micromeso.2012.05.021>.
- [14] G. Majano, J. Pérez-ramírez, Scalable Room-Temperature Conversion of Copper (II) Hydroxide into HKUST-1 (Cu₃(btc)₂), *Adv. Mater.* 25 (2013) 1052–1057. <https://doi.org/10.1002/adma.201203664>.
- [15] Z. Hu, J. Lin, N. Ogiwara, A. Rodriguez, Y. Peng, Y. Wang, S. Horike, D. Zhao, A pH-responsive phase transformation of a sulfonated metal–organic framework from amorphous to crystalline for efficient CO₂ capture, *CrystEngComm.* 18 (2016) 2803–2807. <https://doi.org/10.1039/C6CE00369A>.
- [16] E. Hastürk, C. Schlüsener, J. Quodbach, A. Schmitz, C. Janiak, Microporous and Mesoporous Materials Shaping of metal-organic frameworks into mechanically stable monoliths with poly (vinyl alcohol) by phase separation technique, *Microporous Mesoporous Mater.* 280 (2019) 277–287. <https://doi.org/10.1016/j.micromeso.2019.02.011>.
- [17] T. Tian, J. Velazquez-Garcia, T.D. Bennett, D. Fairen-Jimenez, Mechanically and chemically robust ZIF-8 monoliths with high volumetric adsorption capacity, *J. Mater. Chem. A.* 3 (2015) 2999–3005. <https://doi.org/10.1039/c4ta05116e>.
- [18] A.H. Valekar, K. Cho, U. Lee, S. Lee, W. Yoon, Y.K. Hwang, G. Lee, J. Cho, J. Chang, RSC Advances granules using mesoporous r-alumina as a binder, *RSC Adv.* 7 (2017) 55767–55777. <https://doi.org/10.1039/C7RA11764G>.
- [19] J. Ren, N.M. Musyoka, H.W. Langmi, A. Swartbooi, B.C. North, M. Mathe, A more efficient way to shape metal-organic framework (MOF) powder materials for hydrogen storage applications, *Int. J. Hydrogen Energy.* 40 (2015) 4617–4622. <https://doi.org/10.1016/j.ijhydene.2015.02.011>.
- [20] S. Hindocha, S. Poulston, Study of the scale-up , formulation , ageing and ammonia adsorption capacity of MIL- 100 (Fe), Cu-BTC and CPO-27 (Ni) for use in respiratory protection fi lters, *Faraday Discuss.* 201 (2017) 113–125. <https://doi.org/10.1039/c7fd00090a>.

6. General Conclusion and Perspectives

The present thesis aimed at designing microporous solids with desired physico-chemical properties for application in the catalytic transformation of monosaccharides. For this purpose, two similar reactions were chosen *i.e.* fructose dehydration to HMF and glucose isomerization to fructose proceeding on Brønsted acid sites and Lewis acid or base sites, respectively. Therefore, the microporous solids were, in turn, chosen accordingly so that they exhibited intrinsic acidic properties. Thus, two well-known acid solids were considered in this work: MFI-type ZSM-5 zeolite and UiO-66-type MOFs belonging to inorganic and organic-inorganic hybrid class of microporous crystalline solids, respectively.

Within the scope of this thesis, several important points were addressed in the case of zeolites. First of all, a particular emphasis was given to isomorphous substitution of the framework Al by Zr atoms in the MFI-type zeolite. This resulted in two similar synthesis methods resulting in two major solids: [Si,Zr]-MFI-in and [Si,Zr]-MFI-ex both poorly described in the literature probably because of the difficulties associated with characterization of these solids. Nevertheless, it was shown in this work that it was possible to distinguish [Si,Zr]-MFI-in, the solid with Zr incorporated in the framework, from [Si,Zr]-MFI-ex in which Zr is mostly present as an extra-framework species. It should be noted that Zr is a challenging nucleus for ^{91}Zr MAS NMR and therefore the latter cannot be used as a conventional technique to examine the coordination of Zr atoms within the MFI framework. This encouraged us to seek alternative approaches to characterize Zr-silicates and investigate the location and chemical environment of Zr atoms. This was done by combination of bulk and surface techniques which enabled qualitative and quantitative insights into Zr atoms in the two Zr-silicates. Further characterization demonstrated that, in spite of its location, Zr considerably modifies acidic properties of zeolites by eliminating completely Brønsted acid sites

General Conclusion and Perspectives

and generating rather weak Lewis acid sites. When further applied as catalysts, both solids showed no activity towards fructose dehydration to HMF regardless the used solvent. This was somewhat expected as neither [Si,Zr]-MFI-in nor [Si,Zr]-MFI-ex exhibited Brønsted acid sites. Besides, a dramatic dissolution was observed upon catalytic tests in DMSO. However, when applied in glucose isomerization [Si,Zr]-MFI-in showed no conversion either therefore allowing to make a few important conclusions. First: weak Lewis acid sites are incapable of glucose isomerization and second: another strategy should be considered to make Zr-silicates active in the given reaction. In this regard, the base-catalyzed glucose isomerization route seemed pertinent. Due to the NaOH used for the synthesis, [Si,Zr]-MFI-ex exhibited a certain amount of basic sites probed by CO₂-TPD and accounted for 34 μmol·g⁻¹. The latter are associated with zirconium oxide amorphous phase deposited on the surface of SiO₂ crystals and therefore available for guest molecules. As a consequence, it displayed a good catalytic performance converting 26 % glucose and yielding 25 % fructose after 3 h of reaction at 120 °C. When compared to the literature, these results are similar to the best reported so far over the hierarchical micro/mesoporous basic NaY zeolite impregnated with 5 wt.% MgO. The latter showed the remarkable 100 % fructose selectivity at 34 % glucose conversion after 2 h of reaction at 100 °C. However, this solid is the product of a difficult and long synthesis procedure including hierarchization and impregnation, while [Si,Zr]-MFI-ex seems relatively easy to prepare and requires no additional post-synthesis steps after calcination.

Similarly, a considerable attention was given to alteration of acidic properties in the case of UiO-66 which yielded a series of functionalized MOFs. Firstly, it was shown that direct framework functionalization *via* insertion of -SO₃H groups could yield UiO-66-SO₃H with 25 %, 50 %, 75 % and 100 % functionalization degree at a progressive drop of textural properties. This was feasible due to DMF used as solvent in which the two employed linkers *i.e.* terephthalic acid and

General Conclusion and Perspectives

monosodium 2-sulfoterephthalic acid are readily soluble. All functionalized UiO-66-SO₃H-D exhibited the same crystallographic properties as the parent UiO-66. Besides, as it was demonstrated by IR spectroscopy, DMF was still present in the synthesized solids in spite of several consecutive washing steps. Thus, when applied in fructose dehydration in DMSO, UiO-66-SO₃H-DMOFs demonstrated illogical trends with UiO-66-SO₃H-D-25 outperforming UiO-66-SO₃H-D-50 and UiO-66-SO₃H-D-75 in terms of HMF selectivity (58 % vs 51 % vs 51 %) in spite of the lower functionalization degree. This was attributed to the inhibiting effect of DMF on fructose dehydration in DMSO. At the same time, UiO-66-SO₃H-D-100 displayed the highest activity converting 97 % fructose and yielding 64 % HMF after 2 h of reaction at 100 °C. However, when performed the kinetic study, UiO-66-SO₃H-D-100 showed slow conversion rates after 30 min and 1 h (29 % and 50 %) lower than that of the blank test (45 % and 55 %). This further supports the inhibiting effect of DMF on fructose dehydration in DMSO.

In order to eliminate this negative effect, DMF was replaced by water for the direct functionalization of UiO-66 to form UiO-66-SO₃H-W. This is only possible at 100 % functionalization degree because of the limited solubility of terephthalic acid in water. Nevertheless, this water-assisted synthesis resulted in a highly porous but yet highly defective framework. The increased number of the structural defects are at the origin of its increased unit cell and subsequent lowering of the crystallographic symmetry. Thus, it changes from the face-centered cubic system of UiO-66 topology (*Fm-3m* with $a = 20.7809(3)$ Å) to the body-centered cubic system (*Im-3* with $a = 41.4440(8)$ Å). Nevertheless, UiO-66-SO₃H-W showed the highest activity in fructose dehydration among all the tested solids in this work. It readily reaches the complete conversion (>98 %) after only 30 min of reaction at 100 °C in DMSO yielding 48 % HMF. The kinetic profile showed a gradual increase of HMF formation reaching the maximum of

General Conclusion and Perspectives

78 % after 6 h. Besides, UiO-66-SO₃H-W demonstrated a decent performance at lowered temperature of 80 °C converting 81 % fructose with 52 % HMF yield after 3 h while DMSO had no contribution. Even at a lower temperature of 60 °C, UiO-66-SO₃H-W showed its superior catalytic activity converting 68 % fructose with 39 % HMF yield after 24 h. This agrees well with respectively 69 % and 41 % demonstrated by Amberlyst-15[®], a commercial solid acid, under the same conditions. Also, upon 3 consecutive catalytic runs at 80 °C and 100 °C, UiO-66-SO₃H-W lost its catalytic activity but retained its structural integrity up to 9 consecutive runs. This suggests rather a robust and stable framework and its deactivation by a remarkable humin deposition on its active sites and not by structural collapse.

UiO-66-SO₃H-W also demonstrated an appealing performance in glucose isomerization to fructose. It allowed the direct transformation of glucose to HMF through the intermediate Lewis acid catalyzed glucose-to-fructose isomerization and Brønsted acid catalyzed fructose-to-HMF dehydration steps. This is possible due to their positive synergetic effect. Thus, after 3 h of reaction at 120 °C, UiO-66-SO₃H-W converted 13 % glucose yielding 7 % HMF. This is somewhat different from the results reported in the literature which stated rather high fructose yields without considerable HMF formation. The latter might be due to the effect of DMF which inhibits further fructose dehydration as UiO-66-SO₃H is predominantly synthesized in DMF. This further underlines the importance of avoiding the use of this solvent for synthesis purpose.

Such DMF-free synthesis approach was also applied to a series of functionalized UiO-66 MOFs and included UiO-66-COOH, UiO-66-OH and UiO-66-NH₂. All the three yielded highly crystalline microporous solids. Despite its clearly acidic nature, UiO-66-COOH showed no activity in fructose dehydration in DMSO showing nearly the same performance as the blank test itself. Therefore, this suggests weak Brønsted acid sites generated by insertion of carboxylic

General Conclusion and Perspectives

groups. In this regard, UiO-66-OH somewhat surpassed the performance of UiO-66-COOH converting 23 % fructose with 5 % HMF yield after 24 h of reaction at 60 °C while the latter showed no conversion. Finally, upon glucose isomerization over the basic UiO-66-NH₂, conversion reached 11 % with only 2 % fructose yield. Such low selectivity towards fructose agrees well with the results reported in the literature and is explained by the strong basic properties of amino groups which strongly bind glucose. Therefore, UiO-66-SO₃H-W demonstrated the highest catalytic activity in fructose dehydration to HMF as well as in glucose isomerization to fructose further provoking its dehydration to HMF.

Based on its exceptional catalytic performances, UiO-66-SO₃H-W was further chosen as the candidate for synthesis upscaling and shaping. Water-assisted synthesis was thus beneficial as to avoid the aggressive and toxic DMF. After a quick optimization of the synthesis on milligram scale, a 30-times scale-up was successfully performed resulting in a highly crystalline microporous solid similar to the one derived from the small-scale synthesis. Upon pelletization, surface area of UiO-66-SO₃H-W drastically dropped by 75 % from 600 m²·g⁻¹ to 150 m²·g⁻¹ at the same time experiencing a partial amorphization due to the applied pressure. Nevertheless, UiO-66-SO₃H-W pellets still exhibited activity in fructose dehydration reaching 20 % conversion with 6 % HMF yield as compared to respectively 43 % and 17 % of the parent powder. This means that the active -SO₃H are still available after pelletization. In the case of extrusion, UiO-66-SO₃H-W was found to be highly dependent on the binder content, 2-hydroxyethylcellulose. Specifically, at 4 wt.% (Extrudate4) the binder completely blocked the available surface area while at 2 wt.% (Extrudate2) the 68 % decrease from 600 m²·g⁻¹ to 192 m²·g⁻¹ was observed. The latter exhibited 14 % fructose conversion with 3 % HMF yield due to a part of surface area still available after formulation. Importantly, such dramatic drop of textural properties and amorphization of UiO-66-SO₃H-W after

General Conclusion and Perspectives

extrusion with a low amount of binder was hypothesized to originate from its strong interaction with the MOF *via* H-bonding.

With this being said, the further progress of this work should be focused on several points:

-complete evaluation of [Si,Zr]-MFI-ex on glucose isomerization by optimizing reactions conditions: temperature, duration and catalyst loading. Catalyst reusability and regeneration under the optimized conditions should be addressed. Cation exchange to replace Na^+ by K^+ or Mg^{2+} to increase the catalyst basicity is possible with a special care given to cation leaching.

-[Si,Zr]-MFI-in could be further studied to give more insights into the chemical environment and local structure of Zr atoms in the MFI framework. X-Ray Absorption Spectroscopy performed in a synchrotron facility might provide valuable information.

-UiO-66-SO₃H-W should be further studied on glucose isomerization. Similar to [Si,Zr]-MFI-ex, the reaction conditions need to be optimized with a special interest in HMF. Therefore, the potential of UiO-66-SO₃H-W in the direct glucose-to-HMF conversion should be further examined.

-Shaping procedure UiO-66-SO₃H-W should be optimized as well. A detailed study on the binder choice needs to be done for extrusion with a slight preference for inorganic binders. Ideally, the most appropriate shaping technique for UiO-66-SO₃H-W (extrusion, 3D printing or granulation) should be established.

ANNEX

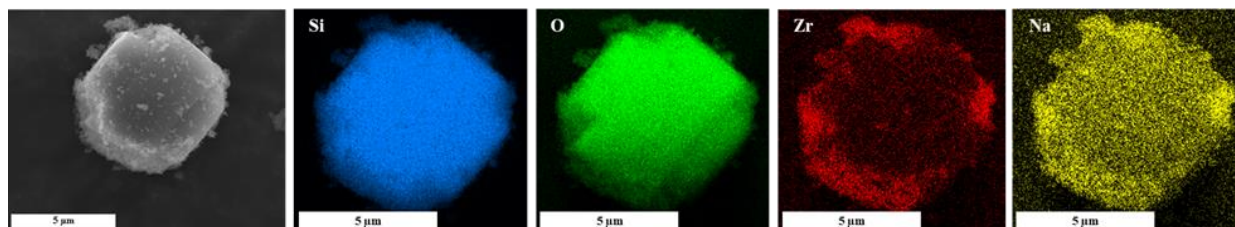
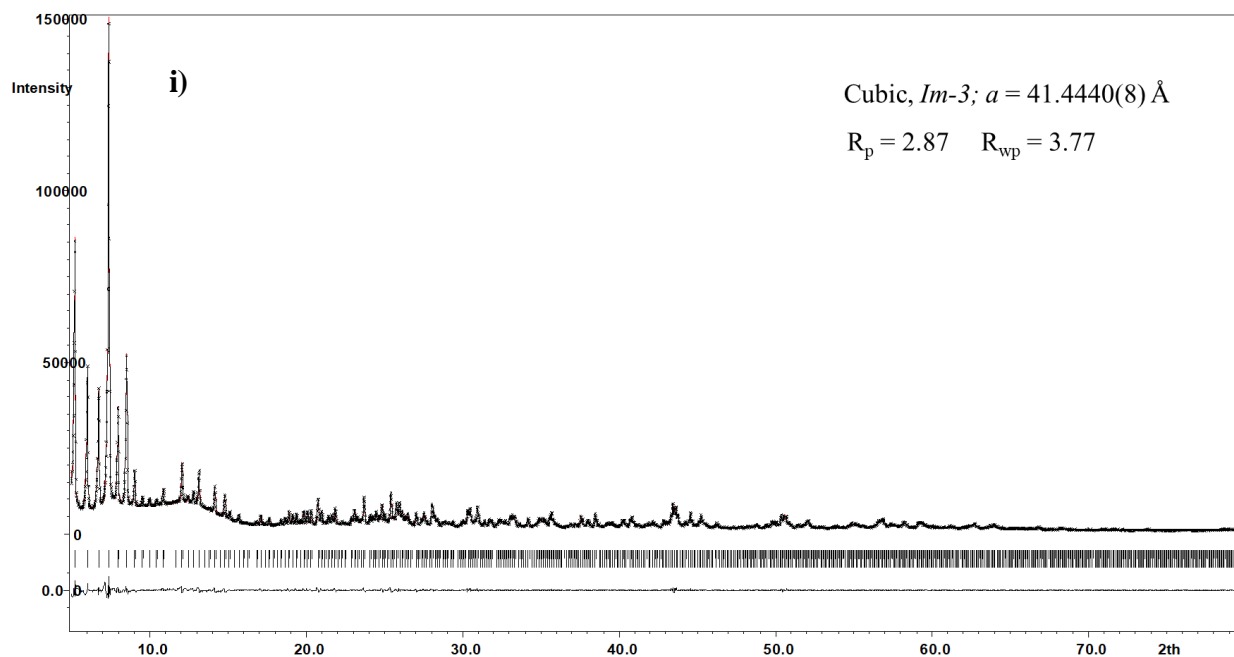


Figure annex-1. SEM micrograph and elemental mappings of [Si,Zr]-MFI-ex showing the near localization of Zr and Na to one another.



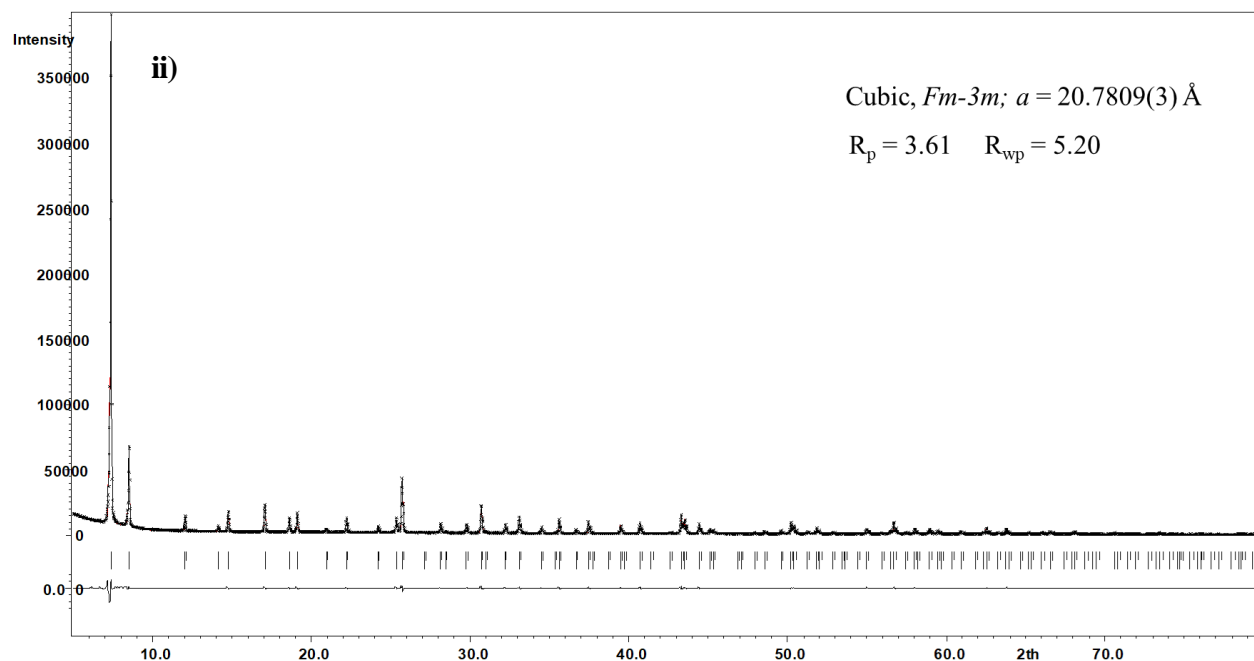


Figure annex-2. Structural refinement of UiO-66-SO₃H-W (i) and UiO-66 (ii) by Le Bail fitting with the difference between observed and calculated patterns. Refinement details and reliability factors (R_p and R_{wp}) are given in the inset.

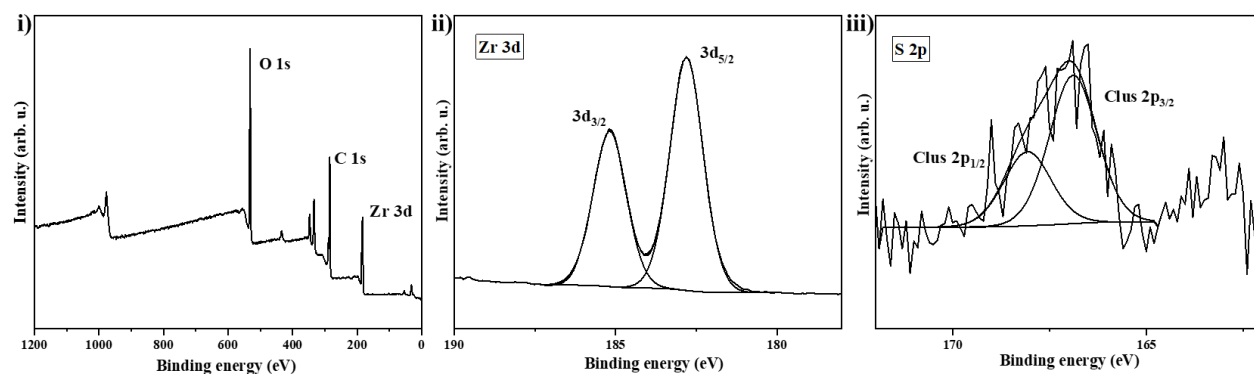


Figure annex-3. XPS survey spectrum (i) as well as Zr 3d (ii) and S 2p (iii) contributions showing the presence of S-species in the cluster of UiO-66.

Annex



Figure annex-4. Color of two blank tests: in DMSO only (left) and in 3:1 (v:v) DMSO/DMF mixture (right) mixture after 2 h at 100 °C.